THESIS FOR THE DEGREE OF DOCTOR OF PHILOSOPHY

AC microgrids for grid capacity and resilience enhancement

On the sizing and control of AC microgrids to alleviate grid capacity bottleneck and facilitate secure island transition of critical facilities

AHMED SUNJAQ

Department of Electrical Engineering
CHALMERS UNIVERSITY OF TECHNOLOGY
Gothenburg, Sweden, 2025

AC microgrids for grid capacity and resilience enhancement

On the sizing and control of AC microgrids to alleviate grid capacity bottleneck and facilitate secure island transition of critical facilities

Ahmed Sunjaq

ISBN 978-91-8103-302-1

Doktorsavhandlingar vid Chalmers tekniska högskola
Ny serie nr 5759
ISSN 0346-718X
https://doi.org/10.63959/chalmers.dt/5759

Department of Electrical Engineering
Chalmers University of Technology
SE-412 96 Gothenburg, Sweden
Phone: +46 (0)31 772 1000

Cover:
Two generic microgrids interconnected by power electronics and operating normally in grid-connected mode with the ability to transfer to island mode.

Printed by Chalmers Digital Printing
Gothenburg, Sweden, November 2025

AC microgrids for grid capacity and resilience enhancement

On the sizing and control of AC microgrids to alleviate grid capacity bottleneck and facilitate secure island transition of critical facilities

AHMED SUNJAQ
Department of Electrical Engineering
Chalmers University of Technology

Abstract

Sweden's climate goals drive large-scale electrification across the industrial, transportation, and heat sectors, challenging electricity system operators due to infrastructure overloading. Upgrading this infrastructure is time-consuming and could hinder electrification efforts. Alongside this, grid operators must meet increasing demand while ensuring reliable power supply, especially for critical facilities. Traditionally, these facilities rely on gas or diesel generators for backup, which are environmentally unfriendly.

This thesis investigates the microgrid solution powered by renewable generation and energy storage to facilitate the electrification process. The thesis focuses on the use of microgrid solution to provide two critical grid functions.

The first one being the alleviation of grid capacity bottleneck by **reducing local peak net demand**. Various microgrid solutions are explored, including separate microgrids based on battery energy storage system (BESS), and interconnected microgrids by back-to-back (B2B) converter or multiport converter (MPC). A linear optimization problem is developed to find the cost-optimal solution without the net demand exceeding microgrids power subscription limit. Results suggest MPC interconnection can reduce investment in energy storage and power electronics when microgrids exhibit a low or intermediate coincidence factor of their net load profiles.

The second microgrid function addresses the **unplanned secure island transition** of a critical facility, using a hydro-powered microgrid as a case study. A criterion for secure island transition is developed that accounts for frequency and voltage security constraints.

To meet frequency security constraints, a novel BESS frequency controller based on a Proportional-Integral (PI) controller with droop is developed. The controller tuning accounts for the response time of the hydro power plant (HPP) governor to provide coordinated and communication-less frequency support without over-sizing the energy storage. The proposed controller is validated through performance comparison with existing controllers in the literature and laboratory experiments. Results indicate the PI-based droop controller requires less energy reserve from the battery than the commonly used proportional (P) controller.

The voltage stability of the microgrid is challenged by significant reactive power drawn by industry motors during island transition transients. Analysis shows key factors for voltage stability are the online HPP capacity and the point of applicability of the reactive power requirement.

Keywords: Microgrid, interconnected microgrids, battery energy storage system (BESS), back-to-back (B2B) converter, multiport converter (MPC), island operation, island transition, grid capacity bottleneck, frequency stability, voltage stability.

To my family, friends, and teachers.

Contents

2 Sizing of BESS and multiport converter in microgrids to mitigate grid capacity bottleneck 17

3 Control of BESS to improve frequency stability of hydro-powered microgrid during island transition 59

Acknowledgments

First and foremost, I offer my deepest gratitude to Allah for providing me with the steadfastness needed to complete this long journey of more than five years.

I am profoundly grateful to my main supervisor, Associate Professor Peiyuan Chen, for his invaluable guidance and constructive feedback throughout my studies. I extend my thanks to my assistant supervisors, Adjunct Docent Ritwik Majumder (Epiroc), Adjunct Professor Jan R Svensson (Hitachi Energy Research), and Bengt Johansson (Solvina), for their insightful feedback, particularly regarding industrial practices. Special thanks go to my examiner Professor Massimo Bongiorno, for his exceptional commitment in participating in my supervision meetings despite his demanding schedule.

This work would not have been possible without the generous funding provided by the Swedish Energy Agency, initially through the ERA-Net Smart Energy Systems REGSYS, and subsequently through the program on kunskaps- och kompetensutveckling för framtidens elsystem. I am deeply appreciative of this support.

I am also very thankful to my office mate, Doctor Anant Narula, for the valuable discussions and for sharing his expertise in grid forming control, which significantly enriched the content of this thesis.

Finally, I would like to express my heartfelt gratitude to my family and friends for their unwavering support and companionship, which made this journey more enjoyable and manageable.

Ahmed Sunjaq
Gothenburg, Sweden
October 2025

Acronyms

AC:	Alternating current
aFRR:	Automatic frequency restoration reserve
AVR:	Automatic voltage regulator
BESS:	Battery energy storage system
B2B:	Back-to-back
CAPEX:	Capital expenditure
CB:	Circuit breaker
C&I:	Commercial & industrial
DC:	Direct current
DCC:	Demand Connection Code
DSO:	Distribution System Operator
EENS:	Expected energy not served
EIFS:	Energimarknadsinspektionens föreskrifter
EMF:	Electromotive force
EMT:	Electromagnetic transient
ENTSO-e:	European Network of Transmission System Operators for Electricity
FACTS:	Flexible AC transmission system
FCR-D:	Frequency containment reserve for disturbances
FCR-N:	Frequency containment reserve for normal operation
FFR:	Fast frequency reserve

FSM:	Frequency sensitive mode
GFL:	Grid following
GFM:	Grid forming
HPP:	Hydro power plant
HV:	High voltage
LFSM-O:	Limited frequency sensitive mode for over frequency
LFSM-U:	Limited frequency sensitive mode for under frequency
LOLE:	Loss of load expectation
mFRR	Manual frequency restoration reserve
MPC:	Multiport converter
MV:	Medium voltage
OFRT:	Over-frequency ride through
OPEX:	Operational expenditure
OVRT:	Over-voltage ride through
O&M:	Operation & maintenance
P:	Proportional
PCC:	Point of common coupling
PF:	Power factor
PI:	Proportional integral
PLL:	Phase locked loop
POA:	Point of applicability
POC:	Point of connection
PPM:	Power park module

PV:	Photovoltaic
RfG:	Requirement for Generator
RoCoF:	Rate of change of frequency
RR:	Replacement reserve
SAIDI:	System average interruption duration index
SAIFI:	System average interruption frequency index
SCC:	Short circuit capacity
SG:	Synchronous generator
SOC:	State of charge
STATCOM:	Static synchronous compensator
SvK:	Svenska Kraftnät
TSO:	Transmission System Operator
UFRT:	Under-frequency ride through
UVRT:	Under-voltage ride through
VSI:	Voltage source inverter

CHAPTER 1

Introduction

This chapter presents the background and motivation that lays the foundation of this thesis. This is followed by reviewing the relevant literature and stating the specific research questions. The purpose of the thesis and its main contributions that link to the specific research questions are then presented. Finally, the thesis outline is provided and the chapter is concluded with the list of publications.

1.1 Background and motivation

As an effort to mitigate global warming, the Paris agreement, an internationally binding agreement, was established in 2015, with the set target of limiting the temperature rise to 1.5 °C above the pre-industrial period by the end of this century [1]. To achieve this international target, Sweden has set the national target of net zero greenhouse gas emissions by 2045 [2]. This has led to a strong drive for electrification, particularly in the industrial, transportation, and heat sectors [3], [4]. However, existing distribution and transmission infrastructure may not be able to accommodate the increase in electrical demand due to electrification, especially in urban areas with high load concentration [5], [6]. The upgrade of the infrastructure can take a long time, with transmission lines having a lead time between seven and twelve years [7]. This could hinder the electrification process if it has a shorter lead time than grid expansion [6].

Alongside this, many commercial and industrial (C&I) facilities require high reliability of the power supply, and interruptions, even short ones, may not be acceptable [8]–[10]. The reliability of power supply in Sweden is regulated by the energy market inspectorate. According to regulations, the acceptable amount of interruptions is four per calendar year, with a duration of 2-12 hours per each interruption, depending on the interruption scale [11]. Such interruptions may result in significant economic loss for C&I facilities. Therefore, C&I facilities may have an agreement with the system operator to provide them with a higher supply reliability, e.g. through a redundant supply. However, the system operator cannot guarantee reliable power supply against extreme weather conditions that result in multiple contingencies. Thus, some C&I facilities may invest in backup gas or diesel generators to maintain power supply during an outage.

Microgrids based on renewable resources and energy storage systems are an environmentally friendly solution to improve the reliability of power supply to C&I facilities especially when equipped with island operation capability [12]. In addition, microgrids can provide the flexibility needed during peak demand without extensive grid upgrades. This can accelerate electrification due to the shorter implementation time of microgrids compared to grid upgrades [13]. However, the cost of energy storage can be a limiting factor for microgrid implementation, particularly in prolonged congestion or/and extended island operation. The cost can be mitigated by stacking different services or functions, making the microgrid solution more competitive than traditional grid upgrades designed to handle one problem at a time [13], [14]. Furthermore, the benefits of a single microgrid can be reinforced by interconnecting microgrids sharing resources among them and reducing the required energy storage size [13], [15]. The question of whether a single microgrid solution or interconnection of microgrids is more cost-effective depends on the functions needed by the local grid and the grid users and needs further investigation.

1.2 Literature review on the role of power electronics in microgrids to enhance power system reliability

1.2.1 Definition of reliability of power supply

The power system is reliable when electricity is delivered to customers with minimal interruptions and acceptable power quality [5]. For a power system to be reliable, it must be adequate and secure in addition to being resilient. Figure 1.1 summarizes the reliability of power systems and its classifications [5], [16].

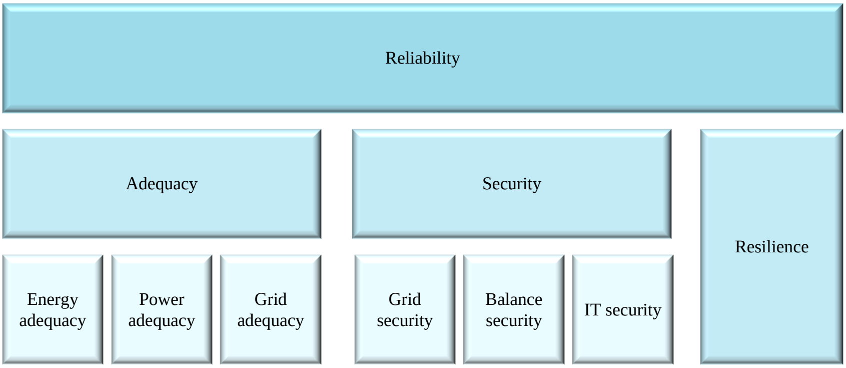

Figure 1.1: Illustration of reliability in power systems [5], [16].

Adequacy has to do with the availability of adequate power and energy to meet the demand in normal operation. The power system is said to be adequate if it fulfills the following three conditions:

Energy adequacy Energy adequacy refers to meeting the long-term energy needs of the power system. For example, the system operator in Sweden must obtain adequate energy resource to compensate for the low hydro production during the dry seasons.

Power adequacy The power system must be in power balance at all times. Therefore, the system operator must ensure adequate power generation to meet demand variations.

Grid adequacy Transmission and distribution networks must have adequate capacity to deliver power from energy carriers to end users.

The security of the power system has to do with the ability to achieve power equilibrium with acceptable security constraints after being subjected to a disturbance. The power system is said to be secure if it fulfills the following three conditions:

Grid security Grid security is the ability of the power system to handle network disruptions due to internal failures or external causes such as extreme weather conditions.

Balance security Balance security is the ability of the power system to handle the power imbalance caused by a disturbance. The power imbalance is initially handled by the inertial response followed by the activation of automatic and manual reserves.

IT security IT security is the ability to handle disruptions in the IT system due to internal failures or external attacks. IT security is becoming critical today because the power system is being digitalized and many of its tasks are being automated.

Power system resilience is defined as the ability to limit the extent, severity, and duration of system degradation following an extreme event [16]. Unlike power system security, which accounts for N-1 contingencies, power system resilience covers extreme weather conditions that result in multiple contingencies at a time. Although power system planning and operation often focus on the N-1 criterion due to cost considerations, it is crucial to address the impact of extreme events that result in multiple contingencies. Therefore, enhancing resilience to limit the consequences of such events is highly desirable.

1.2.2 Responsibility by different power system actors to achieve reliability of power supply

To achieve a reliable power supply, each actor in the power system has different responsibilities, as shown in Table 1.1 [11], [17]–[27]. The first row of the table, if read in an upright position, illustrates the different actors in the power system, including transmission system operators (TSOs), distribution system operators (DSOs), local producers, and local consumers/prosumers. The first two columns illustrate reliability classification. The classification divides reliability into three main groups, which are the adequacy, security and resilience of the power system, followed by a summary of typical reliability performance indices. The adequacy and security are then further divided into sub-groups taking into consideration different phenomena and time scales. Each cell in the table summarizes the responsibility of the respective actor towards the corresponding area of reliability. The color code in the table classifies those responsibilities into four categories: services that are remunerated by the system operator (blue), requirements by the grid code (green), emerging services/requirements that have not been implemented yet (red), and potential services/requirements that may be needed in the future (brown).

The table shows the involvement of new players that traditionally did not have a role in the control and operation of the grid. Those players are local producers, consumers, and prosumers. Compared to traditional TSO and DSO solutions, these actors provide additional benefits, including a lower carbon footprint and shorter lead times. This thesis focuses on the role of microgrids in mitigating local grid capacity bottleneck through peak net load reduction and improving the resilience of the local grid through island operation as these two functions address critical issues in local renewable integration, electrification and energy security in the society. As microgrid solutions typically involve energy storage systems and power-electronic converters, the following section reviews various power electronic technologies existing in microgrids and their applications.

1.2.3 Functions provided by power electronics in microgrids

This section reviews the following technologies typically used in microgrids: battery energy storage system (BESS), back-to-back (B2B) converter and multiport converter (MPC).

Table 1.1: Responsibility of grid operators for a reliable power system and functional requirements on grid users. The responsibilities are classified by the following color code: remunerated service (blue), requirement by the grid code (green), emerging service/requirement (red), and potential service/requirement (brown) [11], [17]–[27].

Actor / Reliability classification		TSO	DSO	Local producer	Local consumer/Prosumer
Adequacy	Power adequacy	• Procuring balancing reserves: aFRR, mFRR, & RR [17]	N/A	• Reducing forecast errors of renewable energy • Providing balancing services	Providing balancing services
	Grid adequacy	• Transmission grid reinforcement [18] • Procurement of demand side flexibility to relieve grid capacity bottleneck	• Distribution grid reinforcement • Procurement of local flexibility resources to relieve grid capacity bottleneck (Effekthandel Väst [19])	• Flexibility provision to relieve grid capacity bottleneck	Flexibility provision through load shifting and/or peak load shaving
Security	Power quality	• Reactive power compensation & voltage regulation of transmission network [25] • Harmonic and flicker mitigation [26]	• Reactive power compensation & voltage regulation of distribution network (EN50160 [23], EIFS 2023:3 [11]) • Other voltage quality fulfillment (EN50160 [23], EIFS 2023:3 [11])	• Reactive power capability & voltage regulation (EIFS 2018:2 [21]) • Limit harmonic current (IEEE 1547-2018 [27])	• Power factor correction • Limit harmonic current (IEEE 519 [24])
	Balancing power	Procuring balancing reserves: aFRR, mFRR, & RR [17]	N/A	Providing balancing services	Providing balancing services
	Frequency quality & stability	• Inertial support • FFR [17] • FCR-D & FCR-N [17]	N/A	• RoCoF and over-/under-frequency ride through (EIFS 2018:2 [21]) • LFSM (EIFS 2018:2 [21]) • Maximum power reduction capability (EIFS 2018:2 [21]) • Providing frequency ancillary services	• RoCoF and over-/under-frequency ride through of demand response units (EIFS 2019:6 [22]) • Under frequency load shedding • Providing frequency ancillary services
	Fault ride through & fast fault current injection	Fast fault current injection for protection of transmission network	Fast fault current injection for protection of distribution network	• Fault ride through fulfilment (EIFS 2018:2 [21]) • Fast fault current injection	Fault ride through enhancement
	Power oscillation damping	Deployment of generators and FACTS for power oscillation damping	Local grid strength enhancement	Power oscillation damping between generator & weak grid (EIFS 2018:2 [21])	Power oscillation damping with controlled active load
Resilience		• Clearing the corridor • Deployment of generators with black start capability	• Underground cables • Deployment of distributed generators with black start capability	Provide black start service	• Island transition capability • Island operation • Fast black start • Grid resynchronization
Reliability performance index		Fulfill EENS & LOLE [20]	Fulfill SAIFI & SAIDI (EIFS 2023:3 [11])	N/A	N/A

1.2.3.1 BESS

Table 1.2 shows the leading BESS system integrators in 2021 by MW according to their market share for BESS commercial and industrial and front-of-the-meter projects [28]. The table also shows the range of commercial BESS products offered by each integrator, alongside the functions they are capable of delivering, as per their marketing [29]–[38]. The key functions BESSs are marketed for are frequency regulation, power quality improvement, island operation, peak net load shaving, profit maximization, and cost minimization. The marketing of these functions reflects their need among different actors in the power system.

Table 1.3 showcases several notable front-of-the-meter large scale BESS projects, alongside with the BESS power and energy capacities, and the functions they are designed to serve [39]–[47]. The sizing of a BESS is fundamentally determined by the intended primary function. For instance, FlexGen's delivery of a 12 MW/ 5.4 MWh BESS for black starting Indiana's natural gas power plant illustrates a scenario where energy demand is not intensive. Hence, the BESS is designed with a duration of about half an hour.

BESSs dedicated for enhancing the power system stability typically exhibit power-intensive functions. Notable examples include the TESLA Megapack BESS in Hornsdale, Australia and the Fluence Ultrastack BESS in Lithuania, both engineered to provide stability-related functions such as frequency regulation, inertial support, seamless island transition, and power oscillation damping. These installations have a BESS duration of 1.3 hours and 1 hour, respectively.

Functions such as profit maximization and balancing reserves require BESSs units with duration not less than one hour to enable effective market participation. Noteworthy examples include BESS installations in Hertforshire and Minety, UK.

For functions demanding high energy intensity, such as alleviation of grid capacity bottleneck and island operation, BESS duration is tailored to the length of the bottleneck or the desired island duration. Notable examples of such energy-intensive BESS deployments include the NEXTera ENERGT BESS in California (4 hours), Powin's Energy Stacks in California (4 hours), and Nidec's BESS in Italy (6.5 hours).

Table 1.2: Top BESS system integrators in 2021 by MW according to their market share for BESS commercial and industrial and front-of-the-meter projects along with their BESS products and the functions they can provide [29]–[38].

BESS system integrators		Tesla	Fluence	NEXTera ENERGY	Wärtsilä	Powein Energy	FlexGen	SMA Sunbelt	Sungrow	Nidec	
BESS Commercial products		Tesla Megapack, Tesla Powerwall	Fluence Gridstack, Fluence Ultrastack, Fluence Sunstack, Fluence Edgestack	NEXTera ENERGY BESS	GridSolv Quantum	Stacks	FlexGen ESS	Sunny Tripower Storage X, SMA Commercial Storage	PowerStack, PowerTitan, etc	Nidec BESS	
Energy & balancing market optimization	Profit maximization	√			√	√	√	√	√	√	7 out of 9
	Cost minimization	√	√			√	√	√	√	√	6 out of 9
	Balancing reserves (aFRR, mFRR & RR)									√	1 out of 9
Active power transfer capability	Reduce grid capacity bottleneck	√	√		√	√					4 out of 9
	Improve generation capacity adequacy		√	√		√					3 out of 9
	Increase capacity credit of renewable intermittent renewable generation		√	√	√	√				√	5 out of 9
	Reduce renewable energy curtailment		√	√							2 out of 9
	Peak net load shaving	√	√		√		√	√	√	√	7 out of 9
	Maximize self-consumption	√						√			2 out of 9
Frequency quality & stability	Frequency regulation (FFR & FCR)	√	√	√	√	√	√	√	√	√	9 out of 9
	Inertial support	√	√					√			3 out of 9
Power quality		√	√		√	√		√	√	√	7 out of 9
Reliability & resiliency	Seamless island transition	√						√			2 out of 9
	Island operation	√	√	√	√	√		√	√		7 out of 9
	Black start		√		√			√			3 out of 9
	Grid resynchronization							√			1 out of 9
	Fault ride through								√		1 out of 9
Power oscillation damping			√								1 out of 9

Table 1.3: Front-of-the-meter large scale BESS projects along with the BESS sizing and the primary functions the BESS provides [39]–[47].

Project		Hornsdale Power Reserve	Baltic Synchronization	Solar power plant in California	City of Martinsville	Industrial heartland of southern California	Black starting Indiana's natural gas power plant	BESS in Hertfordshire, UK	BESS in Minety, UK	BESS in Campania, Italy
BESS commercial product		TESLA Megapack	Fluence Ultrastack	NEXTera ENERGY	Wärtsilä GridSolv Quantum	Powin Energy Stacks	FlexGen BESS	SMA Sunbelt Battery Storage	Sungrow PowerTitan	Nidec BESS
Customer		Power producer	Transmission system operators	Power producer	Electric utility	Power producer	Electric utility	Power producer	Power producer	Transmission system operators
Energy & balancing market optimization	Profit maximization					√		√	√	
	Cost minimization									
	Balancing reserves (aFRR, mFRR & RR)							√	√	
Active power transfer capability	Reduce grid capacity bottleneck				√	√		√	√	
	Improve generation capacity adequacy			√		√		√	√	
	Increase capacity credit of renewable intermittent renewable generation		√	√						
	Reduce renewable energy curtailment									√
	Peak net load shaving									
	Maximize self-consumption									
Frequency quality & stability	Frequency regulation (FFR & FCR)	√	√		√	√		√	√	√
	Inertial support	√	√							
Power quality										√
Reliability & resiliency	Seamless island transition	√								
	Island operation	√	√							√
	Black start						√			√
	Grid resynchronization									
Power oscillation damping			√							
BESS size		150 MW/193.5 MWh	200 MW/200 MWh	230 MW/920 MWh	9 MW/15.6 MWh	20 MW/80 MWh	12 MW/5.4 MWh	50 MW/50 MWh	150 MW/150 MWh	34.8 MW/226.2 MWh

1.2.3.2 interconnection of microgrids

The cost of BESS could be a limiting factor in microgrid implementation, especially for energy-intensive functions such as grid capacity bottleneck alleviation and island operation. The interconnection of microgrid may reduce the needed storage size thanks to recourse sharing. The interconnection of microgrids through power electronic converters is advantageous over a direct AC connector as the former can provide power flow control, independent voltage regulation, and fault isolation, among others [48]. The power-electronic interconnection technologies at the distribution system are typically referred to as soft open points [48]–[50], flexible power link [51] or power routers [52].

Back-to-back converter The B2B converter is a special case for two-terminal applications [48]–[53]. Existing studies have focused on the use of B2B converter for congestion mitigation of the upstream grid [51], load balancing between two feeders [49], losses reduction [49], voltage quality improvement [50], [53].

Multiport converter In contrast to a B2B converter, an MPC offers multiple ports in AC or DC configuration. These ports can be utilized to interconnect various energy resources, storages, or loads relying on power electronics. Some potential applications of an MPC found in the existing literature include: 1) household with rooftop solar photovoltaic (PV) and BESS [54]; 2) electric vehicle charging station with BESS and PV cells [55]; 3) electric vehicles with hybrid storage and solar roof [56], [57]; 4) interconnection of microgrids [58]. What these applications have in common is the dependency on power electronics. The MPC is useful in such applications since it can reduce the number of conversion stages. The MPC for the interconnection of microgrids is relatively a new concept and is still under research and development [59], [60].

1.3 Specific research questions

This thesis addresses the following specific research questions:

1. What are the drivers for interconnection of microgrids compared to separate microgrids to mitigate the grid capacity bottleneck?

  - What drives MPC interconnection compared to a B2B converter or even individual BESS investment?
  - What are the key factors that influence the sizing of an MPC with integrated BESS and DC load for microgrid interconnection to mitigate the grid capacity bottleneck?

2. How to design a microgrid with island capability and the ability to transition to island mode in a secure manner during an unplanned outage?
   - How to design a frequency controller of a BESS to facilitate a frequency-secure unplanned island transition of a hydro-powered microgrid?
   - What are the key factors for sizing of a BESS to simultaneously mitigate the grid capacity bottleneck and facilitate island operation with a frequency-secure unplanned island transition?
   - What are the key factors for sizing of a B2B converter in interconnected microgrids to facilitate a frequency-secure unplanned island transition of a hydro-powered microgrid?
   - What are the key factors in the voltage stability of an industrial microgrid during an unplanned island transition?

1.4 Purpose of the thesis and main contributions

The purpose of this thesis is to investigate different microgrid solutions to address the grid capacity bottleneck and improve the resilience of power supply to critical facilities. The investigated microgrid solutions include separate microgrids with individual BESSs, interconnected microgrids by B2B converter where each microgrid has its own BESS, and interconnected microgrids by MPC where a BESS is integrated to the DC link of the MPC and shared by both microgrids. In particular, this thesis focuses on the sizing of BESS, B2B converter with individual BESSs, and MPC with integrated BESS to reduce the peak net demand of two microgrids. In addition, the sizing and control of the BESS and B2B converter is investigated to facilitate the island operation and island transition of a critical facility. The contributions of the thesis include:

- Illustrating the advantage of interconnection of microgrids with complementary net load profiles in reducing the size of BESS needed for peak net load reduction. Additionally, the analysis also illustrates the advantage of interconnection by MPC with integrated BESS compared to interconnection by B2B converter with individual BESSs in reducing the size of power electronics.

- Development of a simple rule-of-thumb method for the dimensioning of MPC with integrated BESS and DC load to mitigate the grid capacity bottleneck in interconnected microgrids. The rule-of-thumb method relies on the net load profile of two microgrids and their grid power subscription as inputs. The rule-of-thumb sizing is verified against the optimal sizing obtained by linear programming. An industrial and community microgrid is used as a case study for the analysis.

- Development of a simple PI-based droop frequency controller and its tuning for a BESS to facilitate a frequency-secure unplanned island transition of a hydro-powered microgrid. To validate the proposed frequency controller, its performance is compared against existing controllers in the literature, and validated in a laboratory experiment. Compared to controllers in the literature, this controller strikes a balance between simplicity and effectiveness.

- Identification of key factors for BESS size to mitigate grid capacity bottleneck, facilitate frequency-secure island transition under an unplanned islanding event, and facilitate island capability through power balancing. The analysis shows that the size of the BESS power capacity is determined by the requirement for a frequency-secure island transition. Whereas, the size of the BESS energy capacity is a function of both requirements for capacity bottleneck alleviation and island operation. However, if the correlation between a capacity bottleneck in the gird and the occurrence of an islanding event is low, this can reduce storage size of the BESS substantially.

- Identification of key factors for sizing of B2B converter in interconnected microgrids to facilitate a frequency-secure unplanned island transition of a hydro-powered microgrid. The analysis shows that the size of the B2B converter should account for the maximum active power exchange between the microgrid and the upstream grid. Furthermore, dynamic analysis shows that the converter controlling the DC-link voltage of the B2B converter has to be slightly larger than the other one without losing control over the DC-link voltage.

- Assessment of key factors for the voltage stability of a hydro-powered industrial microgrid during unplanned island transition. In particular, the point of applicability (POA) of the reactive power requirement is a factor that is overlooked in the existing literature. Two alternative points for the POA of reactive power requirement are compared: first, the POA being the point of connection (POC) of distributed generators and loads, which is the case today in Sweden; and second, the POA being the point of common coupling (PCC) of the microgrid. The analysis shows that the former requirement allows for larger reactive power exchange with the upstream grid; thus, challenging the voltage stability of the microgrid during an unplanned islanding.

1.5 Thesis outline

The remainder of the thesis is organized as follows:

- **Chapter 2** investigates different solutions for the mitigation of grid capacity bottleneck by peak net load reduction of two microgrids. The investigated solutions are: separate microgrids where each microgrid has its own BESS; interconnected microgrids by B2B converter where each microgrid has its own BESS; interconnected microgrids by MPC where a BESS is integrated to the DC-link of MPC and shared by both microgrids. Furthermore, a simple rule-of-thumb method is developed for dimensioning of MPC-integrated BESS for peak net load reduction of two microgrids. The size obtained using rule-of-thumb method is compared with the optimal size obtained by linear programming in an industrial and community microgrids context.
- **Chapter 3** develops a BESS frequency controller to facilitate a frequency-secure unplanned island transition of a hydro-powered microgrid. First, a BESS frequency controller and its tuning are proposed to fulfill the microgrid frequency security constraints. The proposed controller is verified through dynamic simulations, and its effectiveness is compared with

existing controllers in the literature. Finally, the controller is validated in a laboratory test.

- **Chapter 4** investigates the updated BESS size obtained in Chapter 2 to additionally facilitate island operation with island transition capability of a microgrid. This is achieved by updating the linear programming problem developed in Chapter 2 to account for the additional constraints for island transition based on the dynamic simulations in Chapter 3. In addition, the updated formulation accounts for the capability of the microgrid to sustain island operation for a specific time duration.
- **Chapter 5** tests the effectiveness of the proposed frequency controller in Chapter 3 on a B2B converter interconnected industrial and community microgrids without relying on a BESS.
- **Chapter 6** investigates the voltage stability of industrial hydro-powered microgrid under unplanned island contingency. This chapter adjusts the microgrid model in Chapter 3 to invoke more voltage stability issues by adding long feeders, using a more realistic industrial load model suitable for transient voltage stability studies, and accounting for the reactive power requirement of a microgrid.
- **Chapter 7** concludes the thesis by summarizing key results and providing suggestions for future work.

Table 1.4 summarizes the scope of the thesis.

Table 1.4: Scope of the thesis.

Provided function / Microgrid solution	Peak net load reduction	Island transition	Island operation
Separate microgrids with individual BESSs	✓	✓	✓
Interconnected microgrids by B2B converter with individual BESSs	✓	✓	Future work
Interconnected microgrids by MPC with integrated BESS	✓	Future work	Future work

1.6 List of publications

This thesis is based on the following publications:

I. **A. Sunjaq**, P. Chen, M. Bongiorno, R. Majumder and J. R. Svensson, "Frequency control by BESS for smooth Island transition of a hydro-powered microgrid," in *IET Smart Grid*, vol. 7, no. 1, pp. 63-77, Feb. 2024.
This paper forms the basis of Chapter 3.
Contributions: Ahmed Sunjaq: Conceptualisation; Data curation; Investigation; Methodology; Software; Validation; Visualisation; Writing – original draft. Peiyuan Chen: Conceptualisation; Investigation; Supervision; Validation; Writing – original draft; Writing – review & editing. Massimo Bongiorno: Supervision; Writing – review & editing. Ritwik Majumder: Supervision; Writing – review & editing. Jan Svensson: Supervision; Writing – review & editing

II. **A. Sunjaq**, P. Chen, M. Bongiorno, R. Majumder and J. R. Svensson, "Control and Sizing of Back-to-Back Converter in Interconnected Microgrids," *2023 IEEE PES Innovative Smart Grid Technologies Europe (ISGT EUROPE)*, Grenoble, France, 2023, pp. 1-5.
This paper forms the basis of Chapter 5.
Contributions: Ahmed Sunjaq: Conceptualisation; Data curation; Investigation; Methodology; Software; Validation; Visualisation; Writing – original draft. Peiyuan Chen: Conceptualisation; Investigation; Supervision; Validation; Writing – original draft; Writing – review & editing. Massimo Bongiorno: Supervision; Writing – review & editing. Ritwik Majumder: Supervision; Writing – review & editing. Jan Svensson: Supervision; Writing – review & editing

Other publications not included in the thesis:

III. M. Ahouad, **A. Sunjaq**, E. Wikner and T. Thiringer, "Economic Assessment of Battery Energy Storage for Frequency Regulation in the Nordic Power Systems," *2024 20th International Conference on the European Energy Market (EEM)*, Istanbul, Turkiye, 2024, pp. 1-5.

IV. P. Ollas, T. Thiringer, N. Samuelsson and **A. Sunjaq**, "Reducing Electrical Losses in Buildings: A Study of Load-Side DC/DC Converter

Topologies for Low–Power Appliances," *2023 IEEE PES Innovative Smart Grid Technologies Europe (ISGT EUROPE)*, Grenoble, France, 2023, pp. 1-5.

V. **A. Sunjaq** and P. Chen, "Evaluation of Efficient Frequency Control Strategies in a Wind-Hydro Dominated Power System," *2021 IEEE Power & Energy Society General Meeting (PESGM)*, Washington, DC, USA, 2021, pp. 1-5.

CHAPTER 2

Sizing of BESS and multiport converter in microgrids to mitigate grid capacity bottleneck

This chapter investigates different solutions to mitigate grid capacity bottleneck by peak net load reduction of two microgrids.

Nomenclature

Indices

t_{GC}	index of time in [h]
y	index of year in [yr]
m	index of microgrid

Parameters

Time-related parameters

Δt_{GC}	time interval of time index t_{GC} in [h]
T_{GC}	final time of time index t_{GC} in [h]
$P^{\mathrm{L,AC}}_{t_{\mathrm{GC}},m}$	AC net load time series in [p.u.]

$P^{\mathrm{L,DC}}_{t_{\mathrm{GC}}}$	DC load time series in [p.u.]

Technical-related parameters

$\eta_{\mathrm{con}}, \eta_{\mathrm{inv}}, \eta_{\mathrm{tran}}$	efficiency of DC/DC converter, DC/AC converter, transformer
$\eta_{\mathrm{dis}}, \eta_{\mathrm{ch}}$	battery discharge and charge efficiencies
$\eta_{\mathrm{dis,eq}}, \eta_{\mathrm{ch,eq}}$	BESS discharge and charge efficiencies
η_{rt}	BESS roundtrip efficiency
$SOC_{\mathrm{min,GC}}$	minimum battery SOC level
$SOC_{\mathrm{max,GC}}$	maximum battery SOC level
N	project duration in [yr]
$P^{\mathrm{MG,max}}_{m}$	microgrid power subscription in [p.u.]

Financial-related parameters

C_{el}	electricity spot market price in [kEUR/MWh]
$C_{\mathrm{I,B}}$	battery investment cost in [kEUR/MWh]
$C_{\mathrm{I,con}}$	DC/DC converter investment cost in [kEUR/MW]
$C_{\mathrm{I,inv}}$	DC/AC converter investment cost in [kEUR/MW]
$C_{\mathrm{I,tran}}$	transformer investment cost in [kEUR/MVA]
$C_{\mathrm{I,cable}}$	cable investment cost in [kEUR/MVA.km]
$C_{\mathrm{OM,fix,B}}$	battery fixed OPEX in [kEUR/MWh/year]
$C_{\mathrm{OM,fix,con}}$	DC/DC converter fixed OPEX in [kEUR/MW/year]
$C_{\mathrm{OM,fix,inv}}$	DC/AC converter fixed OPEX in [kEUR/MW/year]
$C_{\mathrm{OM,fix,tran}}$	transformer fixed OPEX in [kEUR/MVA/year]
$C_{\mathrm{OM,var,B}}$	battery variable OPEX in [kEUR/MWh]
$C_{\mathrm{OM,var,con}}$	DC/DC converter variable OPEX in [kEUR/MWh]
$C_{\mathrm{OM,var,inv}}$	DC/AC converter variable OPEX in [kEUR/MWh]
r	discount rate in [%]
K_{DF}	discount factor

Variables

BESS-related variables

$P^{\mathrm{B,DC}}_{t_{\mathrm{GC}},m}$	BESS DC power in [p.u.]
$\overset{\frown}{P}^{\mathrm{B,DC}}_{t_{\mathrm{GC}},m}$	estimated BESS DC power by rule-of-thumb method in [p.u.]
$P^{\mathrm{B,DC,ch}}_{t_{\mathrm{GC}},m}$	BESS charge DC power in [p.u.]
$\overset{\frown}{P}^{\mathrm{B,DC,ch}}_{t_{\mathrm{GC}},m}$	estimated BESS charge DC power by rule-of-thumb method in [p.u.]
$P^{\mathrm{B,DC,dis}}_{t_{\mathrm{GC}},m}$	BESS discharge DC power in [p.u.]
$\overset{\frown}{P}^{\mathrm{B,DC,dis}}_{t_{\mathrm{GC}},m}$	estimated BESS discharge DC power by rule-of-thumb method in [p.u.]
$P^{\mathrm{B,AC}}_{t_{\mathrm{GC}},m}$	BESS AC power in [p.u.]
$P^{\mathrm{B,AC,ch}}_{t_{\mathrm{GC}},m}$	BESS charge AC power in [p.u.]
$P^{\mathrm{B,AC,dis}}_{t_{\mathrm{GC}},m}$	BESS discharge AC power in [p.u.]
$P^{\mathrm{B,DC,max}}_{m}$	BESS maximum DC power in [p.u.]
$P^{\mathrm{B,AC,max}}_{m}$	BESS maximum AC power in [p.u.]
$e^{\mathrm{B}}_{t_{\mathrm{GC}},m}$	BESS energy storage level in [p.u.h]
$E^{\mathrm{B,max}}_{m}$	BESS maximum energy storage in [p.u.h]
$E^{\mathrm{B,init}}_{m}$	BESS initial energy storage in [p.u.h]
$C_{\mathrm{CAPEX,B}}$	BESS CAPEX in [kEUR]
$C_{\mathrm{OPEX,B}}$	BESS total OPEX in [kEUR]
$C_{\mathrm{OPEX,fix,B}}$	BESS fixed OPEX in [kEUR]
$C_{\mathrm{OPEX,var,B}}$	BESS variable OPEX in [kEUR]
$C_{\mathrm{loss,B}}$	BESS cost of losses

B2B converter-related variables

$P^{\mathrm{B2B}}_{t_{\mathrm{GC}},m}$	B2B converter power in [p.u.]
$P^{\mathrm{B2B,in}}_{t_{\mathrm{GC}},m}$	B2B converter input power in [p.u.]
$P^{\mathrm{B2B,out}}_{t_{\mathrm{GC}},m}$	B2B converter output power in [p.u.]
$P^{\mathrm{B2B,loss}}_{t_{\mathrm{GC}},m}$	B2B converter power losses in [p.u.]
$P^{\mathrm{B2B,max}}_{m}$	B2B converter maximum power in [p.u.]

$C_{\mathrm{CAPEX,B2B}}$	B2B converter CAPEX in [kEUR]
$C_{\mathrm{OPEX,B2B}}$	B2B converter total OPEX in [kEUR]
$C_{\mathrm{OPEX,fix,B2B}}$	B2B converter fixed OPEX in [kEUR]
$C_{\mathrm{OPEX,var,B2B}}$	B2B converter variable OPEX in [kEUR]
$C_{\mathrm{loss,B2B}}$	B2B converter cost of losses in [kEUR]
	MPC-related variables
$P_{t_{\mathrm{GC}},m}^{\mathrm{MPC}}$	MPC power in [p.u.]
$\overset{\frown}{P}_{t_{\mathrm{GC}},m}^{\mathrm{MPC}}$	estimated MPC power by rule-of-thumb method in [p.u.]
$P_{t_{\mathrm{GC}},m}^{\mathrm{MPC,in}}$	MPC input power in [p.u.]
$\overset{\frown}{P}_{t_{\mathrm{GC}},m}^{\mathrm{MPC,in}}$	estimated MPC input power by rule-of-thumb method in [p.u.]
$P_{t_{\mathrm{GC}},m}^{\mathrm{MPC,out}}$	MPC output power in [p.u.]
$\overset{\frown}{P}_{t_{\mathrm{GC}},m}^{\mathrm{MPC,out}}$	estimated MPC output power by rule-of-thumb method in [p.u.]
$P_{m}^{\mathrm{MPC,max}}$	MPC maximum power in [p.u.]
$\overset{\frown}{P}_{m}^{\mathrm{MPC,max}}$	estimated MPC maximum power by rule-of-thumb method in [p.u.]
$P_{t_{\mathrm{GC}},m}^{\mathrm{MPC,loss}}$	MPC power losses in [p.u.]
$C_{\mathrm{CAPEX,MPC}}$	MPC CAPEX in [kEUR]
$C_{\mathrm{OPEX,MPC}}$	MPC total OPEX in [kEUR]
$C_{\mathrm{OPEX,fix,MPC}}$	MPC fixed OPEX in [kEUR]
$C_{\mathrm{OPEX,var,MPC}}$	MPC variable OPEX in [kEUR]
$C_{\mathrm{loss,MPC}}$	MPC cost of losses in [kEUR]
	Other variables
$P_{t_{\mathrm{GC}},m}^{\mathrm{MG}}$	microgrid power import in [p.u.]
$P_{t_{\mathrm{GC}}}^{\mathrm{L,DC,B}}$	DC load power component fed by the BESS in [p.u.]
$P_{t_{\mathrm{GC}}}^{\mathrm{L,DC,MG}}$	DC load power component fed by the AC microgrids in [p.u.]

2.1 Introduction

This chapter investigates three microgrid solutions to alleviate a grid capacity bottleneck:

(a) Separate microgrids where each microgrid has its own BESS,

(b) Interconnected microgrids through B2B converter where each microgrid has its own BESS,

(c) Interconnected microgrids through MPC where BESS is integrated at the DC link of the MPC and shared by both microgrids.

Solution (a) can alleviate a capacity bottleneck by shifting power in time through charging/discharging BESS. Solutions (b) and (c), in addition to shifting power in time, can also shift power in space by rerouting the power to a neighboring microgrid that has spare capacity.

The cost-effectiveness of the three solutions is investigated by formulating a linear optimization problem with the objective function being to minimize the total capital expenditure (CAPEX), operational expenditure (OPEX) and losses costs of power electronics, transformers, storages and cable interconnecting the microgrids. The optimization problem models the microgrid as a power balance model and accounts for the maximum power exchange with the upstream grid in addition to the maximum capacity of power electronics and storages.

This chapter also proposes a simple rule-of-thumb method for dimensioning MPC and BESS under a realistic scenario of industrial and community microgrids. The rule-of-thumb method accounts for the cases without/with a DC load integrated into the DC link of the MPC. The effectiveness of the proposed rule-of-thumb sizing is verified by comparing it with optimal sizing by linear programming.

2.2 Optimization problem description

This section describes the optimization problem formulation, while the detailed mathematical formulation is summarized in Appendix A.

2.2.1 Investigated solutions for alleviation of grid capacity bottleneck

Figure 2.1 shows the investigated solutions for alleviating grid capacity bottleneck, which include:

(a) Separate microgrids where each microgrid has its own BESS,

(b) Interconnected microgrids by B2B converter where each microgrid has its own BESS,

(c) Interconnected microgrids by MPC where BESS is integrated at the DC link of the MPC and shared by both microgrids.

The grid capacity bottleneck here refers to scenarios where the net load of a microgrid exceeds its corresponding power subscription for power import or/and export with its connecting upstream grid. The capacity bottleneck can be alleviated by discharging/charging BESS if the microgrid is in power deficit/surplus. Alternatively, it can be alleviated by importing/exporting power from/to an adjacent microgrid that has spare capacity. Solution (a) utilizes the first strategy, while solutions (b) and (c) utilize a combination of the first and second strategies.

2.2.2 Objective function for minimization of investment and operational costs

The optimization problem is treated as three separate problems, one for each investigated solution. The objective function is to minimize the total cost of investment, operation, and losses in power electronics, storages, transformers, and cable (highlighted in the colors in Figure 2.1) needed to alleviate the capacity bottleneck in the upstream grid. The minimized costs include:

- CAPEX: CAPEX of batteries, DC/DC converters, DC/AC converters, transformers, and cable for interconnecting microgrids,
- OPEX: OPEX of batteries, DC/DC converters, DC/AC converters, and transformers,
- Losses cost: cost of losses in batteries, DC/DC converters, DC/AC converters, and transformers.

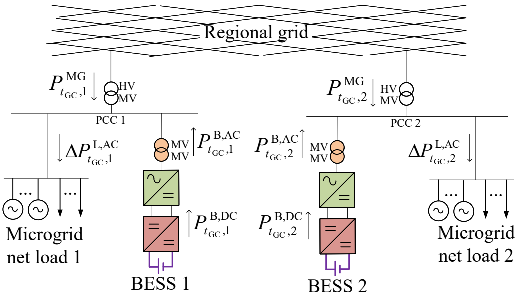

(a) Separate microgrids

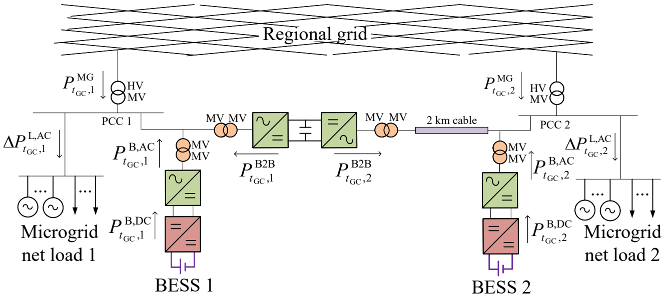

(b) Interconnected microgrids by B2B converter

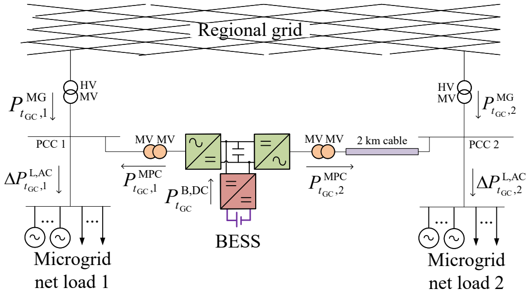

(c) Interconnected microgrids by MPC

Figure 2.1: Two microgrids with three solutions for the alleviation of grid capacity bottleneck.

The OPEX is divided into fixed OPEX and variable OPEX. Fixed OPEX is expressed in EUR/MW/year and is fixed irrespective of how the equipment is operated. It includes, for example, administration, operational staff, payments for operation and maintenance (O&M) service agreements, network or system charges, property tax, and insurance [61]. The variable OPEX is expressed in EUR/MWh and depends on how the equipment is operated. It includes consumption of auxiliary materials (water, lubricants, fuel additives), treatment and disposal of residuals, repair and maintenance related to production, and spare parts [61].

The assumptions made when formulating the objective function are as follows:

- The total CAPEX is assumed to be the aggregated CAPEX of the individual elements, e.g. batteries, converters, that make up the final product, i.e., B2B converter and MPC. This assumption is made due to the lack of cost data for B2B converter and MPC,
- The cost of losses is treated as an independent parameter from the OPEX, although in some of the references the cost of losses is part of the variable OPEX,
- The cable is assumed to have negligible fixed and variable OPEX. The transformer is assumed to have negligible variable OPEX,
- The OPEX and the cost of losses account for the entire project lifetime of 20 years.
- Services that bring revenue stream such as energy arbitrage and frequency ancillary services are not included in this formulation. The focus here is to determine the size of the MPC to provide the required technical functions.

2.2.3 Constraints for mitigating grid capacity bottleneck

The optimization problem constraints include:

- Maximum power import and export between the microgrid and the upstream distribution grid,
- Maximum power capacity of BESS, B2B converter and MPC,

- Maximum and minimum energy capacity of BESS,
- Energy level of BESS,
- DC-link power balance of B2B converter and MPC.

The assumptions made when formulating the constraints are as follows:

- The maximum power exchange between the microgrid and the upstream distribution grid is treated as a hard constraint instead of imposing a penalty in the objective function for exceeding the power subscription,
- The permissible range for BESS state of charge (SOC) level is between 20% and 80%,
- The model used here is a power balance model where voltage drops are neglected, i.e. voltage is 1 p.u.,
- The power losses through battery, DC/DC and DC/AC converters and transformer are assumed to have a linear relationship with the power flow through the respective element,
- Load side flexibility is not considered.

2.3 Peak net load reduction of two generic microgrids

This section investigates the size of MPC interconnected microgrids to mitigate grid capacity bottleneck by reducing peak net load of two generic microgrids. The economical feasibility of the interconnection by MPC is compared against the solution of separate microgrids and the solution of interconnected microgrids by B2B converter. Two generic mcirogrids with sinusoidal net load profiles are used as a case study for the analysis.

2.3.1 Net load profile of generic microgrids

Figure 2.2 (left) shows the net load profile of two generic microgrids during a single day with a resolution of one hour. Both microgrids have sinusoidal net load variations with peak hour in Microgrid 1 occurring at 12:00 PM and that in Microgird 2 at 06:00 PM. The microgrids exceed their corresponding power subscription of 1 p.u. with the upstream distribution network. Microgrid 1 exceeds its power subscription between 09:00 AM and 04:00 PM and Microgrid 2 between 03:00 PM and 10:00 PM. The microgrids exceed their power subscription simultaneously between 03:00 PM and 04:00 PM. In this chapter, the term grid capacity bottleneck refers to the situation when a net load of a microgrid exceeds its power subscription to the upstream distribution network.

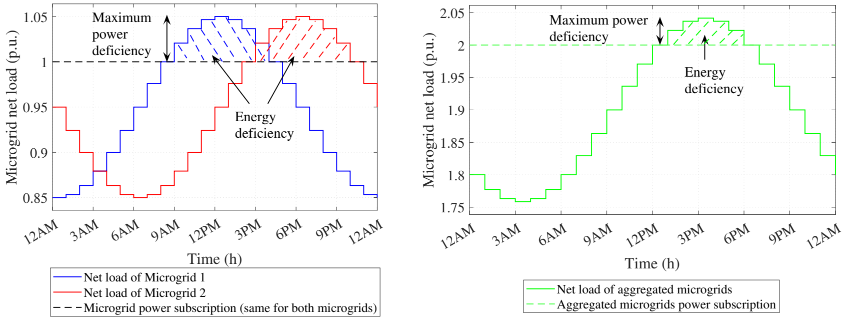

Figure 2.2: Hourly net load profile of two generic microgrids during a single day (left), and their aggregated net load profile (right).

2.3.2 Base case scenario

The capacity bottleneck in the grid is alleviated by one of the three solutions illustrated in Figure 2.1. The cost-optimal dimensioning of power electronics and storages is obtained by the optimization problem described in Appendix A and the results are shown in Figure 2.3 in red font. The base power for the per unit values is the maximum power exchange between a single microgrid and the corresponding upstream grid, which is identical for both microgrids. This is used as a base power through out this section. To gain insight into the factors affecting the size, Figures 2.4, 2.5 and 2.7 show the optimal dispatch of power electronics and storages.

In the separate microgrids solution, the dimensioning of BESS in each microgrid is identical. This is because the capacity bottleneck is similar in both microgrids in terms of power and energy deficiencies. Therefore, the analyses here focus only on Microgrid 1. Figure 2.4 shows the optimal power dispatch of BESS 1 and its energy storage dynamics during a single day. The reference power direction of the BESS is illustrated in Figure 2.3, where the positive/negative power of the BESS corresponds to the battery being discharged/charged. The BESS charges during off-peak hours, between 01:00 AM and 08:00 AM, and discharges during peak hours, between 09:00 AM and 04:00 PM. The BESS is in standby for the remainder of the day. The peak power discharge occurs at 12:00 PM, corresponding to the peak net load of the microgrid (see Figure 2.2 left). Note that the peak power discharge is equal to 5%, which is equal to the maximum power deficiency of the microgrid, i.e., the maximum difference between the peak net load and the microgrid power subscription. The size of the BESS storage capacity is equivalent to the accumulated energy deficiency, which is the area highlighted with dashed lines in Figure 2.2 left. The BESS storage capacity is overdimensioned to account for the round-trip BESS losses of 10.5%.

The interconnected microgrids by B2B converter has a significant reduction in the BESS size compared to separate microgrids. The size of the BESS power capacity has been reduced by 2.4 times and its energy storage capacity by 3 times. This reduction in the size of the BESS needed for capacity bottleneck alleviation is due to the flexibility available through power rerouting between the microgrids. Interconnected microgrids can be thought of as a single entity. Such a single entity would have a net load profile as shown in Figure 2.2 (right). The dashed area in this figure reflects the remaining capacity bottleneck that cannot be relieved through power re-rerouting. Therefore, an additional BESS is needed to provide temporal flexibility by discharging during those hours. This is illustrated by the optimal power dispatch of the BESSs shown in Figure 2.5 (top left), where the two BESSs discharge during those hours when both microgrids are power deficit. In fact, the aggregated size of the two BESSs corresponds to the maximum power deficiency and the maximum accumulated energy deficiency of the aggregated microgrids, as illustrated in Figure 2.2 (right).

When it comes to the allocation of the BESS capacity in the two microgrids, if the capacity bottleneck only occurs in one of the microgrid, then installing the BESS in that microgrid is more cost optimal. This is because having the BESS in the neighboring microgrid will result in the full BESS power passing through the B2B converter increasing its size. In this case, since the capacity

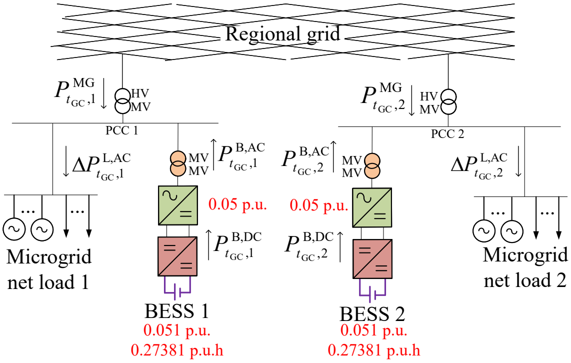

(a) Separate microgrids

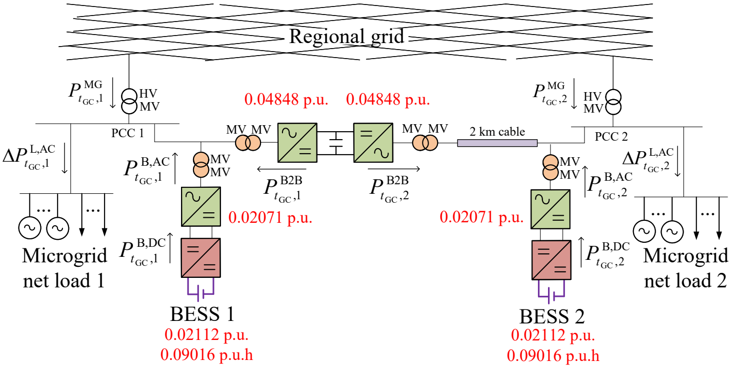

(b) Interconnected microgrids by B2B converter

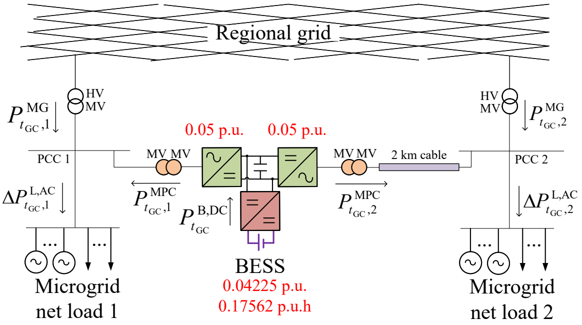

(c) Interconnected microgrids by MPC

Figure 2.3: Dimensioning of power electronics and storages for grid capacity bottleneck alleviation (base case). Base power is the maximum power exchange between a single microgrid and the corresponding upstream grid (same for both microgrids).

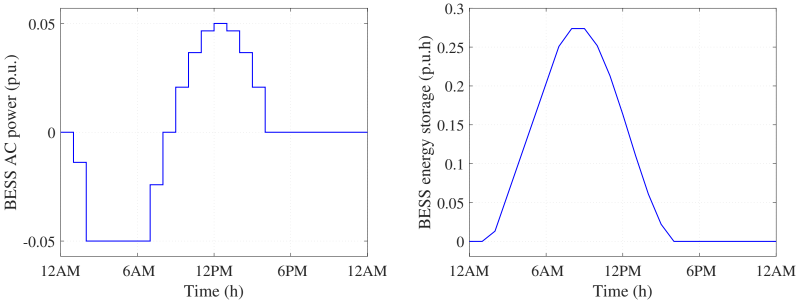

Figure 2.4: Optimal dispatch of separate microgrids solution: BESS 1 optimal power dispatch (left), and corresponding BESS 1 storage dynamics (right). Positive/negative power of the BESS corresponds to the battery being discharged/charged. Base power is the maximum power exchange between microgrid and the upstream grid.

bottleneck is similar in both microgrids, investing in two equivalent BESSs located at each microgrid is a logical choice.

The dimensioning of the B2B converter is driven by the power deficiency in Microgrid 1 (blue arrows in Figure 2.6) when there is a spare capacity in Microgrid 2 (red arrows in Figure 2.6). The dimensioning could also be driven by the other scenario when there is a power deficiency in Microgrid 2 and available spare capacity in Microgrid 1. However, since the capacity bottleneck is similar in both microgrids, only the former scenario is illustrated. If at a certain hour the red arrow is longer than the blue arrow, this means that microgrid 2 has sufficient spare capacity to alleviate capacity bottleneck in microgrid 1. On the other hand, if the red arrow is shorter than the blue arrow, this means that microgrid 2 does not have sufficient spare capacity to alleviate capacity bottleneck in microgrid 1 through power rerouting. In this case, BESS must provide power support. The dimensioning incident of the B2B converter is dictated by the hour at which the red arrow is equal to or just larger than the blue arrow. In this case, the dimensioning incident is at 12:00 PM and both arrows are equal in size and equal to 5%. This analysis is confirmed by the optimal power dispatch of the B2B converter, shown in Figure 2.5 (bottom left), which shows a maximum power flow from microgrid 2 to microgrid 1 occurring at 12:00 PM and is equal to 4.7%. The reason it is

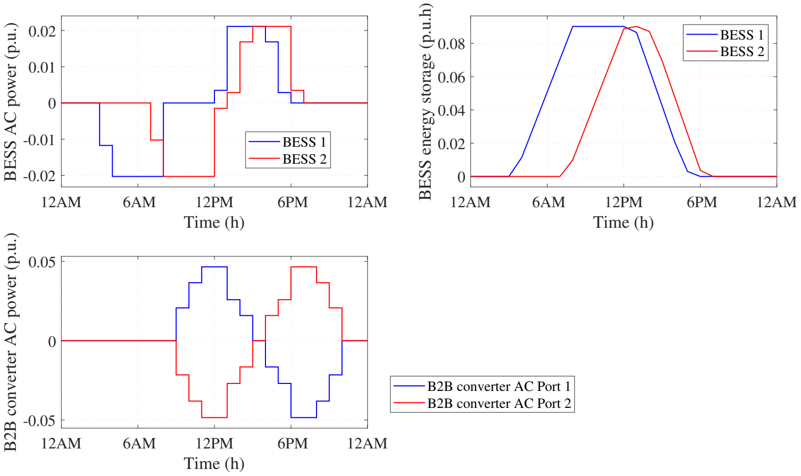

Figure 2.5: Optimal dispatch of interconnected microgrids by B2B converter: BESS 1 and BESS 2 optimal power dispatch (top left), and their corresponding storage dynamics (top right); B2B converter optimal power dispatch (bottom left). The reference power direction is illustrated in Figure 2.3 (b). Base power is the maximum power exchange between microgrid and the upstream grid.

less than the 5% needed to alleviate the capacity bottleneck is because BESS 1 also provides power support to microgrid 1 by 0.3% at 12:00 PM. This slightly increases the size of the BESS energy capacity, but it simultaneously reduces the size of the B2B converter. The optimal compromise between the size of the storage and the B2B converter is obtained by the optimization problem according to the input data of their capital costs. According to the input data, 1 MWh of storage has half the capital cost of a 1 MW B2B converter. This means that if there is a 1 MW power deficiency occurring in microgrid 1 that lasts for one hour, optimization will most likely prioritize investment in storage. However, in case of a longer lasting capacity bottleneck (longer than two hours) and if it could be alleviated through power rerouting, it may be more cost optimal to invest in a B2B converter than a storage. An additional factor that plays a role in the choice of investment is the efficiency of each of the BESS and B2B converter. The former has a round trip efficiency of 89.5%, while the latter has an efficiency of 96%. Therefore, if both solutions have the same capital cost, the B2B converter becomes advantageous due to its lower operational cost.

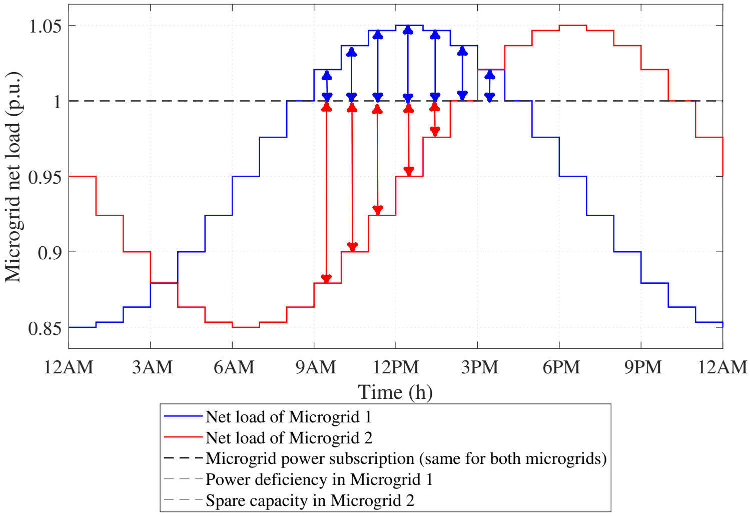

Figure 2.6: Hourly net load profile of two generic microgrids illustrating the Power deficiency in Microgrid 1 (blue arrows) and the spare capacity in Microgrid 2 (red arrows).

In the case of interconnected microgrids by MPC, there is only one BESS shared by both microgrids and integrated with the MPC. Figure 2.3 shows that the size of the BESS (the battery and its DC/DC converter) is equivalent to the aggregated size of the two BESSs in the interconnected microgrids by B2B converter. Thus, the same principle for dimensioning the BESS applies here, i.e. the size is dictated by the maximum power deficiency and maximum accumulated energy deficiency of the aggregated microgrids. Figure 2.7 (top left) shows the optimal power dispatch of the BESS. The BESS discharges between t=13:00 PM and t=06:00 PM, when the aggregated microgrids are power deficit.

The dimensioning of the AC ports of the MPC is dictated by the maximum power deficiency of the microgrid at which the AC port is interfaced. The maximum power deficiency of Microgrid 1 is equal to 5% and occurs at 12:00 PM, and that of Microgrid 2 is also equal to 5% and occurs at 06:00 PM. This is also confirmed by the optimal power dispatch of the AC ports of the MPC shown in Figure 2.7 (bottom left and bottom right), which shows that AC Port 1 and AC Port 2 have a maximum power output of 5% occurring at 12:00 PM and 06:00 PM, respectively.

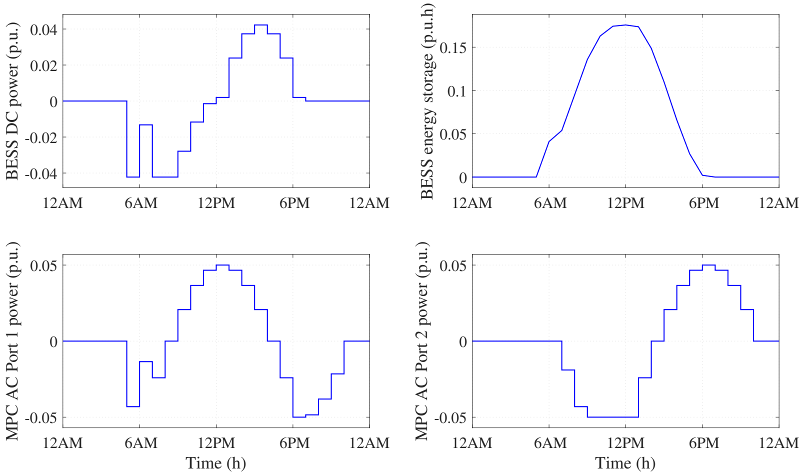

Figure 2.7: Optimal dispatch of interconnected microgrids by MPC: BESS optimal power dispatch (top left), and its corresponding energy storage dynamics (top right); MPC AC Port 1 and AC Port 2 optimal power dispatch (bottom left and bottom right). The reference power direction is illustrated in Figure 2.3 (c). Base power is the maximum power exchange between microgrid and the upstream grid.

Table 2.1 summarizes the size and cost of the three investigated solutions. The separate microgrids solution has the highest cost, twice as much compared to interconnected microgrids. The main driver for the high cost of separate microgrids is the large energy storage size needed to alleviate the capacity bottleneck. While both technologies for interconnection show a similar size for the storage and DC/DC converter, the interconnection by MPC distinguishes itself by requiring less investment on DC/AC converter. This is due to the integration of the BESS with the MPC instead of the BESS having its own DC/AC converter. Consequently, the interconnection by MPC is 11.7% cheaper than interconnection by B2B converter.

Table 2.1: Summary of size and cost of power electronics and storages for capacity bottleneck alleviation (base case). The per unit values are on the base of microgrid power subscription.

	Separate microgrids	Interconnected microgrids by B2B converter	Interconnected microgrids by MPC
Aggregated size of energy storage	0.54762 p.u.h	0.18032 p.u.h	0.17562 p.u.h
Aggregated size of DC/DC converters	0.102 p.u.	0.04224 p.u.	0.04225 p.u.
Aggregated size of DC/AC converters	0.10 p.u.	0.1392 p.u.	0.10 p.u.
Total CAPEX, OPEX & losses cost	$112.1\ \frac{\text{kEUR}}{\text{MW}}\text{p.u.}$	$57.2\ \frac{\text{kEUR}}{\text{MW}}\text{p.u.}$	$50.51\ \frac{\text{kEUR}}{\text{MW}}\text{p.u.}$

2.3.3 Impact of microgrids coincidence factor

In the base case scenario, the two microgrids experience capacity bottleneck at different times of the day, with Microgrid 1 experiencing it around the noon and Microgrid 2 around the evening. The likelihood of the two microgrids to peak simultaneously can be measured by the coincidence factor. This section explores various coincidence factors between the net load profiles of the two microgrids (as illustrated in Figure 2.8):

- Low coincidence factor: when the two microgrids do not experience capacity bottleneck simultaneously,
- Intermediate coincidence factor (base case): when the two microgrids experience capacity bottleneck simultaneously but for a limited time duration,
- High coincidence factor: when the two microgrids experience capacity bottleneck simultaneously and for an extended amount of time.

Figure 2.9 compares the optimal size and cost for the three solutions to alleviate grid capacity bottleneck corresponding to various coincidence factors. The results reveal that interconnection of microgrids is cheaper solution than separate microgrids in case of low and intermediate coincidence factors, with a corresponding reduction in the cost by 82.3% and 50% (roughly), respectively.

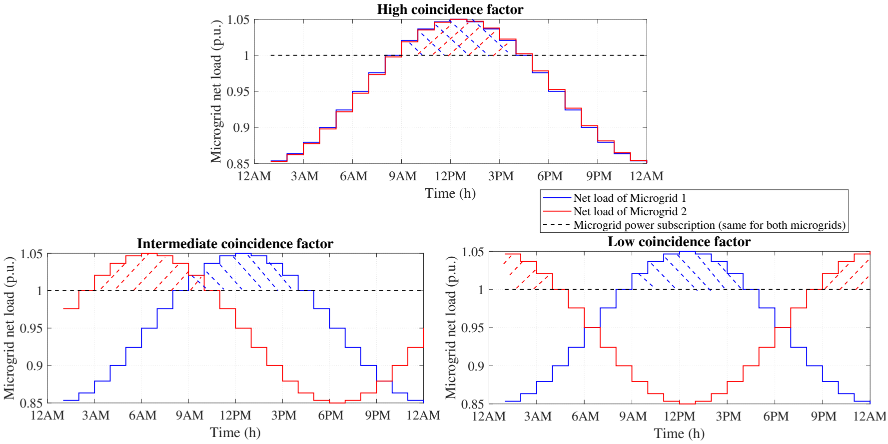

Figure 2.8: Hourly net load profile of two generic microgrids during a single day and with various coincidence factors.

This reduction in the cost is attributed to the fact that the two microgrids have different peak hours, which facilitates capacity bottleneck alleviation through power rerouting. This reduces the storage requirement significantly, with no investment required in the case of low coincidence factor and some investment needed in the case of intermediate coincidence factor but still much lower than separate microgrids. In case of high coincidence factor, interconnection of microgrids is not advantageous compared to separate microgrids. This is obvious as the two microgrids are congested simultaneously, which hinders the possibility of power rerouting.

2.4 Peak net load reduction of industrial and community microgrids

The previous section has illustrated that an MPC with integrated BESS can reduce the size of battery and power electronics needed for peak net load reduction of two generic microgrids. This section illustrates the sizing of MPC with integrated BESS in a realistic scenario of industrial and community microgrids. In addition, a simple rule-of-thumb method is developed to estimate the size of the MPC with integrated BESS. The estimated size is

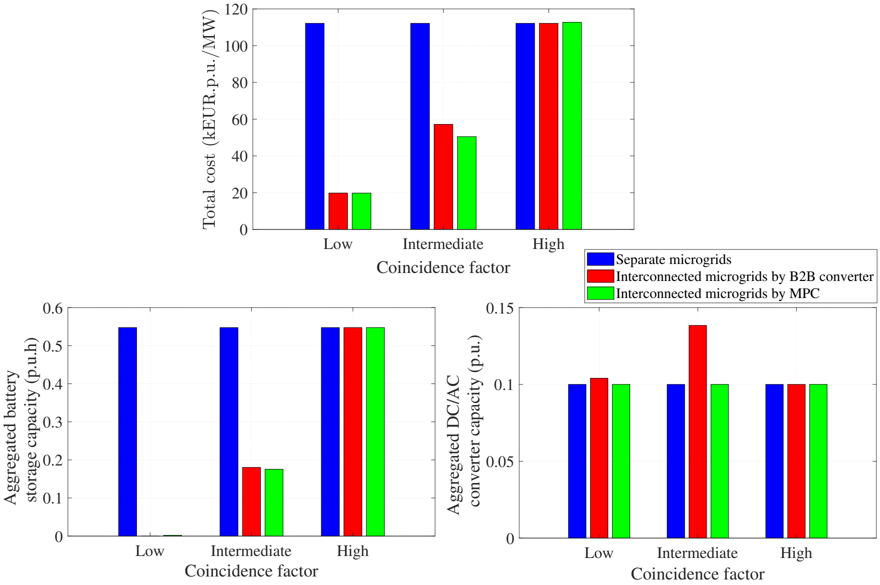

Figure 2.9: Impact of microgrids coincidence factor on the size and cost of three potential solutions for the mitigation of grid capacity bottleneck.

then compared to the solution obtained by optimization. Two scenarios are investigated: without and with DC load integrated into the MPC.

It is necessary to clarify some of the terms used in this section. Microgrid 1 and Microgrid 2 refer to industrial and community microgrids, respectively. AC Port 1 and AC Port 2 of the MPC are interfaced to Microgrid 1 and Microgrid 2, respectively. The positive/negative power of any AC port means injection/absorption of power into/from the microgrid. When a microgrid is power deficient/surplus, it means that the net load profile of the microgrid exceeds its power subscription limit for power import/export with the respective Distribution System Operator (DSO). When aggregated microgrids are power deficient/surplus, it means that the net load profile of aggregated microgrids exceed the aggregated power subscription limit for power import/export. A capacity bottleneck occurs when single microgrid/aggregated microgrids cannot meet corresponding power subscription limits of power import or/and export.

2.4.1 Net load profile of industrial and community microgrids

Figure 2.10 (top) shows the net load profile of industrial and community microgrids obtained from real measurements carried out over one calendar year and with a resolution of one hour. The powers are given in per unit with respect to the power subscription of the industrial microgrid (24.3 MW). This base power is used throughout this section. The industrial microgrid consists of a paper and pulp factory and a HPP, whereas the community microgrid consists of a municipality and wind turbines. Industrial and community microgrids experience a capacity bottleneck during different times of the year, the former during the summer and winter seasons and the latter during the winter and spring seasons. Figure 2.10 (bottom) shows the aggregated net load profile of the two microgrids. It can be seen that by aggregating the microgrids, the duration of the capacity bottleneck is significantly reduced, occurring only in the winter season, specifically in November and December.

Figure 2.11 shows the corresponding heat map of the net load profile of the industrial and community microgrids. The x-axis represents the day of the year starting from January 1, and the y-axis represents the hour of the day with hour 1 corresponding to 01:00 AM, and so on. The heat map shows that both microgrids complement each other not just on a seasonal basis but also on a daily basis. This is clear as the industrial microgrid has peak demand during night hours while the community microgrid has it during day hours. Thus, industrial and community microgrids make a good case study for interconnection.

Figure 2.12 (top) shows net load profile of industrial and community microgrids at December 6. The industrial microgrid exceeds its power subscription during night hours, while the community microgrid exceeds it during the day hours. When aggregating the two microgrids, as shown in Figure 2.12 (bottom), the capacity bottleneck is significantly reduced, occurring only for one hour at 08:00 PM.

2.4.2 Proposed rule-of-thumb method for dimensioning of multiport converter with integrated BESS

2.4.2.1 Definition of key parameters

Before deliberating in the proposed rule-of-thumb method, it is necessary to define some key parameters that will simplify the mathematical formulation.

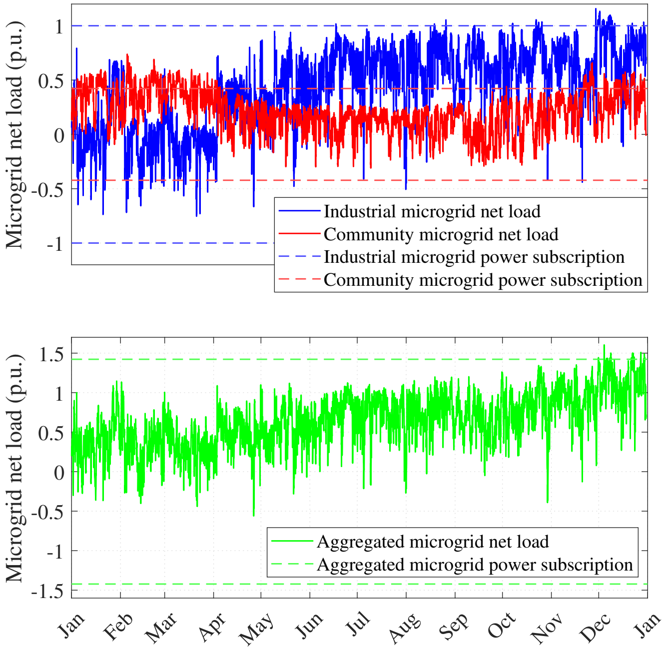

Figure 2.10: Recording of industrial and community microgrids net load profile (top), and their aggregation (bottom), recorded over one calender year.

The power deficiency in Microgrid m due to the net load exceeding the corresponding power subscription for power import is defined as follows:

$$\Delta P^{\mathrm{MG,def}}_{t_{\mathrm{GC}},m} = \max\left(\Delta P^{\mathrm{L,AC}}_{t_{\mathrm{GC}},m} - P^{\mathrm{MG,max}}_{m}, 0\right) \quad \forall t_{\mathrm{GC}} \forall m, \tag{2.1}$$

The power surplus in Microgrid m due to the net load exceeding the corresponding power subscription for power export is defined as follows:

$$\Delta P^{\mathrm{MG,plus}}_{t_{\mathrm{GC}},m} = \max\left(-\Delta P^{\mathrm{L,AC}}_{t_{\mathrm{GC}},m} - P^{\mathrm{MG,max}}_{m}, 0\right) \quad \forall t_{\mathrm{GC}} \forall m, \tag{2.2}$$

The additional power that Microgrid m can import from the local grid before reaching the corresponding power subscription for power import is defined as follows:

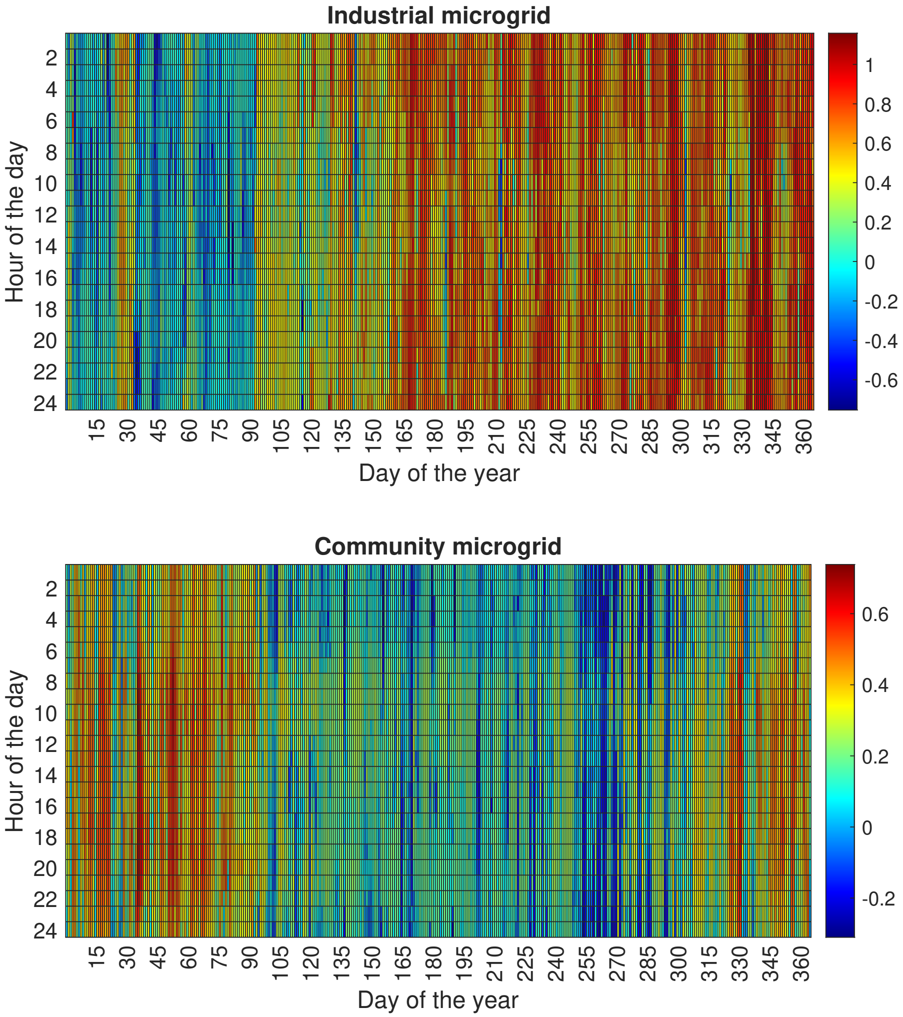

Figure 2.11: Heat map of industrial and community microgrids showing their seasonal and daily net load variations during one calender year. The x-axis representes the day of the year with day 1 corresponding to January 1, and so on. The y-axis represents the hour of the day, where hour 1 corresponds to 01:00 AM, and so on.

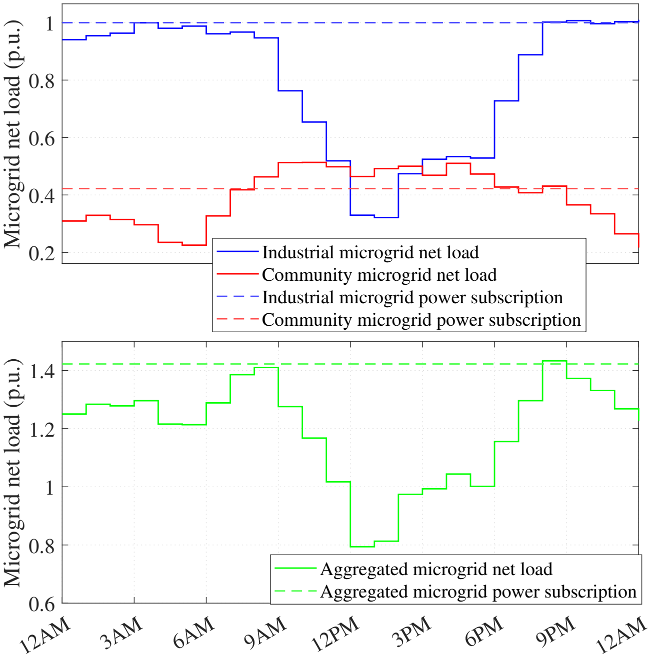

Figure 2.12: Recording of industrial and community microgrids net load profile (top), and their aggregation (bottom), recorded on December 6.

$$\Delta P^{\mathrm{MG,imp}}_{t_{\mathrm{GC}},m} = \max\left(P^{\mathrm{MG,max}}_{m} - \Delta P^{\mathrm{L,AC}}_{t_{\mathrm{GC}},m}, 0\right) \quad \forall t_{\mathrm{GC}} \forall m, \tag{2.3}$$

The additional power that Microgrid m can export to the local grid before reaching the corresponding power subscription for power export is defined as follows:

$$\Delta P^{\mathrm{MG,exp}}_{t_{\mathrm{GC}},m} = \max\left(\Delta P^{\mathrm{L,AC}}_{t_{\mathrm{GC}},m} + P^{\mathrm{MG,max}}_{m}, 0\right) \quad \forall t_{\mathrm{GC}} \forall m, \tag{2.4}$$

Note that all previously defined parameters have non-negative values. Note also that the power deficiency of Microgird m $\Delta P^{\mathrm{MG,def}}_{t_{\mathrm{GC}},m}$ and the additional reserve that Microgrid m has for power import $\Delta P^{\mathrm{MG,imp}}_{t_{\mathrm{GC}},m}$ do not occur simultaneously. Similarly, the power surplus of Microgrid m $\Delta P^{\mathrm{MG,plus}}_{t_{\mathrm{GC}},m}$ and the additional reserve that Microgrid m has for power export $\Delta P_{t_{\mathrm{GC}},m}^{\mathrm{MG,exp}}$ do not occur simultaneously.

2.4.2.2 Dimensioning of BESS power capacity

To estimate BESS power capacity, its power dispatch is first estimated based on a pre-defined operation. The pre-defined operation assumes that the BESS is only discharged/charged when the aggregated microgrids are power deficient/surplus:

$$\overset{\frown}{P}_{t_{\mathrm{GC}}}^{\mathrm{B,DC,dis}} = \frac{\max\left(\sum\limits_{m=1}^{2} \Delta P_{t_{\mathrm{GC}},m}^{\mathrm{MG,def}} - \sum\limits_{m=1}^{2} \Delta P_{t_{\mathrm{GC}},m}^{\mathrm{MG,imp}}, 0\right)}{\eta_{\mathrm{tran}}\eta_{\mathrm{inv}}} \quad \forall t_{\mathrm{GC}}, \tag{2.5a}$$

$$\overset{\frown}{P}_{t_{\mathrm{GC}}}^{\mathrm{B,DC,ch}} = \eta_{\mathrm{tran}}\eta_{\mathrm{inv}} \max\left(\sum_{m=1}^{2} \Delta P_{t_{\mathrm{GC}},m}^{\mathrm{MG,plus}} - \sum_{m=1}^{2} \Delta P_{t_{\mathrm{GC}},m}^{\mathrm{MG,exp}}, 0\right) \quad \forall t_{\mathrm{GC}}, \tag{2.5b}$$

$$\overset{\frown}{P}_{t_{\mathrm{GC}}}^{\mathrm{B,DC}} = \overset{\frown}{P}_{t_{\mathrm{GC}}}^{\mathrm{B,DC,dis}} - \overset{\frown}{P}_{t_{\mathrm{GC}}}^{\mathrm{B,DC,ch}} \quad \forall t_{\mathrm{GC}}. \tag{2.5c}$$

Note that the above equations do not account for BESS recovering its initial SOC level after supporting in relieving a capacity bottleneck. This is because the sole purpose of defining the BESS operation is to find its power capacity needed to alleviate the capacity bottleneck. Moreover, recovering the initial SOC level of BESS should not be a dimensioning incident for the BESS power capacity.

Figure 2.13 (top) compares the estimated BESS power dispatch obtained by (2.5a)-(2.5c) with that obtained by the optimization problem defined in Appendix A. The two power dispatches agree that the BESS should discharge to alleviate the capacity bottleneck of the aggregated microgrids that occurs in November and December (see Figure 2.13 bottom). The main difference between the two power dispatches is that the optimal one accounts for recovering of the SOC level, which explains the negative power. However, recovering the BESS SOC level is not a dimensioning factor. The dimensioning incident of the BESS power capacity occurs on December 5 (see the zoomed subplot), when the aggregated microgrids reach their peak net demand. The 0.185 p.u. BESS power capacity is slightly higher than the maximum power deficiency

0.182 p.u. due to losses occurring in the DC/AC converter and transformer. Observe also that the estimated power dispatch captures the dimensioning incident very accurately.

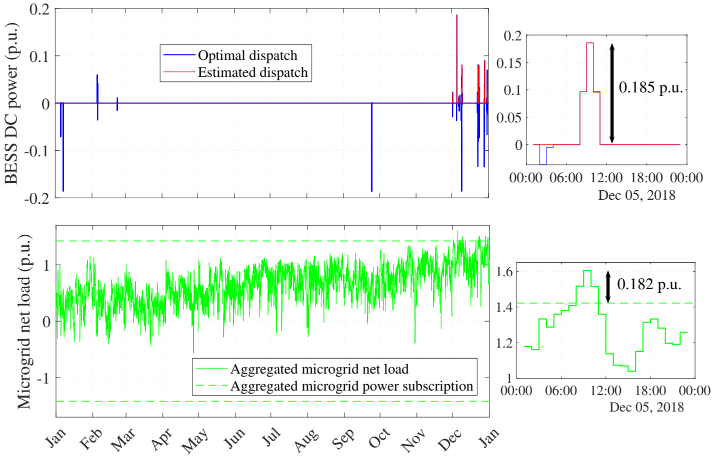

Figure 2.13: Optimal and estimated BESS power dispatch (top); net load profile of aggregated microgrids (bottom). The zoomed subplots show the dimensioning incident of BESS power capacity occurring on December 5.

2.4.2.3 Dimensioning of BESS energy capacity

The dimensioning of the BESS energy capacity depends on the maximum accumulated power deficiency/surplus of the aggregated microgrids. When analyzing the net load profile of the aggregated microgrids, it was found that the highest accumulated energy deficiency occurs on December 9, which is illustrated by the dashed area in Figure 2.14. The energy deficiency lasts for 9 hours starting from 11:00 AM and ending at 08:00 PM, and carries an accumulated energy of 0.3661 p.u.h. Thus, the dimensioning of the energy storage should be 0.3661/0.895 = 0.40491 p.u.h., when accounting for the round trip efficiency of 89.5%. This value is similar to the one obtained by optimization 0.4002 p.u.h.

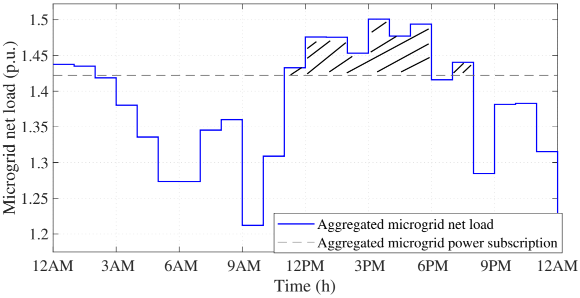

Figure 2.14: Dimensioning incident of BESS energy capacity showing the maximum accumulated energy deficiency of aggregated industrial and community microgrids on December 9.

2.4.2.4 Dimensioning of multiport converter AC port 1

To estimate MPC AC Port 1 power capacity, its power dispatch is first estimated based on a predefined operation:

$$\overset{\frown}{P}{}^{\text{MPC,out}}_{t_{\text{GC}},1} = \Delta P^{\text{MG,def}}_{t_{\text{GC}},1} + \min\left(\eta^2_{\text{tran}}\eta^2_{\text{inv}}\Delta P^{\text{MG,plus}}_{t_{\text{GC}},2}, \Delta P^{\text{MG,exp}}_{t_{\text{GC}},1}\right) \quad \forall t_{\text{GC}}, \tag{2.6a}$$

$$\overset{\frown}{P}{}^{\text{MPC,in}}_{t_{\text{GC}},1} = \Delta P^{\text{MG,plus}}_{t_{\text{GC}},1} + \min\left(\frac{\Delta P^{\text{MG,def}}_{t_{\text{GC}},2}}{\eta^2_{\text{tran}}\eta^2_{\text{inv}}}, \Delta P^{\text{MG,imp}}_{t_{\text{GC}},1}\right) \quad \forall t_{\text{GC}}, \tag{2.6b}$$

$$\overset{\frown}{P}{}^{\text{MPC}}_{t_{\text{GC}},1} = \overset{\frown}{P}{}^{\text{MPC,out}}_{t_{\text{GC}},1} - \overset{\frown}{P}{}^{\text{MPC,in}}_{t_{\text{GC}},1} \quad \forall t_{\text{GC}}, \tag{2.6c}$$

where (2.6a) defines the output power of AC Port 1, (2.6b) defines the input power of AC Port 1, and (2.6c) accounts for the net power. The first term of (2.6a) corresponds to the scenarios where Microgrid 1 is deficient in power and power is injected by AC Port 1. The second term of (2.6a) corresponds to the scenarios where Microgrid 2 has surplus power and the power is exported to Microgrid 1. The first term of (2.6b) corresponds to the scenarios where Microgrid 1 has surplus power and the power is absorbed by AC port 1. The second term of (2.6b) corresponds to the scenarios where Microgrid 2 is deficient in power and the power is imported from Microgrid 1.

Figure 2.15 (top) compares the estimated and optimal power dispatch of

AC Port 1. To help understand the power dispatch of AC Port 1, the net load profiles of industrial and community microgrids are presented in Figure 2.15 (middle). It can be seen that AC Port 1 has positive power when the industrial microgrid is power deficit, negative power when the community microgrid is power deficit and the industrial microgrid has spare capacity, and zero power during the remainder of the year. The estimated power dispatch replicates the optimum one very accurately with a mismatch of only 2%:

$$\frac{\sum\limits_{t_{\mathrm{GC}}=1}^{T_{\mathrm{GC}}} \left| \overset{\frown}{P}{}^{\mathrm{MPC}}_{t_{\mathrm{GC}},1} - P^{\mathrm{MPC}}_{t_{\mathrm{GC}},1} \right|}{\sum\limits_{t_{\mathrm{GC}}=1}^{T_{\mathrm{GC}}} \left| P^{\mathrm{MPC}}_{t_{\mathrm{GC}},1} \right|} = 2\%.$$

However, the estimated power dispatch does not accurately depict the dimensioning incident. The dimensioning incident occurred on February 5 at 10:00 AM and is shown in the zoomed subplot of Figure 2.15. The dimensioning incident corresponds to the scenario in which the community microgrid experiences its maximum power deficiency of 0.32 p.u. and power is imported from the industrial microgrid. The estimated power dispatch imports the entire power 0.33 p.u. from the industrial microgrid (additional 0.01 p.u. due to power losses in the MPC) while the BESS is in standby (see the bottom subplot of Figure2.15). On the other hand, the optimal solution imports only 0.25 p.u. of power from the industrial microgrid with additional power support from the BESS by 0.07 p.u. Thus, the estimated dispatch leads to over-sizing AC Port 1 by 32%:

$$\frac{\left| \overset{\frown}{P}{}^{\mathrm{MPC,max}}_{1} - P^{\mathrm{MPC,max}}_{1} \right|}{P^{\mathrm{MPC,max}}_{1}} = \frac{0.33 - 0.25}{0.25} = 32\%.$$

This shows that the rule-of-thumb method may result in overestimating the size of an AC port of the MPC. This is because the rule-of-thumb method underestimates the role of the BESS, especially under the condition when one microgrid experiences a capacity bottleneck while the other microgrid has sufficient spare capacity to support the former microgrid. In this case, the estimated power dispatch assumes that the power is re-routed to the other microgrid. However, this may result in over-dimensioning the other AC port of the MPC. Instead, the optimization method suggests that the BESS takes some of the power burden, especially if the BESS has sufficient capacity and storage, which may reduce the size of the other AC port of the MPC. Therefore, the rule-of-thumb method can be seen as a quick method to obtain an upper limit for the MPC size.

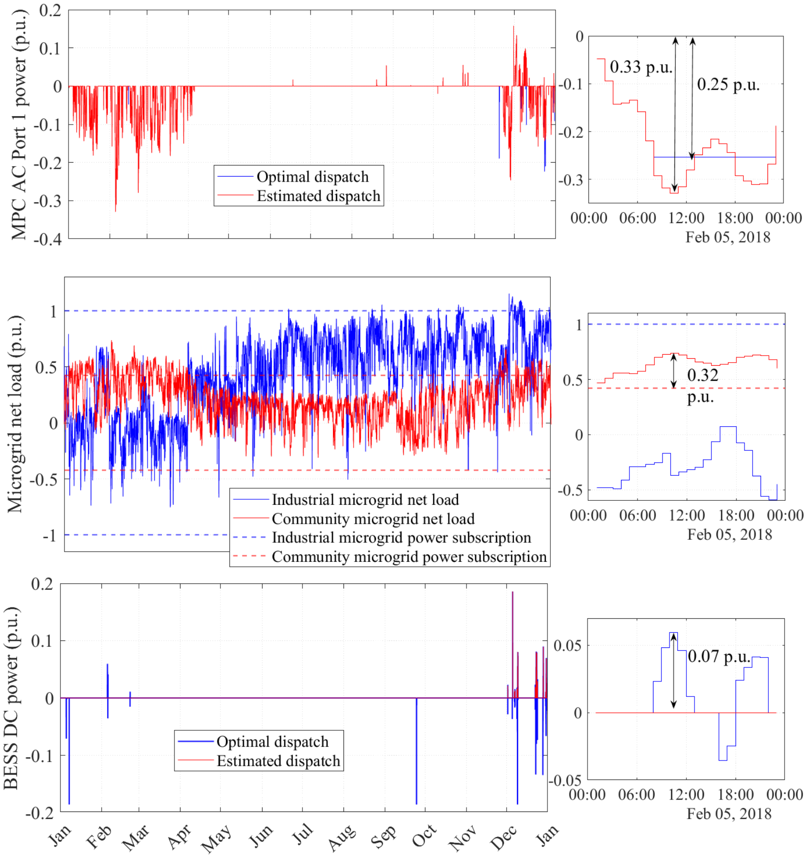

Figure 2.15: Optimal and estimated MPC AC Port 1 power dispatch (top); net load profile of industrial and community microgrids (middle); optimal and estimated BESS power dispatch (bottom). The zoomed subplots show the dimensioning incident of MPC AC Port 1 occurring on February 5, 10:00 AM.

2.4.2.5 Dimensioning of multiport converter AC port 2

To estimate MPC AC Port 2 power capacity, its power dispatch is first estimated based on a predefined operation:

$$\overset{\frown}{P}^{\mathrm{MPC,out}}_{t_{\mathrm{GC}},2} = \Delta P^{\mathrm{MG,def}}_{t_{\mathrm{GC}},2} + \min\left(\eta^2_{\mathrm{tran}}\eta^2_{\mathrm{inv}}\Delta P^{\mathrm{MG,plus}}_{t_{\mathrm{GC}},1}, \Delta P^{\mathrm{MG,exp}}_{t_{\mathrm{GC}},2}\right) \quad \forall t_{\mathrm{GC}}, \tag{2.7a}$$

$$\overset{\frown}{P}^{\mathrm{MPC,in}}_{t_{\mathrm{GC}},2} = \Delta P^{\mathrm{MG,plus}}_{t_{\mathrm{GC}},2} + \min\left(\frac{\Delta P^{\mathrm{MG,def}}_{t_{\mathrm{GC}},1}}{\eta^2_{\mathrm{tran}}\eta^2_{\mathrm{inv}}}, \Delta P^{\mathrm{MG,imp}}_{t_{\mathrm{GC}},2}\right) \quad \forall t_{\mathrm{GC}}, \tag{2.7b}$$

$$\overset{\frown}{P}^{\mathrm{MPC}}_{t_{\mathrm{GC}},2} = \overset{\frown}{P}^{\mathrm{MPC,out}}_{t_{\mathrm{GC}},2} - \overset{\frown}{P}^{\mathrm{MPC,in}}_{t_{\mathrm{GC}},2} \quad \forall t_{\mathrm{GC}}, \tag{2.7c}$$

where (2.7a) defines the output power of AC Port 2, (2.7b) defines the input power of AC Port 2, and (2.7c) accounts for the net power. The first term of (2.7a) corresponds to the scenarios where Microgrid 2 is deficient in power and power is injected by AC Port 2. The second term of (2.7a) corresponds to the scenarios where Microgrid 1 has surplus power and the power is exported to Microgrid 2. The first term of (2.7b) corresponds to the scenarios where Microgrid 2 has surplus power and the power is absorbed by AC port 2. The second term of (2.7b) corresponds to the scenarios where Microgrid 1 is deficient in power and the power is imported from Microgrid 2.

Figure 2.16 (top) compares the estimated and optimal power dispatch of AC Port 2. To help understand the power dispatch of AC Port 2, the net load profiles of industrial and community microgrids are presented in Figure 2.16 (bottom). It can be seen that AC Port 2 has positive power when the community microgrid is power deficit, negative power when the industrial microgrid is power deficit and the community microgrid has spare capacity, and zero power during the remainder of the year. The estimated power dispatch replicates the optimum one very well with a mismatch of only 1.6%:

$$\frac{\sum_{t_{\mathrm{GC}}=1}^{T_{\mathrm{GC}}}\left|\overset{\frown}{P}^{\mathrm{MPC}}_{t_{\mathrm{GC}},2} - P^{\mathrm{MPC}}_{t_{\mathrm{GC}},2}\right|}{\sum_{t_{\mathrm{GC}}=1}^{T_{\mathrm{GC}}}\left|P^{\mathrm{MPC}}_{t_{\mathrm{GC}},2}\right|} = 1.6\%.$$

The dimensioning incident is also accurately replicated as shown in the zoomed subplots of Figure 2.16. The dimensioning incident occurs on February 5 at 10:00 (same as dimensioning incident for AC Port 1), and corresponds to the maximim power deficiency in the community microgrid of 0.32 p.u. Therefore, AC Port 2 injects 0.32 p.u. power to alleviate the capacity bottleneck. There is no mismatch between the estimated and optimal capacity of AC Port 2.

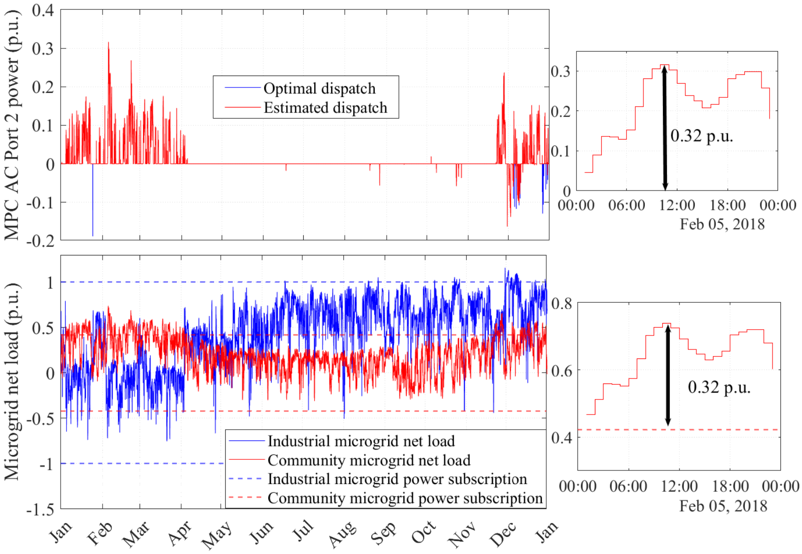

Figure 2.16: Optimal and estimated MPC AC Port 2 power dispatch (top); net load profile of industrial and community microgrids (bottom). The zoomed subplots show the dimensioning incident of MPC AC Port 2 power capacity occurring on February 5, 10:00 AM.

This section has only focused on the use of the MPC with integrated BESS to alleviate the grid capacity bottleneck. Therefore, it is evident that the utilization rate of MPC and BESS is quite low, with the utilization rate of AC Port 1 and AC Port 2 of MPC being 15.9%, and that of BESS being 1.29%. This may raise a question about the economic feasibility of the project. Additional functions that may bring a revenue stream, such as energy arbitrage and frequency ancillary services, can increase the utilization of the MPC with integrated BESS and facilitate its payback. However, this is not the focus of this chapter.

Figure 2.17 summarizes the rule-of-thumb method for dimensioning MPC with integrated BESS to interconnect microgrids to mitigate grid capacity bottleneck. The maximum size of AC Port 1 and AC Port 2 should account for the worst among the four scenarios illustrated in the figure. The size of the BESS power and energy capacities should account for the worst among the two illustrated scenarios. Note that the rule-of-thumb method gives an upper bound for the size of MPC and BESS, as compared to the size obtained by optimization. Thus, the rule-of-thumb method can be used to obtain a quick and rough size of the MPC and BESS.

2.4.3 Proposed rule-of-thumb method for dimensioning of multiport converter with integrated BESS and DC load

The previous section has illustrated the proposed rule-of-thumb method for dimensioning of MPC with integrated BESS to interconnect microgrids for mitigating grid capacity bottleneck. This section illustrates the updated rule-of-thumb for dimensioning of MPC and BESS if a DC load is integrated to the DC link of the MPC.

2.4.3.1 Load profile of DC load

Figure 2.18 (top) shows the DC load profile, and Figure 2.18 (bottom) shows the net load profile of industrial and community microgrids. The DC load profile is obtained by assuming that 20% of the industrial demand is a DC demand and that this DC demand is integrated with the MPC. Note that the net load profile of the industrial microgrid excludes the DC load. This is done for practical reasons to simplify the analysis of dimensioning the MPC. However, the aggregated net load profile of the two microgrids with the DC load remains the same as in the previous section. Therefore, it is not shown here.

2.4.3.2 Definition of key parameters

Additional parameters in addition to those defined in Section 2.4.2.1 must be defined that will serve to simplify the analysis of the size of the MPC with integrated BESS and DC load. The DC load profile $P_{t_{\mathrm{GC}}}^{\mathrm{L,DC}}$ is divided into two components, the first being supplied by Microgrid 1 and Microgrid 2 $P_{t_{\mathrm{GC}}}^{\mathrm{L,DC,MG}}$, and the second being supplied by BESS $P_{t_{\mathrm{GC}}}^{\mathrm{L,DC,B}}$:

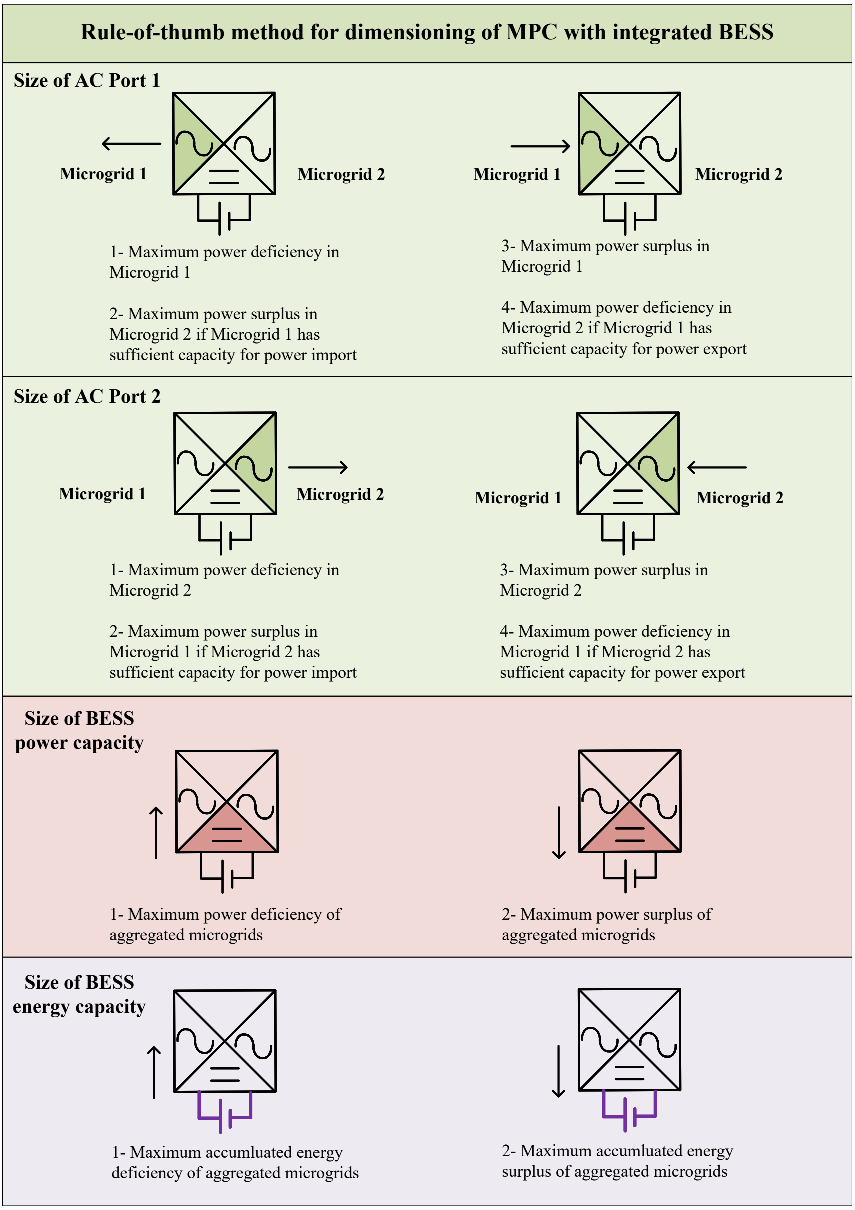

1- Maximum power deficiency in Microgrid 1

2- Maximum power surplus in Microgrid 2 if Microgrid 1 has sufficient capacity for power import

3- Maximum power surplus in Microgrid 1

4- Maximum power deficiency in Microgrid 2 if Microgrid 1 has sufficient capacity for power export

1- Maximum power deficiency in Microgrid 2

2- Maximum power surplus in Microgrid 1 if Microgrid 2 has sufficient capacity for power import

3- Maximum power surplus in Microgrid 2

4- Maximum power deficiency in Microgrid 1 if Microgrid 2 has sufficient capacity for power export

1- Maximum power deficiency of aggregated microgrids

2- Maximum power surplus of aggregated microgrids

1- Maximum accumluated energy deficiency of aggregated microgrids

2- Maximum accumluated energy surplus of aggregated microgrids

Figure 2.17: Rule-of-thumb method for dimensioning of MPC with integrated BESS to interconnect microgrids for mitigating grid capacity bottleneck. Note that the sizing referred to here is active power sizing.

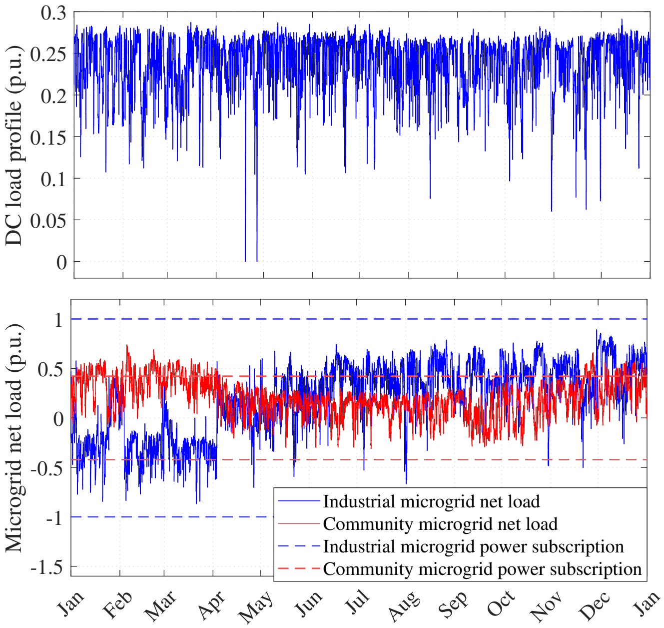

Figure 2.18: Recording of DC load profile (top), and industrial and community microgrids net load profiles (bottom), recorded over one calender year.

$$P_{t_{\mathrm{GC}}}^{\mathrm{L,DC}} = P_{t_{\mathrm{GC}}}^{\mathrm{L,DC,MG}} + P_{t_{\mathrm{GC}}}^{\mathrm{L,DC,B}} \quad \forall t_{\mathrm{GC}}, \tag{2.8}$$

where

$$P_{t_{\mathrm{GC}}}^{\mathrm{L,DC,MG}} = \min\left(\eta_{\mathrm{tran}}\eta_{\mathrm{inv}}\left(\sum_{m=1}^{2}\Delta P_{t_{\mathrm{GC}},m}^{\mathrm{MG,imp}}\right), P_{t_{\mathrm{GC}}}^{\mathrm{L,DC}}\right) \quad \forall t_{\mathrm{GC}}, \tag{2.9}$$

and

$$P_{t_{\mathrm{GC}}}^{\mathrm{L,DC,B}} = P_{t_{\mathrm{GC}}}^{\mathrm{L,DC}} - P_{t_{\mathrm{GC}}}^{\mathrm{L,DC,MG}} \quad \forall t_{\mathrm{GC}}. \tag{2.10}$$

The rule-of-thumb method assumes that the DC load is primarily supplied from the AC grid through the AC Ports of the MPC, as long as the two microgrids have sufficient spare capacity. In case the spare capacity of the microgrids was not sufficient, the BESS supplies the remainder of the DC load. The main reason for prioritizing the AC grid over the BESS for supplying the DC load is that investment in energy storage is expensive, especially for extended duration. Keep in mind that this section does not attempt to propose an operating method for the MPC with BESS, but rather focuses on finding an estimated size for grid capacity bottleneck alleviation.

2.4.3.3 Dimensioning of BESS power and energy capacities

As illustrated in Section 2.4.2, the estimated power and energy capacities of BESS are based on the net load profile of the aggregated microgrids (including the DC load in this case). Since the aggregated microgrid net load profile has not changed, the estimated size of the BESS remains the same. However, the optimal size of the BESS obtained by optimization shows a slight increase, with power capacity increasing from 0.185 p.u. to 0.190 p.u. and energy capacity from 0.40491 p.u.h to 0.4233 p.u.h. This increase in the size is due to the additional losses occurring in the MPC to feed the DC load, which did not exist in the case when the DC load was not integrated in the MPC. However, the rule-of-thumb method do not account for the power losses since it does not contribute to a large portion of the final size.

2.4.3.4 Dimensioning of multiport converter AC port 1

To estimate MPC AC Port 1 power capacity, its power dispatch is first estimated based on a predefined operation. The operation of AC Port 1 follows the same principle as in Section 2.4.2 but accounts additionally for the supply of DC load:

$$\overset{\frown}{P}{}^{\mathrm{MPC,out}}_{t_{\mathrm{GC}},1} = \Delta P^{\mathrm{MG,def}}_{t_{\mathrm{GC}},1} + \min\left(\eta_{\mathrm{tran}}\eta_{\mathrm{inv}} \min\left(\eta_{\mathrm{tran}}\eta_{\mathrm{inv}}\Delta P^{\mathrm{MG,plus}}_{t_{\mathrm{GC}},2} - P^{\mathrm{L,DC}}_{t_{\mathrm{GC}}}, 0\right), \Delta P^{\mathrm{MG,exp}}_{t_{\mathrm{GC}},1}\right) \quad \forall t_{\mathrm{GC}}, \tag{2.11a}$$

$$\overset{\frown}{P}{}^{\mathrm{MPC,in}}_{t_{\mathrm{GC}},1} = \Delta P^{\mathrm{MG,plus}}_{t_{\mathrm{GC}},1} + \min\left(\frac{\Delta P^{\mathrm{MG,def}}_{t_{\mathrm{GC}},2}}{\eta^2_{\mathrm{tran}}\eta^2_{\mathrm{inv}}} + \frac{\Delta P^{\mathrm{MG,imp}}_{t_{\mathrm{GC}},1}}{\Delta P^{\mathrm{MG,imp}}_{t_{\mathrm{GC}},1} + \Delta P^{\mathrm{MG,imp}}_{t_{\mathrm{GC}},2}} \frac{P^{\mathrm{L,DC}}_{t_{\mathrm{GC}}}}{\eta_{\mathrm{tran}}\eta_{\mathrm{inv}}}, \Delta P^{\mathrm{MG,imp}}_{t_{\mathrm{GC}},1}\right) \quad \forall t_{\mathrm{GC}}, \tag{2.11b}$$

$$\overset{\frown}{P}{}^{\mathrm{MPC}}_{t_{\mathrm{GC}},1} = \overset{\frown}{P}{}^{\mathrm{MPC,out}}_{t_{\mathrm{GC}},1} - \overset{\frown}{P}{}^{\mathrm{MPC,in}}_{t_{\mathrm{GC}},1} \quad \forall t_{\mathrm{GC}}, \tag{2.11c}$$

where (2.11a) defines the output power of AC Port 1, (2.11b) defines the input power of AC Port 1, and (2.11c) accounts for the net power. The first term of (2.11a) corresponds to the scenarios where Microgrid 1 is deficient in power and power is injected by AC Port 1. The second term of (2.11a) corresponds to the scenarios where Microgrid 2 has surplus power, and if that surplus power exceeds the DC load demand, the remaining is exported to Microgrid 1. The first term of (2.11b) corresponds to the scenarios where Microgrid 1 has surplus power and the power is absorbed by AC port 1. The second term of (2.11b) corresponds to the scenarios where Microgrid 2 is deficient in power and the power is imported from Microgrid 1. In addition to exporting power to Microgrid 2, this term also accounts for the power needed to supply the DC load.

Figure 2.19 (top) shows the estimated and optimal power dispatch of MPC AC Port 1. It is clear that there is a large difference between the two power dispatches. This is mainly because optimal dispatch may have several optimal solutions, since the DC load can be supplied through AC Port 1 or AC Port 2 with equal penalty on the losses. The equal penalty for losses is due to neglecting losses occurring in the cable interconnecting microgrids in the optimization problem. Otherwise, Microgrid 1 would have been more favorable for supplying the DC load since it is electrically closer. However, irrespective of which AC Port is supplying the DC load, the total dimensioning of both AC ports should be optimal. The dimensioning incident of AC Port 1 occurs when the aggregated community microgrid net load with the DC load demand reaches a peak value (see the middle subplot). This occurred on February 22, 09:00 AM, with a total power deficiency of 0.54 p.u. The estimated power dispatch borrows all the needed power from the industrial microgrid, i.e. 0.56 p.u. (additional 0.02 p.u. to account for losses in the MPC), while the BESS is in standby (see the bottom subplot). On the other hand, the optimal dispatch provides additional power support of 0.08 p.u. from the BESS, which reduces the power needed from the industrial microgrid. This reduces the size of AC Port 1 to 0.48. Thus, the estimated size of MPC AC Port 1 is larger by 16.7%:

$$\frac{\left|\overset{\frown}{P}_1^{\mathrm{MPC,max}} - P_1^{\mathrm{MPC,max}}\right|}{P_1^{\mathrm{MPC,max}}} = \frac{0.56 - 0.48}{0.48} = 16.7\%$$

As explained in the previous section, the overestimation of AC port 1 of the MPC is because the rule-of-thumb method underestimates the role of BESS. The rule-of-thumb method assumes that the BESS is always in standby unless both microgrids have exceeded their maximum power exchange with the upstream grid. Thus, the usage of BESS is very restricted in the rule-of-thumb method. However, the rule-of-thumb method can be seen as a quick method to obtain a higher limit for the MPC size.

2.4.3.5 Dimensioning of multiport converter AC port 2

The estimated dispatch of AC Port 2 follows the same principle as in Section 2.4.2 but accounts additionally for the supply of DC load:

$$\overset{\frown}{P}_{t_{\mathrm{GC}},2}^{\mathrm{MPC,out}} = \Delta P_{t_{\mathrm{GC}},2}^{\mathrm{MG,def}} + \min\left(\eta_{\mathrm{tran}}\eta_{\mathrm{inv}} \min\left(\eta_{\mathrm{tran}}\eta_{\mathrm{inv}}\Delta P_{t_{\mathrm{GC}},1}^{\mathrm{MG,plus}} - P_{t_{\mathrm{GC}}}^{\mathrm{L,DC}}, 0\right), \Delta P_{t_{\mathrm{GC}},2}^{\mathrm{MG,exp}}\right) \quad \forall t_{\mathrm{GC}}, \tag{2.12a}$$

$$\overset{\frown}{P}_{t_{\mathrm{GC}},2}^{\mathrm{MPC,in}} = \Delta P_{t_{\mathrm{GC}},2}^{\mathrm{MG,plus}} + \min\left(\frac{\Delta P_{t_{\mathrm{GC}},1}^{\mathrm{MG,def}}}{\eta_{\mathrm{tran}}^2\eta_{\mathrm{inv}}^2} + \frac{\Delta P_{t_{\mathrm{GC}},2}^{\mathrm{MG,imp}}}{\Delta P_{t_{\mathrm{GC}},1}^{\mathrm{MG,imp}} + \Delta P_{t_{\mathrm{GC}},2}^{\mathrm{MG,imp}}} \frac{P_{t_{\mathrm{GC}}}^{\mathrm{L,DC}}}{\eta_{\mathrm{tran}}\eta_{\mathrm{inv}}}, \Delta P_{t_{\mathrm{GC}},2}^{\mathrm{MG,imp}}\right) \quad \forall t_{\mathrm{GC}}, \tag{2.12b}$$

$$\overset{\frown}{P}_{t_{\mathrm{GC}},2}^{\mathrm{MPC}} = \overset{\frown}{P}_{t_{\mathrm{GC}},2}^{\mathrm{MPC,out}} - \overset{\frown}{P}_{t_{\mathrm{GC}},2}^{\mathrm{MPC,in}} \quad \forall t_{\mathrm{GC}}, \tag{2.12c}$$

where (2.12a) defines the output power of AC Port 2, (2.12b) defines the input power of AC Port 2, and (2.12c) accounts for the net power. The first term of (2.12a) corresponds to the scenarios where Microgrid 2 is deficient in power and power is injected by AC Port 2. The second term of (2.12a)

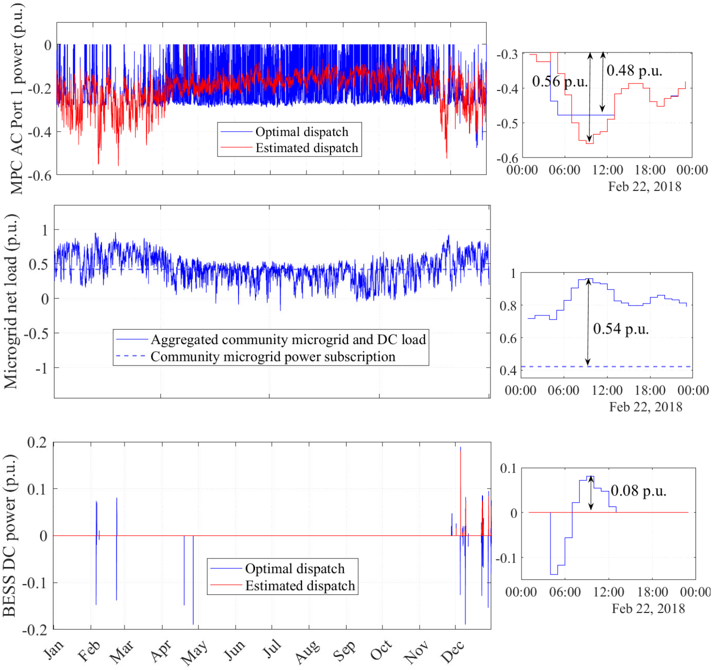

Figure 2.19: Optimal and estimated MPC AC Port 1 power dispatch (top); aggregated net load profile of community microgrid with DC load (middle); optimal and estimated BESS power dispatch (bottom). The zoomed subplots show the dimensioning incident of MPC AC Port 1 occurring on February 22, 09:00 AM.

corresponds to the scenarios where Microgrid 1 has surplus power, and if that surplus power exceeds the DC load demand, the remaining is exported to Microgrid 2. The first term of (2.12b) corresponds to the scenarios where Microgrid 2 has surplus power and the power is absorbed by AC port 2. The second term of (2.12b) corresponds to the scenarios where Microgrid 1 is deficient in power and the power is imported from Microgrid 2. In addition to exporting power to Microgrid 1, this term also accounts for the power needed to supply the DC load.

Figure 2.20 (top) shows the estimated and optimal power dispatches of MPC AC Port 2. Similar to the case of AC Port 1, the mismatch between the estimated and optimal power dispatch is also large. As explained earlier, this is because there are many optimal solutions where the DC load can be supplied from Microgrid 1 or Microgrid 2. However, irrespective of whether the DC load is supplied from Microgrid 1 or Microgrid 2, this should not lead to over-dimensioning of the AC ports. The dimensioning incident of AC Port 2 occurs on February 5, 10:00 AM, when the community microgrid reaches its peak net demand (see the bottom subplot). The power capacity of AC Port 2 in this case is determined by the maximum power deficiency of Microgrid 2 0.32 p.u. The estimated power capacity of AC Port 2 matches exactly with the optimal solution.

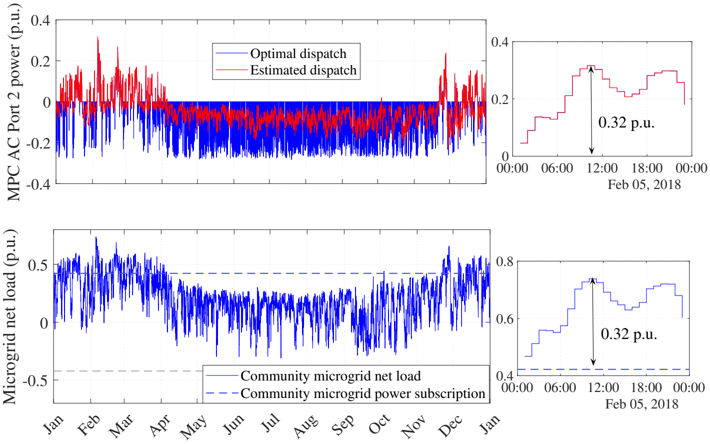

Figure 2.20: Optimal and estimated MPC AC Port 2 power dispatch (top); net load profile of community microgrids (bottom). The zoomed subplots show the dimensioning incident of MPC AC Port 2 occurring on February 5, 10:00 AM.

Figure 2.21 summarizes the rule-of-thumb method for dimensioning MPC with integrated BESS and DC load to interconnect microgrids for mitigating grid capacity bottleneck. The maximum size of AC Port 1 and AC Port 2 should account for the worst among the four scenarios illustrated in the figure. The size of the BESS power and energy capacities should account for the worst among the two illustrated scenarios. Note that the rule-of-thumb method gives an upper bound for the size of MPC and BESS, as compared to the size obtained by optimization. Thus, the rule-of-thumb method can be used to obtain a quick and rough size of the MPC and BESS.

2.4.3.6 Sensitivity analysis of BESS cost

The previous analysis considers the CAPEX of the BESS as of 2020. Although BESS costs have witnessed an exponential decrease during the previous decade (2010-2019), the first half of the current decade (2020-2025) had a more moderate decrease in costs, which is expected to continue at the same rate according to forecasts [62]. This section analyses the impact of the reduction of BESS CAPEX on the resulting size of the MPC with integrated BESS. The BESS CAPEX here refers to two cost components, the DC/DC converter and the storage. The DC/AC converter is not considered as part of the BESS in this context, as the BESS is integrated with the MPC. This implies that the DC/AC converter has other functions such as integrating the DC load and performing power rerouting.

Figure 2.22 shows the resulting size of MPC AC Port 1 and AC Port 2 in addition to the energy and power capacities of BESS when sweeping the BESS CAPEX from 100% to 5% of its base CAPEX. The results show that the BESS energy capacity does not change until the BESS CAPEX is reduced to 8% of its original CAPEX (reduction of twelve times). This shows that the size is not very sensitive to the BESS CAPEX. To understand the reason behind that, we first need to understand the drivers behind sizing AC Port 1 and AC Port 2. The size of AC Port 2 does not change throughout the entire range of BESS cost. This is because the dimensioning of AC Port 2 is determined by the maximum power deficiency in Microgrid 2. This means that whether the power needed to alleviate the capacity bottleneck in Microgrid 2 comes from the BESS or from Microgrid 1, it definitely has to go through AC Port 2.

On the other hand, the dimensioning incident of AC Port 1 is due to capacity bottleneck in Microgrid 2. This leads to power export from Microgrid 1 to Microgrid 2 while simultaneously supplying the DC load. If the BESS takes some of the DC load power burden or helps alleviate the capacity bottleneck in Microgrid 2, this may reduce the required size of AC port 1. However, to find the additional size of energy storage needed if the BESS to take some of the power burden from AC Port 1, one should analyze the duration during which AC Port 1 utilizes its maximum power. The results show that the longest duration for which AC Port 1 maintains its maximum power is during

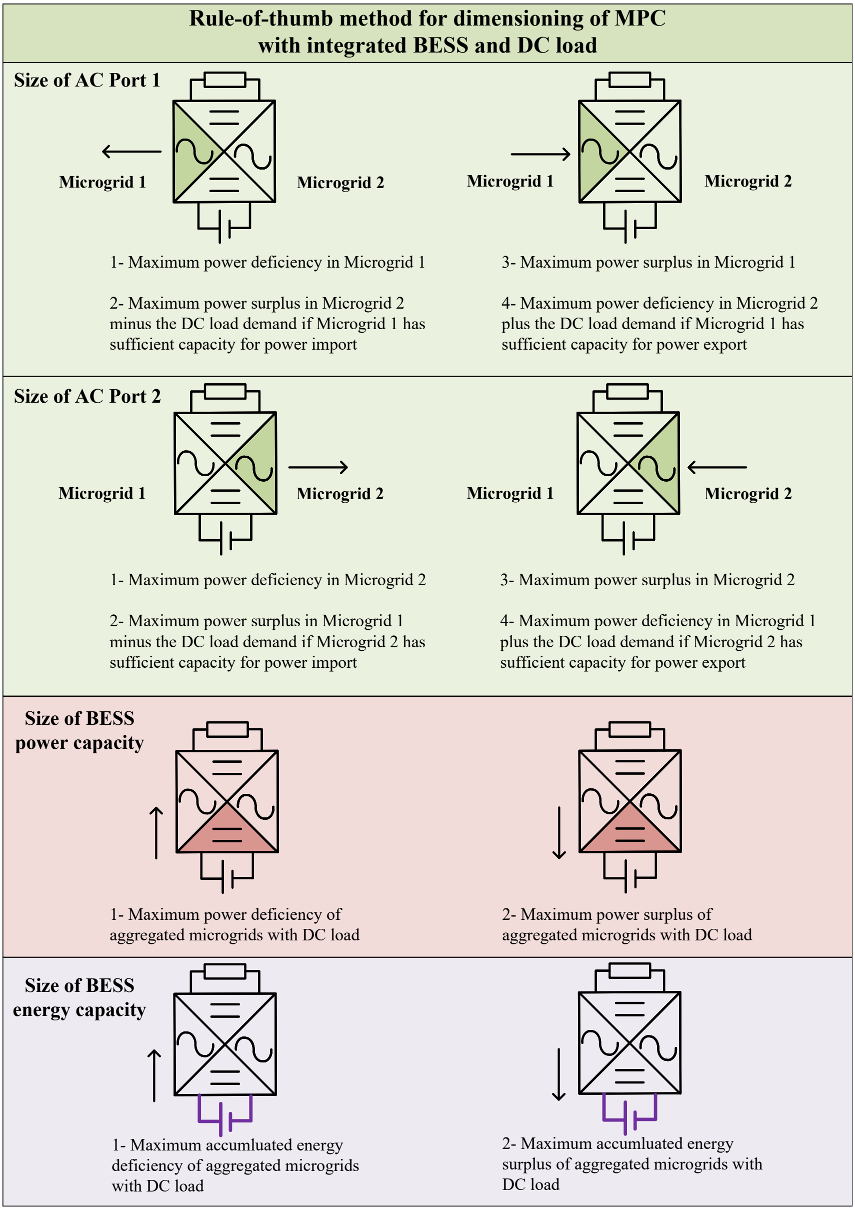

Size of AC Port 1

1- Maximum power deficiency in Microgrid 1

2- Maximum power surplus in Microgrid 2 minus the DC load demand if Microgrid 1 has sufficient capacity for power import

3- Maximum power surplus in Microgrid 1

4- Maximum power deficiency in Microgrid 2 plus the DC load demand if Microgrid 1 has sufficient capacity for power export

Size of AC Port 2

1- Maximum power deficiency in Microgrid 2

2- Maximum power surplus in Microgrid 1 minus the DC load demand if Microgrid 2 has sufficient capacity for power import

3- Maximum power surplus in Microgrid 2

4- Maximum power deficiency in Microgrid 1 plus the DC load demand if Microgrid 2 has sufficient capacity for power export

Size of BESS power capacity

1- Maximum power deficiency of aggregated microgrids with DC load

2- Maximum power surplus of aggregated microgrids with DC load

Size of BESS energy capacity

1- Maximum accumluated energy deficiency of aggregated microgrids with DC load

2- Maximum accumluated energy surplus of aggregated microgrids with DC load

Figure 2.21: Rule-of-thumb method for dimensioning of MPC with integrated BESS and DC load to interconnect microgrids for mitigating grid capacity bottleneck. Note that the sizing referred to here is active power sizing.

February 5 and for 12 continuous hours. This explains why the battery cost has to decrease by around twelve times, before the optimization decides to increase the investment in BESS on behalf of AC Port 1. Despite the fact that the BESS energy capacity has increased significantly, its power capacity remained the same. This indicates that the BESS needed for this case study is of high energy density, i.e., high energy to power ratio.

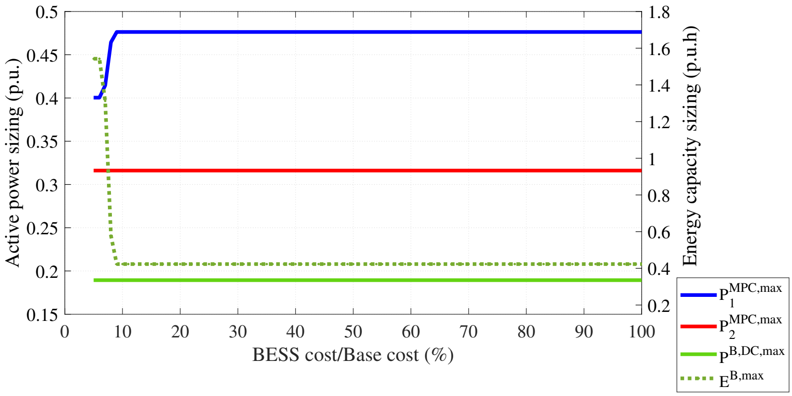

Figure 2.22: Sensitivity of the size of MPC AC Port 1 and AC Port 2 ($P_1^{\mathrm{MPC,max}}$ and $P_2^{\mathrm{MPC,max}}$) and BESS power and energy capacities ($P^{\mathrm{B,DC,max}}$ and $E^{\mathrm{B,max}}$) to reduction in BESS CAPEX from 100% to 5% of its base CAPEX.

2.5 Summary

This chapter has investigated the interconnected microgrid by MPC as a potential solution to mitigate the grid capacity bottleneck by reducing the peak net load of two microgrids. First, the interconnected microgrids by MPC is compared against existing solutions for peak net load reduction, namely the separate microgrids with individual storages and the interconnected microgrids by B2B converter with individual storages. The simulation results using generic load profiles show that the interconnection of microgrids can reduce or even eliminate the need for an additional energy storage system if the two microgrids have a low or intermediate coincidence factor. Furthermore, interconnection by MPC reduces the aggregated size of all DC/AC converters compared to the B2B converter counterpart thanks to its integrated BESS at the DC-link. Second, the dimensioning of the MPC with integrated BESS and DC load is illustrated under a realistic scenario of industrial and community microgrids. The results show that the dimensioning of an AC port of the multiport converter should account for the following scenarios: a) maximum power deficiency/surplus in the microgrid to which the AC port is interfaced; b) power deficiency/surplus in the neighboring microgrid that coincides with high/low DC load demand and available power capacity in the microgrid to which the AC port is interfaced. In case power rerouting between the two microgrids through the MPC is not sufficient to reduce the peak net load, an additional investment in BESS is needed to provide temporal power support. The dimensioning of the BESS power capacity should account for the maximum power deficiency/surplus of aggregated microgrids, and its energy capacity should account for the maximum accumulated energy deficiency/surplus of the aggregated microgrids.

CHAPTER 3

Control of BESS to improve frequency stability of hydro-powered microgrid during island transition

This chapter developes a frequency controller of a BESS to facilitate a frequency-secure unplanned island transition of a hydro-powered microgrid.

3.1 Introduction

Commercial and industrial (C&I) facilities are critical loads requiring high degree of electricity supply reliability and resiliency [8]–[10], and the traditional N-1 supply reliability is not applicable. Thus, many C&I facilities have their own local backup gas or diesel generators for island operation in case of grid outage. However, this generation type is not environmentally friendly, and many C&I facilities have set their own targets for reducing CO2 emissions. One solution is to replace these fossil fuel powered generators with a BESS. However, long outage duration requires a large storage capacity, which makes the BESS uneconomical for C&I facility owners.

In Sweden, many C&I facilities are located close to a river where hydro generators are installed. For instance, a paper and pulp factory is supplied from the same substation to which a HPP in a close-by river is connected [63]. Another example is the ongoing Ludvika microgrid project in Sweden, where hydro generators will power the local community in island operation if an outage occurs in the upstream grid [64]. However, the main reason that hydro generators do not take the main responsibility for frequency regulation in island operation is because of their technical limitations. These limitations include: 1) limited fast frequency control capability caused by the regulation speed of the wicket gate and by the time delay of a long penstock [65]-[66], and 2) sustained frequency oscillations caused by the backlash in the gear when changing the direction of the wicket gate position [67]. One solution to assist the hydro generator for frequency regulation during island operation is to use a fast-acting device such as a BESS [68], which is interfaced to the grid by a voltage source inverter (VSI). Thus, how to design the frequency controller of the BESS in coordination with hydro generators for microgrid application becomes a relevant issue.

Several existing studies available in the literature have addressed the frequency control of BESS in microgrid applications [69]–[75]. In microgrids with only inverter-based resources, the conventional proportional-based (P-based) droop controller is deployed for the frequency regulation of BESS in island operation [69]–[71]. However, for microgrids where both synchronous generators (SGs) and inverter-based resources participate in frequency regulation, various droop-based frequency control strategies have been proposed for the BESS [72]–[75]. A P-based droop control with non-linear droop constant is used in [72] for the BESS to improve the frequency regulation of a diesel-powered microgrid during island operation. A similar non-linear droop is proposed in [73] to improve the frequency stability of the Maui Hawaiian Island. The performance of the controller is good for small frequency deviations but deteriorates in case of large frequency disturbances as the droop constant increases. In [74], BESS and thermostatically controlled loads are used to provide fast frequency support in an islanded microgrid with a relatively slow diesel engine governor. The BESS frequency controller is modeled as a P-based droop, while the diesel engine is in isochronous control mode, which allows the BESS to contribute in frequency support dynamically without depleting the storage in steady state. Authors in [75] propose a lag compensator for the frequency controller of BESS in a microgrid with a gas turbine. The strategy works well as the gas turbine has a fast frequency-regulating capability, which is not the case for hydro turbines. Consequently, such a frequency control strategy may not be able to fulfill the frequency nadir requirement in a hydro-powered microgrid. However, little literature has been found on the coordinated frequency control between BESS and hydro generators for microgrid applications.

On the other hand, for transmission system applications there exists some literature on coordinated frequency control between BESS and hydro generators [76], [77]. A first-order high-pass filter-based frequency controller has been developed for coordinated frequency regulation between BESS and hydro generators [76]. However, the gain of the frequency controller is tuned to be similar to the transient gain of a hydro governor, which is typically very small and may not be sufficient for mitigating the frequency nadir in a low inertia system such as a microgrid. Authors in [77] propose a 4^{th} order high-pass filter for the BESS to support hydro generators in grid frequency regulation. The filter parameters are tuned numerically for a specific system scenario, with no clear indication on how the control parameters should be adjusted when the system context changes such as for microgrid applications. Moreover, such a 4^{th} order frequency control structure further complicates the parameter tuning in reality, where delays in programmable logic controllers and nonlinearities in the turbine-governor system are present.

This chapter aims at developing the frequency controller of a BESS to facilitate a frequency-secure unplanned island transition of a hydro-powered microgrid. This chapter is structured as follows. In Section 3.2, the microgrid network diagram is presented and the mathematical model of the hydro turbine-governor system and BESS controller are summarized. Then, the proposed tuning of the BESS frequency controller is described in detail in Section 3.3, where the tuning strategy is summarized in Figure 3.5. In Section 3.4, the microgrid case study is first introduced, which is followed by the small-signal stability analysis of the proposed tuning. Section 3.5 presents the dynamic simulation results, where the proposed control strategy is compared with major existing strategies in the literature. Sensitivity analyses of the controller parameters on the performance of the frequency controller during microgrid island transition is also conducted. The proposed strategy is further validated through a laboratory experiment in Section 3.6. Section 3.7 discusses key assumptions made in the modeling and their implications. Finally, key findings are summarized in Section 3.8.

3.2 Microgrid model for island transition studies

3.2.1 Network diagram of hydro-powered microgrid

Figure 3.1 shows the network diagram of an actual medium-voltage (MV) distribution system in the west coast of Sweden to be operated as a microgrid. The paper and pulp factory is supplied from a 140/11 kV substation, to which a HPP is also connected. To enable a secure island transition of the microgrid, a BESS is installed at the factory bus. In the following sections, we elaborate on the control adopted for each of the hydro and BESS systems.

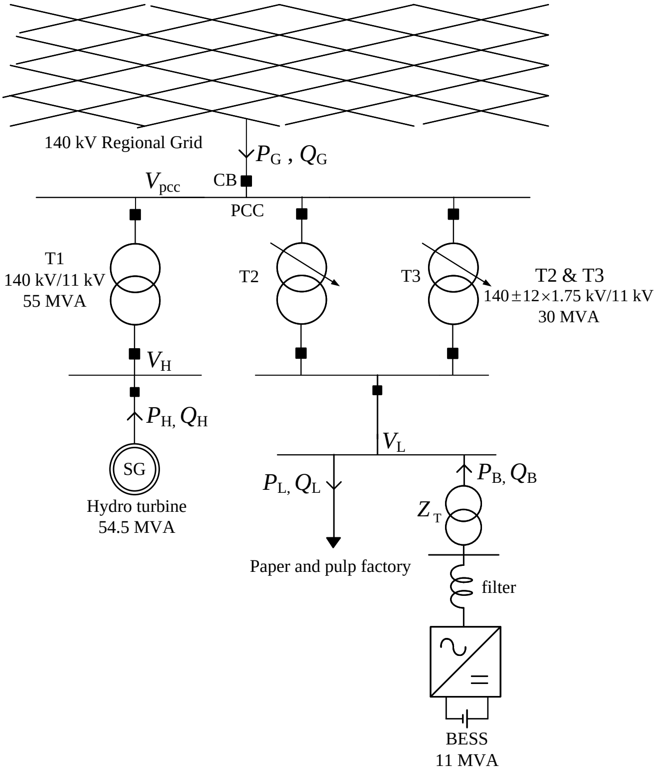

Figure 3.1: Hydro-powered microgrid equipped with a BESS to facilitate a secure island transition of a paper and pulp facility.

3.2.2 Hydro turbine with governor and exciter model

Figure 3.2 shows a generic Francis hydro turbine model for the provision of frequency containment reserve (FCR). The model includes a speed governor, an actuator of the wicket gate with ramp rate limiter and a turbine and penstock model [78]. The automatic voltage regulator (AVR) of the hydro generator is implemented as a standard PI controller with a static exciter model typically used in the Nordic 32 power system model [79]. For a detailed description of the AVR and the exciter model, the readers are referred to [79].

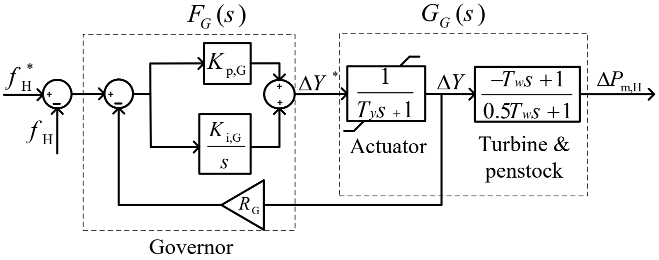

Figure 3.2: Simplified model of a Francis hydro turbine and governor for the provision of frequency containment reserve.

The open-loop transfer function of the output mechanical power with respect to the input frequency deviation of the hydro turbine can be expressed as

$$\begin{aligned}\frac{\Delta P_{\mathrm{m,H}}}{-\Delta f_{\mathrm{H}}} = &\left(\Gamma_{\mathrm{tr,G}}\frac{T_{\mathrm{G}}s}{T_{\mathrm{G}}s+1}+\Gamma_{\mathrm{ss,G}}\frac{1}{T_{\mathrm{G}}s+1}\right)\left(\frac{S_{\mathrm{b}}^{\mathrm{MG}}}{P_{\mathrm{b}}^{\mathrm{H}}}\right)\\ &\left(\frac{1}{T_{\mathrm{y}}s+1}\right)\left(\frac{-T_{\mathrm{w}}s+1}{0.5T_{\mathrm{w}}s+1}\right),\end{aligned} \tag{3.1}$$

where $\Delta f_{\mathrm{H}} = f_{\mathrm{H}} - f_{\mathrm{H}}^*$, and

$$\Gamma_{\mathrm{ss,G}} = \frac{1}{R_{\mathrm{G}}} \frac{P_{\mathrm{b}}^{\mathrm{H}}}{S_{\mathrm{b}}^{\mathrm{MG}}}, \tag{3.2a}$$

$$\Gamma_{\mathrm{tr,G}} = \frac{K_{\mathrm{p,G}}}{1 + R_{\mathrm{G}} K_{\mathrm{p,G}}} \frac{P_{\mathrm{b}}^{\mathrm{H}}}{S_{\mathrm{b}}^{\mathrm{MG}}}, \tag{3.2b}$$

$$T_{\mathrm{G}} = \frac{1 + R_{\mathrm{G}} K_{\mathrm{p,G}}}{R_{\mathrm{G}} K_{\mathrm{i,G}}}. \tag{3.2c}$$

In the previous equations, $\Gamma_{\mathrm{ss,G}}$ is the governor steady-state frequency regulation strength, $\Gamma_{\mathrm{tr,G}}$ is the governor transient frequency regulation strength, T_{G} is the governor time constant, $P_{\mathrm{b}}^{\mathrm{H}}$ is the HPP rated active power, and $S_{\mathrm{b}}^{\mathrm{MG}}$ is the microgrid base power. Note that the conventional PI-based droop of the hydro governor with the parameters, $K_{\mathrm{p,G}}$, $K_{\mathrm{i,G}}$ and R_{G}, is equivalent to a high-pass filter plus low-pass filter with the parameters, $\Gamma_{\mathrm{ss,G}}$, $\Gamma_{\mathrm{tr,G}}$ and T_{G}. In this chapter, the former parameters are expressed in per unit with respect to the HPP rated active power $P_{\mathrm{b}}^{\mathrm{H}}$, while the latter parameters are expressed in per unit with respect to the microgrid base power $S_{\mathrm{b}}^{\mathrm{MG}}$.

3.2.3 Control of BESS

3.2.3.1 Grid-following vs. grid-forming control

Traditionally, BESS is controlled in a grid-following (GFL) mode when connected to a strong grid. However, the GFL control has shown poor small-disturbance stability under weak grid connection when using phase-locked-loop (PLL) for grid synchronization [80]. In contrast, the grid-forming (GFM) control typically uses active power relation for obtaining the synchronization angle and has shown a better stability performance under weak grid or island operation [81]. Furthermore, the use of GFM control makes it easier for the BESS to transition between the grid-connected and island operation modes without switching the controller for obtaining the synchronization angle, especially during an unplanned islanding event. This also mitigates the impact of island detection delay [81], [82]. Thus, the GFM control will be implemented in this chapter.

3.2.3.2 Implemented grid-forming control structure

Figure 3.3 shows a standard GFM control structure of a BESS for both grid-connected and island operation in a microgrid [83]. The active power controller calculates the synchronization angle of the inverter. The PI-based active power controller in [84] is adopted in this work. The voltage controller uses an integrator-based droop control. A virtual impedance is implemented to calculate the reference current, which is sent to the vector current controller for calculating the reference voltage that the converter should output. The proposed frequency controller will be discussed in the following subsection.

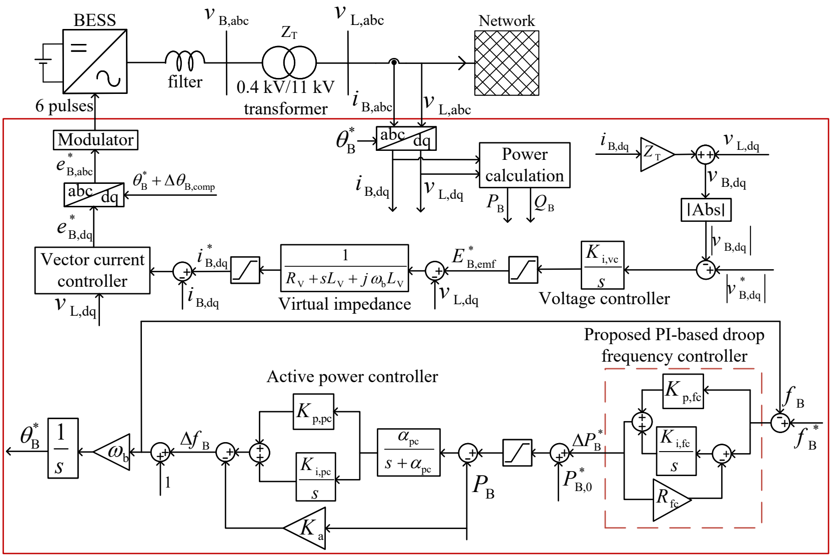

Figure 3.3: Implemented grid forming control of BESS. The vector current controller is a standard controller based on [85], and the active power controller is based on [84].

3.2.3.3 Proposed PI-based droop for frequency control of BESS

This work proposes a PI-based droop for a frequency controller in cascade with an active power controller. Figure 3.3 shows the corresponding control diagram. The open-loop transfer function of the frequency controller can be expressed as

$$\frac{\Delta P_{\mathrm{B}}^{*}}{-\Delta f_{\mathrm{B}}}=\left(\Gamma_{\mathrm{tr,fc}}\frac{T_{\mathrm{fc}}s}{T_{\mathrm{fc}}s+1}+\Gamma_{\mathrm{ss,fc}}\frac{1}{T_{\mathrm{fc}}s+1}\right)\left(\frac{S_{\mathrm{b}}^{\mathrm{MG}}}{P_{\mathrm{b}}^{\mathrm{B}}}\right), \tag{3.3}$$

where $\Delta f_{\mathrm{B}}=f_{\mathrm{B}}-f_{\mathrm{B}}^{*}$, and

$$\Gamma_{\mathrm{ss,fc}}=\frac{1}{R_{\mathrm{fc}}}\frac{P_{\mathrm{b}}^{\mathrm{B}}}{S_{\mathrm{b}}^{\mathrm{MG}}}, \tag{3.4a}$$

$$\Gamma_{\mathrm{tr,fc}}=K_{\mathrm{p,fc}}\frac{P_{\mathrm{b}}^{\mathrm{B}}}{S_{\mathrm{b}}^{\mathrm{MG}}}, \tag{3.4b}$$

$$T_{\mathrm{fc}}=\frac{1}{R_{\mathrm{fc}}K_{\mathrm{i,fc}}}. \tag{3.4c}$$

In the previous equations, $\Gamma_{\mathrm{ss,fc}}$ is the steady-state frequency regulation strength of the BESS frequency controller, $\Gamma_{\mathrm{tr,fc}}$ is the transient regulation strength, T_{fc} is the frequency controller time constant, and $P_{\mathrm{b}}^{\mathrm{B}}$ is the BESS rated active power. Note that the PI-based droop of the BESS frequency controller with the parameters, $K_{\mathrm{p,fc}}$, $K_{\mathrm{i,fc}}$ and R_{fc}, is equivalent to a high-pass filter plus low-pass filter with the parameters, $\Gamma_{\mathrm{ss,fc}}$, $\Gamma_{\mathrm{tr,fc}}$ and T_{fc}. In this chapter, the former parameters are expressed in per unit with respect to the BESS rated active power $P_{\mathrm{b}}^{\mathrm{B}}$, while the latter parameters are expressed in per unit with respect to the microgrid base power $S_{\mathrm{b}}^{\mathrm{MG}}$.

3.2.4 Microgrid island detection

A communication-based island detection is used by monitoring the breaker status of the grid in-feed line. The communication is usually based on Ethernet cable or optical fiber and the communication delay is in the order of a few milliseconds and has little impact on the controller response [86]. A passive island detection method, e.g. based on local frequency measurement, is typically adopted to handle communication failure [87]. The impact of communication failure will be discussed later.

3.3 Proposed tuning of BESS frequency controller

In the case that only the BESS regulates the microgrid frequency during island transition, the classical P-based droop control can be adopted as described in [69]–[71]. This will not be further discussed. This chapter focuses on cases where the BESS is used to assist HPP in regulating the microgrid frequency during island transition.

3.3.1 Criteria for secure island transition

The following two criteria are specified for the microgrid to achieve a secure island transition:

- maximum instantaneous frequency deviation (Δf^{max}).
- maximum steady-state frequency deviation ($\Delta f_{\mathrm{ss}}^{\mathrm{max}}$).

Steady state here refers to the period of time after the frequency has stabilized and before the activation of the secondary frequency reserve to restore the frequency to 50 Hz.

3.3.2 Steady-state power sharing between BESS and HPP

To fulfill the requirement on the maximum allowed steady-state frequency deviation $\Delta f_{\mathrm{ss}}^{\mathrm{max}}$, the minimum required frequency regulation strength of the microgrid $\Gamma_{\mathrm{ss,tot}}^{\mathrm{min}}$ should be set according to

$$\Gamma_{\mathrm{ss,tot}}^{\mathrm{min}} = -\frac{\Delta P_{\mathrm{dm}}}{\Delta f_{\mathrm{ss}}^{\mathrm{max}}} - D_{\mathrm{L}}, \tag{3.5}$$

where ΔP_{dm} is the dimensioning disturbance and D_{L} is the load frequency dependence. Both ΔP_{dm} and D_{L} are in per unit with respect to microgrid base power $S_{\mathrm{b}}^{\mathrm{MG}}$. If the frequency regulation strength of the hydro turbine $\Gamma_{\mathrm{ss,G}} \geq \Gamma_{\mathrm{ss,tot}}^{\mathrm{min}}$, there is no need for the BESS to provide steady-state frequency reserve, i.e. $\Gamma_{\mathrm{ss,fc}} = 0$. However, if $\Gamma_{\mathrm{ss,G}} < \Gamma_{\mathrm{ss,tot}}^{\mathrm{min}}$, then the BESS needs to provide the missing frequency reserve in steady state. In summary, the BESS regulation strength $\Gamma_{\mathrm{ss,fc}}$ is

$$\Gamma_{\mathrm{ss,fc}} = \begin{cases} 0, & \Gamma_{\mathrm{ss,G}} \geq \Gamma_{\mathrm{ss,tot}}^{\mathrm{min}} \\ \frac{-\Delta P_{\mathrm{dm}}}{\Delta f_{\mathrm{ss}}^{\mathrm{max}}} - D_{\mathrm{L}} - \frac{1}{R_{\mathrm{G}}} \frac{P_{\mathrm{b}}^{\mathrm{H}}}{S_{\mathrm{b}}^{\mathrm{MG}}}. & \Gamma_{\mathrm{ss,G}} < \Gamma_{\mathrm{ss,tot}}^{\mathrm{min}} \end{cases} \tag{3.6}$$

In case of $\Gamma_{\mathrm{ss,fc}} = 0$, the frequency controller reduces to a high-pass filter with a transient gain of $\Gamma_{\mathrm{tr,fc}}$ (HF-based) according to (3.3).

3.3.3 Proposed dynamic power coordination between the BESS and HPP

As the hydro turbine-governor system has limited power ramping capability, the BESS is deployed to provide a fast power response to fulfill the maximum allowed instantaneous frequency deviation during an unintentional islanding event of the microgrid.

3.3.3.1 Design of transient regulation strength of BESS

To fulfill the maximum allowed instantaneous frequency deviation ($\Delta f^{\max}$), the total transient regulation strength of the microgrid should be set at least according to

$$\Gamma_{\mathrm{tr,tot}}^{\min} = -\frac{\Delta P_{\mathrm{dm}} + D_{\mathrm{L}}\Delta f^{\max}}{\Delta f^{\max}}. \tag{3.7}$$

The total transient regulation strength of the microgrid corresponds to that of the HPP and BESS. Figure 3.4 shows the bode diagram of the hydro-turbine-governor system (solid blue curve) and BESS (solid green curve) according to (3.1) and (3.3), respectively. It is clearly seen that the hydro gain decays rapidly for frequencies above 10 rad/s. Therefore, the contribution of hydro to transient regulation strength is neglected. Thus, the transient regulation strength of BESS frequency controller is designed as

$$\Gamma_{\mathrm{tr,fc}} = \begin{cases} \Gamma_{\mathrm{tr,tot}}^{\min}, & \Gamma_{\mathrm{ss,fc}} < \Gamma_{\mathrm{tr,tot}}^{\min} \\ \Gamma_{\mathrm{ss,fc}}. & \Gamma_{\mathrm{ss,fc}} \geq \Gamma_{\mathrm{tr,tot}}^{\min} \end{cases} \tag{3.8}$$

In case $\Gamma_{\mathrm{ss,fc}} \geq \Gamma_{\mathrm{tr,tot}}^{\min}$, the frequency controller transient gain is designed to be equal to its steady-state gain, i.e. $\Gamma_{\mathrm{tr,fc}} = \Gamma_{\mathrm{ss,fc}}$. Thus, the PI-based droop controller reduces to a P-based droop controller according to (3.3).

3.3.3.2 Design of frequency controller time constant (T_{fc})

The BESS frequency controller time constant T_{fc} determines, relatively, how long will the BESS support the microgrid with the transient regulation strength.

Thus, the time constant tuning also has a critical role in achieving a secure island transition. The tuning of the BESS frequency controller time constant is also divided into two cases, depending on whether the HPP has sufficient reserve to cover the largest power imbalance.

BESS and HPP share steady-state reserve Two sub-cases are considered under this case, depending on the frequency controller structure of the BESS whether it is a P-based droop or a PI-based droop. The controller structure can be found by looking at the relation between $\Gamma_{\mathrm{tr,fc}}$ and $\Gamma_{\mathrm{ss,fc}}$ of the BESS frequency controller. According to (3.6) and (3.8) for the BESS frequency controller, it is not difficult to find that

$$\begin{cases} \Gamma_{\mathrm{tr,fc}} = \Gamma_{\mathrm{ss,fc}}, & \frac{1}{R_{\mathrm{G}}} \leq |\Delta P_{\mathrm{dm}}|\left(\frac{1}{|\Delta f_{\mathrm{ss}}^{\max}|} - \frac{1}{|\Delta f^{\max}|}\right)\frac{S_{\mathrm{b}}^{\mathrm{MG}}}{P_{\mathrm{b}}^{\mathrm{H}}} \\ \Gamma_{\mathrm{tr,fc}} > \Gamma_{\mathrm{ss,fc}}. & |\Delta P_{\mathrm{dm}}|\left(\frac{1}{|\Delta f_{\mathrm{ss}}^{\max}|} - \frac{1}{|\Delta f^{\max}|}\right)\frac{S_{\mathrm{b}}^{\mathrm{MG}}}{P_{\mathrm{b}}^{\mathrm{H}}} < \frac{1}{R_{\mathrm{G}}} \\ & < \left(|\frac{\Delta P_{\mathrm{dm}}}{\Delta f_{\mathrm{ss}}^{\max}}| - D_{\mathrm{L}}\right)\frac{S_{\mathrm{b}}^{\mathrm{MG}}}{P_{\mathrm{b}}^{\mathrm{H}}} \end{cases}$$

The design of the BESS frequency controller time constant corresponding to these two cases will be illustrated in the following sections.

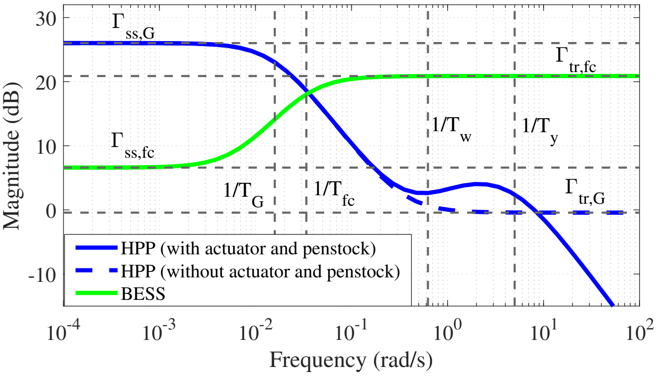

Figure 3.4: Bode magnitude plot of HPP and BESS according to the transfer functions given by (3.1) and (3.3), respectively.

i) $\frac{1}{R_{\mathrm{G}}} \leq |\Delta P_{\mathrm{dm}}|\left(\frac{1}{|\Delta f_{\mathrm{ss}}^{\max}|} - \frac{1}{|\Delta f^{\max}|}\right)\frac{S_{\mathrm{b}}^{\mathrm{MG}}}{P_{\mathrm{b}}^{\mathrm{H}}}$

This case arises when the HPP has a very large droop constant R_{G} and thus provides a very small amount of reserve in steady state, whereas BESS needs to provide a rather high amount of reserve in steady state. As in this case, $\Gamma_{\mathrm{tr,fc}} = \Gamma_{\mathrm{ss,fc}}$, the controller reduces to a P-based droop, and the time constant T_{fc} becomes irrelevant.
ii) $|\Delta P_{\mathrm{dm}}|\Big(\frac{1}{|\Delta f_{\mathrm{ss}}^{\max}|} - \frac{1}{|\Delta f^{\max}|}\Big)\frac{S_{\mathrm{b}}^{\mathrm{MG}}}{P_{\mathrm{b}}^{\mathrm{H}}} < \frac{1}{R_{\mathrm{G}}} < \Big(|\frac{\Delta P_{\mathrm{dm}}}{\Delta f_{\mathrm{ss}}^{\max}}| - D_{\mathrm{L}}\Big)\frac{S_{\mathrm{b}}^{\mathrm{MG}}}{P_{\mathrm{b}}^{\mathrm{H}}}$
This case arises when the HPP has a relatively small droop that provides a high amount of reserve in steady state, whereas the BESS provides a relatively small amount of reserve in steady state. In this case, the BESS has a higher regulation strength during transients than in steady state, and tuning the time constant T_{fc} is crucial for meeting the frequency quality requirements. The criteria used for tuning the time constant T_{fc} is that the total power from the HPP and BESS should be monotonically increasing when applying a step change in the reference frequency, i.e.

$$\frac{d}{dt}\Delta P_{\mathrm{tot}}(t) \geq 0, \tag{3.9}$$

where $\Delta P_{\mathrm{tot}}(t) = \Delta P_{\mathrm{m,H}}(t)\frac{P_{\mathrm{b}}^{\mathrm{H}}}{S_{\mathrm{b}}^{\mathrm{MG}}} + \Delta P_{\mathrm{B}}^{*}(t)\frac{P_{\mathrm{b}}^{\mathrm{B}}}{S_{\mathrm{b}}^{\mathrm{MG}}}$. $\Delta P_{\mathrm{m,H}}(t)$ and $\Delta P_{\mathrm{B}}^{*}(t)$ are defined as the unit step responses of the hydro governor (according to (3.1)) and BESS frequency controller (according to (3.3)), respectively. It is not difficult to find out that

$$\Delta P_{\mathrm{m,H}}(t) = \left(-\Delta\Gamma_{\mathrm{G}}e^{-\frac{t}{T_{\mathrm{G}}}} + \Gamma_{\mathrm{ss,G}}\right)\left(\frac{S_{\mathrm{b}}^{\mathrm{MG}}}{P_{\mathrm{b}}^{\mathrm{H}}}\right), \tag{3.10a}$$

$$\Delta P_{\mathrm{B}}^{*}(t) = \left(\Delta\Gamma_{\mathrm{fc}}e^{-\frac{t}{T_{\mathrm{fc}}}} + \Gamma_{\mathrm{ss,fc}}\right)\left(\frac{S_{\mathrm{b}}^{\mathrm{MG}}}{P_{\mathrm{b}}^{\mathrm{B}}}\right), \tag{3.10b}$$

where $\Delta\Gamma_{\mathrm{G}} = \Gamma_{\mathrm{ss,G}} - \Gamma_{\mathrm{tr,G}}$ and $\Delta\Gamma_{\mathrm{fc}} = \Gamma_{\mathrm{tr,fc}} - \Gamma_{\mathrm{ss,fc}}$. Since the hydro governor bandwidth is at a much lower frequency as compared to penstock and actuator dynamics (see Figure 3.4), the dynamics of the subsequent ones are neglected when obtaining (3.10a). The total change in power is the summation of (3.10a) and (3.10b), expressed with respect to microgrid base power, i.e

$$\Delta P_{\mathrm{tot}}(t) = \Delta\Gamma_{\mathrm{fc}}e^{-\frac{t}{T_{\mathrm{fc}}}} - \Delta\Gamma_{\mathrm{G}}e^{-\frac{t}{T_{\mathrm{G}}}} + \Gamma_{\mathrm{ss,tot}}, \tag{3.11}$$

where $\Gamma_{\mathrm{ss,tot}} = \Gamma_{\mathrm{ss,G}} + \Gamma_{\mathrm{ss,fc}}$. The first-order Taylor series expansion of (3.11) gives

$$\begin{aligned}\Delta P_{\text{tot}}(t) &\approx \Delta P_{\text{tot}}(t=0) + \frac{d\Delta P_{\text{tot}}(t)}{dt}\Big|_{t=0} t \\ &= \Delta\Gamma_{\text{fc}}(1 - \frac{1}{T_{\text{fc}}}t) - \Delta\Gamma_{\text{G}}(1 - \frac{1}{T_{\text{G}}}t) + \Gamma_{\text{ss,tot}}.\end{aligned} \tag{3.12}$$

Applying the condition in (3.9) to (3.12), the minimum time constant of the BESS frequency controller obtained is

$$T_{\text{fc}} = \frac{\Delta\Gamma_{\text{fc}}}{\Delta\Gamma_{\text{G}}}T_{\text{G}} = \frac{\Gamma_{\text{tr,fc}} - \Gamma_{\text{ss,fc}}}{\Gamma_{\text{ss,G}} - \Gamma_{\text{tr,G}}}T_{\text{G}}. \tag{3.13}$$

By substituting (3.2), (3.6) and (3.8) in (3.13), the time constant becomes

$$T_{\text{fc}} = \left[1 - R_{\text{G}}\Delta P_{\text{dm}}\left(\frac{1}{\Delta f^{\max}} - \frac{1}{\Delta f_{\text{ss}}^{\max}}\right)\frac{S_{\text{b}}^{\text{MG}}}{P_{\text{b}}^{\text{H}}}\right]\frac{(1 + R_{\text{G}}K_{\text{p,G}})^2}{R_{\text{G}}K_{\text{i,G}}}. \tag{3.14}$$

Only the HPP provides steady-state power This case arises when the HPP provides the total reserve in steady state, whereas BESS provides no reserve in steady state ($\Gamma_{\text{ss,fc}} = 0$). Thus, the BESS frequency controller reduces to a high-pass filter (see (3.3)). This case is applicable when the hydro turbine droop constant is given by $\frac{1}{R_{\text{G}}} \geq \left(|\frac{\Delta P_{\text{dm}}}{\Delta f_{\text{ss}}^{\max}}| - D_{\text{L}}\right)\left(\frac{S_{\text{b}}^{\text{MG}}}{P_{\text{b}}^{\text{H}}}\right)$ (see Section 3.3.2). By substituting (3.2), (3.6) and (3.8) in (3.13), the time constant becomes

$$T_{\text{fc}} = -\frac{\Delta P_{\text{dm}} + D_{\text{L}}\Delta f^{\max}}{\Delta f^{\max}}\frac{(1 + R_{\text{G}}K_{\text{p,G}})^2}{K_{\text{i,G}}}\frac{S_{\text{b}}^{\text{MG}}}{P_{\text{b}}^{\text{H}}}. \tag{3.15}$$

Figure 3.5 summarizes all the scenarios and the corresponding tuning of the BESS frequency controller proposed in this section.

3.4 Microgrid case study and frequency stability analysis

3.4.1 Description of hydro-powered microgrid

The dimensioning disturbance for secure island transition of the microgrid depends on the maximum power import from the main grid (P_{G} in Figure

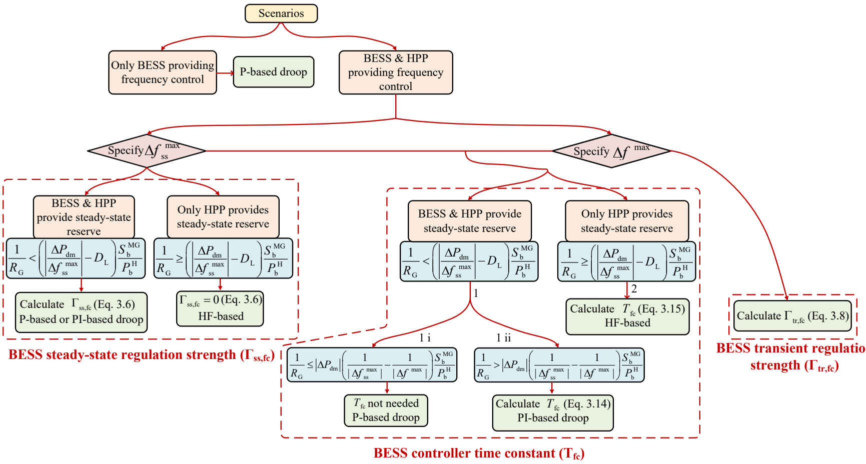

Figure 3.5: Flow chart of the proposed BESS frequency controller design and tuning.

3.1). Figure 3.6 shows the time duration curve of the import power P_G, which is measured in 2018 at a substation in the west coast of Sweden. The measurement data has an hourly resolution. The negative value indicates power export to the main grid. The imported power is below 10.3 MWh/h for 98% of the year, which is considered to be the dimensioning disturbance ΔP_{dm} for the unplanned island transition of the microgrid [88]. Even though the maximum export power is also relatively high, it can be handled by automatically switching on the factory electric boiler once an over-frequency event is detected. Thus, only the power import scenario is considered for the dimensioning disturbance of the microgrid.

Table 3.1 summarizes the dimensioning disturbance, frequency performance criteria, load and hydro turbine-governor parameters (see Figure 3.2) for dynamic frequency studies of the industrial microgrid.

For secure island transition, the minimum allowed frequency nadir is set to 49 Hz, i.e. $|\Delta f^{max}| = 0.02$ p.u. (1 Hz), whereas the maximum steady-state frequency deviation is $|\Delta f_{ss}^{max}| = 0.01$ p.u. (0.5 Hz). These settings are adopted from the requirements in the Nordic Synchronous Area [89]. The effectiveness of BESS controller tuning under various frequency security constraints is illustrated in Section 3.5.2.2. In this chapter, the microgrid base power is

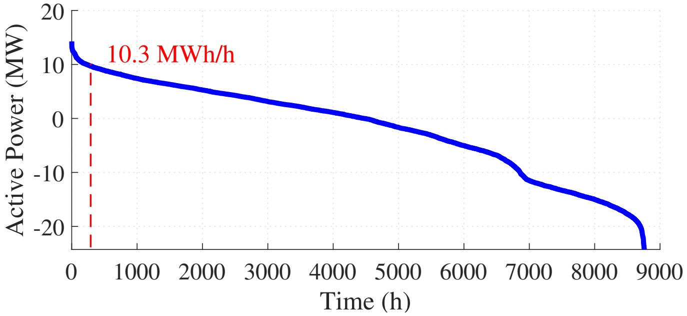

Figure 3.6: Time duration curve of the measured active power exchange between the upstream grid and the microgrid in 2018, where positive values indicate import to microgrid. The dimensioning disturbance of 10.3 MWh/h corresponds to 98 percentile of the curve.

chosen to be equal to the HPP rated active power, i.e. $S_{\mathrm{b}}^{\mathrm{MG}} = P_{\mathrm{b}}^{\mathrm{H}} = 46.3$ MVA.

3.4.2 Parameter tuning of BESS frequency controller

Figure 3.7 (top) shows the resulting tuning of the steady-state gain $\Gamma_{\mathrm{ss,fc}}$, the transient gain $\Gamma_{\mathrm{tr,fc}}$ and the time constant T_{fc} of the proposed PI-based droop frequency controller for the BESS. The top figure is plotted according to (3.6), (3.8), (3.14) and (3.15) as the hydro governor droop constant R_{G} increases from 1% to 10%. First, when the hydro governor droop increases from 1% to 4.5%, the hydro generator supplies the load fully in steady state during island operation, and thus the steady-state gain of BESS $\Gamma_{\mathrm{ss,fc}} = 0$. The transient gain of the BESS $\Gamma_{\mathrm{tr,fc}}$ is constant and equal to 11.1 p.u., which is mainly determined by the dimensioning disturbance and the frequency nadir requirement according to (3.8). The time constant T_{fc} slightly increases as the hydro governor droop increases up to 4.5% according to (3.15). Second, as the hydro governor droop increases from 4.5% to 9%, the BESS starts to provide more and more steady-state reserve with $\Gamma_{\mathrm{ss,fc}}$ increasing from 0 to 11.1 p.u. according to (3.6). The transient gain $\Gamma_{\mathrm{tr,fc}}$ remains unchanged, whereas the time constant T_{fc} starts to decrease as BESS increases its steady-state power sharing. Third, as the hydro governor droop constant increases above 9%, the BESS increases its steady-state power sharing such that the steady-state

Table 3.1: Microgrid dimensioning disturbance, frequency performance criteria [5], load and hydro turbine-governor parameters [78], [90].

Design criteria			**Hydro turbine**		
Parameter	Value	Base	Parameter	Value	Base
$\lvert\Delta f^{\mathrm{max}}\rvert$	0.02 p.u.	f_{b}	T_{y}	0.2 s	-
$\lvert\Delta f_{\mathrm{ss}}^{\mathrm{max}}\rvert$	0.01 p.u.	f_{b}	T_{w}	1.6 s	-
ΔP_{dm}	0.22 p.u.	$S_{\mathrm{b}}^{\mathrm{MG}}$	H_{H}	4.5 s	$S_{\mathrm{b}}^{\mathrm{H}}$
D_{L}	0 p.u.	$S_{\mathrm{b}}^{\mathrm{MG}}/f_{\mathrm{b}}$	**Base values**		
Hydro governor			Parameter	Value	-
Parameter	Value	Base	f_{b}	50 Hz	-
R_{G}	0.05 p.u.	$f_{\mathrm{b}}/P_{\mathrm{b}}^{\mathrm{H}}$	$S_{\mathrm{b}}^{\mathrm{H}}$	54.5 MVA	-
$K_{\mathrm{p,G}}$	1.0 p.u.	$P_{\mathrm{b}}^{\mathrm{H}}/f_{\mathrm{b}}$	$P_{\mathrm{b}}^{\mathrm{H}}$	46.3 MW	-
$K_{\mathrm{i,G}}$	0.33 rad/s	$P_{\mathrm{b}}^{\mathrm{H}}/f_{\mathrm{b}}$	$S_{\mathrm{b}}^{\mathrm{MG}}$	46.3 MVA	-

gain becomes higher than the minimum threshold for the transient gain. In this case, the transient gain of the BESS $\Gamma_{\mathrm{tr,fc}}$ is set equal to its steady-state gain $\Gamma_{\mathrm{ss,fc}}$, and the time constant is equal to zero. In the following dynamic analysis, a hydro governor droop constant of 5% is considered. The corresponding BESS frequency controller tuning is illustrated with the green dotted line in Figure 3.7. Table 3.2 shows the parameters for the BESS GFM control (see Figure 3.3), whereas Table 3.3 shows the selected tuning for the BESS frequency controller and hydro governor.

3.4.3 Microgrid small-disturbance stability

To analyze how the proposed frequency controller of the BESS affects the small-disturbance stability of the microgrid during island operation, the response of the microgrid frequency Δf_{MG} is evaluated when subject to an imbalance in active power ΔP_{L}, i.e. $\frac{\Delta f_{\mathrm{MG}}(s)}{\Delta P_{\mathrm{L}}(s)}$. The microgrid frequency is calculated following the concept of frequency of center of inertia as described in [91]. The microgrid is linearized with the aid of Simulink Model Linearizer. The initial operating point considered for the linearization is illustrated in Table 3.4 (inside parenthesis). In this study, the factory is modeled as a constant power load, which is the worst case scenario in terms of stability. Figure 3.8 (top) shows the zero-pole map of the closed-loop transfer function

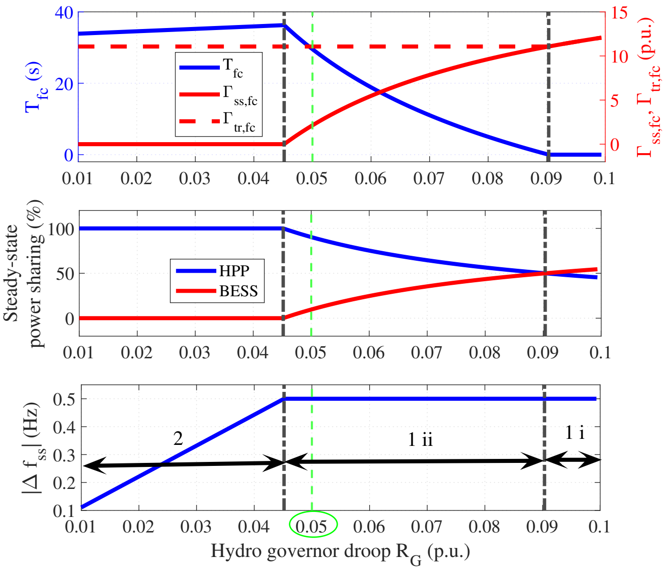

Figure 3.7: BESS frequency controller tuning (top), percentage of power sharing between HPP and BESS in steady state (middle) and steady-state frequency deviation (bottom) at different hydro governor droop constants. The three different regions 1 i, 1 ii and 2, are illustrated in Figure 3.5. The green dashed line corresponds to the tuning selected for dynamic analysis.

$\frac{\Delta f_{\mathrm{MG}}(s)}{\Delta P_{\mathrm{L}}(s)}$ when the BESS is not equipped with a frequency controller. The dominant complex poles have an oscillation frequency of 0.174 rad/s with a damping ratio of 0.1. The bottom plot shows the movement of these two complex poles when the BESS is equipped with the frequency controller while sweeping different values of the transient gain $\Gamma_{\mathrm{tr,fc}}$ and time constant T_{fc} of the controller. The steady-state gain $\Gamma_{\mathrm{ss,fc}}$ is set to zero in this analysis, but the impact of the steady-state gain on the small signal stability is illustrated later. When the transient gain is increased from 0 to 11.1 p.u. (blue color) or the time constant is increased from 0 to 29.4 s (red color), the damping ratio of the two complex poles increases from 0.1 to 0.7. This indicates that a BESS frequency controller with a larger transient gain and time constant improves the damping of the microgrid frequency in island operation. The

Table 3.2: BESS grid forming control parameters.

Virtual impedance			**Frequency controller**		
Parameter	Value	Base	Parameter	Value	Base
R_{V}	0.075 p.u.	$Z_{\mathrm{b}}^{\mathrm{B}}$	$K_{\mathrm{p,fc}}$	49.3 p.u.	$P_{\mathrm{b}}^{\mathrm{B}}/f_{\mathrm{b}}$
L_{V}	0.15 p.u.	$L_{\mathrm{b}}^{\mathrm{B}}$	$K_{\mathrm{i,fc}}$	0.337 rad/s	$P_{\mathrm{b}}^{\mathrm{B}}/f_{\mathrm{b}}$
Voltage controller			R_{fc}	0.1 p.u.	$f_{\mathrm{b}}/P_{\mathrm{b}}^{\mathrm{B}}$
Parameter	Value	Base	**Base values**		
Z_{T}	0.06 p.u.	$Z_{\mathrm{b}}^{\mathrm{B}}$	Parameter	Value	-
$K_{\mathrm{i,vc}}$	52.36 rad/s	-	f_{b}	50 Hz	-
Active power controller			ω_{b}	$2\pi(f_{\mathrm{b}})$ rad/s	-
Parameter	Value	Base	V_{b}	400 V	-
$K_{\mathrm{p,pc}}$	0.011 p.u.	$f_{\mathrm{b}}/P_{\mathrm{b}}^{\mathrm{B}}$	$S_{\mathrm{b}}^{\mathrm{B}}$	11 MVA	-
$K_{\mathrm{i,pc}}$	0.35 rad/s	$f_{\mathrm{b}}/P_{\mathrm{b}}^{\mathrm{B}}$	$P_{\mathrm{b}}^{\mathrm{B}}$	10.5 MW	-
K_{a}	0.022 p.u.	$f_{\mathrm{b}}/P_{\mathrm{b}}^{\mathrm{B}}$	$Z_{\mathrm{b}}^{\mathrm{B}}$	0.0145 Ω	-
α_{pc}	62.8 rad/s	-	$L_{\mathrm{b}}^{\mathrm{B}}$	46.3 μH	-

Table 3.3: Selected parameters for BESS frequency controller and hydro governor. All values are in per unit with respect to microgrid base power, i.e. $S_{\mathrm{b}}^{\mathrm{MG}} = P_{\mathrm{b}}^{\mathrm{H}} = 46.3$ MVA.

$\Gamma_{\mathrm{ss,fc}}$	2.2 p.u.	$\Gamma_{\mathrm{tr,fc}}$	11.1 p.u.	T_{fc}	29.4 s
$\Gamma_{\mathrm{ss,G}}$	20 p.u.	$\Gamma_{\mathrm{tr,G}}$	0.95 p.u.	T_{G}	63 s

sensitivity to steady-state gain has also been tested by sweeping $\Gamma_{\mathrm{ss,fc}}$ from 0 to 2.2 p.u., which results in increasing the damping ratio of the complex poles further from 0.7 to 0.76 (result is not shown). It is worth mentioning that the aforementioned tests have also been done with different operating points of the BESS, i.e. $P^{*}_{\mathrm{B},0} = 0$ MW and $P^{*}_{\mathrm{B},0} = 10$ MW. The results are very similar, and therefore not shown. For the following dynamic simulation, the steady-state gain $\Gamma_{\mathrm{ss,fc}} = 2.2$ p.u., the transient gain $\Gamma_{\mathrm{tr,fc}} = 11.1$ p.u. and the time constant $T_{\mathrm{fc}} = 29.4$ s are used for the BESS frequency controller as listed in Table 3.3.

Using the same control parameters as in Table 3.3, the bode diagram of the open loop transfer function $\frac{\Delta f_{\mathrm{B}}}{\Delta f^{*}_{\mathrm{B}}}$ is shown in Figure 3.9. The loop is open by removing the feedback signal Δf_{B} of the frequency controller. There are two crossover frequencies: 1) at 0.033 rad/s (0.0053 Hz) with a corresponding phase margin of 83°, 2) at 1 rad/s (0.159 Hz) with a corresponding phase margin of -85°. The system with the added BESS frequency controller is stable with relatively high phase margins between these two crossover frequencies. The dip in the bode magnitude plot at the frequency 4 rad/s (0.64 Hz) corresponds to the electro-mechanical oscillations between the BESS and the HPP.

Table 3.4: Steady-state power flow of the microgrid in Figure 3.1 before (outside parenthesis) and after the disturbance (inside parenthesis). The post-disturbance power flow corresponds to the base case scenario.

	Active power (MW)	Reactive power (MVAr)	Voltage (p.u.)
Grid	$P_{\mathrm{G}} = 10.3$ (0)	$Q_{\mathrm{G}} = 10.5$ (0)	$V_{\mathrm{pcc}} = 1$ (0.9815)
HPP	$P_{\mathrm{H}} = 8.1$ (17.4)	$Q_{\mathrm{H}} = 0.07$ (8.7)	$V_{\mathrm{H}} = 1$ (1)
BESS	$P_{\mathrm{B}} = 0$ (1)	$Q_{\mathrm{B}} = 1.24$	$V_{\mathrm{L}} = 0.993$ (0.979)
Factory	$P_{\mathrm{L}} = 18.4$ (18.4)	$Q_{\mathrm{L}} = 10.8$ (10.8)	$V_{\mathrm{L}} = 0.993$ (0.979)

3.5 Microgrid dynamic simulation results

The dynamic model of the microgrid shown in Figure 3.1 is implemented in Matlab/Simulink using phasor simulation. The factory is modeled as a constant power load with no voltage or frequency dependency. As both the HPP and the factory are located very close to the substation, no MV cables are modeled in the base case. The impact of the distance between the HPP and the factory will be discussed in Section 3.7. Table 3.4 shows the steady-state voltage and power flow before (outside parentheses) and after (inside parentheses) the islanding event of the microgrid according to the base case scenario. It can be seen from the power flow that the microgrid imports 10.3 MW and 10.5 MVAr from the main grid right before the islanding event. The default parameters of the HPP and BESS are summarized in Table 3.1, Table 3.2 and Table 3.3, if not otherwise stated.

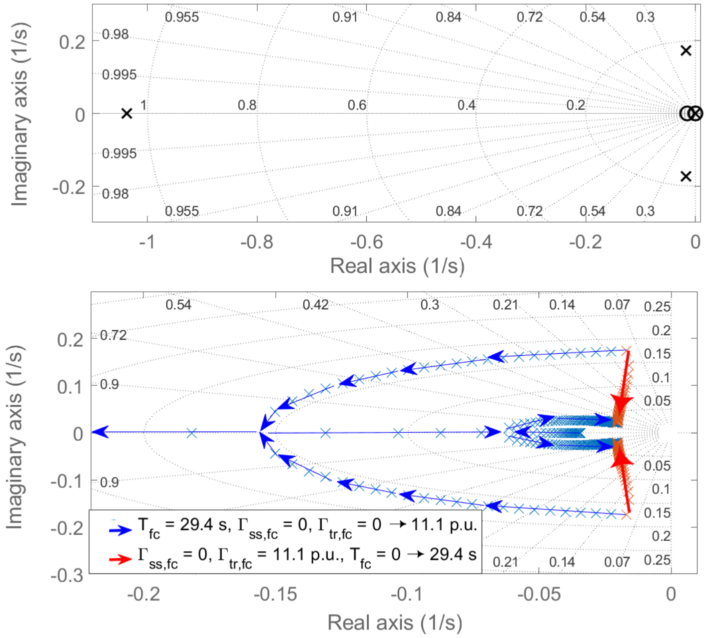

Figure 3.8: Zero-pole map of the closed loop transfer function between the factory active power demand and the frequency of centre of inertia of the microgrid in island operation when BESS frequency controller is disabled (top); corresponding root loci of the dominant pair of poles when changing BESS frequency controller parameters (bottom).

3.5.1 Comparison with existing coordinated frequency controllers between BESS and HPP

3.5.1.1 PI-based droop vs. P-based droop

Figure 3.10 shows the microgrid frequency (upper), active power output from the hydro generator P_{H} (middle) and the BESS P_{B} (bottom) during an islanding event, where the frequency controller of the BESS uses either the P-based or the PI-based droop control. The islanding event occurs at $t = 5$ s, before which the microgrid was importing 10.3 MW of active power from the main grid. For the P-based droop, two different settings of the proportional gain are shown, where one sets the proportional gain $K_{\mathrm{p,fc}}$ to the desired steady-state

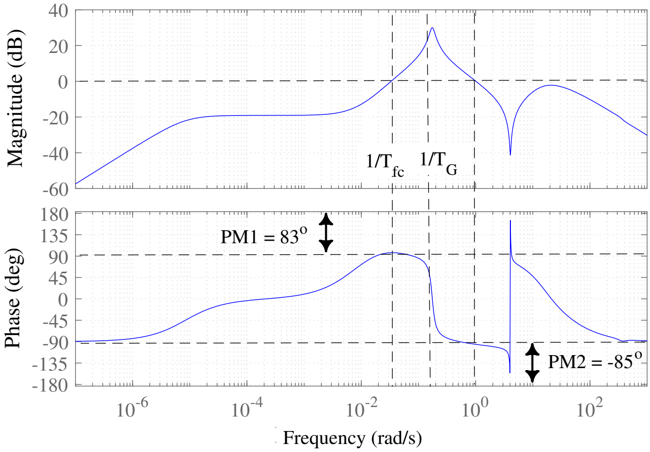

Figure 3.9: Bode magnitude and phase plots of BESS open frequency control loop $\frac{\Delta f_{\mathrm{B}}}{\Delta f_{\mathrm{B}}^{*}}$.

regulation strength $\Gamma_{\mathrm{ss,fc}}$ =2.2 p.u (low gain), and the other one sets $K_{\mathrm{p,fc}}$ to the desired transient regulation strength $\Gamma_{\mathrm{tr,fc}}$ =11.1 p.u. (high gain). The former tuning leads to a very low frequency nadir of 46.6 Hz, while the latter one requires more active power and energy from the BESS in steady state as shown in the bottom plot of the figure. As compared to the P-based droop, the PI-based droop has an additional degree of freedom, where the transient and steady-state gains can be set independently. Thus, the requirements for both the frequency nadir and the steady-state frequency can be fulfilled without unnecessarily consuming the energy storage. The secondary frequency control by the hydro turbine is not implemented here, which will bring the microgrid frequency back to 50 Hz and release the fast frequency reserve supplied by the BESS.

3.5.1.2 Comparison with virtual power plant with 4th order frequency controller

In [77], a virtual power plant composed of a hydro turbine and a BESS is proposed to ride through frequency disturbances in the Nordic synchronous area. The derived frequency controller of the BESS is a 4^{th} order controller,

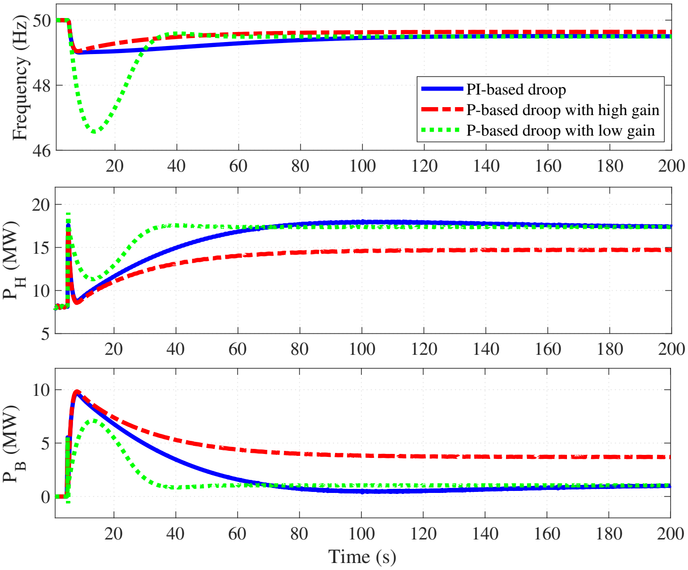

Figure 3.10: Impact analysis of BESS frequency controller structure: frequency of center of inertia (top), hydro generator active power P_{H} (middle) and BESS active power P_{B} (bottom).

which is modelled here for comparison with our PI-based droop controller for microgrid application. The tuning of the 4th order frequency controller in [77] is made specific to a grid condition through trial and error, with 0.07 p.u. of power disturbance, 0.98 p.u. of load frequency dependence, and an inertia constant of 4.58 s. Therefore, the same per-unit values are also used here in the microgrid comparison (refer to Table 3.1 for base values). Actuator and water time constants are kept the same as in Table 3.1. Three cases are evaluated for both controllers:

- Case 1: $H_{\mathrm{H}} = 4.58$ s, $D_{\mathrm{L}} = 0.98$ p.u., and 0 s controller time delay in the hydro turbine-governor system;
- Case 2: $H_{\mathrm{H}} = 1.5$ s, $D_{\mathrm{L}} = 0$ p.u., and 0 s controller time delay in the hydro turbine-governor system;
- Case 3: $H_{\mathrm{H}} = 1.5$ s, $D_{\mathrm{L}} = 0$ p.u., and 1 s controller time delay in the hydro turbine-governor system.

Figure 3.11 shows the frequency response when disconnecting the grid at $t = 20$ s while importing 0.07 p.u. (3.2 MW), with the BESS frequency controller and hydro governor implemented and tuned according to [77] (top), or according to our proposed BESS frequency controller (bottom). Both BESS frequency control strategies manage to limit the frequency nadir to 49 Hz in Case 1. In fact, the 4^{th} order frequency controller drives the frequency to steady state faster than the PI-based droop controller, which indicates that the 4^{th} order controller has a relatively faster integral action. However, in Case 2, where the inertia constant of the HPP is reduced from 4.58 s to 1.5 s and the load frequency dependence from 0.98 p.u. to 0 p.u., the control strategy of [77] becomes ineffective in limiting the frequency nadir to 49 Hz. This is because the RoCoF is relatively higher in this case (-0.32 Hz/s), which causes the microgrid frequency to drop faster, and the hydro turbine to reach its maximum ramp rate limit. As a result, frequency oscillations are observed. The frequency oscillations may be even amplified when the hydro turbine-governor system has a time delay of 1 s as shown in Case 3. On the other hand, by tuning the BESS frequency controller according to our method, the frequency nadir barely drops below 49 Hz and no oscillations are observed even under low-inertia conditions and with a 1 s delay. Moreover, the proposed BESS frequency controller is of 1^{th} order, which makes it easier to tune as compared to the 4^{th} order controller in [77].

3.5.2 Sensitivity analysis on the tuning of the proposed PI-based droop controller

3.5.2.1 Impact of controller time constant

Figure 3.12 shows the impact of BESS frequency controller time constant tuning on the frequency response. The base value of the controller time constant is 29.4 s (see Table 3.3). With a shorter controller time constant of 5 s, BESS reduces its frequency reserve much quicker than the hydro turbine can increase its FCR. This leads to a poor frequency response with a frequency nadir of 48.34 Hz, which is below the requirement of 49 Hz. On the other hand, a longer controller time constant of 70 s will lead to a longer decay time of BESS frequency reserve, and thus, more energy consumption.

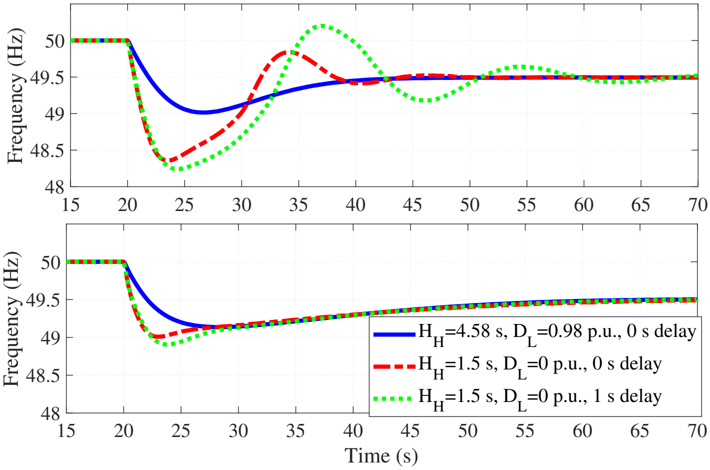

Figure 3.11: Frequency of center of inertia when the microgrid is disconnected from the regional grid at t=20 s while importing 0.07 p.u. (3.2 MW) of active power. The subplots correspond to hydro governor and BESS frequency controller design according to [77] (top), or according to our proposed BESS frequency controller design (bottom). The sensitivity of the two strategies to the inertia constant of the HPP, load frequency dependence, and communication delay is displayed.

3.5.2.2 Impact of performance criteria on frequency nadir

Figure 3.13 shows the corresponding results when the performance criteria of the minimum allowed frequency nadir is reduced from 49 Hz to 48.5 Hz and to 48 Hz. As the minimum allowed frequency nadir is reduced from 49 Hz to 48.5 Hz, the hydro turbine increases its FCR more quickly due to a larger frequency error signal. This shortens the frequency support duration of the BESS, allowing it to ramp down its power faster. Thus, less energy is required from the BESS. However, by further reducing the minimum allowed frequency nadir to 48 Hz, the reduced energy requirement of the BESS is no longer as significant. This is because the hydro turbine has reached its maximum ramp rate limit. Moreover, the maximum active power of the BESS is reduced slightly when relaxing the frequency nadir requirements. This is because of the longer time to reach the frequency nadir, which allows more time for the hydro turbine to increase its FCR.

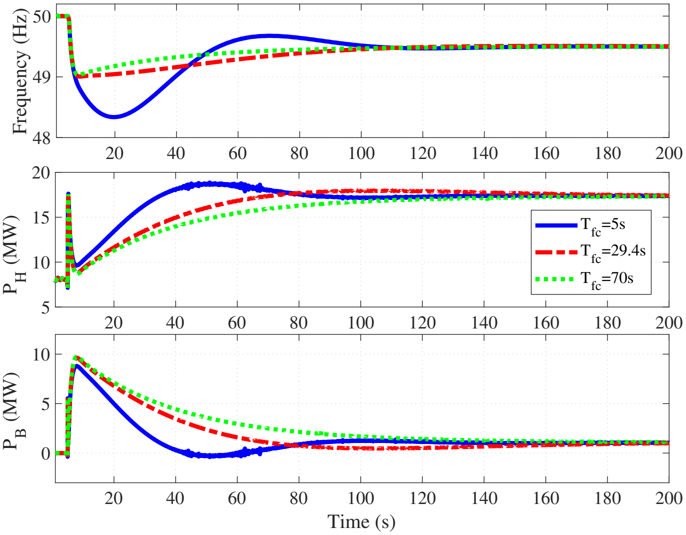

Figure 3.12: Impact analysis of BESS frequency controller time constant: frequency of center of inertia (top), hydro generator active power P_{H} (middle) and BESS active power P_{B} (bottom).

3.6 Experimental validation

3.6.1 Laboratory setup

The proposed PI-based droop frequency controller and its tuning for the BESS is tested using a kW scale 400 V laboratory setup. Figure 3.14 shows the network diagram of the lab setup including ratings of each component, whereas Figure 3.15 shows a photo of the lab setup. The BESS is emulated using a 4-quadrant 30 kVA Regatron ACS power amplifier, which is essentially a controllable voltage source representing the behavior of a VSI in the BESS. The controller of the BESS described in Figure 3.3 is implemented in dSPACE MicroLabBox that sends three-phase reference voltage signals to the amplifier. The amplifier is connected in parallel with the industrial load represented by a 30 kW induction motor. Tap-changing transformer is unavailable in the lab. Instead, switchable shunt capacitor banks are used to regulate the terminal voltage of the induction motor to be around 1 p.u. before the islanding event.

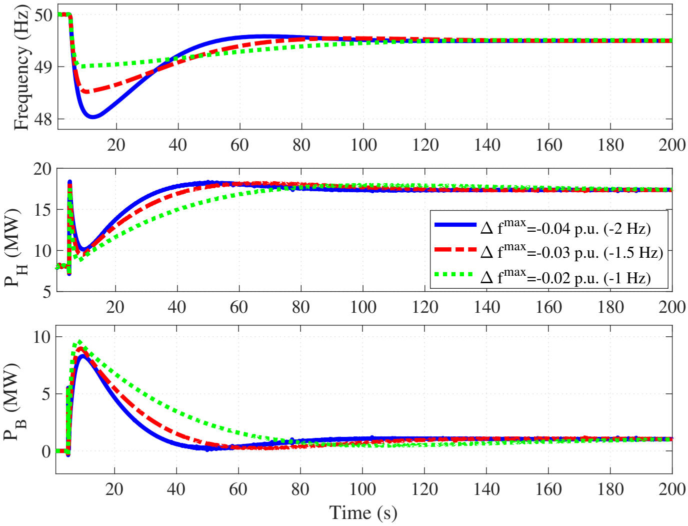

Figure 3.13: Impact analysis of maximum allowed frequency deviation: frequency of center of inertia (top), hydro generator active power P_H (middle) and BESS active power P_B (bottom).

The transformer impedance of the industry and the filter impedance of the BESS are both represented by a series inductor with an impedance of 0.05 + j0.95 Ω. The hydro generator is represented by a 75 kVA synchronous machine driven by a dc motor (turbine) including a flywheel to replicate the inertia of a hydro turbine. The hydro turbine-governor model described in Figure 3.2 and the generator excitation control are implemented in dSPACE 1103. The entire microgrid setup is connected to the local 400 V distribution grid.

3.6.2 Experimental results and analyses

Three tuning strategies of the BESS frequency controller are tested:

1. Proposed PI-based droop ($\Gamma_\mathrm{ss,fc} = 2.2$ p.u., $\Gamma_\mathrm{tr,fc} = 11.1$ p.u., $T_\mathrm{fc} = 29.4$ s)
2. P-based droop with high gain ($\Gamma_\mathrm{ss,fc} = \Gamma_\mathrm{tr,fc} = 11.1$ p.u.)
3. P-based droop with low gain ($\Gamma_\mathrm{ss,fc} = \Gamma_\mathrm{tr,fc} = 2.2$ p.u.)

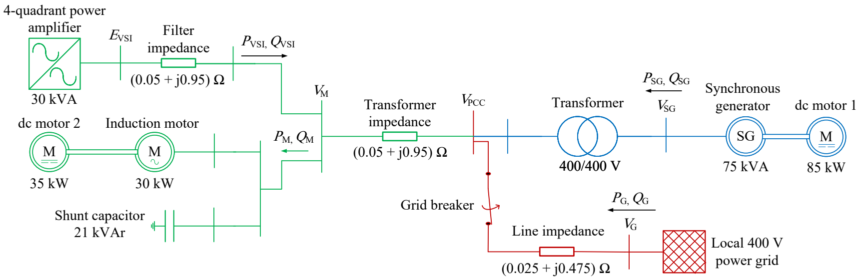

Figure 3.14: Network diagram of laboratory setup: Paper and pulp factory replica (green), hydro turbine replica (blue) and local power grid (red).

The pre-disturbance power flow of the three cases resemble each other and are summarized in Table 3.5. Figure 3.16 shows the microgrid frequency response, the PCC voltage angle and active power output from the SG and the VSI (power amplifier) when an unintentional islanding occurs. Right before the islanding event, the microgrid imports 14.4 kW and 1 kVAr from the local grid. In all the three cases, once the grid is disconnected, an angle jump of around 4 degrees is experienced at the PCC as shown in the top middle plot (the angle is measured with respect to the rotor flux of the SG). Since both the SG and the GFM VSI have a stiff back electromotive force (EMF) angle, they will both experience a sudden increase in the active power at their terminal, as shown in the bottom middle and bottom plots, respectively. As the SG is electrically closer to the disturbance, it experiences a larger active power disturbance at its terminal as compared to the VSI. However, due to the fast frequency response of the VSI, the active power output from the VSI ramps up quickly to limit the frequency drop within the microgrid whereas the turbine-governor system of the SG slowly ramps up its mechanical power. In the case where the BESS frequency controller uses the P-based droop with low gain, the frequency nadir went down to 47.6 Hz, where the protection would shut down the whole microgrid in reality. The frequency nadir is limited to 49.1 Hz if the proportional gain of the P-based droop is increased from 2.2 p.u. to 11.1 p.u. However, this results in a relatively high energy storage demand from the VSI as shown in the bottom middle plot of the figure. This may become an issue in reality when the storage capacity is very limited and easily depleted. On the other hand, the proposed PI-based droop is able to fulfill

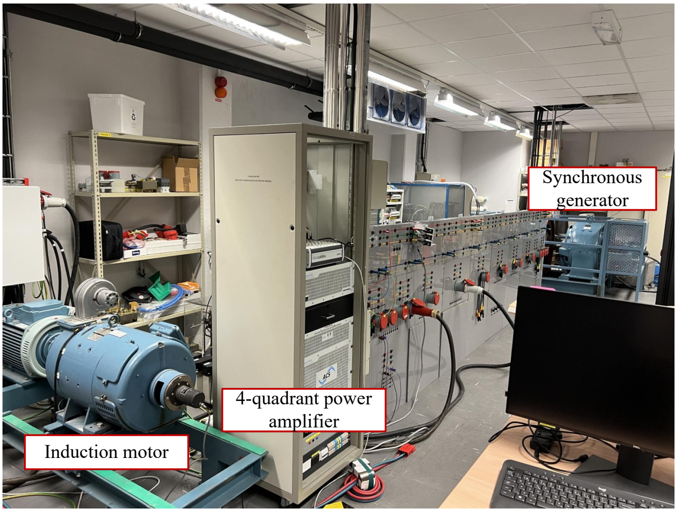

Figure 3.15: Photo of laboratory setup.

the requirement for the frequency nadir while using as low energy storage as possible. This is achieved by tuning the steady-state gain of the BESS frequency controller to be relatively smaller than the transient gain, with a time constant tuned considering the regulating speed of the hydro turbine-governor system as described in Section 3.3.3.2. Both the transient gain and the time constant play an important role in limiting the frequency nadir to a desired value.

Table 3.5: Pre-disturbance power flow of laboratory test (see Figure 3.14).

	Active power	Reactive power
Grid	$P_{\mathrm{G}} = 14.4$ kW	$Q_{\mathrm{G}} = 1$ kVAr
Synchronous generator	$P_{\mathrm{SG}} = 4$ kW	$Q_{\mathrm{SG}} =$ -1.2 kVAr
Power amplifier	$P_{\mathrm{VSI}} = 0$ kW	$Q_{\mathrm{VSI}} = 0$ kVAr
Induction motor & shunt capacitor	$P_{\mathrm{M}} = 18.2$ kW	$Q_{\mathrm{M}} =$ -1.9 kVAr

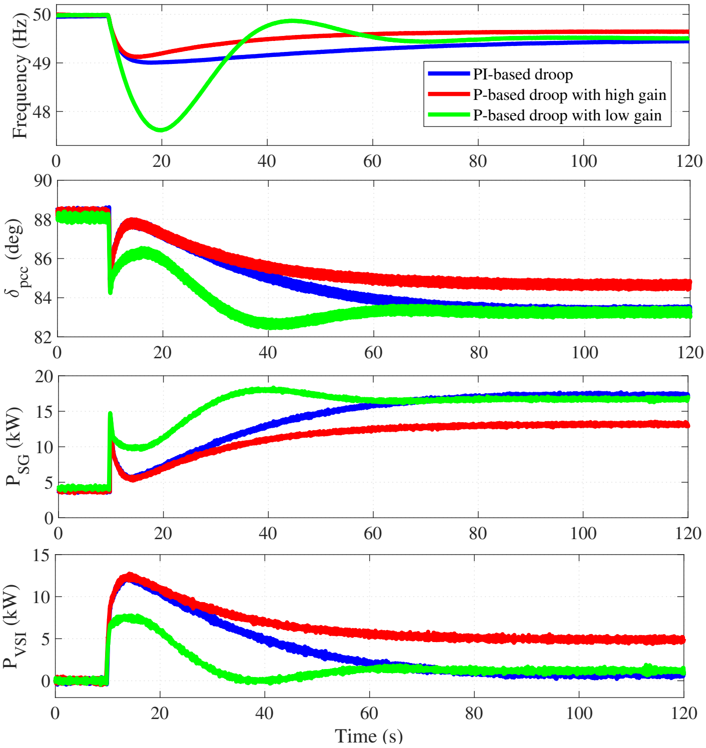

Figure 3.16: Laboratory test comparing the performance of P-based droop and PI-based droop when the grid breaker is opened at $t = 10$ s: synchronous generator frequency (top), PCC voltage angle with respect to rotor flux of the synchronous generator (top middle), synchronous generator active power (bottom middle) and voltage source inverter active power (bottom).

Figure 3.17 (top) shows the VSI terminal voltage (V_{M} in Figure 3.14) during island transition. In all three cases, the voltage dips to 0.996 p.u. right after the disturbance. This causes the VSI reactive power to rise immediately since it is controlled in GFM control model. The voltage controller then takes action and regulates the terminal voltage to 1 p.u. In the case of PI-based droop and P-based droop with high gain, the reactive power needed by the VSI is very little, 0.7 kVAr and 1.1 kVAr, respectively, as shown in the middle subplot. This is because both the VSI and the SG are supplying the induction motor through a relatively small impedance with high X/R ratio, i.e. 0.05 + j0.95 Ω (0.0094 + j0.18 p.u. under 30 kVA and 400 V base). In the case of a P-based droop with low gain, the reactive power needed is much larger (4.3 kVAr). This is because of the low frequency nadir in this case (see Figure 3.16 top), which leads to a reduction in the back EMF of the induction motor and thus larger reactive power demand. In both cases where the frequency nadir is fulfilled, the PI-based droop control has a similar maximum current as the P-based droop control. In other words, the current rating of the VSI is not increased with the proposed PI-based droop as compared to the traditional P-based droop.

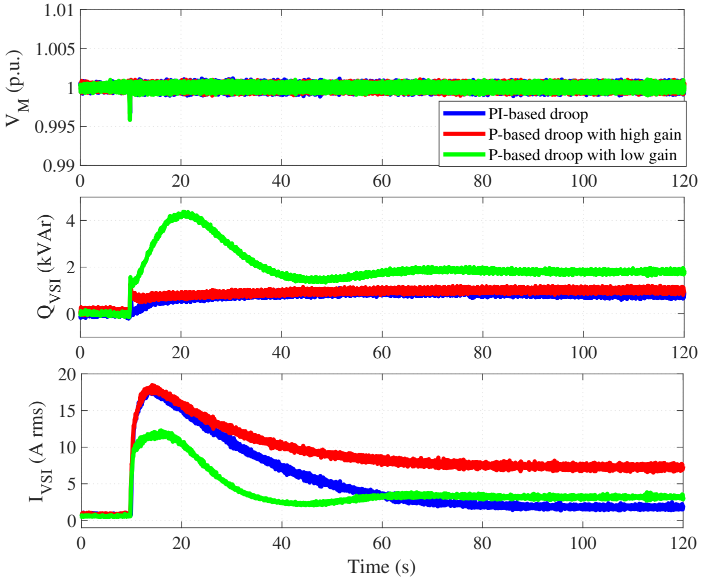

Figure 3.17: Laboratory test comparing the performance of P-based droop and PI-based droop when the grid breaker is opened at t = 10 s: induction motor terminal voltage (top), voltage source inverter reactive power (middle) and voltage source inverter rms current (bottom).

3.7 Further Discussion

The maximum RoCoF is not considered as a dimensioning criterion in this work. However, in a microgrid with very low synchronous inertia, synthetic inertia can be provided by the BESS to limit the RoCoF in case of a large power imbalance. The synthetic inertia can be implemented by adjusting the bandwidth of the active power control loop of the BESS [84] or added as an outer loop together with the frequency controller [92].

If the grid-tie breaker (CB in Figure 3.1) signal of the microgrid should be lost, local measurement signals such as frequency can be used as a backup for island detection. One common passive island detection method is to use frequency deviation as a criterion [87]. If the threshold for the frequency-based island detection method is set to 49 Hz, then the frequency nadir may drop slightly below 49 Hz before the BESS can ramp up its power to bring the frequency back to its acceptable limit.

There is no significant power oscillations observed in the cases analyzed, even when the distance between the HPP and BESS is increased to 30 km. One reason is that the power rating of the BESS is about 5 times smaller than the hydro generator. Another reason is that the BESS is typically designed to provide a large damping power [93], [94]. However, power oscillation may start to appear if the two power sources of comparable sizes are connected through a long cable and that the BESS provides little or no damping as illustrated in [95]. Such a power oscillation can be attenuated with a proper tuning of the active power controller of the BESS.

3.8 Summary

This chapter has developed a simple yet effective frequency control strategy for the BESS to facilitate a secure island transition of a hydro-powered microgrid. The proposed frequency controller uses a PI-based droop, whereas the tuning strategy of the controller accounts for the limitations in the power response of a hydro generator and the desired frequency performance criteria set by the microgrid operator, without over-dimensioning the size of the storage capacity. The effectiveness of the proposed frequency control strategy is demonstrated both in simulation and laboratory tests. The storage capacity requirement of the BESS depends mainly on the steady-state droop and regulating speed of the hydro turbine-governor system, whereas the power capacity depends mainly on dimensioning disturbance of the microgrid, i.e the maximum import/export power of the microgrid in this case. The storage capacity may be further reduced if the frequency nadir requirement is relaxed, provided the maximum ramp rate limit of the hydro turbine is not reached.

CHAPTER 4

Updated sizing of BESS in single microgrid to mitigate grid capacity bottleneck and improve frequency stability during island transition

This chapter combines the work done in Chapter 2 and Chapter 3 to provide an updated BESS size to simultaneously mitigate the grid capacity bottleneck and provide a microgrid with a frequency-secure unplanned island transition in addition to island capability.

Nomenclature

Indices

t_{GC}	index of time for grid-connected operation in [h]
t_{IO}	index of time for island operation in [h]
t_{IT}	index of time for island transition in [h]
y	index of year in [yr]

Parameters

Time-related parameters

$\Delta t_{\mathrm{GC}}, \Delta t_{\mathrm{IO}}$	time interval of time index t_{GC}, t_{IO} in [h]
$T_{\mathrm{GC}}, T_{\mathrm{IO}}, T_{\mathrm{IT}}$	final time of time index t_{GC}, t_{IO}, t_{IT} in [h]
$P^{\mathrm{hy}}_{t_{\mathrm{GC}}}$	hydro power plant power in [p.u.]
$P^{\mathrm{rn}}_{t_{\mathrm{GC}}}$	other converter-interfaced renewable generation power in [p.u.]
$P^{\mathrm{L,AC,ncrit}}_{t_{\mathrm{GC}}}$	non-critical AC load power in [p.u.]
$P^{\mathrm{L,DC,ncrit}}_{t_{\mathrm{GC}}}$	non-critical DC load power in [p.u.]

Technical-related parameters

$\eta_{\mathrm{con}}, \eta_{\mathrm{inv}}, \eta_{\mathrm{tran}}$	efficiency of DC/DC converter, DC/AC converter, transformer
$\eta_{\mathrm{dis}}, \eta_{\mathrm{ch}}$	battery discharge and charge efficiencies
$SOC_{\mathrm{min,GC}}$	minimum battery SOC level in grid-connected operation
$SOC_{\mathrm{max,GC}}$	maximum battery SOC level in grid-connected operation
$SOC_{\mathrm{min,IO}}$	minimum battery SOC level in island operation
$SOC_{\mathrm{max,IO}}$	maximum battery SOC level in island operation
N	project duration in [yr]
$P^{\mathrm{MG,max}}$	microgrid power subscription in [p.u.]
$P^{\mathrm{hy,min}}$	hydro power plant minimum power in [p.u.]
$P^{\mathrm{hy,max}}$	hydro power plant maximum power in [p.u.]
$P^{\mathrm{L,AC,crit}}$	critical AC load power in [p.u.]
$P^{\mathrm{L,DC,crit}}$	critical DC load power in [p.u.]

Financial-related parameters

C_{el}	electricity spot market price in [kEUR/MWh]
$C_{\mathrm{I,B}}$	battery investment cost in [kEUR/MWh]
$C_{\mathrm{I,con}}$	DC/DC converter investment cost in [kEUR/MW]
$C_{\mathrm{I,inv}}$	DC/AC converter investment cost in [kEUR/MW]
$C_{\mathrm{I,tran}}$	transformer investment cost in [kEUR/MVA]
$C_{\mathrm{OM,fix,B}}$	battery fixed OPEX in [kEUR/MWh/year]
$C_{\mathrm{OM,fix,con}}$	DC/DC converter fixed OPEX in [kEUR/MW/year]

$C_{\mathrm{OM,fix,inv}}$	DC/AC converter fixed OPEX in [kEUR/MW/year]
$C_{\mathrm{OM,fix,tran}}$	transformer fixed OPEX in [kEUR/MVA/year]
$C_{\mathrm{OM,var,B}}$	battery variable OPEX in [kEUR/MWh]
$C_{\mathrm{OM,var,con}}$	DC/DC converter variable OPEX in [kEUR/MWh]
$C_{\mathrm{OM,var,inv}}$	DC/AC converter variable OPEX in [kEUR/MWh]
r	discount rate in [%]
K_{DF}	discount factor

Variables

$E^{\mathrm{B,max}}$	BESS maximum energy storage in [p.u.h]
$P^{\mathrm{B,max}}$	BESS maximum power in [p.u.]
$P^{\mathrm{BL,max}}$	BESS and DC load shared DC/AC converter maximum power in [p.u.]
$P^{\mathrm{B}}_{t_{\mathrm{GC}}}$	BESS power in grid-connected mode in [p.u.]
$P^{\mathrm{B}}_{t_{\mathrm{IO}}}$	BESS power in island-operation mode in [p.u.]
$P^{\mathrm{B}}_{t_{\mathrm{IT}}}$	BESS power in island-transition mode in [p.u.]
$P^{\mathrm{B,dis}}_{t_{\mathrm{GC}}}$	BESS discharge power in grid-connected mode in [p.u.]
$P^{\mathrm{B,ch}}_{t_{\mathrm{GC}}}$	BESS charge power in grid-connected mode in [p.u.]
$P^{\mathrm{B,dis}}_{t_{\mathrm{IO}}}$	BESS discharge power in island-operation mode in [p.u.]
$P^{\mathrm{B,ch}}_{t_{\mathrm{IO}}}$	BESS charge power in island-operation mode in [p.u.]
$P^{\mathrm{BL}}_{t_{\mathrm{GC}}}$	BESS and DC load shared DC/AC converter power in grid-connected mode in [p.u.]
$P^{\mathrm{BL}}_{t_{\mathrm{IO}}}$	BESS and DC load shared DC/AC converter power in island-operation mode in [p.u.]
$P^{\mathrm{BL}}_{t_{\mathrm{IT}}}$	BESS and DC load shared DC/AC converter power in island transition mode in [p.u.]
$P^{\mathrm{BL,in}}_{t_{\mathrm{GC}}}$	BESS and DC load shared DC/AC converter input power in grid-connected mode in [p.u.]
$P^{\mathrm{BL,out}}_{t_{\mathrm{GC}}}$	BESS and DC load shared DC/AC converter output power in grid-connected mode in [p.u.]

$P_{t_{\mathrm{IO}}}^{\mathrm{BL,in}}$	BESS and DC load shared DC/AC converter input power in island-operation mode in [p.u.]
$P_{t_{\mathrm{IO}}}^{\mathrm{BL,out}}$	BESS and DC load shared DC/AC converter output power in island-operation mode in [p.u.]
$P_{t_{\mathrm{IT}}}^{\mathrm{BL,in}}$	BESS and DC load shared DC/AC converter input power in island-transition mode in [p.u.]
$P_{t_{\mathrm{IT}}}^{\mathrm{BL,out}}$	BESS and DC load shared DC/AC converter output power in island-transition mode in [p.u.]
$P_{t_{\mathrm{GC}}}^{\mathrm{BL,loss}}$	BESS and DC load shared DC/AC converter power losses in grid-connected mode in [p.u.]
$P_{t_{\mathrm{IO}}}^{\mathrm{BL,loss}}$	BESS and DC load shared DC/AC converter power losses in island-operation mode in [p.u.]
$P_{t_{\mathrm{IT}}}^{\mathrm{BL,loss}}$	BESS and DC load shared DC/AC converter power losses in island-transition mode in [p.u.]
$P_{t_{\mathrm{GC}}}^{\mathrm{MG}}$	microgrid power import in [p.u.]
$E^{\mathrm{B,init}}$	BESS initial energy storage level in [p.u.h]
$e_{t_{\mathrm{GC}}}^{\mathrm{B}}$	BESS energy storage level in grid-connected mode in [p.u.h]
$e_{t_{\mathrm{IO}}}^{\mathrm{B}}$	BESS energy storage level in island-operation mode in [p.u.h]
$P_{t_{\mathrm{IO}}}^{\mathrm{L,AC,ncrit}}$	non-critical AC load power in island-operation mode in [p.u.]
$P_{t_{\mathrm{IT}}}^{\mathrm{L,AC,ncrit}}$	non-critical AC load power in island-transition mode in [p.u.]
$P_{t_{\mathrm{IO}}}^{\mathrm{L,DC,ncrit}}$	non-critical DC load power in island-operation mode in [p.u.]
$P_{t_{\mathrm{IT}}}^{\mathrm{L,DC,ncrit}}$	non-critical DC load power in island-transition mode in [p.u.]
$P_{t_{\mathrm{IO}}}^{\mathrm{hy}}$	hydro power plant power in island-operation mode in [p.u.]
$P_{t_{\mathrm{IO}}}^{\mathrm{rn}}$	other converter-interfaced renewable generation power in island-operation mode in [p.u.]
$\varepsilon_{t_{\mathrm{IO}}}^{\mathrm{rn}}$	percentage of remaining converter-interfaced renewable generation after curtailment in island-operation mode
$\varepsilon_{t_{\mathrm{IO}}}^{\mathrm{L,AC,ncrit}}$	percentage of remaining non-critical AC load after load shedding in island-operation mode
$\varepsilon_{t_{\mathrm{IT}}}^{\mathrm{L,AC,ncrit}}$	percentage of remaining non-critical AC load after load shedding in island-transition mode

$\varepsilon_{t_{\mathrm{IO}}}^{\mathrm{L,DC,ncrit}}$	percentage of remaining non-critical DC load after load shedding in island-operation mode
$\varepsilon_{t_{\mathrm{IT}}}^{\mathrm{L,DC,ncrit}}$	percentage of remaining non-critical DC load after load shedding in island-transition mode
C_{CAPEX}	CAPEX of investment in BESS and DC/AC converter shared by BESS and DC load in [kEUR]
C_{OPEX}	total OPEX of BESS and DC/AC converter shared by BESS and DC load in [kEUR]
$C_{\mathrm{OPEX,fix}}$	fixed OPEX of BESS and DC/AC converter shared by BESS and DC load in [kEUR]
$C_{\mathrm{OPEX,var}}$	variable OPEX of BESS and DC/AC converter shared by BESS and DC load in [kEUR]
$C_{\mathrm{loss,GC}}$	cost of losses of BESS and DC/AC converter shared by BESS and DC load in grid-connected mode in [kEUR]
$C_{\mathrm{loss,IO}}$	cost of losses of BESS and DC/AC converter shared by BESS and DC load in island-operation mode in [kEUR]
$C_{\mathrm{loss,IT}}$	cost of losses of BESS and DC/AC converter shared by BESS and DC load in island-transition mode in [kEUR]

4.1 Introduction

This chapter aims at finding an updated BESS size to provide the following functions:

- Alleviation of grid capacity bottleneck,
- Island capability for certain amount of hours (power balance),
- Frequency-secure island transition.

This chapter extends the optimization problem developed in Chapter 2 to account for the additional functions of the frequency-secure island transition and the island capability. The constraints for achieving a frequency secure island transition are based on the dynamic simulation analysis in Chapter 3. Whereas, the constraints for achieving island capability are based on power balance equations and do not account for microgrid power quality or stability. To not limit the conclusions of the size of the BESS to a specific study case, this chapter uses a generic microgrid model based on sinusoidal variations of production and consumption. The sensitivity of the BESS size to several factors is analyzed, including the coincidence factor between local production and consumption, the percentages of local critical demand and converter-interfaced renewable generation, and the design criterion on island duration.

4.2 Optimization problem description

This section describes the optimization problem qualitatively, while the detailed mathematical formulation is included in Appendix B.

4.2.1 Network diagram of generic microgrid

Figure 4.1 shows the network diagram of a generic microgrid consisting of a HPP, other renewable generation, and AC and DC loads. The microgrid operator is planning to invest in a BESS co-located with a DC load, which is highlighted in colors, to achieve the following functions:

- Alleviation of grid capacity bottleneck,
- Island operation capability,
- Successful island transition capability.

Chapter 2 has investigated the sizing of BESS and other interconnection technologies to alleviate grid capacity bottleneck. However, this chapter is limited to single microgrid, and the corresponding sizing of BESS to not only alleviate grid capacity bottleneck, but also to provide island capability with successful island transition. The sizing problem of BESS is formulated as an optimization problem where the aim is to find the cost-optimal size of BESS needed to fulfill the aforementioned functions. The optimization problem is presented in the following sections.

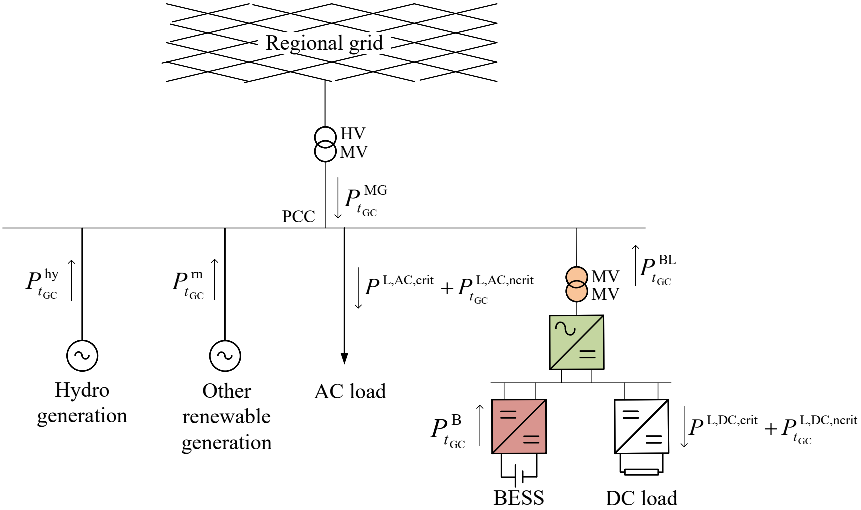

Figure 4.1: Network diagram of generic microgrid with BESS.

4.2.2 Objective function for minimization of investment and operational costs

The objective function minimizes the total cost of the investment and operation of BESS evaluated over the life time of the project. The minimized costs include:

- CAPEX: CAPEX of battery, DC/DC converter, DC/AC converter, and transformer,
- OPEX: OPEX of battery, DC/DC converter, DC/AC converter, and transformer,
- Losses cost: Cost of losses in battery, DC/DC converter, DC/AC converter, and transformer.

The assumptions made when formulating the objective function are as follows:

- The cost of losses is treated as an independent parameter from the OPEX, although in some of the references the cost of losses is part of the variable OPEX,
- The OPEX is only accounted for in grid-connected mode since islanding does not occur very often,
- Cost of losses for battery, DC/DC and DC/AC converters, and transformer are accounted for in island mode. However, only the cost of losses for DC/AC converter and transformer are accounted for in island transition. This is because the battery and DC/DC converter losses affect the size of the BESS energy capacity, whereas the DC/AC converter and transformer losses affect the size of the BESS power capacity. Since the island transition is a short transient, the optimization problem neglects the requirement on BESS energy,
- The OPEX and the cost of losses account for the entire project lifetime of 20 years. This is accounted for by assuming that the net load profile of the microgrid is the same every day for the entire 20 years,
- Services that bring revenue stream such as energy arbitrage and frequency ancillary services are not included in this formulation.

4.2.3 Constraints for mitigation of grid capacity bottleneck

The constraints for the alleviation of grid capacity bottleneck include:

- Maximum power import and export between the microgrid and the upstream distribution grid,
- Maximum power capacity of BESS and DC/AC converter,
- Maximum and minimum energy capacity of BESS,
- Energy level of BESS,
- DC-link power balance of integrated BESS and DC load.

Whenever BESS is mentioned in this chapter, it refers to the battery and its DC/DC converter. The DC/AC converter is considered separate from the BESS since it is shared between the BESS and the DC load.

The assumptions made when formulating the constraints include:

- The maximum power exchange between the microgrid and the upstream distribution grid is treated as a hard constraint instead of imposing a penalty in the objective function for exceeding the power subscription,
- Both critical and non-critical demands must be fulfilled even during a grid capacity bottleneck,
- The HPP does not participate in the alleviation of grid capacity bottleneck,
- BESS SOC level is constrained between 20% and 80%,
- The model used here is a power balance model where voltage drops are neglected, i.e. voltage is 1 p.u.,
- The power losses through battery, DC/DC and DC/AC converters, and transformer are assumed to have a linear relationship with the power flow through the respective element.

4.2.4 Constraints for island operation capability

The constraints for island operation capability include:

- AC power balance without access to the upstream distribution grid,
- Maximum power capacity of BESS and DC/AC converter,
- Maximum and minimum energy capacity of BESS,
- Energy level of BESS,
- DC-link power balance of integrated BESS and DC load.
- Maximum and minimum power capacity of HPP,
- Power balancing by curtailment of converter-interfaced renewable generation,
- Power balancing by AC and DC non-critical load shedding.

The assumptions made in this formulation include:

- Island operation capability is imposed as a constraint instead of imposing penalty on power interruption in the objective function,
- Islanding can occur at any hour of the year with equal likelihood,
- Only the critical load must be fulfilled during island operation,
- No penalty is imposed in the objective function on the curtailment of converter-interfaced renewable generation and the shedding of non-critical load,
- HPP provides flexibility to the microgrid in island operation within its thermal limit,
- BESS SOC level is constrained between 0% and 100%,
- The model used here is a power balance model where voltage drops are neglected, i.e., voltage is 1 p.u.,
- The power losses through battery, DC/DC and DC/AC converters, and transformer are assumed to have a linear relationship with the power flow through the respective element.

4.2.5 Constraints for successful island transition capability

The constraints for successful island transition capability are based on the dynamic analysis in Chapter 3 and include:

- Dynamic AC power balance. Dynamic power balance here means to be able to limit the maximum instantaneous frequency deviation through activation of fast resources,
- Maximum power capacity of BESS and DC/AC converter,
- Dynamic DC power balance of integrated BESS and DC load,
- Dynamic AC and DC non-critical load shedding,

The assumptions made in this formulation include:

- Successful island transition capability is imposed as a constraint instead of imposing penalty on unsuccessful island transition,

- Islanding can occur at any hour of the year with equal likelihood,
- Fast frequency regulation is only achieved through fast flexible resources including BESS and non-critical load shedding,
- HPP and other converter-interfaced renewable generation are not fast enough to contribute in fast frequency regulation. Therefore, it is assumed that they maintain a constant power during island transition,
- BESS energy requirement needed for achieving a successful island transition is neglected,
- Voltage security constraints are neglected,
- The power losses through DC/AC converter and transformer are assumed to have a linear relationship with the power flow through the respective element.

4.2.6 Summary of microgrid flexibility resources in different operation modes

Table 4.1 summarizes the flexibility resources of the microgrid and their role in different microgrid operation modes. The BESS provides flexibility in all microgrid modes, including capacity bottleneck alleviation in grid-connected mode, fast frequency regulation during unplanned islanding, and power balance in the island operation mode. Hydro and other renewable generation are set to not provide capacity bottleneck alleviation as this is the current practice. The analysis in Chapter 3 demonstrated that the hydro turbine-governor system is not fast enough to mitigate frequency deviation during the island transition. Thus, its contribution is neglected in the optimization problem. Additional dynamic analysis is needed to assess the ability of converter-interfaced renewable generation to provide fast frequency regulation through curtailment of power. However, the analysis in this chapter neglects its contribution as well. Hydro and other renewable generation are set to provide power balance to the microgrid in island operation mode. This includes up- and down-regulation by hydro generation and down-regulation by other non-dispatchable renewable generation through curtailment. The non-critical demand is set to support the microgrid during island transition by providing under-frequency load shedding in case of excessive demand. Additionally, the non-critical load contributes in balancing the microgrid in island operation mode through load shedding.

The merit order for the activation of flexibility resources is determined by the optimization problem such that the total operational and investment costs are reduced. Keep in mind that the hydro and other renewable generation in addition to non-critical load are existing infrastructure and do not require additional investment. Thus, the optimization problem will first attempt to fulfill the different functions using the existing infrastructure without reliance on BESS. If that is not possible, then additional investment in BESS is needed.

Table 4.1: Summary of microgrid flexible resources and their role in different microgrid modes.

	Hydro generation	Other renewable generation	Non-critical load	BESS
Grid capacity bottleneck alleviation				✓
Power balance in island mode	✓	✓	✓	✓
Fast frequency regulation for secure island transition			✓	✓

4.3 Sensitivity analysis of BESS size to various microgrid parameters

4.3.1 Base case scenario

Figure 4.2 shows the optimal power dispatch of the microgrid, including AC and DC loads, hydro and other renewable generators, and BESS, in three operational modes: grid connected mode (blue), island mode (red), and island transition mode (green). Note that the optimization problem uses generic sinusoidal profiles for generation and consumption. This serves the purpose of not limiting the conclusions on the size of BESS to a particular case study. In addition, the sensitivity of the BESS size to several microgrid parameters is illustrated in the subsequent sections.

During grid-connected mode, AC and DC daily load variations are modeled as sinusoidal variations with peak hour at 11:00 AM. The share of AC and DC loads with respect to the total load is 90% and 10%, respectively. Hydro and other renewable generation are also modeled to have sinusoidal variations with peak production at 05:00 PM. The share of hydro and other renewable generation with respect to total generation is 30% and 70%, respectively. The net load profile of the microgrid, i.e., the total load including both AC and DC loads minus the total generation including both hydro and other renewable generation, exceeds the microgrid power subscription for power import between 06:00 AM and 10:00 AM. Therefore, BESS discharges during these hours to limit the peak net load. BESS also needs to charge during off-peak hours to be ready for the grid capacity bottleneck. The optimization chooses to charge the BESS between 01:00 AM and 04:00 AM in this case.

The corresponding power dispatch during the island mode is shown in red. The power dispatch is obtained so that the microgrid can sustain 3 hours of island operation, if islanding occurs at any hour of the day and with the minimum storage requirement. Despite that the island duration is only 3 hours, the generation and consumption profiles appear as continuous profiles. However, the requirement of 3 hours is reflected in the size of the BESS energy capacity, as shown in the BESS energy plot. Each curve in this graph corresponds to an islanding incident where the initial BESS energy level is equal to the energy level in grid connected mode, and the subsequent energy level during the following three hours is a function of the BESS power profile in island operation mode. If the energy level is constant, this means that the microgrid is balanced in island operation mode without the need for a BESS. It can be seen that during island operation, the non-critical AC and DC loads are shed and only the critical loads are supplied. Note that the critical load is modeled to have a constant load profile with respect to time. The corresponding power demand of the critical load is equal to 50% of the maximum total critical and non-critical loads. The HPP ramps down its power generation to minimum value of zero between 03:00 PM and 08:00 PM due to excessive converter-interfaced renewable generation. Note that the HPP is not shut down in this case, but is running as a spinning reserve. Converter-interfaced renewable generation is also slightly curtailed between 04:00 PM and 07:00 PM. When the time is between 10:00 PM in the night and 01:00 PM in the afternoon the next day (days are identical), hydro generation ramps up its power to maximum production. This is to compensate for the lack of renewable production. However, despite hydro operating at maximum production, this was not sufficient to meet the critical demand. Therefore, BESS is discharged to account for the power deficiency between 12:00 AM at midnight and 10:00 AM in the next morning. The dimensioning incident for the BESS energy capacity is when islanding occurs at 05:00 AM, i.e., when local renewable production is minimum. The BESS energy plot shows that energy storage is completely depleted at the end of the three-hour island duration if islanding starts at 05:00 AM.

The dynamic power during the island transition is represented by the green arrows. The dynamic power here means the maximum power deviation during island transition needed to limit the maximum instantaneous frequency deviation. A power decrease/increase during the island transition is represented by an arrow pointing down/up. The results cover islanding scenarios that occur at any hour of the day with 24 different possibilities. During the island transition, hydro and other renewable generation cannot change their power set point quickly enough to stabilize the microgrid. Therefore, they resume the same power as in the grid-connected mode. If islanding occurs during morning hours when there is a lack of local generation, the microgrid is stabilized through load shedding and BESS discharge. On the other hand, if islanding occurs in the afternoon when there is more local production, less load shedding is needed, and the BESS power needed for stabilization is much lesser. The energy needed from the BESS to achieve a successful island transition is negligible, since it is a short transient. The dimensioning incident of the BESS power capacity is when islanding occurs at 05:00 AM, i.e., the hour at which total production from hydro and other renewables is minimum. The corresponding size of the BESS power capacity in this case is equivalent to the total critical AC and DC demand.

In summary, the size of the BESS power capacity is dictated by the function of successful island transition, and the size of its energy capacity is dictated by the functions of island capability and alleviation of grid capacity bottleneck. The dimensioning incident for the BESS power capacity is when islanding occurs at 05:00 AM, i.e., the hour at which local production is minimum. Note that since alleviation of grid capacity bottleneck, island capability, and successful island transition, are functions that do not occur simultaneously, the BESS power capacity can be shared among them. Thus, the size of BESS power capacity is the maximum capacity among the three functions. However, this rule does not necessarily apply to the size of BESS energy capacity. This is because the initial SOC level before islanding plays a big role in whether or not the BESS will be able to fulfill the 3 hours island requirement. The initial SOC level before islanding also depends on whether islanding occurs after a capacity bottleneck in the grid when the BESS is depleted or during normal operation when the BESS is charged. Another factor that plays a role in fulfilling the island capability requirement is the available local resources at the time of islanding. The worst-case scenario is where islanding occurs after a grid capacity bottleneck and where the available local converter-interfaced renewable generation is minimum. In that case, the size of BESS energy capacity must account for the summation of energy needed to alleviate the grid capacity bottleneck and that needed for the island capability. However, in this simulation, it was fortunate that the hour at which local converter-interfaced renewable generation is minimum is at 05:00 AM, i.e., just before the beginning of a capacity bottleneck. Thus, the BESS was fully charged at 80%. Therefore, the needed BESS energy capacity was less than the sum of the individual energy capacities needed to alleviate the grid capacity bottleneck and provide island capability.

4.3.2 Impact of coincidence factor between production and consumption

The base case scenario assumes that the production and consumption profiles have a daily sinusoidal variations with peak production at 05:00 PM and peak consumption at 11:00 AM, respectively. The coincidence factor between the production and consumption is said to be intermediate in this case. This section investigates different coincidence factors between production and consumption:

- Low coincidence factor: when production has peak hour at 11:00 PM and consumption at 11:00 AM,
- Intermediate coincidence factor 1 (base case): when production has peak hour at 05:00 PM and consumption at 11:00 AM,
- Intermediate coincidence factor 2: when production has peak hour at 05:00 AM and consumption at 11:00 AM,

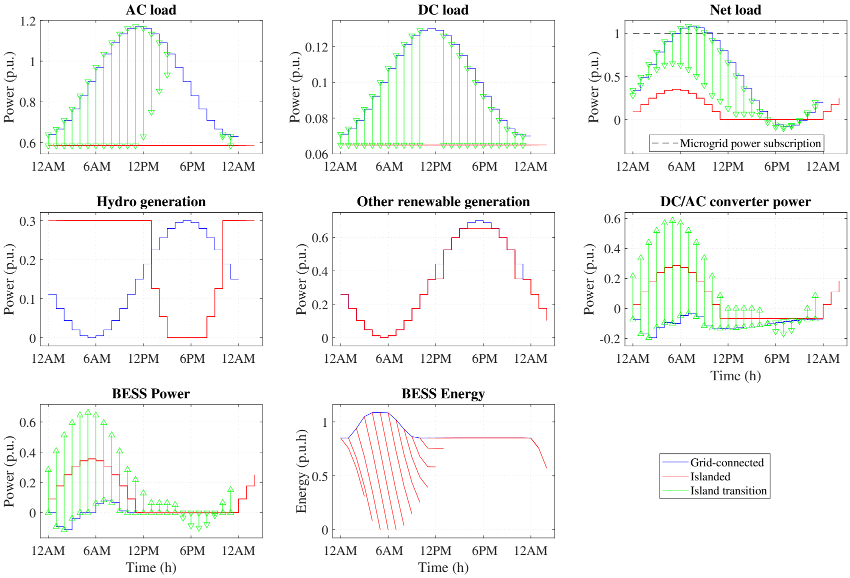

Figure 4.2: Microgrid optimal power dispatch under three operational modes: grid connected, islanded and island transition modes.

- High coincidence factor: when both production and consumption have peak hour at 11:00 AM.

Figure 4.3 shows the impact of the coincidence factor on the cost-optimal size of BESS and DC/AC converter power capacities, $P^{\mathrm{B,max}}$ and $P^{\mathrm{BL,max}}$, respectively. The figure also shows the size needed to deliver different functions: capacity bottleneck alleviation (blue); island capability (red); successful island transition (green); all previous functions (cyan). The power capacity needed for capacity bottleneck alleviation increases with lesser coincidence factors between production and consumption. However, the power capacity needed for the island capability and successful island transition are independent of the coincidence factor. This is because of the way critical demand is modeled. While the non-critical demand varies throughout the day, the critical demand is modeled to have a constant load profile with respect to time. Keep in mind that during an island contingency, it is only the critical demand that must be fulfilled. It is evident that the successful island transition function requires larger size than the function of island capability. This stems from the fact that successful island transition requires fast acting resources which are available in the BESS and not in the hydro and other renewable generation. The power capacity needed to provide all the functions is equal to the size for providing a successful island transition. This is because all three functions occur at different time instants, making it possible to share the converter capacity without having to oversize the converter.

Figure 4.4 shows the cost-optimal size of BESS energy capacity corresponding to different coincidence factors. The size presented is for BESS that delivers the following functions: capacity bottleneck alleviation (blue), island capability (red), and both functions simultaneously (green). The successful island transition function is not considered here since it is a short dynamic that requires a negligible amount of energy.

The BESS energy capacity needed for capacity bottleneck alleviation increases as coincidence factor reduces between production and consumption. However, the BESS energy capacity needed for island capability is completely independent of the coincidence factor. This is because, as mentioned earlier, the critical load is modeled such that it remains constant over time.

The total energy storage needed for delivering both functions should in principle be at least equal to the maximum of the two functions. For high coincidence factor, the microgrid do not experience a capacity bottleneck; thus, the final size for delivering both functions is only dictated by the island capability. For low coincidence factor, the capacity bottleneck alleviation requires more than twice the energy needed for island capability. However, when delivering both functions simultaneously, the needed size of the BESS energy capacity is only equivalent to the size needed for alleviating the grid capacity bottleneck. This is mainly because the allowed SOC range of the BESS during grid-connected mode is 20%-80% (40% of energy capacity is not used) compared to 0%-100% in the island mode. Therefore, even if islanding occurs when BESS is at minimum SOC level, there is still 20% unused energy capacity that can be utilized in island operation.

Despite that intermediate coincidence factor 1 and 2 (Intermediate 1 and Intermediate 2) have identical storage size for delivering each individual function, the final storage size to deliver both functions is different. Intermediate 1 requires a storage capacity of 1.35724 p.u.h compared to 1.60254 p.u.h for Intermediate 2. The main factor in this difference is the BESS initial SOC

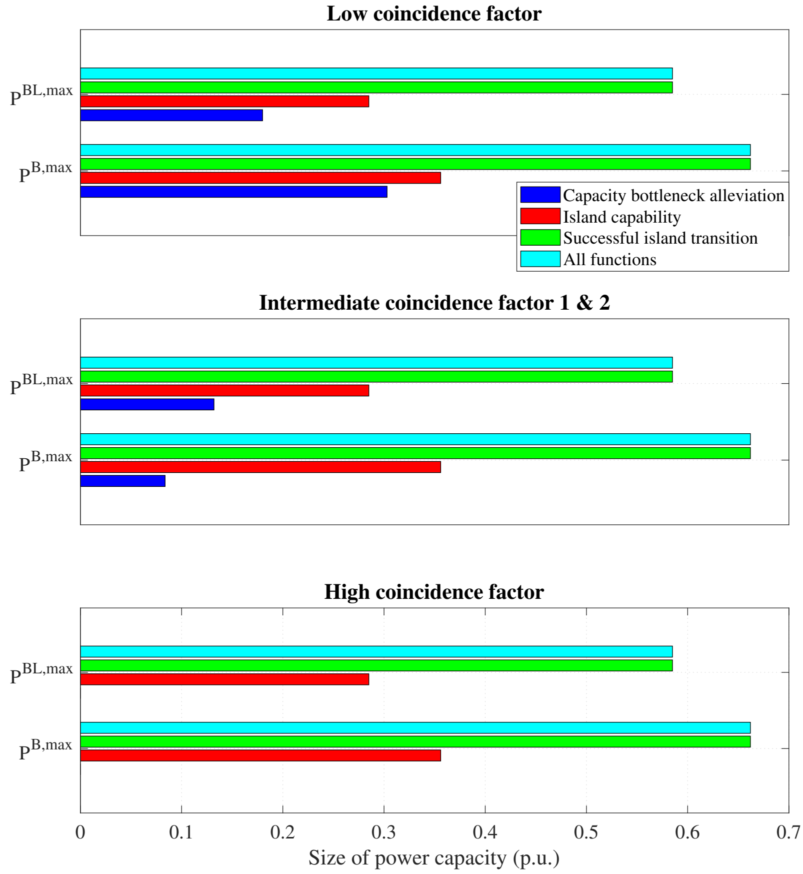

Figure 4.3: Sensitivity of the size of BESS and DC/AC converter power capacities to the coincidence factor between local production and consumption when the BESS is delivering different functions. $P^{\mathrm{B,max}}$ and $P^{\mathrm{BL,max}}$ refer to BESS and DC/AC converter power capacities, respectively.

level before islanding. It was found from the optimization that the dimensioning incident for island capability is when islanding occur with minimum local production. For Intermediate 1, this is at 05:00 AM, just before capacity bottleneck occurs, while for Intermediate 2, this is at 05:00 PM, just after capacity bottleneck occurs. Therefore, in the case of Intermediate 1, the BESS was fully charged at 80% before islanding, since it was ready to support the microgrid before the occurrence of the capacity bottleneck. However, in the case of Intermediate 2, the initial SOC level before islanding was 65%, since the BESS has already been partially discharged during the capacity bottleneck. This explains the higher storage capacity in the latter case. Note that in the case of Intermediate 2, the BESS energy capacity needed to deliver both functions is higher than the sum of the individual functions. This is due to the constraint that the BESS SOC level have to be less than or equal to 80% during grid connected mode.

In summary, it is not straightforward to obtain a general rule of thumb for sizing BESS energy capacity to mitigate grid capacity bottleneck and provide island capability. To be on the safe side, the microgrid operator can dimension the energy capacity to be the sum of the energy capacities needed to provide each function individually and also account for 40% unused energy storage due to SOC constraints. However, this is not an optimal cost design. Instead, if there is clear information about the correlation between the time at which grid capacity bottleneck occurs and the likelihood of an island contingency, then this may guide the design of a more cost-optimal energy storage capacity. In addition to that, the correlation between the local peak production and consumption is a very critical input in the sizing of the BESS energy capacity.

4.3.3 Impact of percentages of local critical demand and converter-interfaced renewable generation

In the base case, the percentage of critical load to maximum total critical and non-critical load was fixed at 50% and the percentage of converter-interfaced renewable generation to total local renewable generation (both hydro and converter-interfaced) was fixed at 70%. Figure 4.5 shows the sensitivity of the size of BESS energy capacity when sweeping the percentage of critical load from 0% to 50% and the percentage of converter-interfaced renewable generation from 0% to 100%. The size of the BESS energy capacity obtained here is the one in which the BESS provides capacity bottleneck alleviation

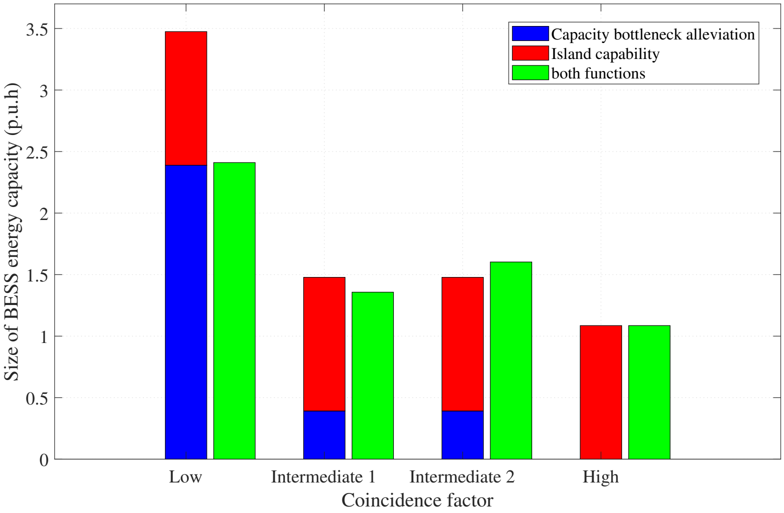

Figure 4.4: Sensitivity of the size of BESS storage capacity to the coincidence factor between local production and consumption when the BESS is delivering different functions.

and island capability. Note that the requirement for island duration capability remains 3 hours as in the base case scenario. Additionally, keep in mind that the energy needed to achieve a successful island transition is neglected in the formulation of the optimization problem. The blue surface means that the energy storage capacity is dictated solely by the function of alleviation of the capacity bottleneck with no additional size needed for island capability. The red surface means that additional storage capacity is needed to meet the island capability requirement.

It can be seen that if the percentages of critical load and converter-interfaced renewable generation are less than a certain threshold, then the BESS energy capacity is constant and is solely determined by the requirement for capacity bottleneck alleviation. The size is constant because both critical and non-critical demands have to be fulfilled during a capacity bottleneck. Furthermore, both converter-interfaced renewable generation and hydro generation are assumed to be non-flexible in grid-connected mode. Thus, the percentages of critical demand and converter-interfaced renewable generation do not play a role in the BESS energy capacity needed to alleviate capacity bottlenecks.

When the percentages of critical demand and converter-interfaced renewable generation exceed a certain threshold, additional BESS energy capacity is needed to meet the island capability requirement. This is because increasing the percentage of converter-interfaced renewable generation comes at the cost of less flexible hydro generation. Consequently, a larger BESS storage capacity is needed to balance the microgrid in island operation. The requirement of the BESS storage capacity may increase further due to the larger percentage of critical demand that must be fulfilled in the island operation mode. The largest storage size is at the highest percentages of critical demand and converter-interfaced renewable generation, i.e. 50% and 100%, respectively. The corresponding storage size is 7 times the size needed to alleviate the capacity bottleneck!

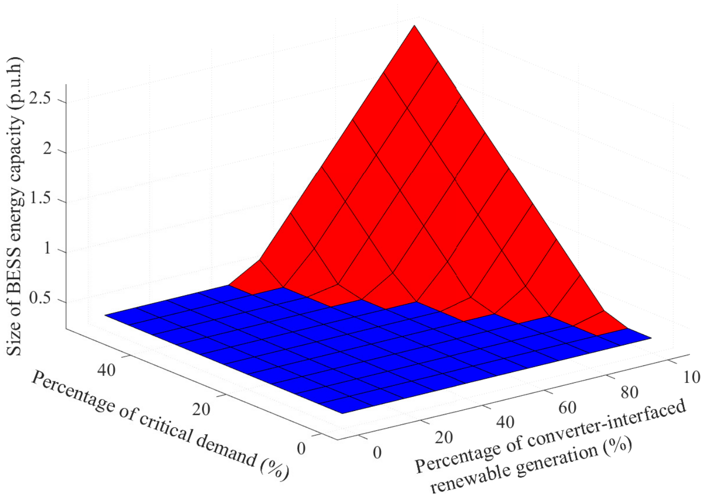

Figure 4.5: Sensitivity of the size of BESS energy capacity to the percentages of critical demand and converter-interfaced renewable generation when BESS is providing capacity bottleneck alleviation and island capability. The color code is as follows: island capability do not add additional requirement on the BESS energy capacity (blue): island capability adds additional requirement on the BESS energy capacity (red).

Figure 4.6 shows the size of the power capacity of the BESS and DC/AC converter when sweeping the percentage of critical demand from 0% to 50% and the percentage of converter-interfaced renewable generation from 0% to 100%. The obtained size is when the BESS delivers the following functions: alleviation of capacity bottleneck, island capability, and successful island transition. The color code indicates the dimensioning function for the BESS power capacity: alleviation of capacity bottleneck (blue); successful island transition (green). Note that the island capability function is not dimensioning in the entire range of percentages of critical demand and converter-interfaced renewable generation. Instead, the size is predominantly determined by the successful island transition function. This is because power imbalance during island operation can be mitigated through slow resources such as hydro generators, whereas a successful island transition exclusively requires a fast acting recourse such as BESS. Although successful island transition is the main function for the size of BESS power capacity, the alleviation of capacity bottleneck becomes the dimensioning incident at percentages of critical demand below 5%. This is because with lesser critical demand, there is a larger percentage of non-critical demand that can be used for stabilizing the microgrid during island transition through under-frequency load shedding. This helps in achieving a successful island transition with lesser power support from the BESS. If the percentage of critical demand is greater than 5% in this case, the BESS power capacity is determined by the successful island transition. The power capacity of the BESS then increases proportionally to the percentage of critical demand.

The size of DC/AC converter is still determined by successful island transition even at low percentage of critical demand. This is because the size of the DC/AC converter is driven by island contingency when there is excessive local generation, which requires the BESS and DC load to absorb the excessive power to avoid over-frequency situation. If the percentage of critical demand exceeds 15%, the size of the DC/AC converter is driven by island contingency when there is excessive demand, which requires the BESS to inject power to avoid under-frequency. The size of the DC/AC converter then increases proportionally to the critical demand for percentages above 15%.

It should be noted that the percentage of converter-interfaced renewable generation does not play a role in the size of the power capacity of the BESS and the DC/AC converter. This is because whether the local generation comes from hydro or other renewable generation, both are considered slow resources that cannot stabilize the microgrid during an island transition.

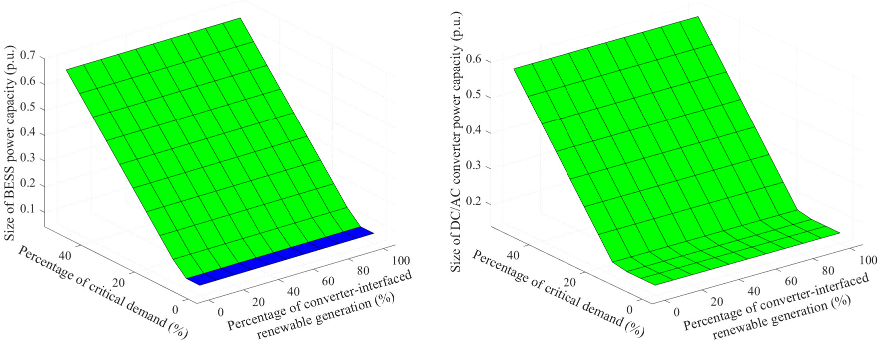

Figure 4.6: Sensitivity of the size of BESS and DC/AC converter power capacities to the percentages of critical demand and converter-interfaced renewable generation when BESS is providing capacity bottleneck alleviation, island capability, and successful island transition. The color code indicates the dimensioning function: alleviation of capacity bottleneck (blue), successful island transition (green).

4.3.4 Impact of design criteria on island duration

Figure 4.7 shows the size of the energy storage capacity if the design criterion on the island duration is 3 or 6 hours. The blue surface indicates that the BESS energy capacity is determined solely by the requirement for alleviation of the capacity bottleneck. Whereas the red surface indicates that additional size is needed for island capability. The figure shows that above a certain threshold of the percentages of critical demand and converter-interfaced renewable generation, additional energy storage capacity is needed to meet the island capability requirement. It is evident that this threshold is independent of the duration for island operation. However, once the threshold is exceeded, the energy storage capacity almost doubles.

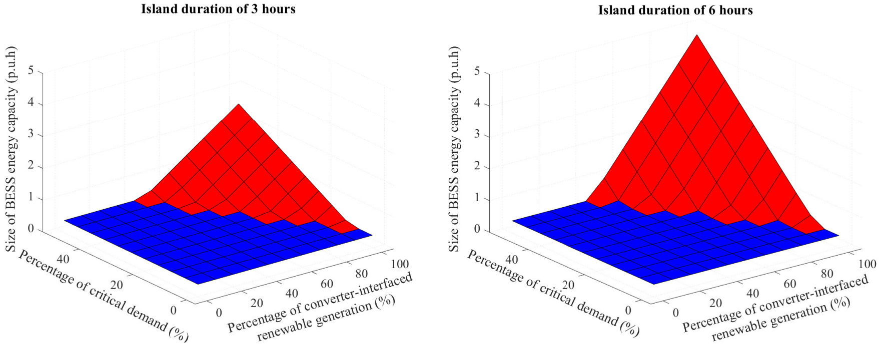

Figure 4.7: Sensitivity of the size of BESS energy capacity to the percentages of critical demand and converter-interfaced renewable generation corresponding to an island duration of 3 hours and 6 hours. The size presented here is when BESS is providing capacity bottleneck alleviation and island capability. The color code is as follows: island capability do not add additional requirement on the BESS energy capacity (blue): island capability adds additional requirement on the BESS energy capacity (red).

4.4 Summary

This chapter has investigated the size of the BESS power and energy capacities needed for the microgrid to provide three functions: island capability, frequency-secure island transition due to unplanned islanding, and alleviation of the grid capacity bottleneck. The analysis shows that the BESS power capacity can be shared among the different functions since they occur during different microgrid operation modes. Furthermore, the maximum power capacity of the BESS is dictated by the function of frequency-secure island transition. This is because unlike the other two functions that can be provided by slower acting flexibility resources, the frequency-secure island transition requires a fast acting flexibility resources which is available in the BESS.

On the other hand, the size of the BESS energy capacity is not dependent on the function of secure island transition, since it is a short transient. The other two functions for alleviating the grid capacity bottleneck and the island capability are critical in sizing the BESS energy capacity. The size needed to fulfill the former is mainly determined by the coincidence factor between local production and consumption, where a weaker correlation between the two may lead to the need for a larger storage capacity. The size needed to fulfill the latter one is dependent on the percentages of local critical demand and non-dispatchable renewable generation, where a larger percentage of the two requires a larger BESS storage capacity to balance the microgrid in island operation mode.

Unlike the power capacity of the BESS that is shared by all three functions, its energy capacity may need to account for the sum of the individual energy capacities to fulfill the different functions. However, additional future work is needed to understand how the energy storage can be co-optimized to reduce peak net load and provide island capability taking into account the correlation between a grid capacity bottleneck and a grid outage.

CHAPTER 5

Sizing and control of B2B converter in interconnected microgrids to mitigate grid capacity bottleneck and improve frequency stability during island transition

This chapter expands on the work done in Chapter 3 by extending the island contingency analysis to focus on interconnected microgrids instead of a single microgrid.

5.1 Introduction

This chapter investigates the size of a B2B converter and its control for interconnection of microgrids to provide the following functions:

- Peak net load reduction,
- Island operation with secure island transition,
- Voltage regulation.

This chapter does not account for BESS and instead rely on power re-routing between the two microgrids to fulfill the aforementioned functions. Industrial and community microgrids are used as a case study for the analysis. First, the MW capacity of the B2B converter is determined to mitigate the grid capacity bottleneck by peak net load reduction of the industrial microgrid. Second, the MVAr capacity of the B2B converter is determined to account for the requirements of the grid code on voltage regulation. Third, this chapter investigates whether an additional MW capacity of the B2B converter is needed to facilitate a frequency-secure island transition of the industrial microgrid. The analysis uses simple equations for dynamic power balance of the microgrid during island transition which accounts for fast acting resources such as the B2B converter and under frequency load shedding. The analysis also illustrates the relation between the MW capacity of the B2B converter and the percentage of time of the year that a frequency-secure island transition can be secured. Finally, a dynamic simulation analysis is performed to verify the implemented size of the B2B converter in fulfilling a frequency-secure island transition. The control of the B2B converter utilizes the same frequency controller implemented in Chapter 3 for a frequency-secure island transition of a hydro-powered microgrid using BESS.

5.2 Steady State Sizing of Back-to-Back Converter for Interconnecting Microgrids

5.2.1 Network Diagram of Interconnected Microgrid

Figure 5.1 shows the network diagram of two real-life MV distribution systems in Sweden for microgrid studies. A paper and pulp factory is supplied from a 140/11 kV substation, to which a HPP is also connected. The factory is undergoing an expansion which will increase its peak load from 20 MW to 31 MW. However, the regional system operator could not increase the peak net load supplying the industrial microgrid because of the bottleneck in the 140 kV grid. On the other hand, there is spare grid capacity from a nearby community microgrid. Thus, a B2B converter is considered as one feasible solution to supply the increased load at the factory from the community microgrid.

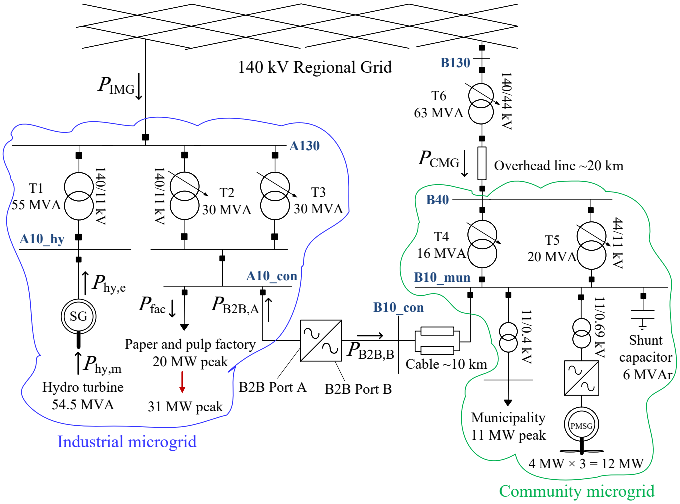

Figure 5.1: Network diagram of interconnected microgrids via B2B converter.

5.2.2 Steady-State Analysis for Sizing of Back-to-Back Converter

In this section, the sizing of the B2B converter is determined for the provision of the following functions:

- Peak net load reduction at industrial microgrid,
- Voltage regulation at both terminals of the B2B converter,
- Island operation with secure island transition of industrial microgrid.

Note that steady-state analysis utilizes simple power balance equations, and optimization is not required as in Chapters 2 and 4. This is because the problem in this chapter is simpler and does not account for BESS in either of the microgrids.

5.2.2.1 Peak Net Load Reduction

Figure 5.2 (left) shows the time duration curve of the industrial microgrid net load P_{IMG} (see Figure 5.1) without (blue) or with (red) the B2B converter.

The B2B converter assists in mitigating the bottleneck in the regional grid by importing power from a nearby community microgrid, which helps in reducing the maximum import from 24.3 MW to 14.3 MW. This has led to an increase in the peak net load of the community microgrid P_{CMG} from 10.2 MW to 14.7 MW, as shown in Figure 5.2 (right). The required capacity of the B2B converter to relieve the bottleneck in the industrial microgrid is 10 MW, as shown in the time series of B2B converter Port A (see Figure 5.3). During normal operation (no congestion), the B2B converter is utilized to maximize the energy exchange between the two microgrids.

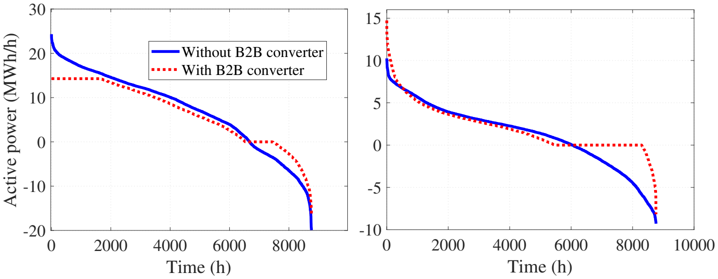

Figure 5.2: Time duration curve of industrial microgrid net load P_{IMG} (left) and community microgrid net load P_{CMG} (right).

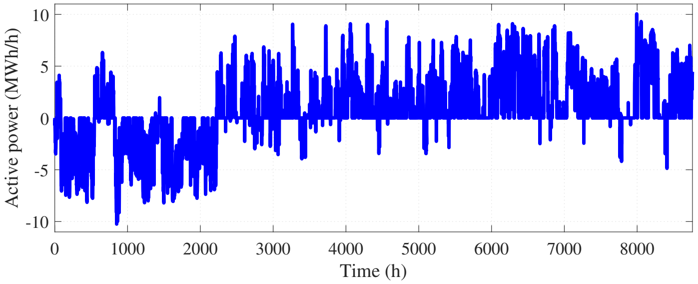

Figure 5.3: B2B converter Port A time series during 2018 with hourly resolution.

5.2.2.2 Voltage Regulation at the Converter Terminal

The B2B converter should maintain the voltage at its terminals in the range of 0.9 p.u.-1.1 p.u. during normal operation [96]. In this chapter, both ports of the B2B converter are designed with a power factor (PF) of 0.95 (3.3 MVAr) for voltage regulation [97].

5.2.2.3 Island Operation with Secure Island Transition

Requirement for Secure Island Transition A secure island transition of an unplanned islanding event is achieved if the following conditions are met: 1) Steady-state frequency is maintained within [49.5, 50.5] Hz in the post-islanding condition; 2) Dynamic frequency variation should be within [49, 51] Hz during disturbances including island transition.

Assessment of Reserve for Frequency Containment The dimensioning disturbance for island transition depends on the maximum power exchange of the industrial microgrid with the regional grid, which is 14.3 MW (import) and 16.7 MW (export) according to Figure 5.2 (left). The frequency is stabilized during an unplanned island transition by fast active power support provided by the B2B converter and the flexible load of the factory. Thereafter, the HPP active power reserve replaces the fast reserve of the converter and the factory in steady state. The up- and down-regulation reserves of B2B converter Port A are defined, respectively, as

$$P^{\mathrm{up}}_{\mathrm{B2B,A}}(t) = P^{\mathrm{max}}_{\mathrm{B2B,A}} - P_{\mathrm{B2B,A}}(t), \tag{5.1a}$$

$$P^{\mathrm{dn}}_{\mathrm{B2B,A}}(t) = P^{\mathrm{max}}_{\mathrm{B2B,A}} + P_{\mathrm{B2B,A}}(t), \tag{5.1b}$$

where $P_{\mathrm{B2B,A}}(t)$ is the active power output from B2B converter Port A at hour t and $P^{\mathrm{max}}_{\mathrm{B2B,A}}$ is its maximum active power. Furthermore, the up- and down-regulation reserves of the factory load flexibility are defined, respectively, as

$$P^{\mathrm{up}}_{\mathrm{fac}}(t) = K_{\mathsf{flex}} P_{\mathrm{fac}}(t), \tag{5.2a}$$

$$P^{\mathrm{dn}}_{\mathrm{fac}}(t) = K_{\mathsf{flex}} (P^{\mathrm{max}}_{\mathrm{fac}} - P_{\mathrm{fac}}(t)), \tag{5.2b}$$

where $P_{\mathrm{fac}}(t)$ is the factory load at hour t and $P^{\mathrm{max}}_{\mathrm{fac}}$ is its maximum active power. To fulfill the requirement on dynamic frequency variation during island transition, the up- and down-regulation reserves of the converter should be

$$\begin{aligned} P^{\mathrm{up}}_{\mathrm{B2B,A}}(t) &\geq P_{\mathrm{IMG}}(t) - P^{\mathrm{up}}_{\mathrm{fac}}(t), && (5.3\mathrm{a}) \\ P^{\mathrm{dn}}_{\mathrm{B2B,A}}(t) &\geq -\left(P_{\mathrm{IMG}}(t) + P^{\mathrm{dn}}_{\mathrm{fac}}(t)\right), && (5.3\mathrm{b}) \end{aligned}$$

Define the variable $\Delta P_{\mathrm{SIT}}(t)$ as

$$\Delta P_{\mathrm{SIT}}(t) = \begin{cases} P^{\mathrm{up}}_{\mathrm{B2B,A}}(t) - \left[P_{\mathrm{IMG}}(t) - P^{\mathrm{up}}_{\mathrm{fac}}(t)\right], & \\ & P_{\mathrm{IMG}}(t) > 0 \\ P^{\mathrm{dn}}_{\mathrm{B2B,A}}(t) + \left[P_{\mathrm{IMG}}(t) + P^{\mathrm{dn}}_{\mathrm{fac}}(t)\right], & \\ & P_{\mathrm{IMG}}(t) < 0 \\ 0. & P_{\mathrm{IMG}}(t) = 0 \end{cases} \tag{5.4}$$

If $\Delta P_{\mathrm{SIT}}(t) \geq 0$ at a certain hour, the converter has sufficient up- or down-regulating reserve to balance the load during an island transition, otherwise not. Figure 5.4 shows the time duration curve of $\Delta P_{\mathrm{SIT}}(t)$ for three different values of K_{flex}. When an unplanned islanding event occurs, the dynamic frequency requirement can only be fulfilled for 51% of a year in case of no flexible load, but increased to 79.7% (97%) of a year when 20% (35%) of the load is flexible. Alternatively, if $K_{\mathrm{flex}} = 0\%$, one needs to increase the converter size from 10 MW to 19.6 MW to achieve a reliability of 97%. This analysis shows that the B2B converter need not to be oversized if there is sufficient flexible load. Moreover, the value stacking of the peak net load reduction service and the secure island transition service results in a better utilization of the B2B converter.

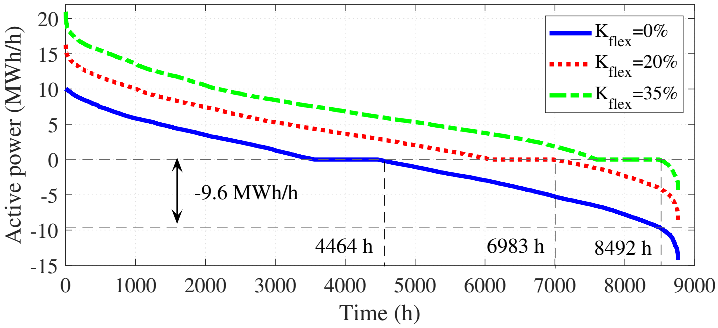

Figure 5.4: Time duration curve of ΔP_{SIT} for different flexibility of the factory.

5.3 Controller Design of Back-to-Back Converter for Secure Island Transition of Industrial Microgrid

5.3.1 Model and Control of Hydro Turbine

The hydro turbine is modeled as a Francis turbine equipped with a PI-based droop governor as shown in Figure 5.5 [78]. The corresponding controller parameters are listed in Table 1.

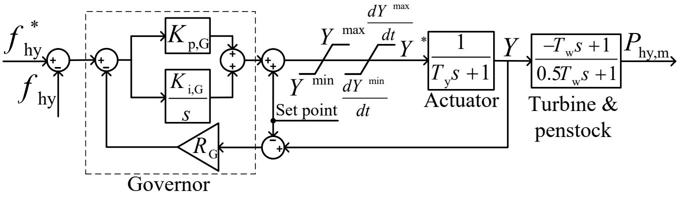

Figure 5.5: Generic hydro Francis turbine model and governor.

5.3.2 Model and Control of Back-to-Back Converter

5.3.2.1 Control Diagram of Back-to-Back Converter

Figure 5.6 shows the control diagram of the B2B converter that interconnects the two microgrids. Port A of the converter is controlled in the GFM mode, where the voltage and power control loop and the inner vector current controller are implemented according to the controller design described in [84]. Port B of the converter is controlled in the GFL mode with the controller design described in detail in [98]. Port B of the converter also controls the dc link voltage. For dynamic simulation, the average model of the B2B converter is implemented instead of the switching model.

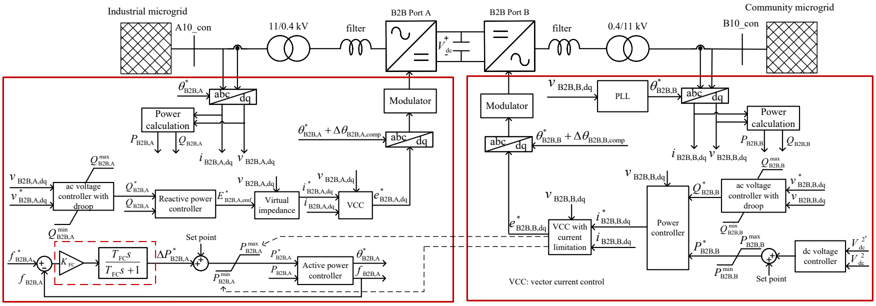

Figure 5.6: Control diagram of back-to-back converter.

5.3.2.2 Frequency Controller Structure and Tuning

To ensure frequency support during island transition, B2B converter Port A has a frequency controller in its outer loop. The frequency controller of Port A is modeled as a high pass filter as shown inside the dotted box of Figure 5.6. The tuning strategy considers the dynamic response of the hydro governor to meet frequency quality requirements according to [99], where the high pass filter gain $\mathrm{K_{FC}}$ and the time constant $\mathrm{T_{FC}}$ are tuned as

$$K_{\mathrm{FC}} = \frac{\Delta P_{\mathrm{dm}} - D_{\mathrm{fac}}\Delta f^{\mathrm{max}}}{\Delta f^{\mathrm{max}}}\frac{1}{P_{\mathrm{B2B,A}}^{\mathrm{max}}}, \tag{5.5}$$

$$T_{\mathrm{FC}} = \frac{\Delta P_{\mathrm{dm}} - D_{\mathrm{fac}}\Delta f^{\max}}{\Delta f^{\max}} \frac{(1 + R_{\mathrm{G}} K_{\mathrm{p,G}})^2}{K_{\mathrm{i,G}}} \frac{1}{P_{\mathrm{hy}}^{\max}}, \tag{5.6}$$

where ΔP_{dm} is the dimensioning disturbance, D_{fac} is the factory load frequency dependence, $\Delta f^{\max}$ is the maximum allowed frequency deviation in Hz, $K_{\mathrm{p,G}}$, $K_{\mathrm{i,G}}$ and R_{G} are hydro governor parameters (see Figure 5.5). In the aforementioned equation, the dimensioning disturbance is defined as

$$\Delta P_{\mathrm{dm}} = \max\{(P_{\mathrm{IMG}}(t) - P_{\mathrm{fac}}^{\mathrm{up}}(t)), -(P_{\mathrm{IMG}}(t) + P_{\mathrm{fac}}^{\mathrm{dn}}(t)).\} \tag{5.7}$$

Table 1 lists the B2B converter parameters.

Table 5.1: Industrial microgrid parameters.

Hydro parameters			**B2B converter parameters**		
Parameter	**Value**	**Base**	**Parameter**	**Value**	**Base**
$S_{\mathrm{hy}}^{\max}$	54.5 MVA	-	$P_{\mathrm{B2B,A}}^{\max}$, $P_{\mathrm{B2B,B}}^{\max}$	10 MW	-
$P_{\mathrm{hy}}^{\max}$	46.3 MW	-	$Q_{\mathrm{B2B,A}}^{\max}$, $Q_{\mathrm{B2B,B}}^{\max}$	3.3 MVAr	-
f_{b}	50 Hz	-	K_{FC}	49.1 p.u.	$P_{\mathrm{B2B,A}}^{\max}/f_{\mathrm{b}}$
$K_{\mathrm{p,G}}$	1 p.u.	$P_{\mathrm{hy}}^{\max}/f_{\mathrm{b}}$	T_{FC}	35 s	-
$K_{\mathrm{i,G}}$	0.33 rad/s	$P_{\mathrm{hy}}^{\max}/f_{\mathrm{b}}$	**System parameters**		
R_{G}	0.05 p.u.	$f_{\mathrm{b}}/P_{\mathrm{hy}}^{\max}$	**Parameter**	**Value**	**Base**
T_{y}	0.2 s	-	ΔP_{dm}	9.81 MW	-
T_{w}	1.6 s	-	D_{fac}	0 MW/Hz	-
H_{hy}	4.5 s	$S_{\mathrm{hy}}^{\max}$	$\lvert\Delta f_{\max}\rvert$	1 Hz	-
-	-	-	K_{flex}	35%	-

5.3.3 Frequency-Based Load Shedding

The frequency regulation reserve of the B2B converter may not be sufficient to balance the load during island transition. Thus, a load shedding scheme based on frequency deviation is adopted as follows: 1) disconnect one-third of the flexible load at 49.5 Hz; 2) disconnect another one-third at 49.3 Hz, 3) disconnect another one-third at 49.1 Hz.

5.4 Simulation Results

The microgrid in Figure 5.1 is modeled in Matlab/Simulink using phasor simulations. Two scenarios are considered for the dynamic simulations with corresponding pre-disturbance power flow summarized in Table 5.2, where B2B converter Port A is lightly loaded prior to island transition in Scenario 1, but heavily loaded in Scenario 2.

Table 5.2: Pre-disturbance power flow of the industrial microgrid.

	P_{IMG}	$P_{\mathrm{hy,e}}$	$P_{\mathrm{B2B,A}}$	P_{fac}	$P_{\mathrm{fac}}^{\mathrm{up}}$
Scenario 1	14.3 MW	13.0 MW	1.0 MW	28.3 MW	10.0 MW
Scenario 2	14.3 MW	6.7 MW	8.0 MW	29.0 MW	10.2 MW

5.4.1 Scenario 1: Lightly Loaded Back-to-Back Converter

Figure 5.7 shows the time-domain simulation results when the industrial microgrid is islanded at $t = 5$ s while importing 14.3 MW. The initial rate-of-change-of-frequency (RoCoF) is 1.23 Hz/s, and the frequency nadir is reached already at $t = 7.4$ s. The hydro generator barely increases its frequency reserve within such a short time despite the initial inertial response. Therefore, it is mainly the B2B converter and the frequency-based load shedding that helps to arrest the frequency fall. The converter is initially operating at 1 MW with an up-regulation reserve of 9 MW, which is not sufficient for balancing the load. However, with a load shedding of 10 MW activated in three stages as shown in the zoomed window of subplot (b), the frequency is arrested at 49.1 Hz, which is above the minimum acceptable frequency nadir of 49 Hz. Eventually, the frequency reserve from HPP replaces the fast frequency reserve from the B2B converter and the frequency settles down at 49.77 Hz in steady state. Despite the fast active support by B2B converter Port A, the dc-link voltage drops slightly to 0.97 p.u. and is quickly regulated back to 1 p.u.

5.4.2 Scenario 2 : Heavily Loaded Back-to-Back Converter

For Scenario 2, the B2B converter Port A is transmitting 8 MW to the industrial microgrid prior to the islanding event. The converter has an up-regulation reserve of 2 MW only, and both Port A and Port B hit the 10 MW power limit immediately after the disturbance. Figure 5.8 shows the resulting dc-link voltage of the B2B converter. Two cases considered here are: a) $P_{\mathrm{B2B,B}}^{\max} =$ 10 MW; b) $P_{\mathrm{B2B,B}}^{\max} = 10.1$ MW. In both cases, $P_{\mathrm{B2B,A}}^{\max} = 10$ MW. When the active power through Port B reaches its limit of 10 MW, the control over the dc-link voltage by converter Port B is lost. Thus, to maintain control over the

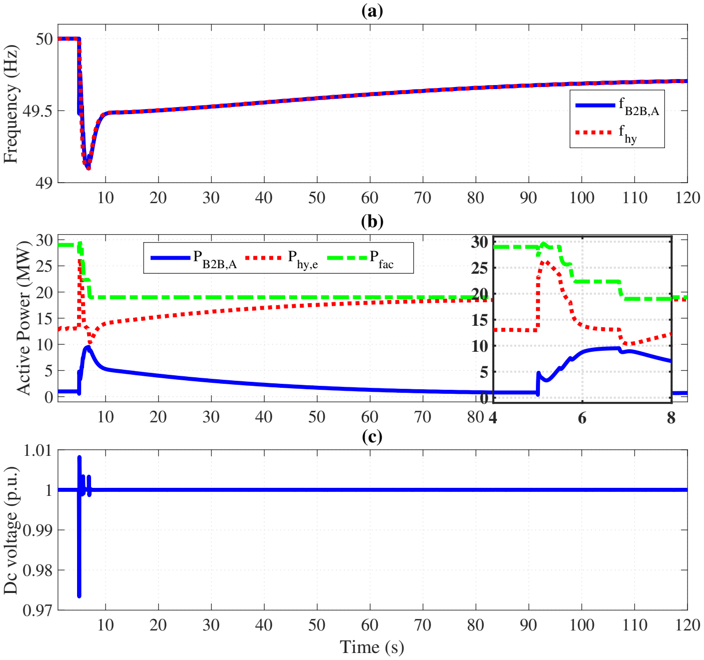

Figure 5.7: Island transition of industrial microgrid at $t = 5$ s corresponding to scenario 1: (a) frequency of B2B converter Port A and HPP, (b) electric power of B2B converter Port A and HPP, and factory demand, (c) B2B converter dc-link voltage.

dc-link voltage, it is necessary to increase the rating of Port B to be slightly above the rating of Port A, e.g. here we have chosen $P_{\text{B2B,B}}^{\text{max}} = 10.1$ MW.

Figure 5.9 shows the corresponding frequency and active power balance of the industrial microgrid during the islanding event where the active power at Port B $P_{\text{B2B,B}}^{\text{max}}$ is limited to 10.1 MW. Besides 2.0 MW of frequency reserve from the B2B converter, a total load of 10.2 MW is disconnected in three stages to arrest the frequency fall. However, this is still not sufficient to balance the load. An additional reserve of 2.1 MW is needed to reach power balance, which must come from the hydro turbine. Due to the slow response of the hydro turbine-governor system, the frequency continues to fall to 48.1 Hz, which is below the minimum acceptable frequency of 49 Hz.

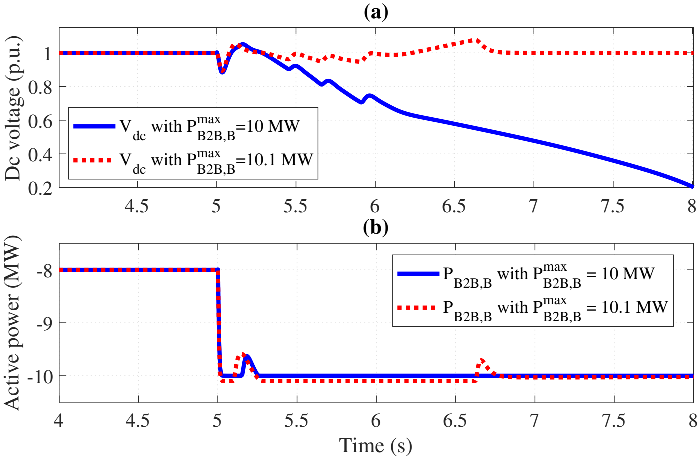

Figure 5.8: Island transition of industrial microgrid at $t = 5$ s corresponding to scenario 2 using 10 MW and 10.1 MW as a maximum active power limit for B2B converter Port B: (a) B2B converter dc-link voltage, (b) electric power of B2B converter Port B.

5.5 Summary

In this chapter, the sizing and control of a B2B converter for interconnecting two adjacent microgrids are developed to provide a set of functions, without resorting to additional investment in energy storage systems. The key factors determining the MW and MVAr sizing of the B2B converter consists of peak net load reduction, voltage quality requirement, as well as secure island transition requirement.

The sizing of the B2B converter MW capacity for peak net load reduction is based on steady-state analysis using simple power balance equations. Whereas, the size needed to facilitate a frequency-secure island transition is based on simple dynamic power balance equations. Those equations only account for the fast acting flexibility resources and exclude slower ones such as the HPP.

The analysis illustrates that by value stacking grid-connected and island-operation functions, this can result in better utilization of the B2B converter. For example, the MW capacity of the B2B converter needed to reduce the peak net load may be sufficient to satisfy a frequency-secure island transi-

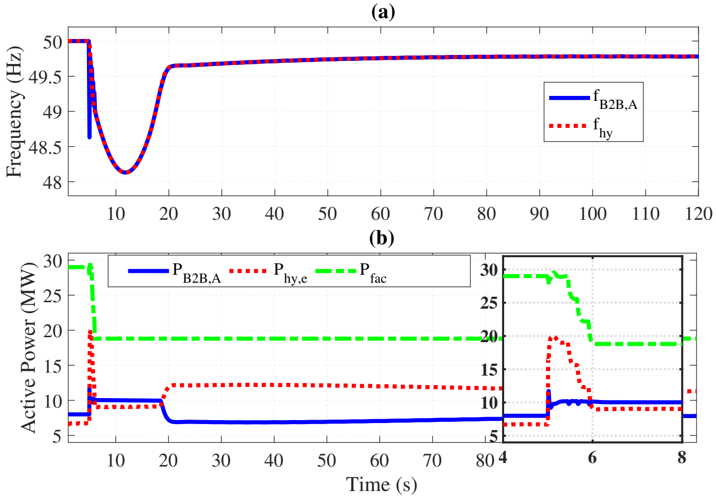

Figure 5.9: Island transition of industrial microgrid at $t = 5$ s corresponding to scenario 2 using 10.1 MW as a maximum active power limit for B2B converter Port B: (a) frequency of B2B converter Port A and hydro, (b) electric power of B2B converter Port A and hydro, and factory demand.

tion. However, an additional size of the B2B converter may be needed if the secure island transition function works 100% of the time. Furthermore, if the microgird is equipped with under-frequency load shedding, this may reduce the required size of the B2B converter to fulfill a frequency-secure island transition.

A dynamic simulation analysis is performed to verify the size of the B2B converter in performing a frequency-secure island transition. The B2B converter utilizes a frequency controller based on a high-pass filter, which is effective in assisting slower ramping hydro turbines. Notable observation from the dynamic analysis is that the converter that controls the dc-link voltage needs to have a slightly larger MW rating than the other one of the B2B converter without losing control over the dc-link voltage.

The MVAr sizing of the B2B converter is based on the grid code requirement for generators specifying the required reactive capability. To comply with the grid code, the B2B converter is designed with a rated power factor of

0.95. The MVAr rating of the B2B converter is verified by monitoring the voltage quality at the B2B converter terminals during the grid-connected mode and in the island transition. The analysis shows that the voltage is within acceptable range in all operation modes. However, further analysis is needed to understand the voltage stability of an industrial microgrid during island transition. This will be investigated in Chapter 6.

In future work, additional analysis is needed to understand if adjustments are needed in the size and control of the B2B converter to provide a secure island transition to the other community microgrid. Furthermore, future research can also focus on integrating local resources and loads that rely on power electronics with the interconnection link to form an MPC. The size and control of the MPC is more complicated than that of the B2B converter and requires further research.

CHAPTER 6

Assessment of the voltage stability of hydro-powered industrial microgrid during island transition

This chapter is an extension of the work done in Chapter 3 on the island contingency of a hydro-powered microgrid. While Chapter 3 has focused on the frequency security constraints for a successful island transition, this chapter gives more emphasis to the voltage security constraints.

6.1 Introduction

The severity of an unplanned islanding event depends mainly on the pre-islanding active and reactive power exchange with the grid. A larger power exchange may lead to faster frequency and voltage deviations, especially in microgrids with a high penetration of inverter-interfaced resources characterized by lower inertia and short-circuit power. If frequency and voltage deviations are excessive, this can lead to the tripping of local generators and critical loads. Therefore, the protection settings of local generators and critical loads must be taken into account when establishing a criterion for a successful island transition.

Various criteria for successful island transition are adopted in the literature [100]–[103]. In [100], the microgrid is modeled as an equivalent swing equation where only frequency security constraints are accounted for in the criterion for successful island transition according to the IEEE Std C37.117-2007 standard [104]. In [101], the successful island transition criterion is based on the voltage and frequency ride-through requirements for generators in Europe, the so-called RfG [97]. The criterion is assessed by comparing the dynamic voltage and frequency of each generator in the microgrid during the island transition with the ride-through characteristics. In [102], the criterion for a successful island transition is based on the frequency and voltage ride characteristics of distributed generators according to the IEEE standard Std 1547-2018 [27]. The authors in [102] adopt less stringent ride-through requirements during the island transition compared to grid-connected operation. The criterion is also assessed according to each individual generator. In [103], two documents are used to establish the criterion for a successful island transition. The first is the local requirement for the quality of the power supply, and the second is the ride-through characteristics of distributed energy resources based on IEEE Std. 1547-2018. The authors in [103] conclude that the latter criterion is more stringent than the former. Thus, it is used as a criterion for assessment. However, the assessment of a successful island transition is performed at the microgrid PCC. Although previous publications account for the ride-through characteristics of generators, the requirement on quality of power supply for loads is left out. Therefore, one of the focuses of this chapter is to establish a more holistic island transition criterion that accounts for both the ride-through requirements of generators and requirements on quality of power supply for critical loads. Moreover, the criterion is assessed at the point of connection (POC) of each individual generator and load instead of being evaluated only at the microgrid PCC.

In case the criterion set for successful island transition is not fulfilled, the microgrid operator may need to invest in improving the inertia and/or the short circuit capacity, or to invest in a faster frequency and/or voltage control. The design of a BESS frequency controller to meet the frequency security constraints has been addressed in Chapter 3. This chapter focuses on reactive power compensation to meet voltage security constraints. In [105], the authors investigate the ability of static synchronous compensator (STATCOM) and static VAR compensator to improve the recovery of the voltage of the Galapagos islands dominated by induction motor when subjected to short circuit. It is demonstrated that STATCOM outperforms the static VAR compensator in improving the voltage recovery because of its better dynamic response. In addition, the paper illustrates that the compensator should be installed as close as possible to the load center for better effectiveness. In [106], the authors propose a voltage support strategy for the PV plant in an islanded microgrid with a low X/R ratio using both active and reactive current injection. The paper demonstrates that the thermal capacity of the PV can be utilized more effectively in improving the recovery of voltage after a fault with the injection of active and reactive currents. In [107], the authors demonstrate the ability of STATCOM to improve voltage stability during a fault-triggered islanding event. The results show that by installing the STATCOM close to the load, it is able to reduce the voltage dip during a fault and damp the post-fault voltage oscillations. However, the previous literature do not account for the regulations on power exchange between the microgrid and the main grid, despite being a critical factor in island contingency analysis. Therefore, this chapter accounts for local DSO regulations that specify the amount of allowed power exchange with the grid. Impact analysis is performed on the location of the point of applicability (POA) of the reactive power requirement, whether it is at the microgrid PCC or at the POC of local generators and loads.

To overcome the short-comings in the literature, this chapter first develops a criterion for successful island transition that not only accounts for the performance requirements of distributed generators, but also for the load requirements on quality of power supply. This chapter then determines the maximum allowed reactive power exchange with the grid if the microgrid is connected to regional grid. Upon that, the effectiveness of various reactive power compensators is evaluated to meet the criterion for a successful island transition under one of the worst operational scenarios for island transition when the microgrid initially imports maximum reactive power. As a test system, this chapter modifies the hydro-powered industrial microgrid used in Chapter 3, to make the microgrid electrically weaker. The contributions of this work include the following:

- Establishing a criterion for successful island transition that accounts for both ride through requirements of generators and quality of power supply for critical loads,
- Investigating the impact of the location of the POA for reactive power

requirement, whether it is at the PCC of the microgrid or the POC of HPP and factory load.

6.2 Criterion for successful island transition

An island transition is deemed successful if critical facilities are not interrupted and distributed generators are not disconnected. Therefore, this section establishes a criterion for a successful island transition by reviewing the following items: 1) power quality standards/requirements for electricity supply, 2) generator connection codes, and 3) load connection codes.

6.2.1 Power quality requirement

The DSO is responsible for delivering an acceptable power quality to the costumers connected to their network as per the regulations set forth by the energy market inspectorate. The regulations specify the criteria for acceptable voltage waveform, including waveform frequency, magnitude, harmonic distortion and symmetry. However, for microgrids operating temporarily in island operation mode, the power quality requirements are either jointly determined by the microgrid operator and microgrid users [108], [109], or similar requirements to the grid connected operation are adopted [110], [111]. Due to the lack of standardized power quality regulations for island operation mode, this section will focus on reviewing power quality regulations for grid-connected mode and assume that the same regulations apply under the island operation mode.

In grid connected mode, the power quality of the microgrid is maintained by the relevant system operator according to the requirements set forth by the EIFS 2023:3 Energy Market Inspectorate [11]. The EIFS 2023:3 is a Swedish grid code and is derived from the European standard EN50160 [23]. Figure 6.1 provides an overview of the EN50160 power quality standard. The power quality is classified on the basis of the phenomena into continuous phenomena and voltage events. Continuous phenomena involve deviations that occur continuously over time, such as those due to the load pattern or the non-linearity of the load. Voltage events are sudden and significant changes in the voltage waveform due to unpredictable events such as faults. As this chapter focuses on analyzing dynamic performance of microgrid during island transition, the requirements on short-term voltage and frequency events are of particular interest.

Figure 6.2 shows the acceptable slow (continuous) and short-term voltage and frequency deviations according to the European standard EN50160 and the Swedish grid code EIFS 2023:3 [11], [23]. According to the figure, the relevant system operator has the obligation of maintaining the voltage and frequency at the connection point of the customers within the ranges [0.9, 1.1] p.u. and [49, 51] Hz, respectively. The voltage is typically regulated by the relevant DSO, while the frequency is maintained by the Transmission System Operator (TSO). Excessive deviations are allowed for a short time.

As this chapter focuses on island contingencies caused by a short-circuit in the grid, more emphasis is placed on the short-term voltage dip requirements, illustrated in Figure 6.3 [11]. A voltage dip is considered acceptable if it has voltage-time characteristics within the green area. If the voltage dip enters the orange area, it is considered unacceptable. The buffer area between the green and orange areas may be considered acceptable depending on the agreement between the system operator and the customer. It can also be seen from the figure that the requirement is more stringent for systems with voltage level higher than 45 kV.

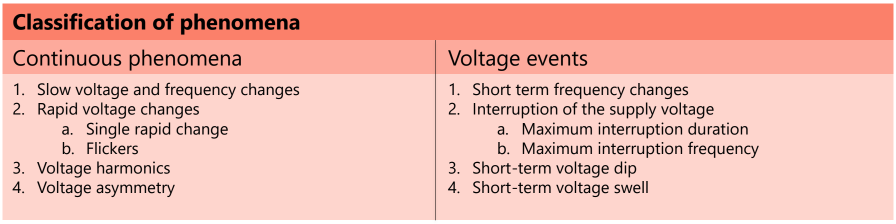

Classification of phenomena

Continuous phenomena	Voltage events
1. Slow voltage and frequency changes	1. Short term frequency changes
2. Rapid voltage changes	2. Interruption of the supply voltage
a. Single rapid change	a. Maximum interruption duration
b. Flickers	b. Maximum interruption frequency
3. Voltage harmonics	3. Short-term voltage dip
4. Voltage asymmetry	4. Short-term voltage swell

Figure 6.1: Power quality classification [23].

6.2.2 Generator connection requirement

Distributed generators must be able to ride through the island transition event, especially those providing frequency and voltage regulation to the microgrid. Due to the lack of standardized regulations on the ride-through requirements for generators operating in island mode, similar requirements are considered to the grid-connected mode. Such requirements are typically set

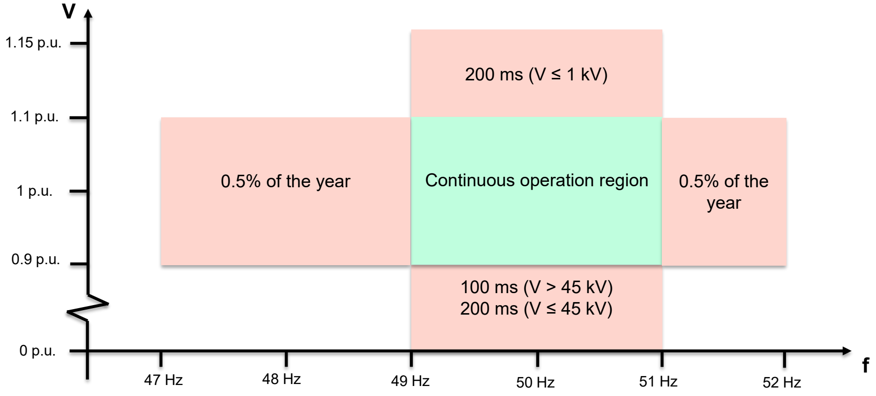

Figure 6.2: Continuous and short term acceptable voltage and frequency deviations in the Swedish distribution system [11], [23].

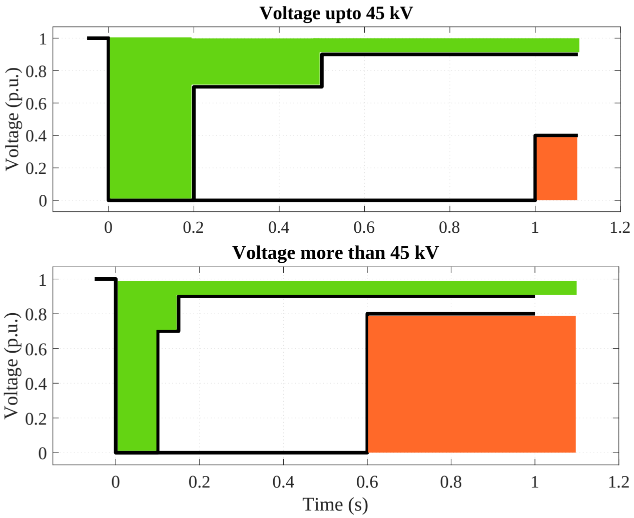

Figure 6.3: Short-term voltage dip requirements [11]: acceptable (green), unacceptable (orange), and buffer area (white).

by the European Network of Transmission System Operators for Electricity (ENTSO-e) [97]. A Swedish version of the requirement for generators (EIFS 2018:2) is regulated by the energy market inspectorate [21]. The generator requirement classifies technology-based generators as a synchronous generator (SG) and a power park module (PPM). It also classifies generators based on size and voltage level into four categories:

- Type A: $V < 110$ kV, $P^{\max} \geq 0.8$ kW
- Type B: $V < 110$ kV, $P^{\max} \geq 1.5$ MW
- Type C: $V < 110$ kV, $P^{\max} \geq 10$ MW
- Type D: $V < 110$ kV, $P^{\max} \geq 30$ MW or $V \geq 110$ kV

Figure 6.4 gives an overview of the Swedish requirement for generator EIFS 2018:2. The requirement indicates the voltage and frequency ranges during which a generator must remain connected infinitely (continuous operation region), and those where a generator must be able to ride through for a temporary time duration. Additionally, generators of all types are required to ride through a RoCoF event of up to 2 Hz/s. Depending on the type of generator, voltage and frequency regulation functions may also be required. Those functions include AVR, frequency sensitive mode (FSM), limited frequency sensitive mode for under frequency (LFSM-U), and limited frequency sensitive mode for over frequency (LFSM-O). Note that the behavior of the generator during simultaneous over/under-voltage and over/under-frequency, indicated with the white areas, is not explained in the grid code EIFS 2018:2.

When comparing the requirements for generators illustrated in Figure 6.4 with the requirements on quality of power supply illustrated in Figure 6.2, a clear miscoordination is observed. First, the quality of power supply declares a continuous operating time in the voltage range [1.05, 1.1] p.u., while in this same voltage range, generators are only required to ride through for a limited amount of time according to EIFS 2018:2. Moreover, generators are not obliged to remain connected to the network if the frequency is outside the range [47.5, 51.5] Hz, whereas power quality requirements allow a wider range of frequency deviation [47, 52] Hz, which can lead to disconnection of some generators.

Since this chapter focuses on islanding events triggered by short circuit contingencies, an additional focus is placed on the under-voltage ride-through

(UVRT) requirements, which is illustrated in Figure 6.5. The UVRT requirements show the voltage-time characteristics that the respective generator has to ride through during a voltage dip. PPMs must endure low voltage for a longer duration than SGs, and larger generators must also withstand lower voltage for a longer time than small generators.

Generators type C and D are required to have reactive capability, which is illustrated in Figure 6.6 (this does not apply for generators type A and B). Although the reactive capability in the EIFS 2018:2 grid code is linearly proportional to the active power (triangular shape) [21], the compliance test performed by Svenska Kraftnät (SvK) assumes a reactive capability that is a function of the maximum active power (square shape) [112], [113]. For PPMs, this reactive capability is symmetrical, while it is non-symmetrical for SGs with the requirement on reactive power injection being larger than consumption. Reactive capability should be available to the system operator at the POC (high-voltage (HV) side of the transformer).

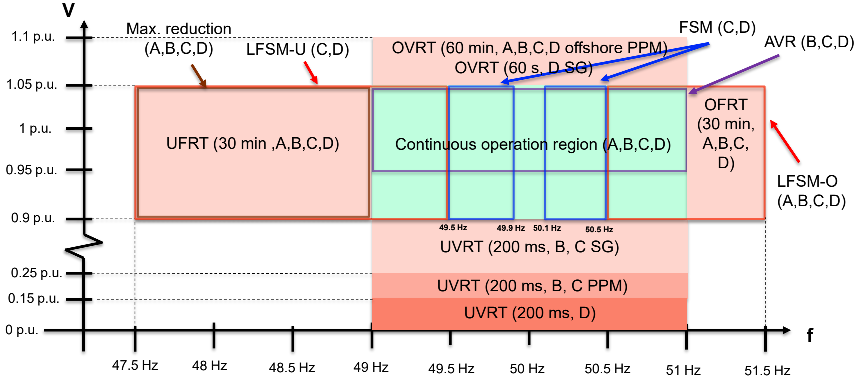

Figure 6.4: Overview of generator connection requirement EIFS 2018:2 [21]. The acronyms in the figure are: under and over frequency ride through (UFRT and OFRT), under and over voltage ride through (UVRT and OVRT), frequency sensitive mode (FSM), limited frequency sensitive mode for under and over frequency (LFSM-U and LFSM-O), automatic voltage regulation (AVR), maximum reduction capability (Max. reduction).

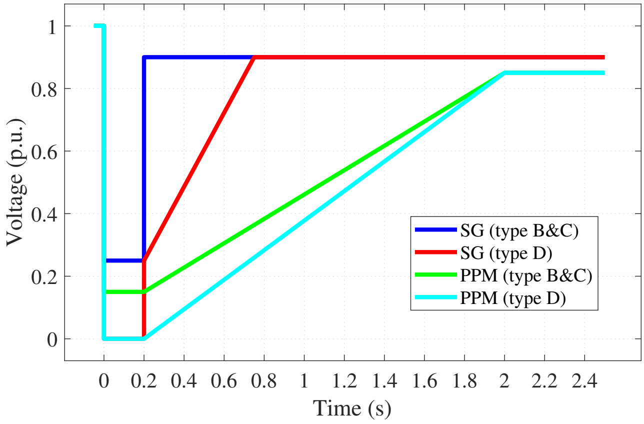

Figure 6.5: Fault ride through requirements [21].

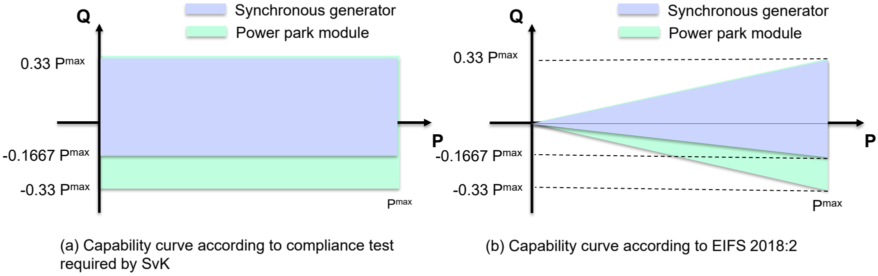

(a) Capability curve according to compliance test required by SvK

(b) Capability curve according to EIFS 2018:2

Figure 6.6: Reactive capability requirements for generators of type C and D [21], [112], [113].

6.2.3 Demand connection requirement

The Demand Connection Code (DCC) establishes requirements for the connection of demands in order to ensure the security of the power system. The DCC is issued by the ENSTO-e [114]. Sweden has its own version of the DCC EIFS 2019:6 [22], which is maintained by the energy market inspectorate. The demand connection code is binding for the following demand categories:

A Transmission-connected demand facilities,

B Transmission-connected distribution facility,

C Distribution systems, including new closed distribution systems,

D Demand units used to provide demand response services,

where a demand facility is a facility that consumes electrical energy, and a demand unit is a sub-installation of a demand facility that can be controlled to provide grid services. Transmission-connected distribution facility is a distribution system connection or the electrical plant and equipment used at the connection of the transmission system. A closed distribution system is a distribution system that distributes electricity within a geographically confined industrial, commercial, or shared services site and does not supply household customers, without prejudice to incidental use by a small number of households located within the area served by the system and with employment or similar associations with the owner of the system.

The connection code covers the following requirements: continuous operation range, ride through capability, permissible PF, permissible harmonic distortion, control and protection requirements. The connection code provides a standardized requirement for the first three items while it leaves the remaining items to individual agreements.

Figure 6.7 shows the frequency and voltage ranges under which a load must remain connected continuously, and that during which the load must ride through shortly [22]. The requirement is quite similar to the generation connection code shown in Figure 6.4 except in the following points:

- This requirement do not emphasis the under voltage ride through requirement,
- Demands, unlike generators, are not required to provide frequency and voltage regulation functions.

In addition to the ability of the demand units to remain connected during situations of excessive over- and under-frequency events, demand units of category D are expected also to tolerate a RoCoF of up to 2 Hz/s. Due to the lack of coordination between the DCC and the power quality requirements illustrated in Figure 6.2, unwanted demand tripping can occur. This is especially the case when operating in the voltage range [1.05, 1.1] p.u. and the frequency ranges [47, 47.5] Hz and [51.5, 52] Hz. This emphasizes the need for better coordination between the two requirements.

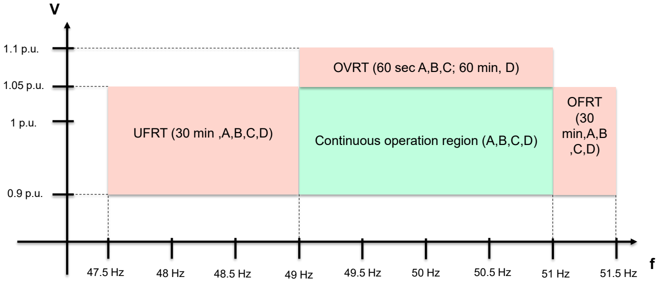

Figure 6.7: Frequency and voltage ranges under which a demand of category A, B, C or D must remain connected to the grid [22].

Demand categories A, B and C must also maintain their reactive power exchange with the grid within 48% of the maximum import or export capacities [114]. This corresponds to a PF of 0.9. There is no requirement for the reactive power range of demand category D. However, if demand category D is connected to a distribution network, it will have to adhere to the reactive power requirements of the relevant DSO. An example of such a requirement for demands connected to Vattenfall's network is provided in Table 6.1. The amount of free reactive power is subject to the tariff level which is illustrated in Figure 6.8.

6.2.4 Selected criterion for successful island transition

Since this chapter focuses on the voltage stability of the microgrid during a short-circuit-triggered islanding, the selected criterion for a successful island transition focuses on voltage security constraints. For the island transition to be successful, both distributed generators and critical loads have to

Table 6.1: Vattenfall's customer free reactive power by tariff level. The reactive power is expressed in percentage with respect to active power subscription except for tariff level T0 [115].

Customer tariff level	Free reactive power withdrawal	Free reactive power input
T0	15 MVAr	15 MVAr
L1 or T13	15%	5%
T1 or T12	25%	10%
L2 or T2	50%	15%

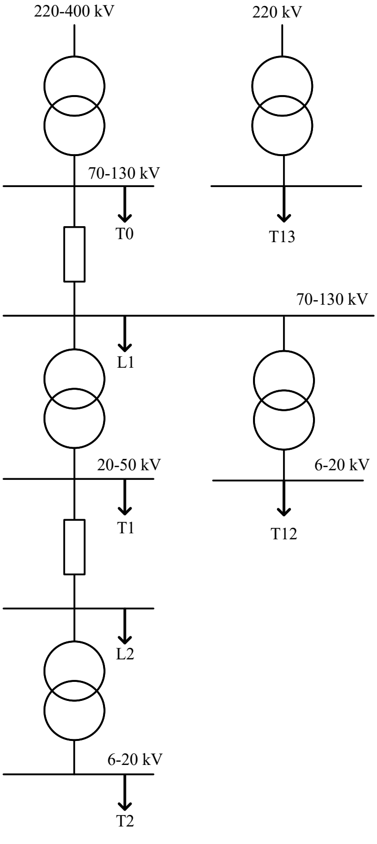

Figure 6.8: Vattenfall's segmented tariff structure [115].

ride-through the islanding incident. Distributed generators must meet the fault-ride requirements of the generators illustrated earlier in Figure 6.5. Additionally, critical load facilities must withstand a short-term voltage dip given by the characteristic in Figure 6.3.

6.3 Description of investigated hydro-powered industrial microgrid

6.3.1 Microgrid network diagram

Figure 6.9 shows the microgrid network diagram used for island contingency analysis in this chapter. The network diagram is modified with respect to the system investigated in Chapter 3. Modifications are made such that the microgrid is realistically weak to make voltage stability analysis more insightful. The modifications made are as follows:

- Instead of the load and generator being directly connected to the substation, an electrical distance have been introduced,
- The voltage level is changed from 140 kV to 44 kV which is also a common voltage level for this microgrid rating. The 44 kV grid usually has a lower short circuit capacity than the 140 kV grid, and has a higher tendency to have voltage-related issues,
- The load facility has its own tap-changing transformer to regulate the voltage at the MV side of the load to 1 p.u.,
- A more realistic industrial load model is implemented for voltage stability studies.

The parameters of the network diagram can be found in the appendix in Table D.2.

6.3.2 Hydropower plant control and tuning

The HPP is equipped with a governor and an AVR for frequency and voltage control, respectively. The governor model was illustrated in Chapter 3. The

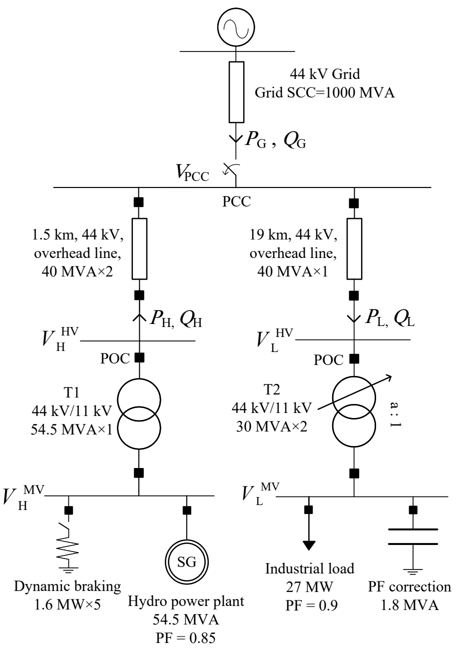

Figure 6.9: Microgrid network diagram for island contingency analysis.

AVR and exciter models are illustrated in Figure 6.10. The AVR is implemented as a standard PI controller with a static exciter model, typically used in the Nordic 32 power system model [79]. The AVR is set to control the MV side of the transformer without implementing any reactive droop. The AVR tuning account for the Swedish grid code requirement for generators EIFS 2018:2 [21]. The Swedish grid code states that when changing the reference voltage stepwise from 0.95 p.u. to 1.05 p.u., the voltage response should have a rise time of not more than 1 second (measured from 0% to 90%), and an overshoot of not more than 15%. The rise time requirement imposes a minimum limit on the voltage control loop bandwidth, whereas the overshoot requirement sets a maximum limit (see Figure 6.11). This requirement is tested when the generator is in idle operation mode. In the remainder of this chapter, the fast control illustrated in Figure 6.11 is adopted. The corresponding tuning of the AVR and the exciter parameters is summarized in the appendix in Table D.4.

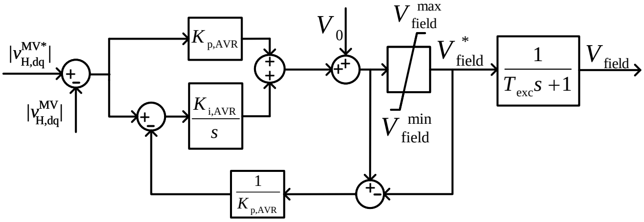

Figure 6.10: Hydropower plant AVR and exciter model.

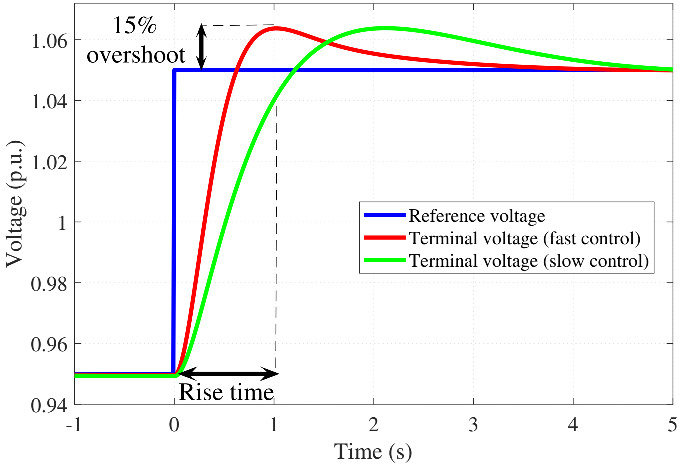

Figure 6.11: AVR step response in idle operation mode.

6.3.3 Industrial load model

The investigated industrial load has the load composition shown in Table 6.2 [116]. The industrial load is mainly composed of motors by 76%, with 20% small motors and 56% large motors. Small motors have a lower PF of 0.86

compared to 0.89 for large motors. The industrial load is also composed of 19% lighting loads with a 0.9 PF and 5% resistive loads with a unity PF. The motors are modeled using a typical dynamic model of an induction motor found in [117]. This is a conservative assumption since most industries will have a certain percentage of their motors connected via variable frequency drives. The lighting and resistive loads are modeled using the constant impedance, constant current, and constant power load model, or the so-called ZIP model found in [118]. The steady state active and reactive powers of the ZIP load model are given by:

$$P_{\mathrm{ZIP}} = P_{\mathrm{n}} \left(p_1 \left(\frac{V}{V_{\mathrm{n}}} \right)^2 + p_2 \left(\frac{V}{V_{\mathrm{n}}} \right) + p_3 \right), \tag{6.1}$$

$$Q_{\mathrm{ZIP}} = Q_{\mathrm{n}} \left(q_1 \left(\frac{V}{V_{\mathrm{n}}} \right)^2 + q_2 \left(\frac{V}{V_{\mathrm{n}}} \right) + q_3 \right), \tag{6.2}$$

where the coefficients p_1, p_2, and p_3 and q_1, q_2, and q_3 define the proportion of each load component. The parameters of the different load components are listed in the appendix in Table D.6.

Figure 6.12 shows the control diagram of the ZIP model. The ZIP load is represented as a current source where the reference currents are calculated based on the terminal voltage to achieve the ZIP characteristics described in (6.1) and (6.2). The reference currents are low-pass filtered with a first-order 5 Hz filter before being injected to the grid. This ensures that the model is stable. Note that the constant current and constant power characteristics are only valid for terminal voltages above 0.7 p.u. If the voltage is lower than or equal to 0.7 p.u., the model behaves as a constant impedance instead. This also ensures the stability of the model during short-circuit analysis. A PLL is needed to estimate the terminal voltage angle in order to decouple active and reactive currents. The PLL is based on a PI controller as in [119] and has a bandwidth of 5 Hz. The PLL is frozen for low voltages below 0.8 p.u. since the voltage may be too low to be tracked by the PLL.

6.3.4 Non-critical load shedding and dynamic braking

As illustrated in Section 6.3.3, the industrial load model is predominantly composed of directly connected induction motors. These motors may draw a

Table 6.2: Load composition of industrial facility [116].

Load component	Percentage	Power factor	Model
Small motors	20%	0.86	Directly connected induction motor
Large motors	56%	0.89	Directly connected induction motor
Lighting	19%	0.90	ZIP model
Resistive loads	5%	1.0	ZIP model

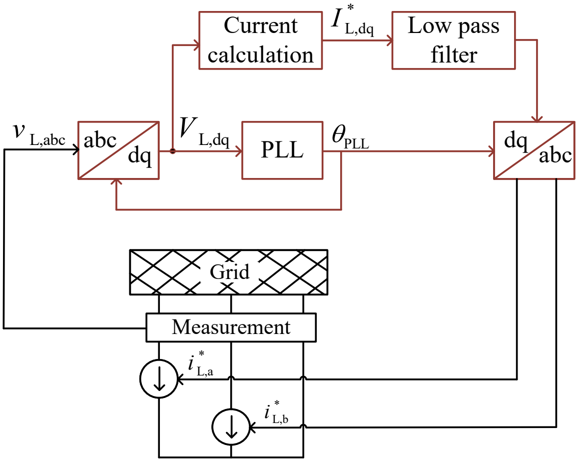

Figure 6.12: ZIP load control diagram.

large reactive current to re-establish their magnetic field when the microgrid is islanded from a faulty grid. Such a large reactive current may cause voltage collapse, especially in an islanded microgrid that is relatively weaker compared to the grid-connected mode. Therefore, the microgrid operator may need to invest in increasing the strength of the microgrid in island mode. Different technologies to improve the strength of the microgrid are investigated later in Section 6.5. Some of the motors that are not critical to the industrial facility may be disconnected upon the detection of the islanding event. This will reduce the reactive current burden and increase the chance of survival of the remaining load.

In this chapter, it is assumed that 45% of the motors are non-critical demands. Thus, they are tripped simultaneously when the microgrid tie-line breaker is opened. However, this percentage of the load being tripped at once is quite large and may result in a severe over-frequency of the HPP. Therefore, a dynamic braking using electrical resistors is used to dissipate the excessive HPP power [118]. The resistors are installed at the HPP terminal as shown in Figure 6.9 and are connected in steps according to the frequency level, as illustrated in Table 6.3. Each connected resistor has a rated power of 3% with respect to the HPP rating. This is to avoid a sudden big change of power at the HPP terminal which may result in a severe under-frequency event.

Table 6.3: Frequency activation level of dynamic braking using electrical resistors. The activation is performed in steps with each step being equal to 3% of the HPP rated power.

Activating frequency (Hz)	50.5	50.7	50.9	51.1	51.3
Step change	3%	3%	3%	3%	3%

6.4 Island contingency study of hydro-powered industrial microgrid

6.4.1 Investigated scenarios

The investigated scenarios for island contingency of hydro-powered microgrid are presented in Table 6.4. The aim of this investigation is to highlight key factors for the successful island transition of hydro-powered industrial microgrid.

The investigated factors include:

- POA of reactive power requirement,
- Percentage of online HPP capacity,
- Line characteristics.

The investigated scenarios are elaborated further in the subsequent sections.

Table 6.4: Investigated scenarios for island contingency of hydro-powered industrial microgrid.

Scenario	POA of reactive power requirement	Power exchange with the grid	Percentage of online HPP capacity	Line characteristics
Base case	At the PCC of the microgrid	Maximum reactive power import	100%	Overhead line
Scenario 1	**At the POC of HPP and industrial load**	Maximum reactive power import	100%	Overhead line
Scenario 2	At the PCC of the microgrid	Maximum reactive power import	**70%**	Overhead line
Scenario 3	At the PCC of the microgrid	Maximum reactive power import	100%	**Cable**

6.4.1.1 Point of applicability of reactive power requirement

The initial reactive power exchange between the microgrid and the upstream distribution grid has a vital impact on the subsequent voltage dynamics of the microgrid during the island transition. This reactive power exchange is regulated by the DSO. The DSO can regulate the reactive power either at the PCC of the microgrid or at the POC of each of the HPP and the industrial load.

An operating envelope is used to depict the feasible range of active and reactive powers at the interface between a customer and the system operator. Figure 6.13 (a) shows the operating envelope of the microgrid, indicating all feasible active and reactive power operating points at the PCC of the microgrid (denoted by P_G and Q_G in Figure 6.9). The reference power direction is into the microgrid with positive power values indicating power import. It can be seen that the allowed operating range for reactive power exchange at the PCC of the microgrid is smaller if the reactive power requirement is imposed at the PCC of the microgrid instead of at the POC of the HPP and industrial load.

If the reactive power requirement is imposed at the PCC, then the entire microgrid is treated as a single customer. Assuming that the microgrid is a customer of Vattenfall's network, the microgrid would then fall under the tariff level called L2, with a corresponding amount of free reactive power withdrawal and injection of 50% and 15%, respectively (see Table 6.1). The percentages are with respect to annual active power subscription. This explains why the limit for reactive power export -3.6 MVAr is much less than that for reactive power import 12.0 MVAr.

If the reactive power requirement is imposed at the POC, then the microgrid is no longer treated as a single customer. The reactive power requirement of the microgrid in this case is a function of the individual operating envelopes of the HPP and the industrial load. The HPP operating envelope follows the SvK generator compliance test (see Section 6.2.2), as shown in Figure 6.13 (b). The operating envelope of the load is shown on the same figure and follows the requirements set forth in the DCC (see Section 6.2.3). Positive power values correspond to power injection for the HPP and power absorption for the load, and vice versa. If the load is operating at its minimum PF, i.e., consuming 13.0 MVAr, and simultaneously the HPP is operating at its maximum under-excitation, i.e., absorbing 7.7 MVAr, then the microgrid would import 20.7 MVAr, as illustrated in the microgrid operating envelope in Figure 6.13 (a). On the other hand, if the load operates at a unity PF, and simultaneously the HPP injects the maximum reactive power, then the microgrid would export 15.4 MVAr to the upstream grid, as illustrated in the microgrid operating envelope shown in Figure 6.13 (a). Note that this analysis neglects the losses in the internal lines of the microgrid.

The active power subscription of the microgrid is assumed to be symmetric in the export and import directions, with a corresponding value of 24 MW, as illustrated in Figure 6.13 (a). The value of the active power subscription is obtained by taking the maximum active power exchange between the microgrid and the upstream grid from historical measurements (see Figure 3.6). This value remains unchanged and is independent of the POA of the reactive power requirement.

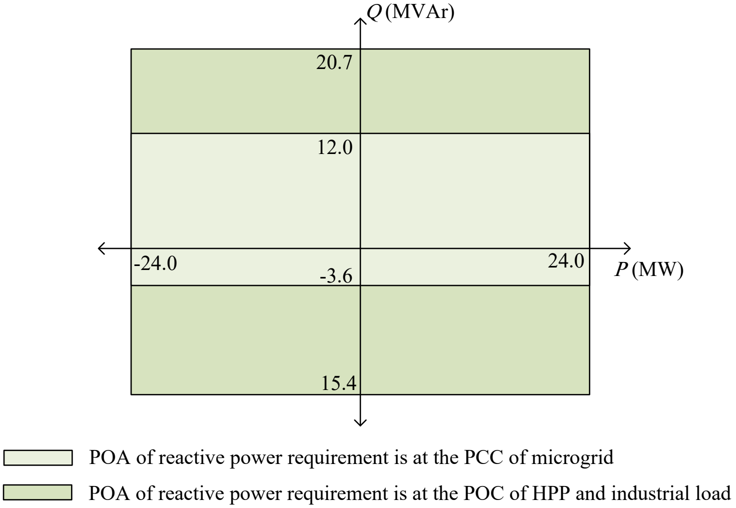

(a) Microgrid operating envelope

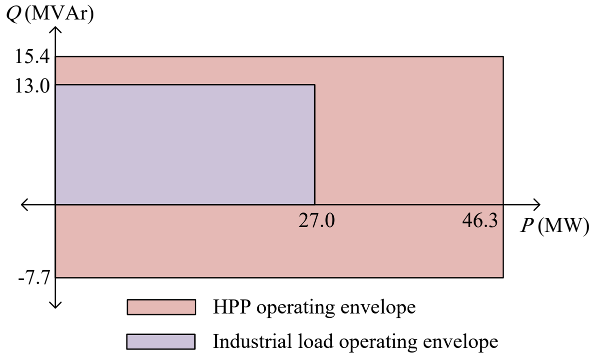

(b) HPP and industrial load operating envelopes

Figure 6.13: (a) Microgrid operating envelope indicating all the possible static operating points of active and reactive powers at the PCC of the microgrid (denoted by P_{G} and Q_{G} in Figure 6.9). Positive power values correspond to power import, and vice versa. (b) HPP and industrial load operating envelopes indicating all the possible static operating points of active and reactive powers (denoted by P_{H}, Q_{H}, P_{L}, and Q_{L} in Figure 6.9). Positive power values correspond to power injection for the HPP and power absorption for the load, and vice versa.

6.4.1.2 Power exchange with the grid

Chapter 3 has analyzed the frequency stability of the microgrid during the island transition when it is initially importing a significant amount of active power. As this chapter focuses on the voltage stability of the microgrid during island transition, it only accounts for scenarios where the initial power exchange between the microgrid and the upstream grid is highly reactive. The operating envelope of the microgrid in Figure 6.13 (a) shows that the microgrid has a larger margin for the import of reactive power than the export. Therefore, this chapter focuses on scenarios with the maximum import of reactive power before islanding, which is 12.0 MVAr if the reactive power requirement is imposed at the PCC and 20.7 MVAr if it is at the HPP and industrial load POC.

6.4.1.3 Online hydropower plant capacity

Another critical factor for island contingency analysis is the online HPP capacity. The HPP operator may decide to take some generators off-line for various technical or economical reasons. If the remaining hydro generators do not have sufficient capacity to meet the load in post islanding steady state condition, islanding may not be possible. Therefore, the analysis in this chapter accounts for the scenarios in which the online generators are 100% or 70% of full HPP capacity.

6.4.1.4 Line characteristics

Parts of the MV network in Sweden is an underground network. Therefore, it is relevant to compare the microgrid dynamics when the microgrid 44 kV network is made of overhead lines or cables. Table 6.5 lists the overhead line and cable parameters used in this study [120]. The main difference is that the cable has lesser inductance per km (by three times), and significantly larger capacitance (by twenty four times).

Table 6.5: Parameters of overhead line and cable [120].

	L	C	R	G
Overhead line	1.15 mH/km	0.01 μF/km	0.1436 Ω/km	0 S/km
Cable	0.36 mH/km	0.24 μF/km	0.1 Ω/km	0 S/km

6.4.2 Base case scenario

The base case scenario illustrated earlier in Table 6.4 is characterized by 100% online HPP capacity, overhead lines, and maximum reactive power import where the POA of the reactive power requirement is at the PCC. Table 6.6 shows the initial power flow of the microgrid before islanding. Refer to the network diagram in Figure 6.9 for location of the measurement and reference power direction. The microgrid initially imports the maximum reactive power of 12 MVAr according to microgrid operating envelope in Figure 6.13. The imported reactive power is not sufficient to meet the reactive power demand of the industrial facility of 13 MVAr, not mentioning the reactive demand of the local lines. Therefore, the HPP injects an additional reactive power of 5 MVAr to account for the missing reactive power to achieve power balance. Due to the heavy loading of the factory, the voltage received at its 44 kV side is quite low at 0.90 p.u. However, the tap-changing transformer raises the voltage at the 11 kV side to 1.00 p.u. HPP generates an active power of 27 MW, matching with the industrial load demand, which limits the active power import from the grid to only 1.7 MW (power losses). Therefore, the power exchange between the microgrid and the upstream grid is mainly reactive.

Table 6.6: Microgrid initial power flow before islanding (base case scenario). Refer to Figure 5.9 for location of the measurement and reference power direction.

Grid	P_{G}	1.7 MW	HPP	P_{H}	27 MW
	Q_{G}	12 MVAr		Q_{H}	5 MVAr
	V_{PCC}	1.00 p.u.		$V_{\mathrm{H}}^{\mathrm{MV}}$	1.02 p.u.
Load	P_{L}	27 MW		$V_{\mathrm{H}}^{\mathrm{HV}}$	1.00 p.u.
	Q_{L}	13 MVAr		E_{H}	1.26 p.u.
	$V_{\mathrm{L}}^{\mathrm{MV}}$	1.00 p.u.			
	$V_{\mathrm{L}}^{\mathrm{HV}}$	0.90 p.u.			
	a	0.8750			

The hydro-powered industrial microgrid is modeled in Matlab/Simulink and simulated by electromagnatic transient (EMT) simulations. Figure 6.14 shows the dynamic simulation results when applying a three-phase bolted fault to the microgrid PCC at t = 1 s. Immediately after the fault, both active and reactive powers of the industrial facility experience a negative surge, i.e. the load acts transiently as a generator. This is because the back EMF voltage of the motors is larger than the terminal voltage. However, after 100 ms, when the magnetic energy stored in the air gap of the motors has decayed, the active and reactive powers tend to zero. In addition, the kinetic energy stored in the rotating masses of the motors also decays. This occurs because of the absence of input electrical power which causes the motors to de-accelerating under the power of the mechanical load. Small motors deaccelerate faster than large motors because of their lower inertia constant.

At t = 1.1 s, the microgrid is islanded from the main grid by opening the microgrid tie-line breaker. The voltage of the microgrid is now regulated by the HPP. The industrial facility is re-magnetized by the HPP, which results in a positive surge in the active and reactive powers of the industrial facility. This surge in power lasts for 100 ms (up to t = 1.2 s), which is the time needed to establish the magnetic field. After the electro-magnetic dynamics have dissipated at t = 1.2 s, the industrial facility still draws a large amount of reactive power (21 MVAr!). This is due to the characteristics of the induction motor, which draws a larger reactive power when operating at lower speeds. Due to the large reactive power demand and the weaker system in island operation, the voltage at the industrial facility is quite low at 0.74 p.u. As a consequence of the low voltage, the electro-magnetic torque was not recovered fully, with only 13 MW of active power being consumed. However, the active power was sufficient to re-accelerate the motors, with small motor re-accelerating at t = 1.2 s and large motors at t = 1.25 s. This is due to the characteristics of the mechanical load with its torque being proportional to the square of the speed. Thus, at lower speed, less electrical power is needed to re-accelerate the motors. As motors begin to regain their speed, the reactive power consumption is reduced. Therefore, the voltage at the industrial facility starts to gradually increase and the active power is recovered. Note that the speed of small and large motors have not reached steady state and their over-speed is caused by the HPP experiencing an over-frequency (not shown here).

It is clear from the results that the voltage response at the terminal of the factory does not fulfill the criterion set for a successful island transition. This is very clear between times t = 1.5 s and t = 1.7 s. One of the main reasons for the slow voltage recovery is the large reactive power consumption of the industrial facility, especially during the re-acceleration phase of the motors. Furthermore, another critical factor is the reactive power capability of the HPP. The results show that the HPP hits its maximum excitation voltage limit of 4 p.u., which hinders the recovery of the voltage. Section 6.5 explores different compensation technologies to improve the voltage response to meet the criterion for a successful island transition. It should also be noted that the HPP terminal voltage (not presented here) satisfies the fault-ride-through characteristics. In fact, the HPP fault-ride-through criterion is less stringent than the short-term voltage-dip criterion of the load.

It should be noted that 45% of the motors are tripped simultaneously with opening of the microgrid tie-line breaker at t = 1.1 s (see Section 6.3.4). If all the motors remain connected in island mode, this may result in a voltage collapsing due to the large reactive demand and the weaker system in island mode. However, when tripping such a large percentage of demand at once, this results in an over-speed of the HPP, as shown in the bottom left subplot of Figure 6.14. Therefore, braking resistances are activated in steps based on the frequency deviation signal (see Section 6.3.4). In fact, the oscillation in the voltage response seen in Figure 6.14 at t = 1.6 s and t = 2.2 s is due to the switch of braking resistances.

6.4.3 Scenario 1: Impact of microgrid reactive power requirement

In the base case, the POA for the reactive power requirement was at the PCC of the microgrid. This section explores the impact of moving the POA to be at the POC of each of the HPP and the industrial facility instead. Table 6.7 shows the updated initial power flow of the microgrid. If changes have occurred with respect to the base case scenario, the new value is shown inside parentheses. The noticeable change is that the import of reactive power has doubled. This is because the microgrid operating envelope (see Figure 6.13 (a)) has a larger margin for reactive power import if the POA for reactive power requirement is at the HPP and the industrial facility POC. Keep in mind that the operating envelope in Figure 6.13 (a) does not account for the losses in the lines. Therefore, the actual import of reactive power (24.7 MVAr) is considerably higher than the one in the operating envelope (20.7 MVAr). The increased import of reactive power in Scenario 1 compared to the base case scenario is attributed to the fact that the HPP operates at its maximum limit for the absorption of reactive power of -7.7 MVAr (see the HPP operating envelope in Figure 6.13 (b)).

To establish a reference value for the strength of the microgrid in island

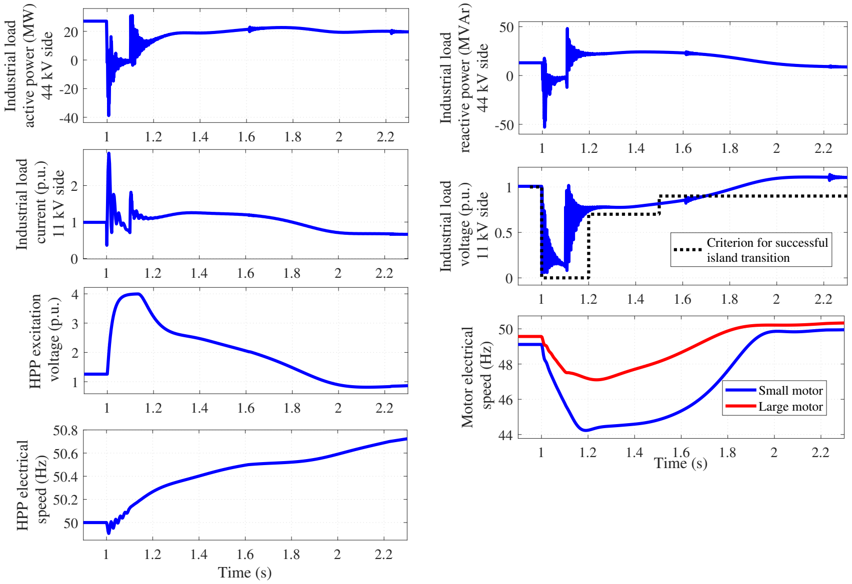

Figure 6.14: Dynamics of hydro-powered industrial microgrid when subject to a three-phase bolted fault at the PCC at t = 1 s followed by islanding at t = 1.1 s (base case scenario).

mode, the short circuit capacity is estimated as seen from the 11 kV terminal bus of the load:

$$SCC = \frac{E_{\mathrm{H}}^2}{\frac{a^2}{S_{\mathrm{b,T2}}}X_{\mathrm{T2}} + \frac{1}{S_{\mathrm{b,T1}}}X_{\mathrm{T1}} + \frac{1}{V_{\mathrm{HV}}^2}X_{\mathrm{OH}} + \frac{1}{S_{\mathrm{b,H}}}X''_{\mathrm{H}}}. \tag{6.3}$$

The parameters used in this equation and their corresponding values are explained in the appendix in Table D.2. This equation makes the assumption that the HPP impedance is equal to its subtransient impedance. Assuming that the back EMF voltage of HPP E_{H} and the tap ratio a are the same as the initial condition before islanding, the resulting short circuit capacity is 97.8 MVA, i.e., around three times the factory rating. This compares to 152 MVA in the base case, i.e., five times the factory rating. The main reason for the reduction in the SCC is the reduction in the HPP back EMF voltage from 1.26 p.u. to 1.01 p.u.

Table 6.7: Microgrid initial power flow before islanding (base case scenario vs Scenario 1). Values for Scenario 1 are presented in parenthesis if changes have occurred with respect to base case scenario.

Grid	P_{G}	1.7 MW	HPP	P_{H}	27 MW
	Q_{G}	12 MVAr (24.7 MVAr)		Q_{H}	5 MVAr (-7.7 MVAr)
	V_{PCC}	1.00 p.u.		$V_{\mathrm{H}}^{\mathrm{MV}}$	1.02 p.u. (0.99 p.u.)
Load	P_{L}	27 MW		$V_{\mathrm{H}}^{\mathrm{HV}}$	1.00 p.u.
	Q_{L}	13 MVAr		E_{H}	1.26 p.u. (1.01 p.u.)
	$V_{\mathrm{L}}^{\mathrm{MV}}$	1.00 p.u.			
	$V_{\mathrm{L}}^{\mathrm{HV}}$	0.90 p.u.			
	a	0.8750			

Figure 6.15 shows the dynamics of the microgrid when subjected to a three-phase bolted fault at the microgrid PCC at t = 1 s followed by the opening of the microgrid tie-line breaker at t = 1.1 s. The base case scenario is illustrated with solid lines and Scenario 1 with dotted lines. The results show that the voltage at the factory after islanding the microgrid has reduced in Scenario 1 compared to the base case scenario. This is because the HPP has a lower initial back EMF voltage in Scenario 1. Due to the lower voltage at the terminal of the factory, its active power consumption has reduced as well. The active power (torque) was not sufficient to re-accelerate the small motor which experiences a stall. However, the large motor was re-accelerated successfully thanks to its large inertia which protects it from stalling. Note that in practice, an under-speed protection would trip the small motor, which is not implemented here.

6.4.4 Scenario 2: Impact of online HPP capacity

This section explores the impact of online HPP capacity where online generation is reduced from 100% in the base case scenario to 70% in Scenario 2. Table 6.8 shows the updated initial power flow. If changes have occurred with respect to the base case, the new value is illustrated in parentheses. The only change in the initial conditions is that the HPP back EMF voltage and 11 kV terminal voltage has increased with respect to the base case scenario. This was done intentionally so that the HPP keeps the same reactive power output

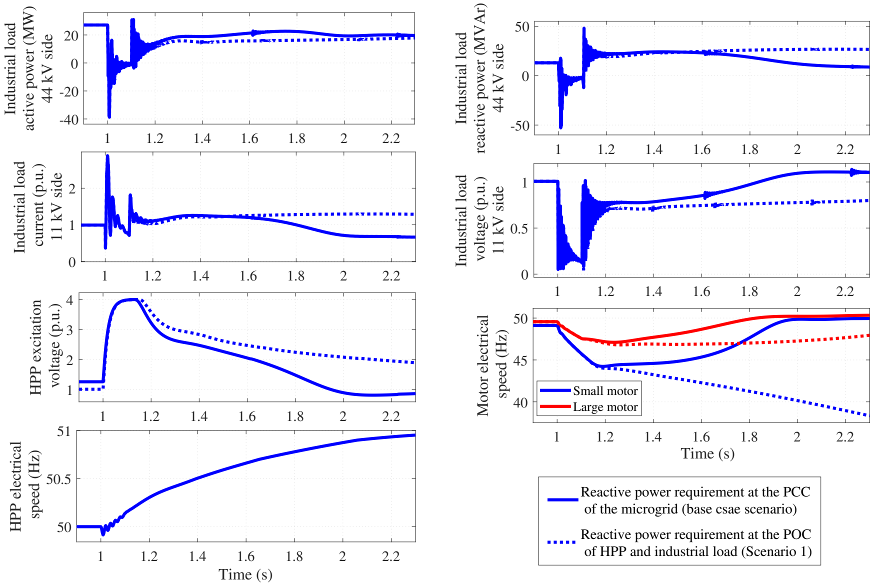

Figure 6.15: Dynamics of hydro-powered industrial microgrid when subject to a three-phase bolted fault at the PCC at t = 1 s followed by islanding at t = 1.1 s (base case scenario vs Scenario 1).

as in the base case scenario. Otherwise, the HPP would inject less reactive power, which will increase the reactive power import beyond the maximum value of 12 MVAr.

The updated SCC of the microgrid in island mode is estimated on the basis of (6.3) and is equal to 161 MVA. This is slightly higher than the base value of 152 MVA. This may be counterintuitive as the online HPP capacity has reduced. However, the reduction in online capacity is balanced by the increase in the back EMF voltage, which makes the final SCC quite similar.

Figure 6.16 shows the dynamics of the microgrid when subjected to a three-phase bolted fault at the PCC at t = 1 s, followed by opening the tie-line breaker at t = 1.1 s. The base case scenario is illustrated with solid lines and Scenario 2 with dotted lines. The results show that after opening the microgrid tie-line breaker at t = 1.1 s, the voltage at the industrial terminal is lower for Scenario 2 compared to the base case scenario. This was not expected as the estimated SCC is slightly higher for Scenario 2 than the base

Grid	P_{G}	1.7 MW	HPP	P_{H}	27 MW
	Q_{G}	12 MVAr		Q_{H}	5 MVAr
	V_{PCC}	1.00 p.u.		$V_{\mathrm{H}}^{\mathrm{MV}}$	1.02 p.u. (1.03 p.u.)
Load	P_{L}	27 MW		$V_{\mathrm{H}}^{\mathrm{HV}}$	1.00 p.u.
	Q_{L}	13 MVAr		E_{H}	1.26 p.u. (1.43 p.u.)
	$V_{\mathrm{L}}^{\mathrm{MV}}$	1.00 p.u.			
	$V_{\mathrm{L}}^{\mathrm{HV}}$	0.90 p.u.			
	a	0.8750			

Table 6.8: Microgrid initial power flow before islanding (base case scenario vs Scenario 2). Values for Scenario 2 are presented in parenthesis if changes have occurred with respect to base case scenario.

case scenario. However, the SCC metric has limitations as it only accounts for the initial SCC of the microgrid at the time of islanding. In actual operation, the back EMF voltage of the HPP is not static as it is controlled by the AVR to regulate the HPP terminal voltage. It is very important also to highlight that the bandwidth of the HPP voltage control loop is inherently dependent on the online capacity of the HPP, i.e., with lower online HPP capacity, the voltage control becomes indeed slower. This can be proved by deriving the transfer function of the voltage control which we will not delve into here. Additionally, despite that the initial HPP excitation voltage in Scenario 2 is slightly higher than base case scenario, both scenarios are limited by the same maximum excitation voltage limit of 4 p.u. Due to the aforementioned factors, Scenario 2 with less online HPP capacity was not able to deliver the needed active power to re-accelerate both small and larger motors, which have experienced a stall.

6.4.5 Scenario 3: Impact of line characteristics

This section replaces the overhead lines illustrated in Figure 6.9 with cables. The parameters used for the cables are listed in Table 6.5. Table 6.9 shows the updated initial power flow. If changes have occurred with respect to the base case scenario, the new value is presented in parentheses. The main change that has occurred is that the HPP absorbs 1.2 MVAr of reactive power compared to injecting 5 MVAr in the base case. The reason for this change in the reactive

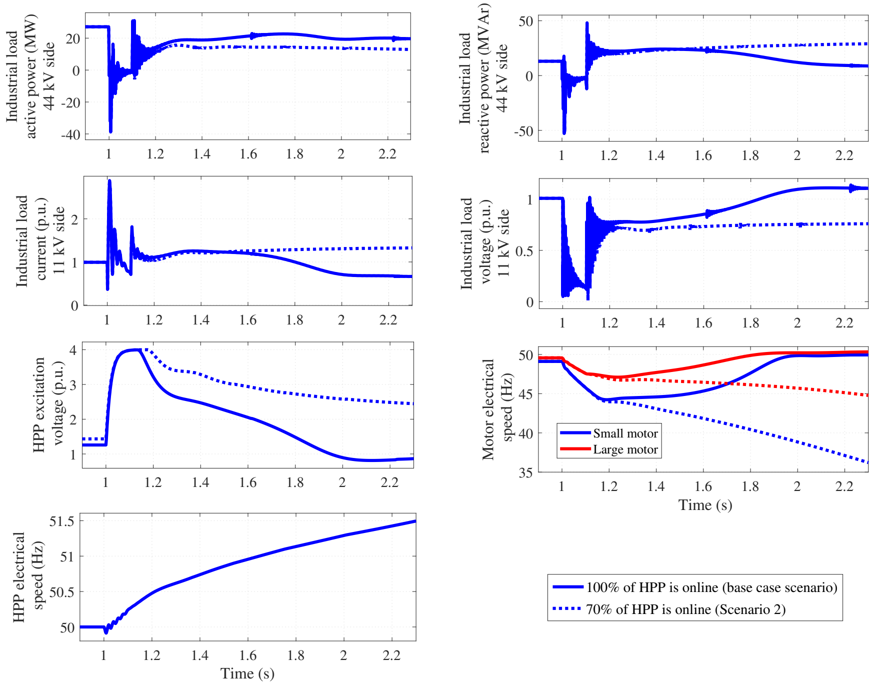

Figure 6.16: Dynamics of hydro-powered industrial microgrid when subject to a three-phase bolted fault at the PCC at t = 1 s followed by islanding at t = 1.1 s (base case scenario vs Scenario 2).

power is that the HPP absorbs the additional reactive power injected by the charging capacitance of the cables, which are much larger than the overhead line. Another change is the higher voltage at the 44 kV terminal of the load with an increase from 0.90 p.u. to 0.96 p.u. Therefore, the tap-changing transformer utilizes fewer taps to maintain the voltage at the 11 kV side at 1 p.u., i.e., the tap setting a has increased from 0.8750 to 0.9375.

The updated SCC of the microgrid in island mode is estimated according to (6.3) and shows a decrease in the SCC from 152 MVA in the base case to 126 MVA in Scenario 3. Even though the cable has three times less reactance than an overhead line, the overall SCC has decreased. This is due to the reduction of the HPP back EMF voltage to absorb the excessive reactive power produced by the cable. Furthermore, the cable has resulted in an increase in tap setting

a, which also contributes to reducing the SCC.

Table 6.9: Microgrid initial power flow before islanding (base case scenario vs Scenario 3). Values for Scenario 3 are presented in parenthesis if changes have occurred with respect to base case scenario.

Grid	P_{G}	1.7 MW (0.95 MW)	HPP	P_{H}	27 MW
	Q_{G}	12 MVAr		Q_{H}	5 MVAr (-1.2 MVAr)
	V_{PCC}	1.00 p.u.		$V_{\mathrm{H}}^{\mathrm{MV}}$	1.02 p.u. (1.01 p.u.)
Load	P_{L}	27 MW		$V_{\mathrm{H}}^{\mathrm{HV}}$	1.00 p.u.
	Q_{L}	13 MVAr		E_{H}	1.26 p.u. (1.13 p.u.)
	$V_{\mathrm{L}}^{\mathrm{MV}}$	1.00 p.u.			
	$V_{\mathrm{L}}^{\mathrm{HV}}$	0.90 p.u. (0.96 p.u.)			
	a	0.8750 (0.9375)			

Figure 6.17 shows the dynamics of the microgrid when subjected to a three-phase bolted fault at the PCC at t = 1 s, followed by opening the tie-line breaker at t = 1.1 s. The results for the base case scenario are illustrated with solid lines and those for Scenario 3 with dotted lines. Despite that Scenario 3 has less SCC than the base case scenario according to the estimated SCC, the former one shows a faster voltage recovery post islanding. This is due to the larger charging capacitance of the cable compared to overhead lines (larger by twenty-four times!). The reactive power injected by charging capacitance increases as the voltage recovers. It has the impact of reducing the reactive power burden on the HPP by providing a natural compensation to reactive power consumption by the load and the inductance of the cable.

It should be mentioned that the estimated SCC in (6.3) does not account for the charging capacitance of the cable. Therefore, (6.3) gives the wrong interpretation that the microgrid is weaker in case of cables compared to overhead lines.

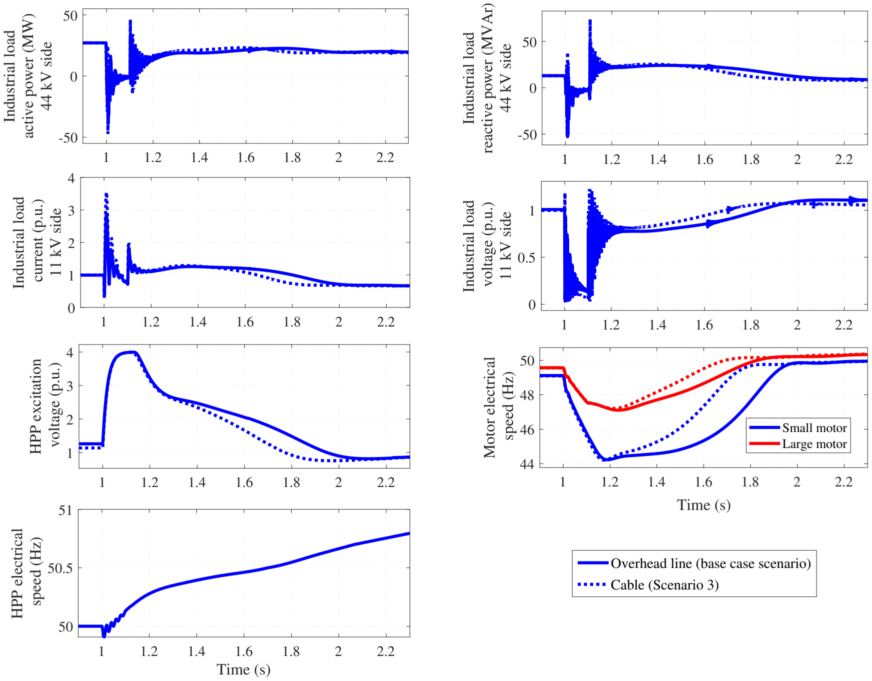

Figure 6.17: Dynamics of hydro-powered industrial microgrid when subject to a three-phase bolted fault at the PCC at t = 1 s followed by islanding at t = 1.1 s (base case scenario vs Scenario 3).

6.5 Technologies to achieve criterion for successful island transition

6.5.1 Investigated technologies to provide reactive compensation

Several reactive compensators are investigated to improve the voltage stability of the hydro-powered industrial microgrid during an island contingency. The investigated reactive compensators include shunt capacitor, synchronous condenser, and STATCOM, as illustrated in Figure 6.18. The compensators are installed at the factory 44 kV terminal instead of the PCC where they are commonly installed, since the aim here is to improve the voltage stability of the load. A comparison between the compensators investigated is summarized in Table 6.10. The shunt capacitor can only provide reactive power compensation. The synchronous condenser and STATCOM can additionally provide dynamic voltage regulation and short circuit current. However, the STATCOM short-circuit current is limited by the thermal capability of semiconductors.

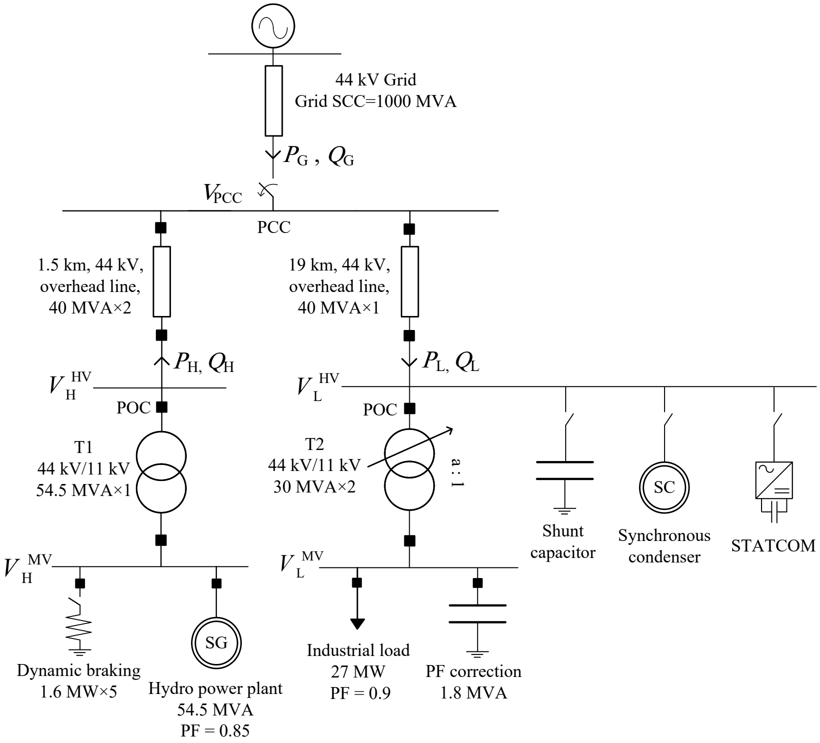

Figure 6.18: Investigated reactive compensators for improving voltage stability of microgrid during an island contingency.

Table 6.10: Comparison of investigated technologies for improving voltage stability of microgrid during island transition.

	Reactive power compensation	Voltage regulation	Short circuit current
Shunt capacitor	✓		
Synchronous condenser	✓	✓	✓
STATCOM	✓	✓	✓ (limited)

6.5.2 Synchronous condenser and STATCOM models

The physical model of the synchronous condenser has the same per unit parameters of the HPP model except that the inertia constant is reduced to 1 s (see Table D.3 in the appendix). The synchronous condenser is controlled in voltage control mode, and its AVR and exciter model are shown in Figure 6.19. The AVR and exciter parameters are presented in Table D.4 in the appendix.

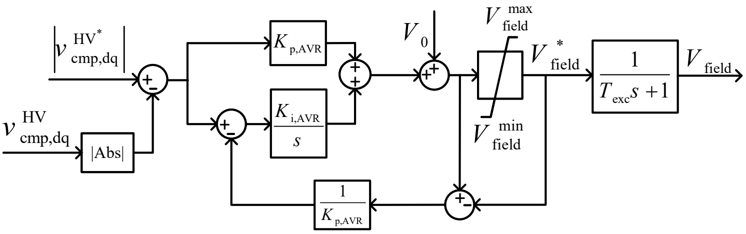

Figure 6.19: Synchronous condenser AVR and exciter model.

The STATCOM control diagram is shown in Figure 6.20. The control diagram follows the same GFM control scheme used for the BESS in Chapter 3. The main difference here is that the STATCOM does not have a frequency controller in its outer loop. Furthermore, the STATCOM is provided with a current limitation strategy to limit the current during short circuits without losing synchronoism with the grid. The method utilizes a dynamic voltage limiter where the maximum limit of the virtual back EMF voltage magnitude is automatically adjusted based on the actual terminal voltage of the STATCOM [121]. In this way, the maximum current of the STATCOM is not exceeded. The control parameters of the STATCOM are presented in Table D.5 in the appendix.

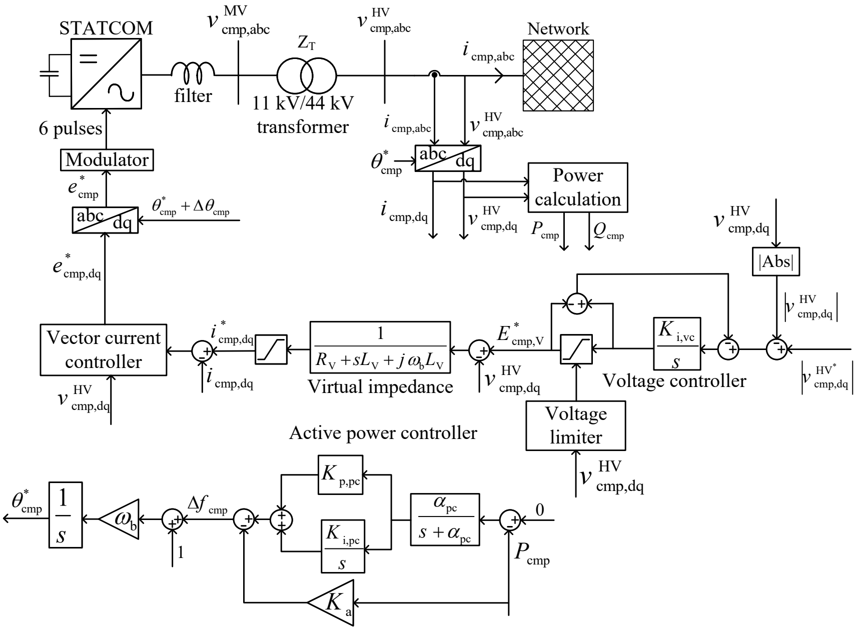

Figure 6.20: STATCOM control diagram.

6.5.3 Island contingency analysis with different compensators

This section compares the effectiveness of three compensators in fulfilling the criterion for a successful island transition. The compensators compared are the shunt capacitor, synchronous condenser, and STATCOM. For fair comparison, all the simulated compensators have the same size of 5 MVAr at a rated voltage of 11 kV. The implemented load of the microgrid is the same as the industrial load explained in Section 6.3.3. The base case scenario illustrated in Section 6.4.2 is used as a reference case, since it does not meet the desired criteria.

Figure 6.21 shows the dynamic simulation results when applying a three-phase bolted fault at the microgrid PCC at t = 1 s, followed by opening the microgrid tie-line breaker at t = 1.1 s. Both the synchronous condenser and the STATCOM have an initial reactive power of zero before the island contingency. However, the reactive power of the shunt capacitor depends on the line voltage and has an initial value of 4.7 MVAr. Due to the initial injection of reactive power by the shunt capacitor, the tap changing transformer feeding the industrial load needed fewer taps, the tap setting a being 0.8938 compared to 0.8750 in the other two compensators. Keep in mind that the tap setting a has an impact on the SCC of the microgrid in the island mode, as illustrated by (6.3). Thus, the shunt capacitor is expected to reduce the SCC at the load terminal because of the use of fewer taps in the tap-changing transformer feeding the industrial load. However, the reduction in SCC is less than 1%.

During the fault, i.e., between t = 1 s and t = 1.1 s, the current of the shunt capacitor and its reactive power reduce to near zero because the terminal voltage is too low. On the other hand, the synchronous condenser has a stiff back EMF voltage, injecting a short circuit current of about 2.5 p.u. This compares to only a short circuit current of 1 p.u. for the STATCOM due to its current limitation. However, despite the significant difference between the three compensators in their current injection during the fault, the difference in load voltage was not substantial, i.e., the voltage in all cases was near zero.

When the microgrid is disconnected from the main grid at t = 1.1 s, the load voltage is immediately restored to 50% - 60% of the nominal value for all compensator solutions. The voltage then gradually increases to the steady-state voltage, which takes around 3 s to reach (not reached here). All the compensators experience a similar voltage ramp up rate with marginal differences, the STATCOM being the fastest, followed by the synchronous condenser, and finally the shunt capacitor. The STATCOM, despite its current limitation, shows faster voltage recovery, since it does not have the physical delays existing in the exciter and field winding of the synchronous condenser.

Active power oscillations are present between the synchronous condenser (or the STATCOM), and the HPP. This occurs because the HPP rotor accelerates during the short circuit between t = 1 s and t = 1.1 s. This creates an accumulated angle difference between the HPP back EMF angle and the internal angle of the synchronous condenser (or the STATCOM). Therefore, when the fault is cleared, a large active power flows from the HPP to the synchronous condenser (or the STATCOM). The power oscillations are damped in both the compensators, but have a larger magnitude and last longer in the case of synchronous condenser. The STATCOM has a better damping for power oscillations thanks to the active damping K_a of its power controller (see the controller in Figure 6.20).

The faster oscillations in the power appear to be in the range of 400-500 Hz. These oscillations are due to the resonance between the 1.8 MVA capacitor installed in the industrial facility for power factor correction (see Figure 6.18) and the cable that feeds the industry. These oscillations are well damped, especially in the STATCOM case. Further analysis is needed to explain why the STATCOM has a better damping for these oscillations.

The zoomed figure in the bottom left subplot shows that the shunt capacitor and the synchronous condenser do not meet the criterion for a successful island transition at t=1.5 s. This is because the injection of reactive power from the shunt capacitor is directly linked to its terminal voltage magnitude, making it less effective at lower voltages. The synchronous condenser, although it injects less reactive power than the shunt capacitor at $t = 1.5$ s, shows a better voltage response. This is because the synchronous condenser has the additional advantage of improving the SCC. However, the negative active power of the synchronous condenser at $t = 1.5$ s increases the loading of the line, leading to a further voltage drop. This makes its voltage response poorer than that of the STATCOM, despite being advantageous in terms of SCC.

Note that the difference in the voltage response between the synchronous condenser and the STATCOM is very insignificant and is very sensitive to the control tuning. Additionally, if the synchronous condenser is equipped with a power system stabilizer, it may have better oscillation damping and improved voltage response. Furthermore, the shunt capacitor, despite being a passive element, shows a slightly slower voltage recovery compared to the other two compensators. If the shunt capacitor is slightly oversized above 5 MVA, it may show a favorable voltage response compared to the other two compensators. Therefore, the shunt capacitor may become a favorable solution, especially because of its cheaper cost. However, one should not neglect the other features of the synchronous condenser and STATCOM, such as voltage regulation, stabilization, and short-circuit current in the case of synchronous condenser.

6.6 Summary

This chapter has investigated the voltage stability of a hydro-powered industrial microgrid under a short-circuit-triggered island contingency. First,

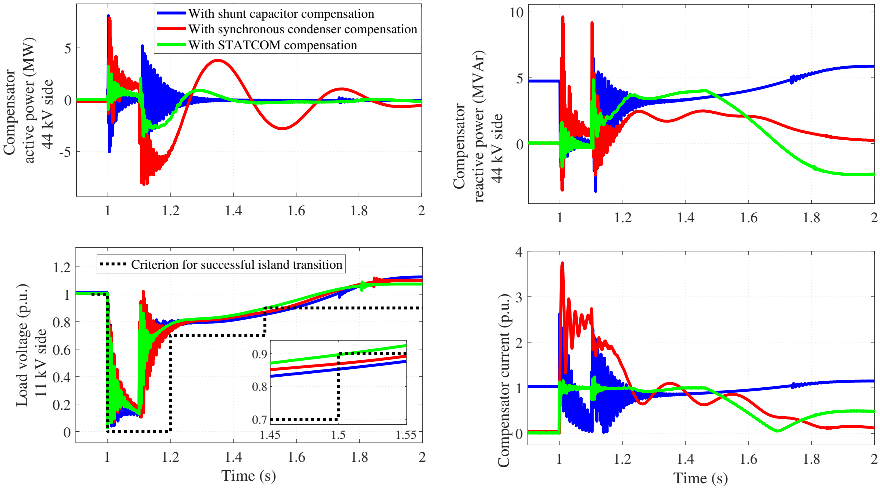

Figure 6.21: Comparison of three compensators to improve the voltage response of hydro-powered industrial microgrid during an island contingency.

a criterion is developed for a successful island transition. The criterion accounts for the voltage quality at the HPP and industrial load terminals. The HPP terminal voltage must comply with the fault-ride-through requirement for type D generators, while the industrial load terminal voltage must comply with the short-term voltage dip requirement for the quality of power supply. The analysis shows that the latter requirement of the load is more challenging to meet, since the load is connected to the microgrid PCC with a long cable, and that the former requirement is less stringent than the latter one.

A critical parameter in the voltage stability of the microgrid during island transition is the reactive power exchange with the upstream grid. The maximum power exchange depends on the POA of reactive power requirement. This chapter has investigated two alternatives for the POA, being at the POC of the HPP and the industry, which is the case today in Sweden, and being at the PCC of the microgrid. The analysis shows that the former allows for a larger exchange of reactive power with the grid. This leads to slower voltage recovery of the microgrid after an unplanned islanding. Thus, increasing the chance of stalling motors, especially small motors with a lower inertia constant.

Finally, different compensators are investigated to meet the criterion for a successful island transition. The compensators are: shunt capacitor, synchronous condenser, and STATCOM. All compensators show a similar voltage response with a minor difference in the speed of voltage recovery. The shunt capacitor has the slowest voltage recovery, and its reactive power injection is proportional to the square of the terminal voltage. The STATCOM shows a faster voltage response compared to the synchronous condenser, despite hitting the current limitation, since it does not have the physical delays of the exciter and the field winding.

In future work, a metric for the strength of a microgrid in island operation is needed to determine the likelihood of a successful island transition. In this chapter, we have investigated one metric that estimates the SCC of the microgrid based on the initial conditions before the islanding. The analysis shows that the metric has some limitations, since it does not account for the capacitive nature of the lines and assumes that the HPP has a constant back-EMF voltage, neglecting its voltage control action. Therefore, a holistic metric that encompasses all of these factors in addition to the load characteristics is desired.

CHAPTER 7

Conclusions and future work

This chapter presents the main conclusions of the work carried out in this thesis and provides suggestions for potential future work.

7.1 Conclusions

This thesis focuses on the sizing of BESS and microgrid interconnection technologies, including B2B converter and MPC, to reduce the peak net load of two microgrids. Furthermore, this thesis investigates the sizing and control of BESS and B2B converter to facilitate island operation with secure island transition of a critical facility.

Chapter 2 compares three solutions for peak net load reduction of two microgrids: a) separate microgrids where each microgrid has its own BESS; b) interconnected microgrids by B2B converter where each microgrid has its own BESS; c) interconnected microgrids by MPC where a BESS is shared by two microgrids and integrated into the DC link of MPC. The size of the power electronics, storages, transformers and interconnecting cable of the three solutions is obtained through a linear programming problem by minimizing the corresponding investment, operational, and losses costs. A simple power balance is used to model the microgrid. The results show that the interconnection of microgrids can significantly reduce the size of BESS or even eliminate its need if the microgrids have a low or intermediate coincidence factor. Furthermore, results show that interconnection by MPC with integrated BESS can reduce the size of power electronics compared to interconnection by B2B converter with individual BESSs.

Next, this chapter develops a simple rule-of-thumb method for the sizing of MPC with integrated BESS and DC load to reduce the peak net load of two microgrids. The rule-of-thumb method is based on the net load profile of the two microgrids and their maximum limit on power import from and export to the upstream grid. The analysis shows that the size of an AC port of the MPC should account for the following scenarios: a) maximum power deficiency/surplus in the microgrid to which the AC port is interfaced; b) power deficiency/surplus in the neighboring microgrid that coincides with high/low DC load demand and available power capacity in the microgrid to which the AC port is interfaced. In case power re-routing is not solely sufficient to reduce the peak net load, an investment in additional BESS is required. The dimensioning of the BESS power capacity should account for the maximum power deficiency/surplus of aggregated microgrids, and its energy capacity should account for the maximum accumulated energy deficiency/surplus of aggregated microgrids. Figure 2.21 provides a summary of the rule-of-thumb sizing. To verify the effectiveness of the rule-of-thumb method, it is compared with optimal sizing obtained by linear programming. The results show that the rule-of-thumb method always gives an equal or larger size than the one obtained by linear programming. Thus, the rule-of-thumb method can serve as a good tool for screening the MPC and BESS sizes during feasibility studies prior to a detailed optimization analysis.

Chapter 3 develops a BESS frequency controller to facilitate a secure island transition of a hydro-powered microgrid during an unplanned grid event. Unlike peak net load reduction, the island transition is a dynamic event that requires analysis through dynamic simulation. Therefore, the analysis is conducted in Matlab/Simulink using phasor simulations. First, the frequency-security constraints of the microgrid are defined. Based on that, a simple PI-based droop frequency controller and its tuning are proposed. The tuning accounts for the microgrid frequency security constraints and the governor response time of the HPP. The tuning aims at providing a frequency-secure island transition with reduced energy storage. The effectiveness of the proposed controller is tested against other existing controllers in the literature and validated in a laboratory experiment. The results show that the PI-based droop controller outperforms the commonly used P-based droop controller in BESS applications. This is due to the additional degrees of freedom that the PI-based droop controller has, allowing the BESS to temporarily provide a large transient gain until the HPP ramps up its power. Consequently, this leads to savings in BESS energy storage. It is also worth noting that this dynamic coordination between the BESS and HPP does not require communication and is based solely on local frequency measurement.

Chapter 4 extends the sizing optimization formulation developed in Chapter 2 for a single microgrid to include the island operation and island transition capabilities of the microgrid. The analysis shows that the size of the BESS power capacity is solely determined by the constraints for the island transition capability. This is because unlike other functions that can be relieved using slower resources, the island transition requires fast acting resources. On the other hand, the size of the BESS energy capacity is determined by the constraints for peak net load reduction and island capability. If the coincidence between a grid capacity bottleneck and an islanding event is low, the size of the BESS energy capacity can be co-optimized to deliver both functions.

Chapter 5 extends the frequency control of BESS in a single microgrid in Chapter 3 to include the island contingency of interconnected microgrids. A B2B converter is utilized for the interconnection and uses the same frequency controller developed in Chapter 3. The developed strategy allows one microgrid to be islanded at a time through fast contingency power support from the healthy microgrid. The analysis shows that the size of the B2B converter is determined primarily by the maximum power exchange between the microgrid and the upstream grid. Furthermore, the analysis also shows that the converter that controls the dc-link voltage needs to have a slightly larger MW rating than the other one of the B2B converter without losing control over the dc-link voltage. This condition occurs when the B2B converter hits its maximum power limit during the island transition.

Chapter 6 investigates the voltage stability of a hydro-powered industrial microgrid during an unplanned island transition. This chapter modifies the hydro-powered industrial microgrid presented in Chapter 3 to invoke more voltage stability issues, through the use of longer feeders and a more accurate industrial load model suitable for voltage stability studies. Criterion for a voltage-secure island transition is first developed. The criterion accounts for the connection requirements of generators and loads in addition to the requirements for quality of power supply. The results show that the point of applicability of the reactive power requirement is an important factor that affects the voltage stability during island transition. In Sweden, the reactive power requirement is typically imposed at the POC of individual generators and loads. However, in a microgrid, the reactive power requirement is typically imposed at the PCC between the microgrid and the main grid. The results show that the latter requirement puts a stricter limit on the reactive power exchange with the grid. This reduces the reactive power disturbance during an unplanned island transition and the subsequent voltage dynamics. Consequently, the size of the reactive power compensator needed to ride the islanding event is reduced.

7.2 Future work

This thesis has developed a linear programming problem for the sizing of various power electronic technologies in microgrids to reduce the peak net load and facilitate island operation with island transition capability.

The linear programming problem models the microgrid using power balance equations where voltage drops are neglected. It may be of interest to account for voltage drops in the network as voltage quality could be a limiting factor for power import/export from/to the grid especially in rural areas where the grid is weak.

Furthermore, the developed optimization problem accounts for the energy security of the microgrid in island operation, i.e., adequate energy and power to meet the critical demand in island operation. It would be of interest to additionally account for the voltage and frequency security constraints in island operation. This is particularly of interest because of the weaker network in island operation, which may require investment in additional resources for the regulation of frequency and voltage.

The implemented optimization problem has focused on the sizing of various power electronic technologies in microgrids to achieve the desired functions. It could be of interest to additionally evaluate the economic feasibility of the microgrid solutions. This can be done by accounting for various revenue streams, e.g., frequency ancillary service markets and energy arbitrage. Such an analysis gives investors an indication of whether the investment is profitable.

This thesis has also investigated, through dynamic analysis, the frequency and voltage stability of a hydro-powered industrial microgrid during an unplanned island transition. Another future work is to analyze the stability of the microgrid in the subsequent island operation. This is particularly interesting in the context of a hydro-powered microgrid where the backlash problem in the HPP mechanical system can deteriorate the power quality.

References

[1] *Paris agreement*, United Nations Framework Convention on Climate Change, 2015.

[2] Swedish Climate Policy Council, “Report of the swedish climate policy council 2024,” Tech. Rep., Mar. 2024.

[3] International Energy Agency. “Share of electricity in total final energy consumption in the net zero scenario, 2005–2030,” Accessed: Apr. 24, 2025. [Online]. Available: `https://www.iea.org/data-and-statistics/charts/share-of-electricity-in-total-final-energy-consumption-in-the-net-zero-scenario-2005-2030`.

[4] Swedish Energy Agency. “Energimyndighetens scenarier visar stora förändringar i det svenska energisystemet,” Accessed: Apr. 24, 2025. [Online]. Available: `https://www.energimyndigheten.se/nyhetsarkiv/2023/energimyndighetens-scenarier-visar--stora-forandringar-i-det-svenska-energisystemet/`.

[5] IVA Royal Swedish Academy of Engineering Sciences, “Reliability in sweden’s electricity system,” Tech. Rep., 2017.

[6] H. A. Turesson and J. Werneskog, “The challenge of providing sufficient grid capacity for electrification to be a key factor in achieving climate neutrality until 2045,” M.S. thesis, Department of Management and Engineering, Energy Systems, Linköping University, Linköping, Sep. 2020.

[7] Energimarknadsinspektionen. “Hur lång tid tar det för ei att besluta om en kraftledning?” Accessed: Apr. 24, 2025. [Online]. Available: `https://ei.se/om-oss/nyheter/2020/2020-03-05-hur-lang-tid-tar-det-for-ei-att-besluta-om-en-kraftledning`.

[8] World Business Council for Sustainable Development (WBCSD), “Microgrids for commercial and industrial companies,” Tech. Rep., Nov. 2017.

[9] Hitachi ABB Power Grids, “Reliable, affordable power with substantial energy savings at an industrial facility,” Tech. Rep., 2021.

[10] Hitachi ABB Power Grids, “Ensuring reliable power for commercial and industrial site,” Tech. Rep., 2021.

[11] *Energimarknadsinspektionens föreskrifter och allmänna råd om krav som ska vara uppfyllda för att överföringen av el ska vara av god kvalitet*, Swedish grid code EIFS 2023:3, 2023.

[12] Grid Deployment Office U.S. Department of Energy, “Microgrid overview,” Tech. Rep., 2024.

[13] O. N. Hurtig et al., “Drivers and barriers to deploy microgrid in sweden,” in *2022 IEEE PES Innovative Smart Grid Technologies Conference Europe (ISGT-Europe)*, 2022, pp. 1–5.

[14] A. Hirsch, Y. Parag, and J. Guerrero, “Microgrids: A review of technologies, key drivers, and outstanding issues,” *Renewable and Sustainable Energy Reviews*, vol. 90, pp. 402–411, 2018.

[15] S. Inamdar, R. Mohanty, P. Chen, R. Majumder, and M. Bongiorno, “On benefits and challenges of nested microgrids,” in *2019 IEEE PES Asia-Pacific Power and Energy Engineering Conference (APPEEC)*, 2019, pp. 1–6.

[16] E. Ciapessoni, D. Cirio, A. Pitto, M. Van Harte, and M. Panteli, “Power system resilience: Definition, features and properties,” *Cigré Science & Engineering Journal*, vol. 30, p. 6, 2023.

[17] “Guidance on the provision of reserves,” SvK, Tech. Rep., 2024.

[18] “Grid development plan 2024—2033,” SvK, Tech. Rep., 2024.

[19] G. Energi. “Flexibilitet - tjäna pengar på er effekt.” Accessed: 2025-04-09. [Online]. Available: `https://www.goteborgenergi.se/foretag/flexibilitet`.

[20] “En bedömning av resurstillräckligheten för svensk elförsörjning,” SvK, Tech. Rep., 2024.

[21] *Energimarknadsinspektionens föreskrifter om fastställande av generellt tillämpliga krav för nätanslutning av generatorer*, Swedish grid code EIFS 2018:2, 2018.

[22] *Energimarknadsinspektionens föreskrifter om fastställande av generellt tillämpliga krav för anslutning av förbrukare*, Swedish grid code EIFS 2019:6, 2019.

[23] *Voltage characteristics of electricity supplied by public electricity networks*, EN 50160, 2020.

[24] “Ieee standard for harmonic control in electric power systems,” *IEEE Std 519-2022 (Revision of IEEE Std 519-2014)*, pp. 1–31, 2022.

[25] “Stödtjänster och avhjälpande åtgärder i ett energisystem under förändring,” SvK, Tech. Rep., 2021.

[26] “Network modelling for harmonic studies,” CIGRE, Tech. Rep., 2019.

[27] *IEEE Standard for Interconnection and Interoperability of Distributed Energy Resources with Associated Electric Power Systems Interfaces*, IEEE Std 1547-2018 (Revision of IEEE Std 1547-2003), 2018.

[28] IHS Markit. “Top energy storage system integrartors in 2021. ”[Online]. Available: `https://infogram.com/1t0dv1018rzxlyf87m31dyz322t32pew4d3`.

[29] Tesla. “Megapack massive energy storage. ”[Online]. Available: `https://www.tesla.com/megapack`.

[30] Tesla. “Powerwall whole-home backup, 24/7. ”[Online]. Available: `https://www.tesla.com/powerwall`.

[31] Fluence. “Fluence’s energy storage. ”[Online]. Available: `https://fluenceenergy.com/energy-storage-technology/`.

[32] NEXTera ENERGY. “Energy storage. ”[Online]. Available: `https://www.nexteraenergyresources.com/products-solutions/reduce/energy-storage.html`.

[33] Wartsila. “Quantum BESS portfolio. ”[Online]. Available: `https://www.wartsila.com/energy/energy-storage/technology/quantum-bess`.

[34] Powin. “The power to change the world. ”[Online]. Available: https://powin.com/.

[35] FlexGen. “Innovating for a more reliable power grid. ”[Online]. Available: https://www.flexgen.com/.

[36] SMA sunbelt. “Large-scale storage solutions from SMA. ”[Online]. Available: https://www.sma.de/en/large-scale/storage-solutions.

[37] Sungrow. “Storage system. ”[Online]. Available: https://en.sungrowpower.com/Solutions/6/storage-system.

[38] Nidec. “Battery energy storage solutions. ”[Online]. Available: https://www.nidec-conversion.com/markets/battery-energy-storage-solutions/.

[39] Hornsdale. “Project overview. ”[Online]. Available: https://hornsdalepowerreserv
com.au/.

[40] Energy Storage News. “Testing starts on fluence 200 MWh battery storage projects in lithuania for spring 2023 activation. ”[Online]. Available: https://www.energy-storage.news/testing-starts-on-fluence-200mwh-battery-storage-projects-in-lithuania-for-spring-2023-activation/.

[41] Energy Storage News. “230 MW BESS comes online at bureau of land management site in california. ”[Online]. Available: https://www.energy-storage.news/230mw-bess-comes-online-at-bureau-of-land-management-site-in-california/.

[42] Wärtsilä. “First wärtsilä gridsolv quantum energy storage system with service agreement will help lower u.s. city’s electricity costs. ”[Online]. Available: https://www.wartsila.com/media/news/14-10-2020-first-wartsila-gridsolv-quantum-energy-storage-system-with-service-agreement-will-help-lower-u-s-city-s-electricity-costs-2798216.

[43] Powin. “Powin delivers high-uptime energy storage close to the load in the industrial heartland of southern california. ”[Online]. Available: http://powin.com/wp-content/uploads/2022/12/Powin_CaseStudy_Johanna.pdf.

[44] Energy Storage News. “Batteries replace diesel for jumpstarting indiana natural gas plants. ”[Online]. Available: `https://www.energy-storage.news/batteries-replace-diesel-for-jumpstarting-indiana-natural-gas-plants/`.

[45] Statera Energy. “Pelham storage: Battery storage. ”[Online]. Available: `https://stateraenergy.co.uk/projects/pelham-storage`.

[46] NS Energy. “Minety battery storage project. ”[Online]. Available: `https://www.nsenergybusiness.com/projects/minety-battery-storage-project/`.

[47] Nidec. “34.8 MW/226.2 MWh electric energy storage systems for terna, italy. ”[Online]. Available: `https://www.nidec-conversion.com/document/electric-energy-storage-systems-case-study/`.

[48] X. Jiang, Y. Zhou, W. Ming, P. Yang, and J. Wu, “An overview of soft open points in electricity distribution networks,” *IEEE Transactions on Smart Grid*, vol. 13, no. 3, pp. 1899–1910, 2022.

[49] W. Cao, J. Wu, N. Jenkins, C. Wang, and T. Green, “Benefits analysis of soft open points for electrical distribution network operation,” *Applied Energy*, vol. 165, pp. 36–47, 2016.

[50] R. You and X. Lu, “Voltage unbalance compensation in distribution feeders using soft open points,” *Journal of Modern Power Systems and Clean Energy*, vol. 10, no. 4, pp. 1000–1008, 2022.

[51] Western Power Distribution, “FPL development and improvement report,” Tech. Rep., 2019.

[52] V. Gadelha, A. Sumper, E. Bullich-Massagué, and M. Aragüés-Peñalba, “Electrical grids based on power routers: Definition, architecture and modeling,” *IEEE Access*, vol. 11, pp. 10 004–10 017, 2023.

[53] T. Larsson, A. Petersson, A. Edris, D. Kidd, and F. Aboytes, “Eagle pass back-to-back tie: A dual purpose application of voltage source converter technology,” in *2001 Power Engineering Society Summer Meeting. Conference Proceedings (Cat. No.01CH37262)*, vol. 3, 2001, pp. 1686–1691.

[54] A. M. Fares, C. Klumpner, and M. Sumner, “A novel modular multiport converter for enhancing the performance of photovoltaic-battery based power systems,” *Applied Sciences*, vol. 9, no. 19, 2019.

[55] Y. Zhang, J. He, and D. M. Ionel, “Modeling and control of a multiport converter based ev charging station with pv and battery,” in *2019 IEEE Transportation Electrification Conference and Expo (ITEC)*, 2019, pp. 1–5.

[56] M. M. Savrun and A. Atay, “Multiport bidirectional DC—DC converter for pv powered electric vehicle equipped with battery and supercapacitor,” *IET Power Electronics*, vol. 13, no. 17, pp. 3931–3939, 2020.

[57] R. Rezaii et al., “Design and implementation of a multiport system for solar EV applications,” in *2023 IEEE Applied Power Electronics Conference and Exposition (APEC)*, 2023, pp. 29–34.

[58] M. Deakin, P. C. Taylor, J. Bialek, and W. Ming, “Design and operation of hybrid multi-terminal soft open points using feeder selector switches for flexible distribution system interconnection,” *Electric Power Systems Research*, vol. 212, p. 108 516, 2022.

[59] ERA-Net Smart Energy Systems. “Cross-sectoral energy control through interconnected microgrids by multiport converter,” Accessed: Apr. 24, 2025. [Online]. Available: `https://eranet-smartenergysystems.eu/global/images/cms/Content/Fact%20Sheets/ERANetSES_ProjectFactSheet_RegSys2018_Multiportgrid.pdf`.

[60] iPLUG. “Innovative power electronics for a greener energy grid.” Accessed: 2025-04-16, Accessed: Apr. 24, 2025. [Online]. Available: `https://iplug-he.eu/`.

[61] Danish Energy Agency, “Technology data for energy storage,” Tech. Rep., 2021.

[62] Bloomberg, “Bloombergnef,” Tech. Rep., 2018.

[63] Vattenfall. “Lilla edet,” Accessed: Apr. 24, 2025. [Online]. Available: `https://fiskevatten.vattenfall.com/lilla-edet/`.

[64] High Voltage Valley. “Ödrift - ett lager med fossilfri energi,” Accessed: Apr. 24, 2025. [Online]. Available: `https://www.highvoltagevalley.se/sv-SE/projekt/%5C%C3%5C%B6drift-i-krafttanken-41360184`.

[65] C. A. Platero, J. A. Sánchez, C. Nicolet, and P. Allenbach, “Hydropower plants frequency regulation depending on upper reservoir water level,” *Energies*, vol. 12, no. 9, 2019.

[66] W. G. Weijia Yang Jiandong Yang and P. Norrlund, "Frequency stability of isolated hydropower plant with surge tank under different turbine control modes," *Electric Power Components and Systems*, vol. 43, no. 15, pp. 1707–1716, 2015.

[67] N. Ung, "The effects of backlash on the frequency stability in a hydro based power system," M.S. thesis, School of Electrical Engineering and Computer Science, KTH University, Stockholm, 2018.

[68] N. Hatziargyriou, H. Asano, R. Iravani, and C. Marnay, "Microgrids," *IEEE Power and Energy Magazine*, vol. 5, no. 4, pp. 78–94, 2007.

[69] M. Karimi-Ghartemani, S. A. Khajehoddin, P. Piya, and M. Ebrahimi, "Universal controller for three-phase inverters in a microgrid," *IEEE Journal of Emerging and Selected Topics in Power Electronics*, vol. 4, no. 4, pp. 1342–1353, 2016.

[70] S. M. Ashabani and Y. A.-R. I. Mohamed, "A flexible control strategy for grid-connected and islanded microgrids with enhanced stability using nonlinear microgrid stabilizer," *IEEE Transactions on Smart Grid*, vol. 3, no. 3, pp. 1291–1301, 2012.

[71] F. Gao and M. R. Iravani, "A control strategy for a distributed generation unit in grid-connected and autonomous modes of operation," *IEEE Transactions on Power Delivery*, vol. 23, no. 2, pp. 850–859, 2008.

[72] M. S. Pilehvar and B. Mirafzal, "Frequency and voltage supports by battery-fed smart inverters in mixed-inertia microgrids," *Electronics*, vol. 9, no. 11, 2020.

[73] R. W. Kenyon, A. Sajadi, A. Hoke, and B.-M. Hodge, "Using a grid-forming inverter to stabilize a low-inertia power system – Maui Hawaiian island," in *2022 IEEE PES Innovative Smart Grid Technologies Conference Europe (ISGT-Europe)*, 2022, pp. 1–6.

[74] S. Acharya, M. S. E. Moursi, and A. Al-Hinai, "Coordinated frequency control strategy for an islanded microgrid with demand side management capability," *IEEE Transactions on Energy Conversion*, vol. 33, no. 2, pp. 639–651, 2018.

[75] A. Mondal and M. S. Illindala, “Improved frequency regulation in an islanded mixed source microgrid through coordinated operation of ders and smart loads,” in *2017 IEEE/IAS 53rd Industrial and Commercial Power Systems Technical Conference (I&CPS)*, 2017, pp. 1–8.

[76] A. Narula, M. Bongiorno, M. Beza, P. Chen, and D. Karlsson, “Coordinated control of grid-forming converters and hydro generators to enhance frequency quality of future power system,” *Electric Power Systems Research*, vol. 212, p. 108 456, 2022.

[77] J. Björk, K. H. Johansson, and F. Dörfler, “Dynamic virtual power plant design for fast frequency reserves: Coordinating hydro and wind,” *IEEE Transactions on Control of Network Systems*, vol. 10, no. 3, pp. 1266–1278, 2023.

[78] ENTSO-e, “FCR-N design of requirements,” Tech. Rep., 2017.

[79] T. Van Cutsem et al., “Test systems for voltage stability studies,” *IEEE Transactions on Power Systems*, vol. 35, no. 5, pp. 4078–4087, 2020.

[80] B. Wen, D. Boroyevich, R. Burgos, P. Mattavelli, and Z. Shen, “Analysis of d-q small-signal impedance of grid-tied inverters,” *IEEE Transactions on Power Electronics*, vol. 31, no. 1, pp. 675–687, 2016.

[81] R. Rosso, X. Wang, M. Liserre, X. Lu, and S. Engelken, “Grid-forming converters: Control approaches, grid-synchronization, and future trends—a review,” *IEEE Open Journal of Industry Applications*, vol. 2, pp. 93–109, 2021.

[82] S. Inamdar, “Passive island detection of microgrid by grid forming inverter,” Licentiate thesis, Department of Electrical Engineering, Chalmers University of Technology, Gothenburg, 2022.

[83] P. Rodriguez, I. Candela, C. Citro, J. Rocabert, and A. Luna, “Control of grid-connected power converters based on a virtual admittance control loop,” in *2013 15th European Conference on Power Electronics and Applications (EPE)*, 2013, pp. 1–10.

[84] A. Narula, M. Bongiorno, M. Beza, and P. Chen, “Tuning and evaluation of grid-forming converters for grid-support,” in *2021 23rd European Conference on Power Electronics and Applications (EPE'21 ECCE Europe)*, 2021, P.1–P.10.

[85] L. Harnefors, L. Zhang, and M. Bongiorno, “Frequency-domain passivity-based current controller design,” *IET Power Electronics*, vol. 1, pp. 455–465, 4 2008.

[86] A. Vukojevic and S. Lukic, “Microgrid protection and control schemes for seamless transition to island and grid synchronization,” *IEEE Transactions on Smart Grid*, vol. 11, no. 4, pp. 2845–2855, 2020.

[87] O. Samuelsson and N. Strath, “Islanding detection and connection requirements,” in *2007 IEEE Power Engineering Society General Meeting*, 2007, pp. 1–6.

[88] U.S. Department of Energy, “The advanced microgrid: Integration and interoperability,” Tech. Rep., 2014.

[89] ENTSO-e, “FCR-D design of requirements,” Tech. Rep., 2017.

[90] J. Näsström, “State-of-the-art development platform for hydropower turbine governors,” M.S. thesis, Department of Applied Physics and Electronics, Umeå University, Umeå, 2017.

[91] ENTSO-e, “Future system inertia,” Tech. Rep., 2018.

[92] P. Imgart, A. Narula, M. Bongiorno, M. Beza, and J. R. Svensson, “A cascaded power controller for robust frequency ride-through of grid-forming converters,” in *2022 IEEE Energy Conversion Congress and Exposition (ECCE)*, 2022, pp. 1–8.

[93] L. Harnefors, M. Hinkkanen, U. Riaz, F. M. M. Rahman, and L. Zhang, “Robust analytic design of power-synchronization control,” *IEEE Transactions on Industrial Electronics*, vol. 66, no. 8, pp. 5810–5819, 2019.

[94] L. Harnefors, M. Schweizer, J. Kukkola, M. Routimo, M. Hinkkanen, and X. Wang, “Generic PLL-based grid-forming control,” *IEEE Transactions on Power Electronics*, vol. 37, no. 2, pp. 1201–1204, 2022.

[95] M. Ganjian-Aboukheili, M. Shahabi, Q. Shafiee, and J. M. Guerrero, “Seamless transition of microgrids operation from grid-connected to islanded mode,” *IEEE Transactions on Smart Grid*, vol. 11, no. 3, pp. 2106–2114, 2020.

[96] *IEEE Recommended Practice for Monitoring Electric Power Quality*, IEEE Std 1159-2019 (Revision of IEEE Std 1159-2009), 2019.

[97] *Establishing a network code on requirements for grid connection of generators*, ENTSO-e RfG, 2016.

[98] M. B. Beza, “Power system stability enhancement using shunt-connected power electronic devices with active power injection capability,” PhD thesis, Department of Electrical Engineering, Chalmers Univesrsity of Technology, Gothenburg, Feb. 2015.

[99] A. Sunjaq, P. Chen, M. Bongiorno, R. Majumder, and J. R. Svensson, “Frequency control by BESS for smooth island transition of a hydro-powered microgrid,” *IET Smart Grid*, vol. 7, no. 1, pp. 63–77, 2024.

[100] M. Javadi, Y. Gong, and C. Y. Chung, “Frequency stability constrained microgrid scheduling considering seamless islanding,” *IEEE Transactions on Power Systems*, vol. 37, no. 1, pp. 306–316, 2022.

[101] A. M. Nakiganda and P. Aristidou, “Resilient microgrid scheduling with secure frequency and voltage transient response,” *IEEE Transactions on Power Systems*, vol. 38, no. 4, pp. 3580–3592, 2023.

[102] A. Vukojevic and S. Lukic, “Microgrid protection and control schemes for seamless transition to island and grid synchronization,” *IEEE Transactions on Smart Grid*, vol. 11, no. 4, pp. 2845–2855, 2020.

[103] P. J. Colorado, V. P. Suppioni, A. J. S. Filho, M. B. C. Salles, and A. P. Grilo-Pavani, “Security assessment for the islanding transition of microgrids,” *IEEE Access*, vol. 10, pp. 17 189–17 200, 2022.

[104] *IEEE Guide for the Application of Protective Relays Used for Abnormal Frequency Load Shedding and Restoration*, IEEE Std C37.117-2007, 2007.

[105] L. A. Paredes, M. G. Molina, and B. R. Serrano, “Enhancing dynamic voltage stability in resilient microgrids using FACTS devices,” *IEEE Access*, vol. 11, pp. 66 150–66 176, 2023.

[106] N. Afrin, M. Islam, J. Lu, and F. Yang, “Sensitivity based voltage support strategy to enhance dynamic stability of islanded microgrid,” *IEEE Transactions on Power Delivery*, vol. 37, no. 4, pp. 3111–3120, 2022.

[107] L. A. Paredes, M. G. Molina, and B. R. Serrano, “Resilient microgrids with FACTS technology,” in *2020 IEEE PES Transmission & Distribution Conference and Exhibition - Latin America (T&D LA)*, 2020, pp. 1–6.

[108] *IEEE Recommended Practice for the Planning and Design of the Microgrid*, IEEE Std 2030.9-2019, 2019.

[109] *IEEE Guide for Design, Operation, and Integration of Distributed Resource Island Systems with Electric Power Systems*, IEEE Std 1547.4-2011, 2011.

[110] *Microgrids - Part 1: Guidelines for microgrid projects planning and specification*, IEC Technical Specification 62898-1, 2017.

[111] *Microgrids - Part 2: Guidelines for operation*, IEC Technical Specification 62898-1, 2018.

[112] SvK, “Synkron kraftproduktionsmodul: Bilaga 6 provning,” Tech. Rep., 2023.

[113] “Kraftparksmodul: Bilaga 6 provning,” SvK, Tech. Rep., 2024.

[114] *Establishing a network code on demand connection*, ENTSO-e DCC, 2016.

[115] Vattenfall, “Application provisions and network tariffs for vattenfall’s regional network,” Tech. Rep., 2024.

[116] J. D. Rios Penaloza, J. A. Adu, A. Borghetti, F. Napolitano, F. Tossani, and C. A. Nucci, “Influence of load dynamic response on the stability of microgrids during islanding transition,” *Electric Power Systems Research*, vol. 190, p. 106 607, 2021.

[117] P. Krause, O. Wasynczuk, S. Sudhoff, and S. Pekarek, *Analysis of Electric Machinery and Drive Systems* (IEEE Press Series on Power and Energy Systems). Wiley, 2013.

[118] P. Kundur, N. Balu, and M. Lauby, *Power System Stability and Control* (EPRI power system engineering series). McGraw-Hill, 1994.

[119] L. Harnefors, M. Bongiorno, and S. Lundberg, “Input-admittance calculation and shaping for controlled voltage-source converters,” *IEEE Transactions on Industrial Electronics*, vol. 54, no. 6, pp. 3323–3334, 2007.

[120] NKT cables AB, “Kraftkabel handboken,” Tech. Rep., 2015.

[121] A. Narula, P. Imgart, M. Bongiorno, M. Beza, J. R. Svensson, and J.-P. Hasler, “Voltage-based current limitation strategy to preserve grid-forming properties under severe grid disturbances,” *IEEE Open Journal of Power Electronics*, vol. 4, pp. 176–188, 2023.

APPENDIX A

Problem formulation for sizing of BESS, B2B converter and MPC to mitigate grid capacity bottleneck

This appendix presents the optimization problem formulation for finding the cost-optimal size of energy storage and power electronics to mitigate grid capacity bottleneck. The appendix is divided into three sections: Section A.1 presents the problem formulation for separate microgrids each having its own BESS; Section A.2 presents the problem formulation of interconnected microgrids by B2B converter each having its own BESS; Section A.3 presents the problem formulation of interconnected microgrids by MPC both microgrids sharing a single BESS integrated with the MPC. The network diagram of the three solutions to mitigate the grid capacity bottleneck is shown in Figure 2.1. This appendix supports the material in Chapter 2.

A.1 Separate microgrids problem formulation

A.1.1 Objective function

$$OF = \mathrm{Min}\{C_{\mathrm{CAPEX,B}} + C_{\mathrm{OPEX,B}} + C_{\mathrm{loss,B}}\}$$

$$C_{\mathrm{CAPEX,B}} = C_{\mathrm{I,B}} \sum_{m=1}^{2} E_m^{\mathrm{B,max}} + C_{\mathrm{I,con}} \sum_{m=1}^{2} P_m^{\mathrm{B,DC,max}} + \left(C_{\mathrm{I,inv}} + C_{\mathrm{I,tran}}\right) \sum_{m=1}^{2} P_m^{\mathrm{B,AC,max}}$$

$$C_{\mathrm{OPEX,B}} = C_{\mathrm{OPEX,fix,B}} + C_{\mathrm{OPEX,var,B}}$$

$$C_{\mathrm{OPEX,fix,B}} = K_{\mathrm{DF}} \left(C_{\mathrm{OM,fix,B}} + C_{\mathrm{OM,fix,con}}\right) \sum_{m=1}^{2} P_m^{\mathrm{B,DC,max}} + K_{\mathrm{DF}} \left(C_{\mathrm{OM,fix,inv}} + C_{\mathrm{OM,fix,tran}}\right) \sum_{m=1}^{2} P_m^{\mathrm{B,AC,max}}$$

$$C_{\mathrm{OPEX,var,B}} = 365 K_{\mathrm{DF}} (C_{\mathrm{OM,var,B}} + C_{\mathrm{OM,var,con}} + C_{\mathrm{OM,var,inv}}) \sum_{m=1}^{2} \sum_{t_{\mathrm{GC}}=1}^{T_{\mathrm{GC}}} P_{t_{\mathrm{GC}},m}^{\mathrm{B,AC,dis}}$$

$$C_{\mathrm{loss,B}} = 365 K_{\mathrm{DF}} C_{\mathrm{el}} \left(1 - \eta_{\mathrm{rt}}\right) \sum_{m=1}^{2} \sum_{t_{\mathrm{GC}}=1}^{T_{\mathrm{GC}}} P_{t_{\mathrm{GC}},m}^{\mathrm{B,AC,ch}}$$

Note that a factor of 365 is introduced in the expressions for the BESS variable OEPX $C_{\mathrm{OPEX,var,B}}$ and the cost of losses $C_{\mathrm{loss,B}}$. This is because we assume that all days of the year have an identical load profile. Furthermore, the problem formulation also assumes that all years during the project life of N have the same load profile.

A.1.2 Constraints

Maximum power import and export between the microgrid and the upstream distribution grid:

$$-P_{m}^{\mathrm{MG,max}} \leq \Delta P_{t_{\mathrm{GC}},m}^{\mathrm{L,AC}} - P_{t_{\mathrm{GC}},m}^{\mathrm{B,AC}} \leq P_{m}^{\mathrm{MG,max}}, \quad \forall t_{\mathrm{GC}} \forall m$$

Maximum power capacity of BESS:

$$0 \leq P_{t_{\mathrm{GC}},m}^{\mathrm{B,AC,dis}}, P_{t_{\mathrm{GC}},m}^{\mathrm{B,AC,ch}} \leq P_{m}^{\mathrm{B,AC,max}}, \quad \forall t_{\mathrm{GC}} \forall m$$

$$0 \leq P_{t_{\mathrm{GC}},m}^{\mathrm{B,DC,dis}}, P_{t_{\mathrm{GC}},m}^{\mathrm{B,DC,ch}} \leq P_{m}^{\mathrm{B,DC,max}}, \quad \forall t_{\mathrm{GC}} \forall m$$

Maximum and minimum energy capacity of BESS:

$$SOC_{\mathrm{min,GC}} E_{m}^{\mathrm{B,max}} \leq e_{t_{\mathrm{GC}},m}^{\mathrm{B}} \leq SOC_{\mathrm{max,GC}} E_{m}^{\mathrm{B,max}}, \quad \forall t_{\mathrm{GC}} \forall m$$

Energy level of BESS:

$$e_{t_{\mathrm{GC}}=1,m}^{\mathrm{B}} = E_{m}^{\mathrm{B,init}} + \eta_{\mathrm{ch,eq}} P_{t_{\mathrm{GC}}=\mathrm{T}_{\mathrm{GC}},m}^{\mathrm{B,AC,ch}} \Delta t_{\mathrm{GC}} - \frac{P_{t_{\mathrm{GC}}=\mathrm{T}_{\mathrm{GC}},m}^{\mathrm{B,AC,dis}}}{\eta_{\mathrm{dis,eq}}} \Delta t_{\mathrm{GC}}, \quad \forall m$$

$$e_{t_{\mathrm{GC}},m}^{\mathrm{B}} = e_{t_{\mathrm{GC}}-1,m}^{\mathrm{B}} + \eta_{\mathrm{ch,eq}} P_{t_{\mathrm{GC}}-1,m}^{\mathrm{B,AC,ch}} \Delta t_{\mathrm{GC}} - \frac{P_{t_{\mathrm{GC}}-1,m}^{\mathrm{B,AC,dis}}}{\eta_{\mathrm{dis,eq}}} \Delta t_{\mathrm{GC}}, \quad \forall t_{\mathrm{GC}} \forall m$$

$$E_{m}^{\mathrm{B,init}} = e_{t_{\mathrm{GC}}=T_{\mathrm{GC}},m}^{B}, \quad \forall m$$

Net power of BESS:

$$P_{t_{\mathrm{GC}},m}^{\mathrm{B,AC}} = P_{t_{\mathrm{GC}},m}^{\mathrm{B,AC,dis}} - P_{t_{\mathrm{GC}},m}^{\mathrm{B,AC,ch}}, \quad \forall t_{\mathrm{GC}} \forall m$$

$$P_{t_{\mathrm{GC}},m}^{\mathrm{B,DC}} = P_{t_{\mathrm{GC}},m}^{\mathrm{B,DC,dis}} - P_{t_{\mathrm{GC}},m}^{\mathrm{B,DC,ch}}, \quad \forall t_{\mathrm{GC}} \forall m$$

Relation between DC and AC power of BESS:

$$P_{t_{\mathrm{GC}},m}^{\mathrm{B,DC,ch}} = \eta_{\mathrm{inv}} \eta_{\mathrm{tran}} P_{t_{\mathrm{GC}},m}^{\mathrm{B,AC,ch}}, \quad \forall t_{\mathrm{GC}} \forall m$$

$$P_{t_{\mathrm{GC}},m}^{\mathrm{B,DC,dis}} = \frac{P_{t_{\mathrm{GC}},m}^{\mathrm{B,AC,dis}}}{\eta_{\mathrm{inv}} \eta_{\mathrm{tran}}}, \quad \forall t_{\mathrm{GC}} \forall m$$

A.2 Interconnected microgrids by B2B converter problem formulation

A.2.1 Objective function

$$\begin{aligned} OF = \mathrm{Min}\{&C_{\text{CAPEX,B}} + C_{\text{OPEX,B}} + C_{\text{loss,B}} \\ &+ C_{\text{CAPEX,B2B}} + C_{\text{OPEX,B2B}} + C_{\text{loss,B2B}}\} \end{aligned}$$

$$\begin{aligned} C_{\text{CAPEX,B}} = C_{\text{I,B}} \sum_{m=1}^{2} E_m^{\text{B,max}} + C_{\text{I,con}} \sum_{m=1}^{2} P_m^{\text{B,DC,max}} \\ + \left(C_{\text{I,inv}} + C_{\text{I,tran}}\right) \sum_{m=1}^{2} P_m^{\text{B,AC,max}} \end{aligned}$$

$$C_{\text{CAPEX,B2B}} = \left(C_{\text{I,inv}} + C_{\text{I,tran}}\right) \sum_{m=1}^{2} P_m^{\text{B2B,max}} + C_{\text{I,cable}} P_2^{\text{B2B,max}}$$

$$C_{\text{OPEX,B}} = C_{\text{OPEX,fix,B}} + C_{\text{OPEX,var,B}}$$

$$\begin{aligned} C_{\text{OPEX,fix,B}} = K_{\text{DF}} \left(C_{\text{OM,fix,B}} + C_{\text{OM,fix,con}}\right) \sum_{m=1}^{2} P_m^{\text{B,DC,max}} \\ + K_{\text{DF}} \left(C_{\text{OM,fix,inv}} + C_{\text{OM,fix,tran}}\right) \sum_{m=1}^{2} P_m^{\text{B,AC,max}} \end{aligned}$$

$$\begin{aligned} C_{\text{OPEX,var,B}} = 365 K_{\text{DF}} (C_{\text{OM,var,B}} + C_{\text{OM,var,con}} \\ + C_{\text{OM,var,inv}}) \sum_{m=1}^{2} \sum_{t_{\text{GC}}=1}^{T_{\text{GC}}} P_{t_{\text{GC}},m}^{\text{B,AC,dis}} \end{aligned}$$

$$C_{\text{OPEX,B2B}} = C_{\text{OPEX,B2B,fix}} + C_{\text{OPEX,B2B,var}}$$

$$C_{\text{OPEX,fix,B2B}} = K_{\text{DF}} \left(C_{\text{OM,fix,inv}} + C_{\text{OM,fix,tran}}\right) \sum_{m=1}^{2} P_m^{\text{B2B,max}}$$

$$C_{\text{OPEX,var,B2B}} = 365 K_{\text{DF}} \frac{C_{\text{OM,var,inv}}}{2} \sum_{m=1}^{2} \sum_{t_{\text{GC}}=1}^{T_{\text{GC}}} \left(P_{t_{\text{GC}},m}^{\text{B2B,in}} + P_{t_{\text{GC}},m}^{\text{B2B,out}}\right)$$

$$C_{\text{loss,B}} = 365 K_{\text{DF}} C_{\text{el}} \left(1 - \eta_{\text{rt}}\right) \sum_{m=1}^{2} \sum_{t_{\text{GC}}=1}^{T_{\text{GC}}} P_{t_{\text{GC}},m}^{\text{B,AC,ch}}$$

$$C_{\text{loss,B2B}} = 365 K_{\text{DF}} C_{\text{el}} \left(1 - \eta_{\text{inv}} \eta_{\text{tran}}\right) \sum_{m=1}^{2} \sum_{t_{\text{GC}}=1}^{T_{\text{GC}}} \left(P_{t_{\text{GC}},m}^{\text{B2B,in}} + P_{t_{\text{GC}},m}^{\text{B2B,out}}\right)$$

Note that a factor of 365 is introduced in the expressions for the BESS variable OEPX $C_{\text{OPEX,var,B}}$ and the cost of losses $C_{\text{loss,B}}$ and that for the B2B converter variable OPEX $C_{\text{OPEX,var,B2B}}$ and the cost of losses $C_{\text{loss,B2B}}$. This is because we assume that all days of the year have an identical load profile. Furthermore, the problem formulation also assumes that all years during the project life of N have the same load profile.

A.2.2 Constraints

Maximum power import and export between the microgrid and the upstream distribution grid:

$$-P_m^{\text{MG,max}} \leq \Delta P_{t_{\text{GC}},m}^{\text{L,AC}} - P_{t_{\text{GC}},m}^{\text{B2B}} - P_{t_{\text{GC}},m}^{\text{B,AC}} \leq P_m^{\text{MG,max}}, \quad \forall t_{\text{GC}} \forall m$$

Maximum power capacity of B2B converter:

$$0 \leq P_{t_{\text{GC}},m}^{\text{B2B,out}}, P_{t_{\text{GC}},m}^{\text{B2B,in}} \leq P_m^{\text{B2B,max}}, \quad \forall t_{\text{GC}} \forall m$$

Maximum power capacity of BESS:

$$0 \leq P_{t_{\text{GC}},m}^{\text{B,AC,dis}}, P_{t_{\text{GC}},m}^{\text{B,AC,ch}} \leq P_m^{\text{B,AC,max}}, \quad \forall t_{\text{GC}} \forall m$$

$$0 \leq P^{\mathrm{B,DC,dis}}_{t_{\mathrm{GC}},m}, P^{\mathrm{B,DC,ch}}_{t_{\mathrm{GC}},m} \leq P^{\mathrm{B,DC,max}}_{m}, \quad \forall t_{\mathrm{GC}} \forall m$$

Maximum and minimum energy capacity of BESS:

$$SOC_{\mathrm{min,GC}} E^{\mathrm{B,max}}_{m} \leq e^{\mathrm{B}}_{t_{\mathrm{GC}},m} \leq SOC_{\mathrm{max,GC}} E^{\mathrm{B,max}}_{m}, \quad \forall t_{\mathrm{GC}} \forall m$$

Energy level of BESS:

$$e^{\mathrm{B}}_{t_{\mathrm{GC}}=1,m} = E^{\mathrm{B,init}}_{m} + \eta_{\mathrm{ch,eq}} P^{\mathrm{B,AC,ch}}_{t_{\mathrm{GC}}=\mathrm{T}_{\mathrm{GC}},m} \Delta t_{\mathrm{GC}} - \frac{P^{\mathrm{B,AC,dis}}_{t_{\mathrm{GC}}=\mathrm{T}_{\mathrm{GC}},m}}{\eta_{\mathrm{dis,eq}}} \Delta t_{\mathrm{GC}}, \quad \forall m$$

$$e^{\mathrm{B}}_{t_{\mathrm{GC}},m} = e^{\mathrm{B}}_{t_{\mathrm{GC}}-1,m} + \eta_{\mathrm{ch,eq}} P^{\mathrm{B,AC,ch}}_{t_{\mathrm{GC}}-1,m} \Delta t_{\mathrm{GC}} - \frac{P^{\mathrm{B,AC,dis}}_{t_{\mathrm{GC}}-1,m}}{\eta_{\mathrm{dis,eq}}} \Delta t_{\mathrm{GC}}, \quad \forall t_{\mathrm{GC}} \forall m$$

$$E^{\mathrm{B,init}}_{m} = e^{B}_{t_{\mathrm{GC}}=T_{\mathrm{GC}},m}, \quad \forall m$$

DC-link power balance of B2B converter:

$$\sum_{m=1}^{2} P^{\mathrm{B2B}}_{t_{\mathrm{GC}},m} + \sum_{m=1}^{2} P^{\mathrm{B2B,loss}}_{t_{\mathrm{GC}},m} = 0, \quad \forall t_{\mathrm{GC}}$$

$$P^{\mathrm{B2B,loss}}_{t_{\mathrm{GC}},m} = (P^{\mathrm{B2B,out}}_{t_{\mathrm{GC}},m} + P^{\mathrm{B2B,in}}_{t_{\mathrm{GC}},m})(1 - \eta_{\mathrm{inv}} \eta_{\mathrm{tran}}), \quad \forall t_{\mathrm{GC}} \forall m$$

Net power of B2B converter:

$$P^{\mathrm{B2B}}_{t_{\mathrm{GC}},m} = P^{\mathrm{B2B,out}}_{t_{\mathrm{GC}},m} - P^{\mathrm{B2B,in}}_{t_{\mathrm{GC}},m}, \quad \forall t_{\mathrm{GC}} \forall m$$

Net power of BESS:

$$P^{\mathrm{B,AC}}_{t_{\mathrm{GC}},m} = P^{\mathrm{B,AC,dis}}_{t_{\mathrm{GC}},m} - P^{\mathrm{B,AC,ch}}_{t_{\mathrm{GC}},m}, \quad \forall t_{\mathrm{GC}} \forall m$$

$$P^{\mathrm{B,DC}}_{t_{\mathrm{GC}},m} = P^{\mathrm{B,DC,dis}}_{t_{\mathrm{GC}},m} - P^{\mathrm{B,DC,ch}}_{t_{\mathrm{GC}},m}, \quad \forall t_{\mathrm{GC}} \forall m$$

Relation between DC and AC power of BESS:

$$P^{\mathrm{B,DC,ch}}_{t_{\mathrm{GC}},m} = \eta_{\mathrm{inv}} \eta_{\mathrm{tran}} P^{\mathrm{B,AC,ch}}_{t_{\mathrm{GC}},m}, \quad \forall t_{\mathrm{GC}} \forall m$$

$$P_{t_{\mathrm{GC}},m}^{\mathrm{B,DC,dis}} = \frac{P_{t_{\mathrm{GC}},m}^{\mathrm{B,AC,dis}}}{\eta_{\mathrm{inv}}\eta_{\mathrm{tran}}}, \quad \forall t_{\mathrm{GC}} \forall m$$

A.3 Interconnected microgrids by MPC problem formulation

A.3.1 Objective function

$$\begin{aligned} OF = \mathrm{Min}\{ & C_{\mathrm{CAPEX,B}} + C_{\mathrm{OPEX,B}} + C_{\mathrm{loss,B}} \\ & + C_{\mathrm{CAPEX,MPC}} + C_{\mathrm{OPEX,MPC}} + C_{\mathrm{loss,MPC}}\} \end{aligned}$$

$$C_{\mathrm{CAPEX,B}} = C_{\mathrm{I,B}} E^{\mathrm{B,max}} + C_{\mathrm{I,con}} P^{\mathrm{B,DC,max}}$$

$$C_{\mathrm{CAPEX,MPC}} = (C_{\mathrm{I,inv}} + C_{\mathrm{I,tran}}) \sum_{m=1}^{2} P_m^{\mathrm{MPC,max}} + C_{\mathrm{I,cable}} P_2^{\mathrm{MPC,max}}$$

$$C_{\mathrm{OPEX,B}} = C_{\mathrm{OPEX,B,fix}} + C_{\mathrm{OPEX,B,var}}$$

$$C_{\mathrm{OPEX,fix,B}} = K_{\mathrm{DF}} \left(C_{\mathrm{OM,fix,B}} + C_{\mathrm{OM,fix,con}} \right) \sum_{m=1}^{2} P_m^{\mathrm{B,DC,max}}$$

$$C_{\mathrm{OPEX,var,B}} \quad = \quad 365 K_{\mathrm{DF}} (C_{\mathrm{OM,var,B}} \; + \; C_{\mathrm{OM,var,con}}) \sum_{m=1}^{2} \sum_{t_{\mathrm{GC}}=1}^{T_{\mathrm{GC}}} P_{t_{\mathrm{GC}},m}^{\mathrm{B,DC,dis}}$$

$$C_{\mathrm{OPEX,MPC}} = C_{\mathrm{OPEX,fix,MPC}} + C_{\mathrm{OPEX,var,MPC}}$$

$$C_{\mathrm{OPEX,fix,MPC}} = K_{\mathrm{DF}} \left(C_{\mathrm{OM,fix,inv}} + C_{\mathrm{OM,fix,tran}} \right) \sum_{m=1}^{2} P_m^{\mathrm{MPC,max}}$$

$$C_{\mathrm{OPEX,var,MPC}} = 365 K_{\mathrm{DF}} \frac{C_{\mathrm{OM,var,inv}}}{2} \sum_{m=1}^{2} \sum_{t_{\mathrm{GC}}=1}^{T_{\mathrm{GC}}} \left(P_{t_{\mathrm{GC}},m}^{\mathrm{MPC,in}} + P_{t_{\mathrm{GC}},m}^{\mathrm{MPC,out}} \right)$$

$$C_{\mathrm{loss,B}} = 365 K_{\mathrm{DF}} C_{\mathrm{el}} \left(1 - \eta_{\mathrm{ch}} \eta_{\mathrm{con}}\right) \sum_{m=1}^{2} \sum_{t_{\mathrm{GC}}=1}^{T_{\mathrm{GC}}} P_{t_{\mathrm{GC}}}^{\mathrm{B,DC,ch}}$$

$$C_{\mathrm{loss,MPC}} = 365 K_{\mathrm{DF}} C_{\mathrm{el}} \left(1 - \eta_{\mathrm{inv}} \eta_{\mathrm{tran}}\right) \sum_{m=1}^{2} \sum_{t_{\mathrm{GC}}=1}^{T_{\mathrm{GC}}} \left(P_{t_{\mathrm{GC}},m}^{\mathrm{MPC,in}} + P_{t_{\mathrm{GC}},m}^{\mathrm{MPC,out}} \right)$$

Note that a factor of 365 is introduced in the expressions for the BESS variable OEPX $C_{\mathrm{OPEX,var,B}}$ and the cost of losses $C_{\mathrm{loss,B}}$ and for the MPC variable OPEX $C_{\mathrm{OPEX,var,MPC}}$ and the cost of losses $C_{\mathrm{loss,MPC}}$. This is because we assume that all days of the year have an identical load profile. This is true for Section 2.3 when a generic load profile has been used. However, in section 2.4, a load profile of industrial and community microgrids is used based on the historical recording of one calendar year. Therefore, in the latter case, the factor of 365 must be omitted from the expressions.

Furthermore, unlike in Sections A.1 and A.2, where the CAPEX, OPEX and losses costs of BESS accounted for the battery, DC/DC converter, and DC/AC converter, this section neglects the DC/AC converter in the BESS cost calculations. This is because the BESS is integrated to the MPC and the associated cost of the DC/AC converter is accounted for in the MPC cost calculations.

A.3.2 Constraints

Maximum power import and export between the microgrid and the upstream distribution grid:

$$-P_{m}^{\mathrm{MG,max}} \leq \Delta P_{t_{\mathrm{GC}},m}^{\mathrm{L,AC}} - P_{t_{\mathrm{GC}},m}^{\mathrm{MPC}} \leq P_{m}^{\mathrm{MG,max}}, \quad \forall t_{\mathrm{GC}} \forall m$$

Maximum power capacity of MPC AC ports:

$$0 \leq P_{t_{\mathrm{GC}},m}^{\mathrm{MPC,out}}, P_{t_{\mathrm{GC}},m}^{\mathrm{MPC,in}} \leq P_{m}^{\mathrm{MPC,max}}, \quad \forall t_{\mathrm{GC}} \forall m$$

Maximum power capacity of BESS:

$$0 \leq P_{t_{\mathrm{GC}}}^{\mathrm{B,DC,dis}}, P_{t_{\mathrm{GC}}}^{\mathrm{B,DC,ch}} \leq P^{\mathrm{B,DC,max}}, \quad \forall t_{\mathrm{GC}}$$

Maximum and minimum energy capacity of BESS:

$$SOC_{\mathrm{min,GC}} E^{\mathrm{B,max}} \leq e_{t_{\mathrm{GC}}}^{\mathrm{B}} \leq SOC_{\mathrm{max,GC}} E^{\mathrm{B,max}}, \quad \forall t_{\mathrm{GC}}$$

Energy level of BESS:

$$e_{t_{\mathrm{GC}}=1}^{\mathrm{B}} = E^{\mathrm{B,init}} + \eta_{\mathrm{ch}}\eta_{\mathrm{con}} P_{t_{\mathrm{GC}}=\mathrm{T}_{\mathrm{GC}}}^{\mathrm{B,DC,ch}} \Delta t_{\mathrm{GC}} - \frac{P_{t_{\mathrm{GC}}=\mathrm{T}_{\mathrm{GC}}}^{\mathrm{B,DC,dis}}}{\eta_{\mathrm{dis}}\eta_{\mathrm{con}}} \Delta t_{\mathrm{GC}}$$

$$e_{t_{\mathrm{GC}}}^{\mathrm{B}} = e_{t_{\mathrm{GC}}-1}^{\mathrm{B}} + \eta_{\mathrm{ch}}\eta_{\mathrm{con}} P_{t_{\mathrm{GC}}-1}^{\mathrm{B,DC,ch}} \Delta t_{\mathrm{GC}} - \frac{P_{t_{\mathrm{GC}}-1}^{\mathrm{B,DC,dis}}}{\eta_{\mathrm{dis}}\eta_{\mathrm{con}}} \Delta t_{\mathrm{GC}}, \quad \forall t_{\mathrm{GC}} \geq 2$$

$$E^{\mathrm{B,init}} = e_{t_{\mathrm{GC}}=T_{\mathrm{GC}}}^{B}, \quad \forall m$$

DC-link power balance of MPC:

$$P_{t_{\mathrm{GC}}}^{\mathrm{B,DC}} = \sum_{m=1}^{2} P_{t_{\mathrm{GC}},m}^{\mathrm{MPC}} + \sum_{m=1}^{2} P_{t_{\mathrm{GC}},m}^{\mathrm{MPC,loss}} + P_{t_{\mathrm{GC}}}^{\mathrm{L,DC}}, \quad \forall t_{\mathrm{GC}}$$

$$P_{t_{\mathrm{GC}},m}^{\mathrm{MPC,loss}} = (P_{t_{\mathrm{GC}},m}^{\mathrm{MPC,out}} + P_{t_{\mathrm{GC}},m}^{\mathrm{MPC,in}})(1 - \eta_{\mathrm{inv}}\eta_{\mathrm{tran}}), \quad \forall t_{\mathrm{GC}} \forall m$$

Net power of MPC:

$$P_{t_{\mathrm{GC}},m}^{\mathrm{MPC}} = P_{t_{\mathrm{GC}},m}^{\mathrm{MPC,out}} - P_{t_{\mathrm{GC}},m}^{\mathrm{MPC,in}}, \quad \forall t_{\mathrm{GC}} \forall m$$

Net power of BESS:

$$P_{t_{\mathrm{GC}}}^{\mathrm{B,DC}} = P_{t_{\mathrm{GC}}}^{\mathrm{B,DC,dis}} - P_{t_{\mathrm{GC}}}^{\mathrm{B,DC,ch}}, \quad \forall t_{\mathrm{GC}} \forall m$$

Note that the expression for the DC-link power balance of MPC assumes that there is a DC load $P_{t_{\mathrm{GC}}}^{\mathrm{L,DC}}$ integrated to the DC-link of the MPC. However, this is only true in Section 2.4.3. In Section 2.4.2, the DC load is neglected in the analysis.

APPENDIX B

Problem formulation for sizing of BESS to mitigate grid capacity bottleneck and facilitate island operation and island transition capabilities of a microgrid

This appendix presents the problem formulation for sizing of a BESS to mitigate grid capacity bottleneck and simultaneously facilitate an island operation and secure island transition capabilities of a microgrid. This appendix supports the material in Chapter 4.

B.1 Objective function

$$OF = \text{Min}\{C_{\text{CAPEX}} + C_{\text{OPEX}} + C_{\text{loss,GC}} + C_{\text{loss,IO}} + C_{\text{loss,IT}}\}$$

$$C_{\text{CAPEX}} \quad = \quad C_{\text{I,B}} E^{\text{B,max}} \; + \; C_{\text{I,con}} P^{\text{B,max}} \; + \; \left(C_{\text{I,inv}} + C_{\text{I,tran}}\right) P^{\text{BL,max}}$$

$$C_{\text{OPEX}} = C_{\text{OPEX,fix}} + C_{\text{OPEX,var}}$$

$$\begin{aligned} C_{\text{OPEX,fix}} = K_{\text{DF}} \left(C_{\text{OM,fix,B}} + C_{\text{OM,fix,con}} \right) P^{\text{B,max}} \\ + K_{\text{DF}} \left(C_{\text{OM,fix,inv}} + C_{\text{OM,fix,tran}} \right) P^{\text{BL,max}} \end{aligned}$$

$$\begin{aligned} C_{\text{OPEX,var}} = 365 K_{\text{DF}} \left(C_{\text{OM,var,B}} + C_{\text{OM,var,con}} \right) \sum_{t_{\text{GC}}=1}^{T_{\text{GC}}} P_{t_{\text{GC}}}^{\text{B,dis}} + \\ 365 K_{\text{DF}} \frac{C_{\text{OM,var,inv}}}{2} \sum_{t_{\text{GC}}=1}^{T_{\text{GC}}} \left(P_{t_{\text{GC}}}^{\text{BL,in}} + P_{t_{\text{GC}}}^{\text{BL,out}} \right) \end{aligned}$$

$$\begin{aligned} C_{\text{loss,GC}} = 365 K_{\text{DF}} C_{\text{el}} \left(1 - \eta_{\text{ch}} \eta_{\text{dis}} \eta_{\text{con}}^{2} \right) \sum_{t_{\text{GC}}=1}^{T_{\text{GC}}} P_{t_{\text{GC}}}^{\text{B,ch}} + \\ 365 K_{\text{DF}} C_{\text{el}} \left(1 - \eta_{\text{inv}} \eta_{\text{tran}} \right) \sum_{t_{\text{GC}}=1}^{T_{\text{GC}}} \left(P_{t_{\text{GC}}}^{\text{BL,in}} + P_{t_{\text{GC}}}^{\text{BL,out}} \right) \end{aligned}$$

$$\begin{aligned} C_{\text{loss,IO}} = C_{\text{el}} \left(1 - \eta_{\text{ch}} \eta_{\text{dis}} \eta_{\text{con}}^{2} \right) \sum_{t_{\text{IO}}=1}^{T_{\text{IO}}} P_{t_{\text{IO}}}^{\text{B,ch}} \\ + C_{\text{el}} \left(1 - \eta_{\text{inv}} \eta_{\text{tran}} \right) \sum_{t_{\text{IO}}=1}^{T_{\text{IO}}} \left(P_{t_{\text{IO}}}^{\text{BL,in}} + P_{t_{\text{IO}}}^{\text{BL,out}} \right) \end{aligned}$$

$$C_{\text{loss,IT}} = C_{\text{el}} \left(1 - \eta_{\text{inv}} \eta_{\text{tran}} \right) \sum_{t_{\text{IT}}=1}^{T_{\text{IT}}} \left(P_{t_{\text{IT}}}^{\text{BL,in}} + P_{t_{\text{IT}}}^{\text{BL,out}} \right)$$

B.2 Constraints for mitigating grid capacity bottleneck

Maximum power import and export between the microgrid and the upstream distribution grid:

$$-P^{\text{MG,max}} \leq P^{\text{L,AC,crit}} + P_{t_{\text{GC}}}^{\text{L,AC,ncrit}} - P_{t_{\text{GC}}}^{\text{hy}} - P_{t_{\text{GC}}}^{\text{rn}} \leq P^{\text{MG,max}}, \quad \forall t_{\text{GC}}$$

Maximum power capacity of DC/AC converter:

$$0 \leq P_{t_{\text{GC}}}^{\text{BL,out}}, P_{t_{\text{GC}}}^{\text{BL,in}} \leq P^{\text{BL,max}}, \quad \forall t_{\text{GC}}$$

Maximum power capacity of BESS:

$$0 \leq P_{t_{\text{GC}}}^{\text{B,dis}}, P_{t_{\text{GC}}}^{\text{B,ch}} \leq P^{\text{B,max}}, \quad \forall t_{\text{GC}}$$

Maximum and minimum energy capacity of BESS:

$$SOC_{\text{min,GC}} E^{\text{B,max}} \leq e_{t_{\text{GC}}}^{\text{B}} \leq SOC_{\text{max,GC}} E^{\text{B,max}}, \quad \forall t_{\text{GC}}$$

Energy level of BESS:

$$e_{t_{\text{GC}}=1}^{\text{B}} = E^{\text{B,init}} + \eta_{\text{ch}}\eta_{\text{con}} P_{t_{\text{GC}}=\text{T}_{\text{GC}}}^{\text{B,ch}} \Delta t_{\text{GC}} - \frac{P_{t_{\text{GC}}=\text{T}_{\text{GC}}}^{\text{B,dis}}}{\eta_{\text{dis}}\eta_{\text{con}}} \Delta t_{\text{GC}}, \quad \forall t_{\text{GC}}$$

$$e_{t_{\text{GC}}}^{\text{B}} = e_{t_{\text{GC}}-1}^{\text{B}} + \eta_{\text{ch}}\eta_{\text{con}} P_{t_{\text{GC}}-1}^{\text{B,ch}} \Delta t_{\text{GC}} - \frac{P_{t_{\text{GC}}-1}^{\text{B,dis}}}{\eta_{\text{dis}}\eta_{\text{con}}} \Delta t_{\text{GC}}, \quad \forall t_{\text{GC}}$$

$$E^{\text{B,init}} = e_{t_{\text{GC}}=T_{\text{GC}}}^{\text{B}}$$

DC-link power balance of integrated BESS and DC load:

$$P_{t_{\text{GC}}}^{\text{B}} = P^{\text{L,DC,crit}} + P_{t_{\text{GC}}}^{\text{L,DC,ncrit}} + P_{t_{\text{GC}}}^{\text{BL}} + P_{t_{\text{GC}}}^{\text{BL,loss}}, \quad \forall t_{\text{GC}}$$

$$P_{t_{\text{GC}}}^{\text{BL,loss}} = \left(P_{t_{\text{GC}}}^{\text{BL,in}} + P_{t_{\text{GC}}}^{\text{BL,out}}\right)\left(1 - \eta_{\text{inv}}\eta_{\text{tran}}\right), \quad \forall t_{\text{GC}}$$

Net power of DC/AC converter:

$$P_{t_{\text{GC}}}^{\text{BL}} = P_{t_{\text{GC}}}^{\text{BL,out}} - P_{t_{\text{GC}}}^{\text{BL,in}}, \quad \forall t_{\text{GC}}$$

Net power of BESS:

$$P^{\mathrm{B}}_{t_{\mathrm{GC}}} = P^{\mathrm{B,dis}}_{t_{\mathrm{GC}}} - P^{\mathrm{B,ch}}_{t_{\mathrm{GC}}}, \quad \forall t_{\mathrm{GC}}$$

B.3 Constraints for island capability

AC power balance without access to the upstream distribution grid:

$$P^{\mathrm{L,AC,crit}} + P^{\mathrm{L,AC,ncrit}}_{t_{\mathrm{IO}}} - P^{\mathrm{hy}}_{t_{\mathrm{IO}}} - P^{\mathrm{rn}}_{t_{\mathrm{IO}}} - P^{\mathrm{BL}}_{t_{\mathrm{IO}}} = 0, \quad \forall t_{\mathrm{IO}}$$

Maximum power capacity of DC/AC converter:

$$0 \leq P^{\mathrm{BL,out}}_{t_{\mathrm{IO}}}, P^{\mathrm{BL,in}}_{t_{\mathrm{IO}}} \leq P^{\mathrm{BL,max}}, \quad \forall t_{\mathrm{IO}}$$

Maximum power capacity of BESS:

$$0 \leq P^{\mathrm{B,dis}}_{t_{\mathrm{IO}}}, P^{\mathrm{B,ch}}_{t_{\mathrm{IO}}} \leq P^{\mathrm{B,max}}, \quad \forall t_{\mathrm{IO}}$$

Maximum and minimum energy capacity of BESS:

$$SOC_{\mathrm{min,IO}} E^{\mathrm{B,max}} \leq e^{\mathrm{B}}_{t_{\mathrm{IO}}} \leq SOC_{\mathrm{max,IO}} E^{\mathrm{B,max}}, \quad \forall t_{\mathrm{IO}}$$

Energy level of BESS:

$$e^{\mathrm{B}}_{t_{\mathrm{IO}}} = e^{\mathrm{B}}_{t_{\mathrm{GC}}=t_{\mathrm{IT}}}, \quad \forall t_{\mathrm{IT}} \forall t_{\mathrm{IO}} = t_{\mathrm{IT}} + (t_{\mathrm{IT}} - 1) T_{\mathrm{IO}}$$

$$e^{\mathrm{B}}_{t_{\mathrm{IO}}} = e^{\mathrm{B}}_{t_{\mathrm{IO}}-1} + \eta_{\mathrm{ch}} \eta_{\mathrm{con}} P^{\mathrm{B,ch}}_{t_{\mathrm{IO}}-1} \Delta t_{\mathrm{IO}} - \frac{P^{\mathrm{B,dis}}_{t_{\mathrm{IO}}-1}}{\eta_{\mathrm{dis}} \eta_{\mathrm{con}}} \Delta t_{\mathrm{IO}}, \quad \forall t_{\mathrm{IO}} = t_{\mathrm{IT}} + (t_{\mathrm{IT}} - 1) T_{\mathrm{ID}} + 1 : t_{\mathrm{IT}} + t_{\mathrm{IT}} T_{\mathrm{ID}}$$

DC-link power balance of integrated BESS and DC load:

$$P^{\mathrm{B}}_{t_{\mathrm{IO}}} = P^{\mathrm{L,DC,crit}} + P^{\mathrm{L,DC,ncrit}}_{t_{\mathrm{IO}}} + P^{\mathrm{BL}}_{t_{\mathrm{IO}}} + P^{\mathrm{BL,loss}}_{t_{\mathrm{IO}}}, \quad \forall t_{\mathrm{IO}}$$

$$P^{\mathrm{BL,loss}}_{t_{\mathrm{IO}}} = \left(P^{\mathrm{BL,in}}_{t_{\mathrm{IO}}} + P^{\mathrm{BL,out}}_{t_{\mathrm{IO}}} \right) (1 - \eta_{\mathrm{inv}} \eta_{\mathrm{tran}}), \quad \forall t_{\mathrm{IO}}$$

Maximum and minimum power capacity of hydro power plant:

$$P^{\mathrm{hy,min}} \leq P^{\mathrm{hy}}_{t_{\mathrm{IO}}} \leq P^{\mathrm{hy,max}}, \quad \forall t_{\mathrm{IO}}$$

Power balancing by renewable generation curtailment:

$$P^{\mathrm{rn}}_{t_{\mathrm{IO}}} = \varepsilon^{\mathrm{rn}}_{t_{\mathrm{IO}}} P^{\mathrm{rn}}_{t_{\mathrm{GC}}=t_{\mathrm{IO}}-(t_{\mathrm{IT}}-1)T_{\mathrm{ID}}}, \quad \forall t_{\mathrm{IT}} \forall t_{\mathrm{IO}} = t_{\mathrm{IT}} + (t_{\mathrm{IT}}-1)T_{\mathrm{ID}} : t_{\mathrm{IT}} + t_{\mathrm{IT}} T_{\mathrm{ID}}$$

$$0 \leq \varepsilon^{\mathrm{rn}}_{t_{\mathrm{IO}}} \leq 1, \quad \forall t_{\mathrm{IO}}$$

Power balancing by AC and DC non-critical load shedding:

$$P^{\mathrm{L,AC,ncrit}}_{t_{\mathrm{IO}}} = \varepsilon^{\mathrm{L,AC,ncrit}}_{t_{\mathrm{IO}}} P^{\mathrm{L,AC,ncrit}}_{t_{\mathrm{GC}}=t_{\mathrm{IO}}-(t_{\mathrm{IT}}-1)T_{\mathrm{ID}}}, \quad \forall t_{\mathrm{IT}} \forall t_{\mathrm{IO}} = t_{\mathrm{IT}} + (t_{\mathrm{IT}}-1)T_{\mathrm{ID}} : t_{\mathrm{IT}} + t_{\mathrm{IT}} T_{\mathrm{ID}}$$

$$P^{\mathrm{L,DC,ncrit}}_{t_{\mathrm{IO}}} = \varepsilon^{\mathrm{L,DC,ncrit}}_{t_{\mathrm{IO}}} P^{\mathrm{L,DC,ncrit}}_{t_{\mathrm{GC}}=t_{\mathrm{IO}}-(t_{\mathrm{IT}}-1)T_{\mathrm{ID}}}, \quad \forall t_{\mathrm{IT}} \forall t_{\mathrm{IO}} = t_{\mathrm{IT}} + (t_{\mathrm{IT}}-1)T_{\mathrm{ID}} : t_{\mathrm{IT}} + t_{\mathrm{IT}} T_{\mathrm{ID}}$$

$$0 \leq \varepsilon^{\mathrm{L,AC,ncrit}}_{t_{\mathrm{IO}}}, \varepsilon^{\mathrm{L,DC,ncrit}}_{t_{\mathrm{IO}}} \leq 1, \quad \forall t_{\mathrm{IO}}$$

Net power of DC/AC converter:

$$P^{\mathrm{BL}}_{t_{\mathrm{IO}}} = P^{\mathrm{BL,out}}_{t_{\mathrm{IO}}} - P^{\mathrm{BL,in}}_{t_{\mathrm{IO}}}, \quad \forall t_{\mathrm{IO}}$$

Net power of BESS:

$$P^{\mathrm{B}}_{t_{\mathrm{IO}}} = P^{\mathrm{B,dis}}_{t_{\mathrm{IO}}} - P^{\mathrm{B,ch}}_{t_{\mathrm{IO}}}, \quad \forall t_{\mathrm{IO}}$$

B.4 Constraints for successful island transition capability

Dynamic AC power balance:

$$P^{\mathrm{L,AC,crit}} + P^{\mathrm{L,AC,ncrit}}_{t_{\mathrm{IT}}} - P^{\mathrm{hy}}_{t_{\mathrm{GC}}} - P^{\mathrm{rn}}_{t_{\mathrm{GC}}} - P^{\mathrm{BL}}_{t_{\mathrm{IT}}} = 0, \quad \forall t_{\mathrm{IT}} = t_{\mathrm{GC}}$$

Maximum power capacity of DC/AC converter:

$$0 \leq P^{\mathrm{BL,out}}_{t_{\mathrm{IT}}}, P^{\mathrm{BL,in}}_{t_{\mathrm{IT}}} \leq P^{\mathrm{BL,max}}, \quad \forall t_{\mathrm{IT}}$$

Maximum power capacity of BESS:

$$-P^{\mathrm{B,max}} \leq P^{\mathrm{B}}_{t_{\mathrm{IT}}} \leq P^{\mathrm{B,max}}, \quad \forall t_{\mathrm{IT}}$$

Dynamic DC power balance of integrated BESS and DC load:

$$P^{\mathrm{B}}_{t_{\mathrm{IT}}} = P^{\mathrm{L,DC,crit}} + P^{\mathrm{L,DC,ncrit}}_{t_{\mathrm{IT}}} + P^{\mathrm{BL}}_{t_{\mathrm{IT}}} + P^{\mathrm{BL,loss}}_{t_{\mathrm{IT}}}, \quad \forall t_{\mathrm{IT}}$$

$$P^{\mathrm{BL,loss}}_{t_{\mathrm{IT}}} = \left(P^{\mathrm{BL,in}}_{t_{\mathrm{IT}}} + P^{\mathrm{BL,out}}_{t_{\mathrm{IT}}}\right)(1 - \eta_{\mathrm{inv}}\eta_{\mathrm{tran}}), \quad \forall t_{\mathrm{IT}}$$

Dynamic AC and DC non-critical load shedding:

$$P^{\mathrm{L,AC,ncrit}}_{t_{\mathrm{IT}}} = \varepsilon^{\mathrm{L,AC,ncrit}}_{t_{\mathrm{IT}}} P^{\mathrm{L,AC,ncrit}}_{t_{\mathrm{GC}}}, \quad \forall t_{\mathrm{IT}} = t_{\mathrm{GC}}$$

$$P^{\mathrm{L,DC,ncrit}}_{t_{\mathrm{IT}}} = \varepsilon^{\mathrm{L,DC,ncrit}}_{t_{\mathrm{IT}}} P^{\mathrm{L,DC,ncrit}}_{t_{\mathrm{GC}}}, \quad \forall t_{\mathrm{IT}} = t_{\mathrm{GC}}$$

$$0 \leq \varepsilon^{\mathrm{L,AC,ncrit}}_{t_{\mathrm{IT}}}, \varepsilon^{\mathrm{L,DC,ncrit}}_{t_{\mathrm{IT}}} \leq 1, \quad \forall t_{\mathrm{IT}}$$

Dynamic DC/AC converter net power:

$$P^{\mathrm{BL}}_{t_{\mathrm{IT}}} = P^{\mathrm{BL,out}}_{t_{\mathrm{IT}}} - P^{\mathrm{BL,in}}_{t_{\mathrm{IT}}}, \quad \forall t_{\mathrm{IT}}$$

APPENDIX C

Financial and technical data of battery energy storage and power electronics

This appendix presents the financial and technical data for battery energy storage and power electronics. The data in this appendix support the content presented in Chapters 2 and 4.

Table C.1: Financial and technical input data for optimization problem in Chapters 2 and 4.

Parameter	Description	Value	Reference	Comment
	Financial data of battery			
$C_{\mathrm{I,B}}$	Battery CAPEX	132 kEUR/MWh	[1]	
$C_{\mathrm{OM,fix,B}}$	Battery fixed OPEX	0.18 kEUR/MW/year	[1]	The battery fixed OPEX is assumed one-third of the total fixed OPEX of a BESS
$C_{\mathrm{OM,var,B}}$	Battery variable OPEX	$0.67 \times 10^{-}3$ kEUR/MWh	[1]	The battery variable OPEX is assumed one-third of the total variable OPEX of a BESS
	Financial data of DC/DC converter			
$C_{\mathrm{I,con}}$	DC/DC converter CAPEX	135 kEUR/MW	[1]	The DC/DC converter CAPEX is assumed to be half of the total CAPEX of BESS power component
$C_{\mathrm{OM,fix,con}}$	DC/DC converter fixed OPEX	0.18 kEUR/MW/year	[1]	The DC/DC converter fixed OPEX is assumed to be one-third of the total fixed OPEX of a BESS
$C_{\mathrm{OM,var,con}}$	DC/DC converter variable OPEX	$0.67 \times 10^{-}3$ kEUR/MWh	[1]	The DC/DC converter variable OPEX is assumed to be one-third of the total variable OPEX of a BESS

Financial data of DC/AC converter				
$C_{\mathrm{I,inv}}$	DC/AC converter CAPEX	135 kEUR/MW	[1]	The DC/AC converter CAPEX is assumed to be half of the total CAPEX of BESS power component
$C_{\mathrm{OM,fix,inv}}$	DC/AC converter fixed OPEX	0.18 kEUR/MW/year	[1]	The DC/AC converter fixed OPEX is assumed to be one-third of the total fixed OPEX of a BESS
$C_{\mathrm{OM,var,inv}}$	DC/AC converter variable OPEX	$0.67 \times 10^{-}3$ kEUR/MWh	[1]	The DC/AC converter variable OPEX is assumed to be one-third of the total variable OPEX of a BESS
Financial data of cable				
$C_{\mathrm{I,cable}}$	Cable CAPEX	6 kEUR/MVA.km	[2]	
$C_{\mathrm{OM,cable}}$	Cable OPEX	0	[3]	There is practically no maintenance on cables
Financial data of transformer				
$C_{\mathrm{I,tran}}$	Transformer CAPEX	11.5 kEUR/MVA	[3]	
$C_{\mathrm{OM,fix,tran}}$	Transformer fixed OPEX	0.05865 kEUR/MVA/year	[3]	The fixed OPEX is 0.51% of the CAPEX per year
$C_{\mathrm{OM,var,tran}}$	Transformer variable OPEX	0	[3]	Variable OPEX are very low and considered to be negligible
Other financial data				
C_{el}	Electricity spot market price	21×10^{-3} kEUR/MWh	[4]	Average day ahead price of the year 2020 in SE3
r	Discount rate	5 %		
K_{DF}	Discount factor	12.46		$K_{\mathrm{DF}} = \sum\limits_{y=1}^{N} \frac{1}{(1+r)^y}$
Technical data				
N	Expected project lifetime	20 years	[1]	
η_{ch}	charging efficiency of battery	98%	[1]	
η_{dis}	discharging efficiency of battery	97%	[1]	
η_{con}	DC/DC converter efficiency	99%	[1]	
η_{inv}	DC/AC converter efficiency	99%	[1]	
η_{tran}	Transformer efficiency	99%	[1]	
$\eta_{\mathrm{ch,eq}}$	Charging efficiency of BESS	95%		$\eta_{\mathrm{ch,eq}} = \eta_{\mathrm{ch}}\eta_{\mathrm{con}}\eta_{\mathrm{inv}}\eta_{\mathrm{tran}}$
$\eta_{\mathrm{dis,eq}}$	Discharging efficiency of BESS	94%		$\eta_{\mathrm{dis,eq}} = \eta_{\mathrm{dis}}\eta_{\mathrm{con}}\eta_{\mathrm{inv}}\eta_{\mathrm{tran}}$
η_{rt}	Round trip efficiency of BESS	89.5%		$\eta_{\mathrm{rt}} = \eta_{\mathrm{ch}}\eta_{\mathrm{dis}}\eta_{\mathrm{con}}^2\eta_{\mathrm{inv}}^2\eta_{\mathrm{tran}}^2$
η_{cable}	Cable efficiency	100%		Losses in the cable are neglected since the cable is short
l_{cable}	Cable length	2 km		
$SOC_{\mathrm{max,GC}}$	Maximum SOC level of battery in grid connected mode	80%		
$SOC_{\mathrm{min,GC}}$	Minimum SOC level of battery in grid connected mode	20%		
$SOC_{\mathrm{max,IO}}$	Maximum SOC level of battery in island mode	100%		
$SOC_{\mathrm{min,IO}}$	Minimum SOC level of battery in island mode	0%		

APPENDIX D

Model parameters of hydro-powered industrial microgrid for voltage stability studies

This appendix presents the model parameters of a hydro-powered industrial microgrid used for voltage stability studies. The parameters in this appendix support the material in Chapter 6.

D.1 Network parameters

Table D.1: Network parameters of hydro-powered industrial microgrid. Refer to Figure 6.9 for the microgrid network diagram.

Symbol	Description	Value	Base power
X_{T1}	Transformer T1 leakage reactance	0.1 p.u.	54.5 MVA
X_{T2}	Transformer T2 leakage reactance	0.1 p.u.	60 MVA
L_{OH}	Overhead line lumped model series inductance	1.15 mH/km	-

Table D.2: Table D.2 continued.

Symbol	Description	Value	Base power
C_{OH}	Overhead line lumped model charging capacitance	0.01 μ F/km	-
R_{OH}	Overhead line lumped model series resistance	0.1436 Ω/km	-
G_{OH}	Overhead line lumped model shunt conductance	0 S/km	-

D.2 Hydro power plant and synchronous condenser parameters

Table D.3: Hydro power plant and synchronous condenser physical parameters [5].

Parameter	Description	Value
X_{d}	d-axis synchronous reactance	1.1 p.u.
$X_{\mathrm{d}}^{'}$	d-axis transient reactance	0.25 p.u.
$X_{\mathrm{d}}^{''}$	d-axis subtransient reactance	0.20 p.u.
X_{q}	q-axis synchronous reactance	0.70 p.u.
$X_{\mathrm{q}}^{''}$	q-axis subtransient reactance	0.20 p.u.
X_{l}	Leakage reactance	0.15 p.u.
$T_{\mathrm{d0}}^{'}$	d-axis transient open-circuit time constant	5 s
$T_{\mathrm{d0}}^{''}$	d-axis subtransient open-circuit time constant	0.05 s
$T_{\mathrm{q0}}^{''}$	q-axis subtransient open-circuit time constant	0.1 s
R_{s}	Stator resistance	0.003 p.u.
F	friction factor	0.0366 p.u.
H_{H}	Hydro power plant inertia constant	4.58 s
H_{SC}	Synchronous condenser inertia constant	1 s

Table D.4: Hydro power plant AVR and governor parameters. Refer to Figures 6.10 and 3.2 for the AVR and governor control diagrams. The AVR model of the synchronous condenser is identical with the HPP, as illustrated in Figure 6.19.

Parameter	Description	Value
AVR of hydro power plant and synchronous condenser		
$K_{\mathrm{p,AVR}}$	AVR proportional gain	13 p.u.
$K_{\mathrm{i,AVR}}$	AVR integral gain	8.7 rad/s
$V_{\mathrm{field}}^{\mathrm{min}}$	Minimum excitation voltage	-3 p.u.
$V_{\mathrm{field}}^{\mathrm{max}}$	Maximum excitation voltage	4 p.u.
T_{exc}	Exciter time constant	20 ms
Governor of hydro power plant		
$K_{\mathrm{p,G}}$	Governor proportional gain	1 p.u.
$K_{\mathrm{i,G}}$	Governor integral gain	0.1 p.u.
R_{G}	Governor droop gain	0.05 p.u.

Table D.5: STATCOM parameters. Refer to Figure 6.20 for the STATCOM control diagram.

Parameter	Description	Value
R_{V}	Virtual resistance	0.05 p.u.
L_{V}	Virtual inductance	0.1 p.u.
$K_{\mathrm{i,vc}}$	Voltage controller integral gain	62.8 rad/s
$K_{\mathrm{p,pc}}$	Power controller proportional gain	0.01 p.u.
$K_{\mathrm{i,pc}}$	Power controller integral gain	0.314 rad/s
K_{a}	Power controller active damping	0.02 p.u.
α_{pc}	Power controller filter bandwidth	62.8 rad/s
I^{max}	Converter maximum current limit	1.0 p.u.

D.3 Industrial load parameters

Table D.6 shows the industrial load parameters. The industrial load is composed of different load components including small and large motors, lighting and resistive loads. The motors are modeled using a typical dynamic model of an induction motor found in [6]. The parameters of the induction motor model are as follows: R_{s} and X_{s} are the stator leakage resistance and inductance, R_{r} and X_{r} are the rotor leakage resistance and inductance, X_{m} is the magnatizing reactance, and H is the inertia constant. The torque-speed curve of the mechanical load is modeled as second order. The lighting and resistive loads are modeled as ZIP model found in [7]. The expression of the ZIP model of the load is illustrated in (6.1) and (6.2). The coefficients p_1, p_2, and p_3, and q_1, q_2, and q_3 reflect the percentages of the Z, I and P characteristics of the load.

Table D.6: Industrial load parameters [8]

Parameter	Load component			
	Small motor	Large motor	Lighting	Resistive loads
R_s (p.u.)	0.031	0.013	-	-
X_s (p.u.)	0.100	0.067	-	-
X_m (p.u.)	3.2	3.8	-	-
R_r (p.u.)	0.018	0.009	-	-
X_r (p.u.)	0.180	0.170	-	-
H (s)	0.70	1.50	-	-
p_1	-	-	0.58	0.92
p_2	-	-	0.53	0.10
p_3	-	-	-0.11	-0.02
q_1	-	-	8.04	0.00
q_2	-	-	-11.42	0.00
q_3	-	-	4.38	0.00